Structural Investigation of Solid-Liquid Interfaces

Metal-Semiconductor Interface

Matthias Denk
Stuttgart, 2006

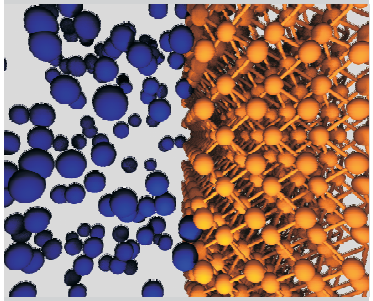

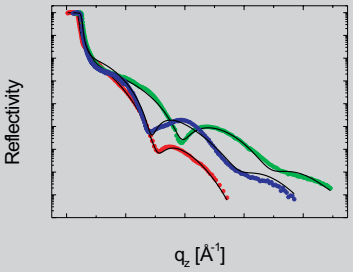

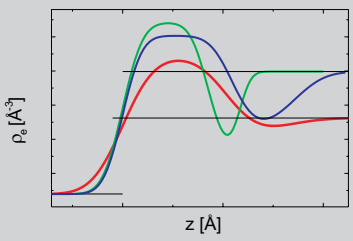

Max-Planck-Institut für Metallforschung in Stuttgart

Institut für Theoretische und Angewandte Physik der Universität Stuttgart

Structural Investigation of Solid-Liquid Interfaces

Metal-Semiconductor Interface

Von der Fakultät Mathematik und Physik
der Universität Stuttgart
zur Erlangung der Würde eines Doktors der
Naturwissenschaften (Dr. rer. nat.) genehmigte Abhandlung

vorgelegt von
MATTHIAS DENK
aus Ulm

Hauptberichter:	Prof. Dr. H. Dosch
Mitberichter:	Prof. Dr. C. Bechinger
Eingereicht am:	31. Juli 2006
Tag der mündlichen Prüfung:	29. November 2006

Institut für Theoretische und Angewandte Physik
der Universität Stuttgart

2006

II

Contents

Deutsche Zusammenfassung **V**
0.1 Motivation V
0.2 Theoretische und Experimentelle Details VI
0.3 Ergebnisse IX
0.4 Ausblick XIV

1 Introduction **1**

2 Basic Principles and Materials **5**
2.1 Introductory Considerations on Liquids 5
2.2 Previous work on Solid-Liquid Interfaces 9
2.3 Silicon Crystals and Surfaces 14
2.4 Liquid Metals: Lead and Indium 19
2.5 Pb and In interacting with Si 20

3 X-ray Scattering from Interfaces **34**
3.1 Opt. Prop. of Mat. in the X-ray Regime 34
3.2 Evaluating Reflectivity 39
3.3 Grazing incidence diffraction 48
3.4 Liquid Structure Factor 55

4 X-ray Experiments **59**
4.1 Beamline ID15A 59
4.2 Beamline Optics 60
4.3 Sample Manipulation 65
4.4 Detector system 68
4.5 In situ sample preparation 70
4.6 Data collection and treatment 72

5 Characterization of the free Si Surface **79**
5.1 Macroscopic Morphology 79

5.2 X-ray reflectivity measurements . . . 82
5.3 Excitation of Bragg Reflections . . . 84

6 The Interface In(liq.)-Si(100) 89
6.1 In Plane Structure . . . 89
6.2 Out of plane structure . . . 95
6.3 Discussion . . . 106

7 The Interface Pb(liq.)-Si(100) 117
7.1 Out of plane structure . . . 117
7.2 Discussion . . . 123

8 The Interface Pb(liq.)-Si(111) 129
8.1 In plane structure . . . 129
8.2 Out of plane structure . . . 136
8.3 Discussion . . . 141

9 The System Pb(bulk)-PbO-Si(111) 148
9.1 The Chemical System Pb-O-Si . . . 148
9.2 In plane structure . . . 150
9.3 Out of plane structure . . . 153
9.4 Discussion . . . 159

10 Conclusions and Outlook 160
10.1 Outlook . . . 164

A Experimental tricks and Beamtimes 165
A.1 Cleaning of Silicon . . . 165
A.2 Cleaning of Lead . . . 167
A.3 Cleaning of Indium . . . 167
A.4 Beamtimes at ID15A . . . 167

B Phase Diagrams 168

C Structure of Metal Adsorbates on Semiconductor Surfaces 170

Acronyms 172

Bibliography 173

Acknowledgments 188

Deutsche Zusammenfassung

0.1 Motivation

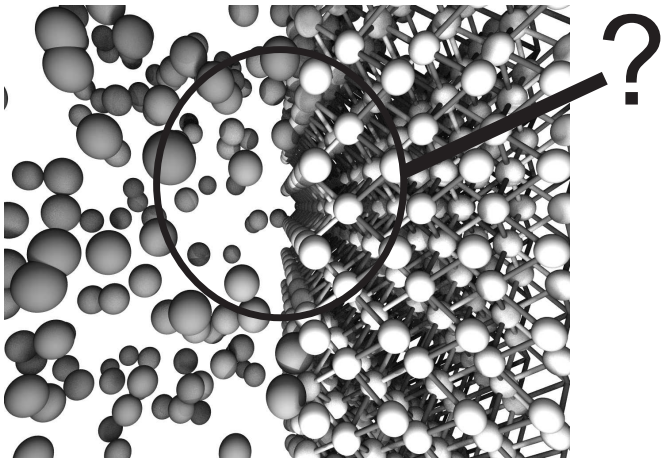

Abbildung 1: *Illustration einer Fest-Flüssig-Grenzfläche.*

Grenzflächen sind im täglichen Leben allgegenwärtig. Besonders im technischen Bereich nimmt ihre Bedeutung mit der rasanten Entwicklung der Nanotechnologie ständig zu. Die Grenzflächen zwischen einer Flüssigkeit und einem Festkörper (s. Abb. 1) sind nicht nur eine der wichtigsten in der Natur, sondern auch am schwierigsten zu untersuchen, da sie komplett im Volumenmaterial eingeschlossen und nicht davon zu trennen sind. Bisher gibt es nur sehr wenige Studien, die als Ziel die Klärung der Struktur der Fest-Flüssig-Grenzfläche haben.

Freie Oberflächen von flüssigen Metallen zeigen geschichtete Atomlagen parallel zur Oberfläche, s. z.B. [Reg95]. Theoretisch wurden solche Lagen bei Flüssigkeiten in Kontakt mit einer ebenen Wand vorhergesagt [Sno77], was bei Gallium auf Diamant auch experimentell nachgewiesen wurde [Hui97]. In diesen Arbeiten wurde die Wand als völlig unstrukturiert, nahezu glatt angenommen.

In den hier gezeigten Experimenten kam eine atomar strukturierte Wand zum Einsatz, um die Struktur der Flüssigkeit nicht nur senkrecht, sondern auch parallel zur Wand zu untersuchen. Diese Experimente sind nicht nur interessant um Rückschlüsse auf das Grenzflächenverhalten zu erlangen, sondern sie erlauben auch Rückschlüsse auf die lokale Struktur der Flüssigkeit.

In dieser Arbeit wurden hochenergetische Röntgenstrahlen zur Untersuchung von Fest-Flüssig-Grenzflächen eingesetzt, um einen Beitrag zum strukturellen Verständnis dieser Grenzflächen auf atomarer Skala zu liefern. Hochenergetische Röntgenstrahlen durchdringen einerseits Volumenmaterial, andererseits sind sie grenzflächenempfindlich.

Die lokale Punktsymmetrie der kurzreichweitigen Ordnung von monoatomaren Flüssigkeiten, wie es die meisten Metalle sind, ist seit Jahrzehnten Gegenstand der Forschung. Alle bisher vorgeschlagenen Modelle konnten jedoch experimentell nicht überprüft werden, wegen der unvermeidlichen Mittelung über Raum und Zeit, die bei Streuexperimenten auftritt. In normalen Streuexperimenten kann lediglich die isotrope radiale Verteilungsfunktion von Flüssigkeiten bestimmt werden.

Um Informationen über die lokale Punktsymmetrie der kurzreichweitigen Ordnung in Flüssigkeiten zu erlangen muss die azimuthale Symmetrie des Strukturfaktors, der durch den Röntgenstrahl gemittelt wird, aufgelöst werden. Dies wird durch eine feste Wand erreicht, die auf atomarer Skala strukturiert ist. Dadurch werden Teile der Flüssigkeitsstrukturen eingefangen und systematisch ausgerichtet. Die 4π-Zentralsymmetrie der Flüssigkeit wird aufgebrochen durch das Einführen einer definierten lokalen kurzreichweitigen Ordnung parallel zum Substrat [Rei00]. Eine langreichweitige Translationssymmetrie muss dabei nicht entstehen. Das Entstehen der Ordnung wird von der strukturellen und chemischen Wechselwirkung zwischen der Flüssigkeit und dem Substrat abhängig sein.

0.2 Theoretische und Experimentelle Details

System	1	2	3	4
Metall	In	Pb	Pb	Pb-PbO
Oberfläche	Si(100)	Si(100)	Si(111)	Si(111)
Dotierung	undotiert	n-dotiert (P)	n-dotiert (P)	n-dotiert (P)

Tabelle 1: *Untersuchte tief vergrabene Grenzflächen.*

Die in dieser Arbeit untersuchten Fest-Flüssig-Grenzflächen bestehen aus

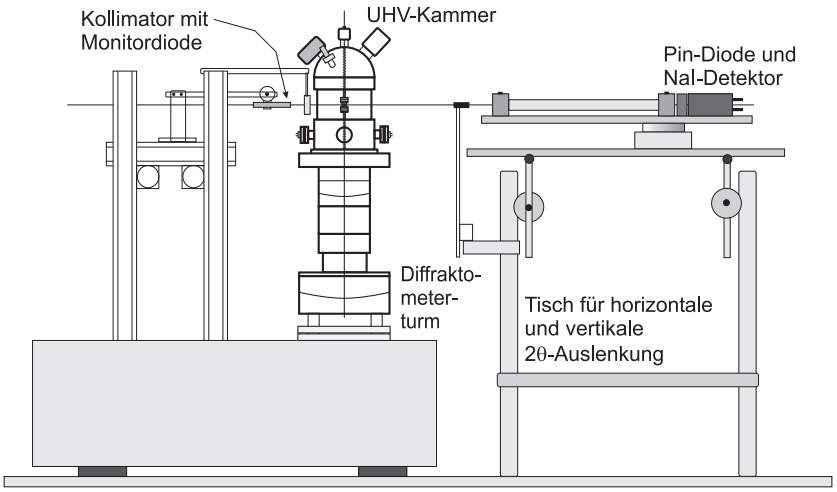

Abbildung 2: *Skizze des Präzissionsdiffraktometers mit der UHV-Probenkammer, dem Kollimator und dem Detektor. Der Detektor und die PIN-Diode sind auf einem separaten Tisch montiert.*

einem Silizium Einkristall in verschiedenen kristallographischen Orientierungen und einem flüssigen Metall. Als erstes Substrat kam eine Si(100)-Oberfläche zum Einsatz, die eine wohlbekannte Struktur besitzt [Eas80]. Als zweites verwendeten wir ein Si(111)-Substrat, das in der obersten Lage weniger dicht gepackt ist als eine Si(100)-Oberfläche. Die freie Si(111)-Oberfläche zeigt verschiedene Rekonstruktionen deren bekannteste die (7×7)-Rekonstruktion ist [Sch59].

Als flüssige Metalle kamen Indium und Blei, jeweils knapp über dem jeweiligen Schmelzpunkt, zum Einsatz. Für strukturelle Untersuchungen unterscheiden sich die beiden Metalle in zwei wesentlichen Punkten: im atomaren Durchmesser und der Gitterkonstante, so dass sie eine unterschiedliche Gitterfehlanpassung auf einer Silizium Oberfläche zeigen. In den chemischen Eigenschaften besteht der wesentliche Unterschied darin, dass Indium drei Valenzelektronen und Blei vier Valenzelektronen besitzt.

Für strukturelle Untersuchungen sind die beiden Systeme In-Si und Pb-Si ideal geeignet, da bei beiden keinerlei chemische Wechselwirkungen bekannt sind. Es können deshalb allein strukturelle Eigenschaften der Fest-Flüssig-Grenzfläche untersucht werden. Dass elektronische Wechselwirkungen ebenfalls eine Rolle spielen können, ist ein wichtiges Ergebnis dieser Arbeit und wird bei den Ergebnissen erläutert.

Bei der Untersuchung einer weiteren Grenzfläche, trat eine gezielte chemische Redoxreaktion an der tief vergrabenen Grenzfläche auf. Der

Ablauf der Reaktion konnte im zeitlichen Verlauf verfolgt werden. Die Grenzfläche setzte sich in diesem Fall aus Blei-Silizium und einer dazwischenliegenden Bleioxidschicht zusammen. Blei besitzt ein geringeres Redoxpotential als Silizium, so dass eine chemische Reaktion auftritt, wenn Bleioxid mit Silizium bei genügend hoher Temperatur in Kontakt kommt [Bit70, Mas90]. In Tab. 1 sind die vier untersuchten Grenzflächen zusammengefasst.

Jahrzehntelang war es unmöglich die Einschränkungen der oberflächensensitiven Untersuchungsmethoden zu überwinden und diese auf vergrabene Grenzflächen anzuwenden. Röntgenstrahlen durchdringen Volumenmaterial und sind nur unter bestimmten experimentellen Bedingungen oberflächenempfindlich. Eine dieser Methoden ist Streuung an der Grenz- oder Oberfläche unter streifendem Einfall (eng. grazing incidence diffraction, GID), bei der die besonderen Eigenschaften der Wechselwirkung von Röntgenstrahlen mit Materie benützt werden [Mar79, Dos92]. Mit dieser Methode kann die Eindringtiefe der Röntgenstrahlen senkrecht zur Grenzfläche präzise eingestellt werden, so dass strukturelle Eigenschaften von Grenzflächen tiefenaufgelöst gemessen werden können. Eine zweite Methode sind Messungen der Reflektivität, mit der Eigenschaften von Grenzflächen untersucht werden können.

In unserer Gruppe haben wir diese Methoden speziell auf tief vergrabene Grenzflächen erweitert. Dabei wurde die Energie der Röntgenstrahlen stark erhöht (> 70keV), so dass die Röntgenphotonen eine makroskopische Strecke im Material zurücklegen können. Die freie Oberfläche des Siliziums ist kein Hindernis, da die Grenzflächenstreuung bei nahezu senkrechtem Einfall vernachlässigbar ist. Erst an der vergrabenen Grenzfläche, auf die der Röntgenstrahl streifend fällt, tritt Streuung auf.

Die charakteristische Größe einer Grenzfläche in Bezug auf Röntgenbeugung ist der kritische Winkel α_c, unterhalb dem die Grenzfläche Strahlung komplett reflektiert. Der kritische Winkel ist abhängig von der Wellenlänge der Strahlung ($\alpha_c \propto \lambda \propto 1/E$). Das bedeutet, dass bei höheren Energien die Winkel sehr viel kleiner werden, was wiederum kleinere Strahlgrößen und größere Proben notwendig macht. Dadurch nehmen die experimentellen Herausforderungen enorm zu, denn die kleinen Winkel müssen mit entsprechend größerer Präzision kontrolliert werden. Der Vorteil besteht darin, dass die Absorption β der verwendeten Materialien bei größerer Energie stärker abnimmt als der Winkel ($\beta \propto \lambda e^{-1/\lambda}$).

Die notwendigen experimentellen Bedingungen sind nur an modernen Synchrotrons der dritten Generation erfüllt. Die in dieser Arbeit vorgestellten Experimente wurden in Grenoble an der ESRF am Messplatz ID15A durchgeführt, an dem für die jeweiligen Messkampagnen ein spezielles hochpräzises Diffraktometer aufgebaut wurde (s. Abb. 2). Der Röntgenstrahl

wurde entweder mit Hilfe eines Kollimators auf 8μm reduziert oder mit speziellen zusammengesetzten Linsen auf 6μm fokussiert. Die Auflösung des Einfalls- und Ausfallwinkels konnte besser als ein tausendstel Grad kontrolliert werden.

Die Fest-Flüssig-Grenzflächen wurden in einer mobilen UHV-Kammer präpariert und in situ zum Synchrotron (ESRF) transportiert, an dem die Experimente durchgeführt wurden.

0.3 Ergebnisse

An einer Pb(fl.)-Si(100) Grenzfläche konnte in einer früheren Arbeit [Kle00, Rei00] eine Modulation des Strukturfaktor von flüssigem Blei parallel zur Grenzfläche nachgewiesen werden. Der Strukturfaktor zeigt eine fünf-zählige Symmetrie, deren Ursprung in der Struktur der Volumenflüssigkeit zu finden ist.

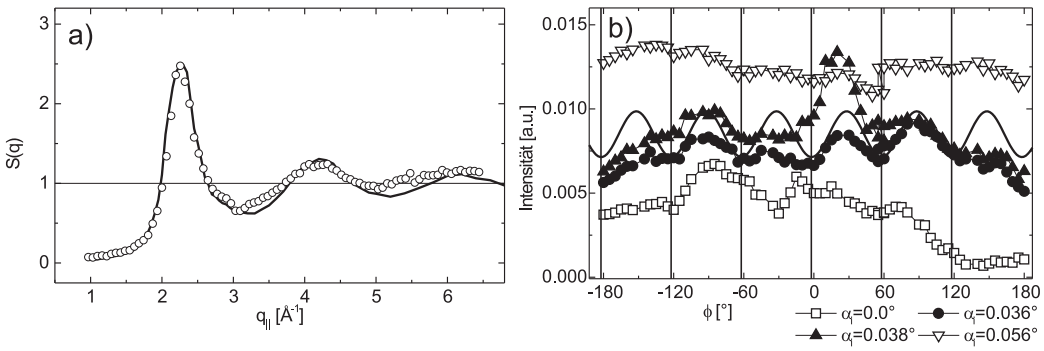

Abbildung 3: *a) Strukturfaktor von flüssigem Blei an einer Pb(fl.)-Si(111)-Grenzfläche (Punkte). Die durchgezogene Linie ist der Strukturfaktor von Blei als Volumenflüssigkeit [Was80]. b) Modulation des ersten Maximums des Strukturfaktors an der Grenzfläche als Funktion des azimuthalen Winkels ϕ senkrecht zur Si(111)-Oberfläche mit dem Einfallswinkel α_i als Parameter. Die sechs Richtungen des Si$\{2\bar{2}0\}$-Reflexes sind durch senkrechte Striche gekennzeichnet. Eine Sinus-Funktion hebt die sechs-zählige Modulation des Strukturfaktors hervor.*

In dieser Arbeit wurde der Flüssigstrukturfaktor an der Grenzfläche von In(fl.)-Si(100) und Pb(fl.)-Si(111) gemessen. In beiden Fällen konnte nachgewiesen werden, dass der Strukturfaktor demjenigen der Volumenflüssigkeit entspricht (s. Abb. 3.a). An der Pb(fl.)-Si(111) Grenzfläche konnte

eine Modulation des Strukturfaktors als Funktion der Substratorientierung nachgewiesen werden. Dazu wurde die Intensität des ersten Maximums des Flüssigstrukturfaktors parallel zur Grenzfläche als Funktion des azimuthalen Winkels ϕ der Grenzfläche gemessen. Die effektive Streutiefe Λ_{eff} der Röntgenstrahlen ist gegeben durch den Einfallswinkel α_i und den Bereich des Ausfallwinkels α_f über den integriert wird.

Abb. 3.b zeigt die gemessene Intensität bei verschiedenen effektiven Streutiefen Λ_{eff}. Bei $\alpha_i = 0.0°$ ($\Lambda_{eff} = 39$Å) ist keine Modulation zu sehen. Durch Streuung an den Kanten der Probe wurde das gemessene Signal von geometrischen Effekten beeinflusst. Bei $\alpha_i = 0.056°$ ($\Lambda_{eff} > 300$nm) zeigte das Signal fast ausschließlich Streuung an der Volumenflüssigkeit. Die gemessene Intensität bei $\alpha_i = 0.036°$ ($\Lambda_{eff} = 80.4$Å) und bei $\alpha_i = 0.038°$ ($\Lambda_{eff} = 109$Å) zeigte eine Intensitätsschwankung, die direkt mit einer Modulation des Flüssigstrukturfaktors an der Grenzfläche zusammenhängt.

Die gefundene sechs-zählige Modulation der Intensität des Strukturfaktors von $8\% \pm 4\%$ kann mit einem Modell von sechs dicht gepackten Pb-Atomen um ein Pb-Atom herum erklärt werden. Diese Anordnungen sitzen auf einem Si-Substratatom. Das Modell ist konsistent mit den Beobachtungen von Pb auf Si(111) in dünnen Schichten bei Temperaturen über 300°C [Wei92]. Die Struktur besitzt keine langreichweitige, sondern lediglich lokale Ordnung. Sie ist die bevorzugte Struktur der Pb-Atome auf der Si(111)-Oberfläche.

Reflektivitätsmessungen

An drei verschiedenen Metall-Silizium-Grenzflächen wurden Reflektivitätsmessungen durchgeführt. die reflektierte Intensität konnte jeweils über neun Größenordnungen detektiert werden, was einem senkrechten Impulsübertrag von $q_z = 0.55$Å^{-1} bis $q_z = 0.9$Å^{-1} entsprach.

In Abb. 4 sind die drei Reflektivitäten dargestellt. An allen drei Grenzflächen weicht die Reflektivität von der reinen Fresnelreflektivität ($R_F \approx (q_c/q_z)^4$) deutlich ab. An den Grenzflächen lag keine korrelierte Rauigkeit vor.

Die Reflektivität kann jeweils mit einem Elektronendichtemodell bestehend aus zwei Lagen unterschiedlicher Dichte zwischen dem Silizium und der Volumenflüssigkeit angepasst werden. Die angepassten Reflektivitäten sind als durchgezogene Linie in Abb. 4 gedruckt. In Abb. 5 sind die angepassten Elektronendichteprofile senkrecht zur Grenzfläche dargestellt. Die einzelnen Lagen sind durch die Rauigkeit des Siliziumsubstrats von $\sigma = 5$Å $- 10$Å ausgeschmiert.

Einerseits gibt es zwischen den Elektronendichteprofilen systematische

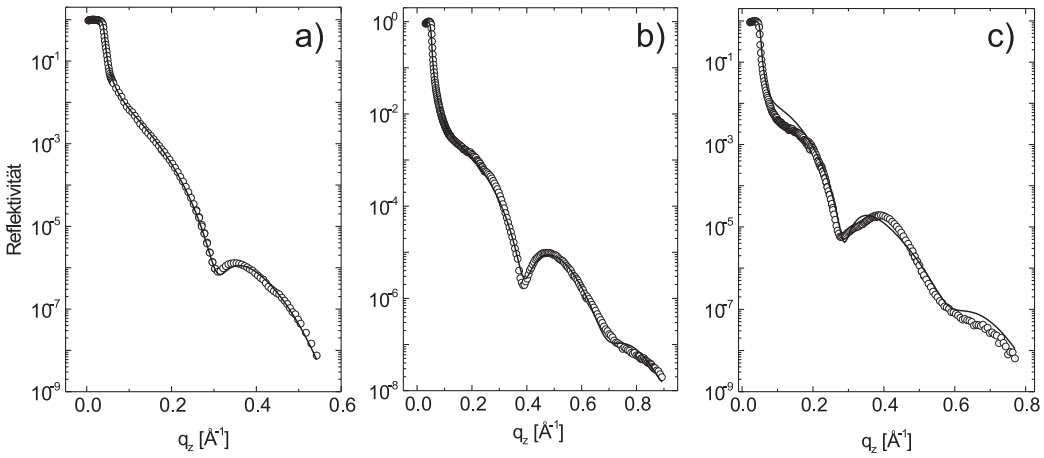

Abbildung 4: *Reflektivitätsmessungen an drei Fest-Flüssig-Grenzflächen. Die Kreise geben die Messwerte an und die durchgehende Linie stellt den Fit dar. a) In(fl.)-Si(100), b) Pb(fl.)-Si(100) und c) Pb(fl.)-Si(111).*

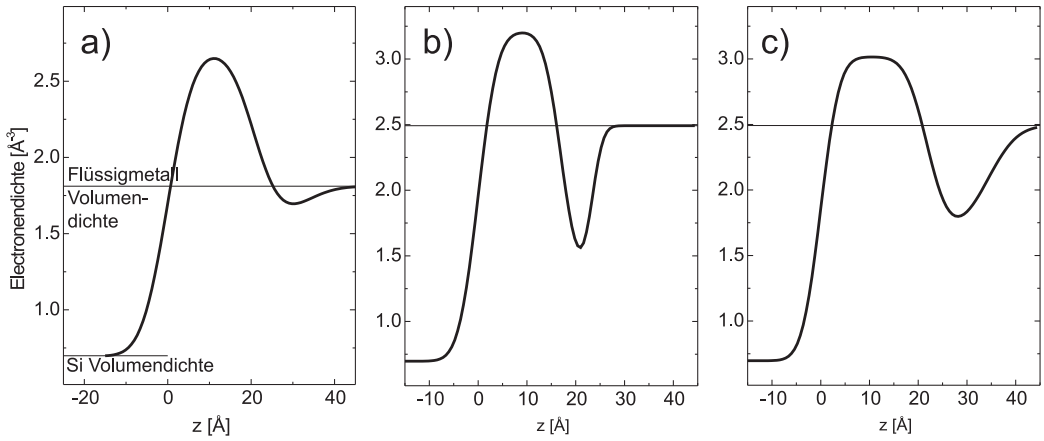

Abbildung 5: *Aus den Reflektivitätsmessungen in Abb. 4 ermittelte Elektronendichteprofile. a) In(fl.)-Si(100), b) Pb(fl.)-Si(100) und c) Pb(fl.)-Si(111).*

Unterschiede jenseits der statistischen Unsicherheiten, andererseits sind sie qualitativ ähnlich. Im Vergleich zur Volumenelektronendichte zeigt die erste Lage eine stark erhöhte Dichte und die zweite Lage eine stark erniedrigte Dichte. Tabelle 2 fasst die Eigenschaften der Profile zusammen und setzt sie in Beziehung zu spezifischen Größen der Metalle (Volumendichte ρ_0, Atomradius r_0). l_{sum} bezeichnet die Gesamtdicke der Dichtemodulation und l_{max} die Dicke der Lage mit erhöhter Dichte. Konventionelle Modelle (z.B. mit Hilfe geometrischer Packung oder der Thomas-Fermi-Abschirmung) zur Erklärung der gefundenen Profile sind unzureichend.

System	In(fl.)-Si(100)	Pb(fl.)-Si(100)	Pb(fl.)-Si(111)
$\rho_{\mathrm{max}}/\rho_0$	1.48	1.29	1.21
l_{sum}/r_0	25.9 (41Å)	12.5 (21.8Å)	18.4 (32.2Å)
l_{max}/r_0	15.5 (24.5Å)	8.0 (14Å)	10.9 (19Å)
$l_{\mathrm{sum}}/l_{\mathrm{max}}$	1.67 ± 0.22	1.56 ± 0.18	1.69 ± 0.14

Tabelle 2: *Vergleich der generischen Eigenschaften an den untersuchten Metall-Silizum Grenzflächen.*

Bisher gibt es kein abschließendes Modell, das die Elektronendichteprofile erklären kann. Die Siliziumoberfläche hebt ihre Rekonstruktion auf, wenn sie in Kontakt mit dem flüssigen Metall kommt. Dadurch entstehen ungebundene Atombindungen (dangling bonds), die ein Elektron aus der Flüssigkeit aufnehmen können. Unter der Annahme, dass dies zu einer geladenen Oberfläche führt und der weiteren Annahme, dass innerhalb des Metalls eine zweite geladene Fläche entsteht, ist es denkbar, dass sich diese gegensätzlich geladenen Flächen anziehen, wie in einem Kondensator. Die entstehende Kraft erzeugt einen Druck auf die Flüssigkeit, der zu einer Dichteerhöung führen kann. Aus der Flächendichte der ungebundenen Si-Bindungen ($4/a_{\mathrm{Si}}^2$ für Si(100) und $2.3/a_{rm}^2$ für Si(111)[1]) ergibt sich ein maximaler Druck von 267GPa für die Si(100)- und von 88.2GPa für die Si(111)-Oberfläche. Unter hohen Drücken ändert sich die Dichte von Metallen mit $\rho/\rho_0 = 0.75 \cdot p^{0.17}$. Aus der maximalen Dichteerhöhung ρ_{max} errechnet sich ein Druck an der jeweiligen Grenzfläche der in Tab. 3 dargestellt ist. Der aus den Elektronendichteprofilen berechnete Druck ist sehr viel niedriger als der mögliche Druck in Folge der Dichte der freien Si-Bindungen. Dies kann daher rühren, dass die Rekonstruktion nicht vollständig aufgehoben wird. Es gibt einen Trend, dass bei geringerer Dichte der freien Si-Bindungen die Dichteerhöhung ebenfalls geringer ist.

[1] Gitterkonstante von Silizium $a_{\mathrm{Si}} = 5.4309$Å

	In(fl.)-Si(100)	Pb(fl.)-Si(100)	Pb(fl.)-Si(111)
$p_{\max}$	56GPa	24GPa	16.7GPa

Tabelle 3: *Maximaler Druck im flüssigen Metall berechnet aus der maximalen Dichteerhöhung.*

Bleioxid-Grenzfläche

An der Grenzfläche mit der Schicht aus Bleioxid zwischen dem Siliziumsubstrat und dem Blei konnte durch Strukturfaktormessungen nachgewiesen werden, dass es sich um amorphes PbO handelt. Aus den Relflektivitätsmessungen ergab sich eine Dicke der Schicht von etwa 260Å. Über einen Zeitraum von sechs Tagen wurden mehrere Reflektivitätsmessungen durchgeführt.

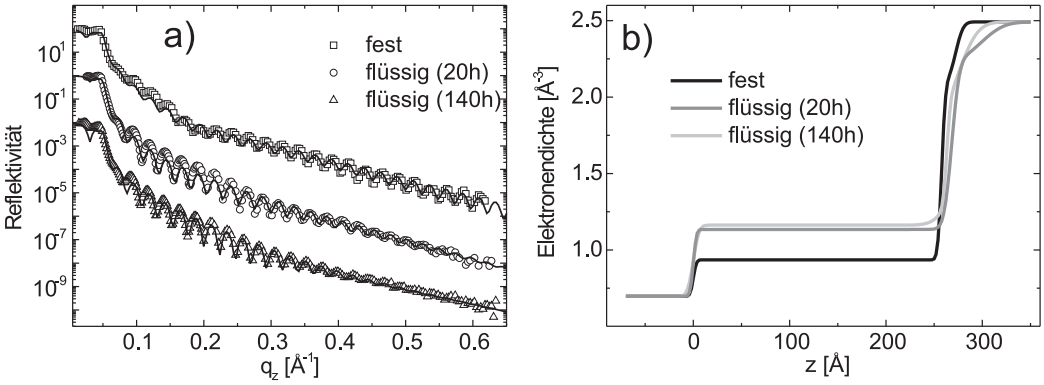

Abbildung 6: *a) Reflektivitätsmessungen an einer Pb(fest/flüssig)-PbO-Si(111) Grenzfläche zu verschiedenen Zeiten: im festen Zustand des Bleis und nach dem Schmelzen nach 20h und 140h. Die Linien sind entsprechende Fits. b) Aus den Fits ermittelte Elektronendichteprofile.*

In Abb. 6.a sind drei Messungen dargestellt. Die erste mit Blei in festem Zustand, die zweite nach dem Verflüssigen und die dritte nach sechs Tagen. Das PbO selbst bleibt fest, trotzdem ist bereits anhand der Reflektivitäten eine leichte Änderung der Grenzfläche erkennbar.

In Abb. 6.b sind die angepassten Elektronendichteprofile dargestellt. Nach dem verflüssigen verbreitert sich die Grenzfläche zwischen der PbO-Schicht und dem Blei. Die wesentliche Änderung ist eine Dichtezunahme der Pbo-Schicht, zusammen mit einer Zunahme der Dicke von 4%.

Als Ursache für die Änderung der PbO-Schicht wird angenommen, dass Pb^{2+}-Ionen zu Pb-Atomen durch Si-Atome reduziert werden, die zu Si^{4+}-

Ionen oxidiert werden und SiO_2 bilden. Damit dieser Prozess stattfinden kann, sind Temperaturen über 600K nötig, erst dann ist die Diffusion in der PbO-Schicht groß genug. Nach einiger Zeit ($\sim$ 20h) hat sich eine passivierende SiO_2-Schicht auf der Si(111)-Oberfläche gebildet und die Redoxreaktion kommt zum Erliegen. Die amorphe PbO-Schicht hat sich mit Pb angereichert und besitzt eine größere Dichte.

0.4 Ausblick

Um das Verständnis der Struktur der flüssigen Metalle senkrecht zu fest-flüssig Grenzflächen voranzutreiben sind neben theoretischen Untersuchungen weitere Experimente notwendig, bei denen systematisch einzelne Parameter der Grenzfläche verändert werden. Da die Präparation von Siliziumoberflächen gut beherrscht wird, bieten sich Siliziumkristalle in weiteren Orientierungen für Experimente an. Die Dotierung der Kristalle dürfte ebenfalls eine Rolle spielen, da davon der Elektronentransport im Halbleiter abhängt. So könnte dieser Parameter systematisch über mehrere Größenordnungen vom n-Typ zum p-Typ geändert werden.

Ebenfalls interessant wäre es, elektrische Felder über die Grenzfläche anzulegen, da dies zu interessanten Ladungsverschiebungen führen könnte. Besonders reizvoll ist daran, dass die Feldstärke in situ während des Experiments geändert werden könnte und so zu einer Änderung des Ladungsübertrages an der Grenzfläche führt.

Chapter 1

Introduction

Surfaces and interfaces between different materials are omnipresent in everyday life. As important as interfaces between the components of mechanical or electronic devices have always been - their importance has increased tremendously with the advent of nanotechnology. If we define the term "bulk material" by dimensions larger by orders of magnitude than atoms, we will soon reach the stage where some devices do not contain bulk material anymore. Solid-liquid interfaces are among the most important in nature and technology. Alas, they are also most difficult to study, since they are completely encased in bulk material (buried). Removing the liquid changes the interface to a surface, cutting the sample perpendicular to the interface is obviously not an option either. Due to these difficulties, there are very few studies of solid liquid interfaces, as reviewed later in this work. High energy x-rays, as they are used in our study, are up to now the only probe which can penetrate bulk material and are sensitive to interfaces at the same time.

As a system, we have chosen the interface between a liquid metal and a semiconductor crystal. The liquids were molten monatomic metals at temperatures slightly above their melting temperature. From the main groups of the elements indium and lead were taken. The liquids were investigated as separate systems. Indium and lead have some similar properties like Fermi energy and low melting temperatures, but show major differences in structural properties like lattice constants and atomic diameter, which leads to a different lattice mismatch with respect to a given surface. Furthermore they are chemically different with three (In) and two or four (Pb) valence electrons.

The solid wall consisted of a silicon single crystal in several crystallographic orientations. It was a basic aim of the studies to use a solid wall that was precisely structured on the atomic length scale, which is the case for a silicon single crystal surface. The investigated interfaces were deeply

buried between the bulk liquid and a thick solid block of the crystal at defined orientations.

As the first substrate we took a Si(100) surface, which has a well known surface structure [Eas80]. The next step was a change of the substrate to Si(111), which is less dense packed in the topmost layer than the Si(100) surface. The free Si(111) surface shows several reconstructions, (7×7) [Sch59], (2×1) [Sch59], or even (1×1) [Eas80]. For all the systems investigated the in plane and out of plane structure was determined.

The fourth interface investigated incorporated a redox reaction and time-resolved experiments at deeply buried interfaces. We picked again the lead-silicon system with an intervening lead-oxide layer. Pure Pb and Si do not alloy or form chemical compounds at any temperature, nor do they show a chemical reaction except for the submonolayer regime [Eas80, Mas90]. However, their oxides do mix and form compounds [Bit70]. Lead is more inert to oxygen than silicon, thus a chemical reaction is expected for a PbO-layer in contact with Si.

For free liquid metal surfaces it is known that they show stratified layers of atoms parallel to the surface, e.g. [Reg95]. Theory predicts such layering of liquids in contact with flat walls [Sno77]. The aim of our experiments was the exploration of the liquid structure in contact with a structured substrate not only to reveal the structure of the interface but to conclude as well on the structure of the liquid itself. The local point symmetry of the short-range order in simple monatomic liquids, as most of the liquid metals are, has been of constant interest for decades. All of the proposed models remained experimentally inaccessible owing to the unavoidable averaging in space and time in scattering experiments. Normal scattering experiments can determine only the isotropic radial distribution function of liquids. Radial distribution functions and its details have been measured since the early stages of x-ray scattering [Fri13, Gin43].

To reveal the local point symmetry of the short-range order in liquids the azimuthal symmetry of the structure factor averaged by the x-ray beam has to be broken. This is done by introducing a solid wall, which is structured on an atomic length scale. This captures and aligns parts of the building blocks of the liquid at the interface in a systematic way and thus breaks the 4π-central symmetry [Rei00], introducing a defined local short-range order parallel to the substrate. It does not necessarily lead to a long-range translational order. The aforementioned effects will depend on the structural and chemical interaction between the liquid and the solid substrate.

For decades it was impossible to overcome the restrictions of the surface

sensitive techniques for structural investigations to be extended to the exploration of buried interfaces. A few years after the invention of atomic force microscopy (AFM) the technique was applied to solid-liquid interfaces with the restriction of having only thin aqueous solutions. It became possible to investigate the solid adjacent to a liquid [Sch87, Dra89].

X-rays can penetrate deeply into bulk material and are surface sensitive under special experimental conditions only. One such method is grazing incidence diffraction (GID). It uses the special properties of the interaction between x-rays and matter to be surface sensitive. It was introduced in 1979 by Marra et al. [Mar79]. With this technique the penetration depth of the x-rays perpendicular to the plane of scattering can be tuned precisely allowing to measure structural properties truly depth resolved. X-ray reflectivity measurements are an additional tool to probe the surface structure.

In our group we extended these x-ray techniques. By increasing the x-ray energy, photons can travel macroscopic distances in bulk material. In theory for electromagnetic waves, as x-rays are, there is no fundamental difference between scattering at a surface and a deeply buried interface. One approach for experimental realization consists of systems of thin layers by penetrating all layers from top down to the substrate [Tol99]. Yet, it is often difficult to separate desired signals from a single interface from perturbing signals caused by other interfaces.

Our approach utilizes the angular dependence of interaction with interfaces and the penetration depth of hard x-rays: under almost perpendicular incidence the refraction and reflection is extremely weak and if the energy of the photons is high enough the absorption is weak, too. Thus a deeply buried interface can be accessed from the side of the sample by high energetic x-rays. This method was first used by Huisman et al. [Hui97] in reflectivity measurements at medium x-ray energies.

The important characteristic feature of an interface is the critical angle α_c, below which the interface shows total external reflection. The critical angle depends on the x-ray wave length as $\alpha_c \propto \lambda \, (\propto 1/E)$. This means that at higher energies one has to work with much smaller angles, which requires smaller beam sizes and larger samples. The experimental demands are much higher, too, the angles have to be controlled with a very high precision. The advantage of the higher energy (shorter wavelength) is the reduced absorption β that depends on the wave length as $\beta \propto \lambda e^{-1/\lambda}$. Because of the exponential dependence of the absorption from the x-ray wavelength, it decreases faster than the critical angle. Thus, one gains more intensity by using a higher energy than one looses due to the decreased angle.

We extended and completed this technique to grazing incidence diffraction and reflectivity measurements at deeply buried interfaces, independent of the

samples used.

The structure of the thesis is as follows: In Chap. 2 an overview of the current knowledge about solid-liquid interfaces is presented. In Chap. 3 an introduction to the physical fundamentals of scattering at interfaces and its extension to buried interfaces is given and the required data treatment is described. In Chap. 4 the special experimental techniques to collect high quality data are depicted and a short description of the beamline at ESRF where the experiments were carried out is given. Included in this chapter is a comprehensible description of the in situ preparation process of the solid-liquid interfaces used in the experiments. In Chap. 5 experiments and calculations for free silicon surfaces are presented, which are necessary to discuss the interface sensitive signals in the later chapters. The measurements at the four different interfaces investigated are presented in Chaps. 6 to 9. Chap. 10 gives a summary and links the results of the investigated interfaces.

Chapter 2

Basic Principles and Materials

In this chapter an overview of the literature and research done in this field is given. The basic properties of the system and materials investigated in this work are introduced. Some key data to the specific *solids* and *liquids* that we used and the reason why these properties are important to perform the experiments in this work are presented.

2.1 Introductory Considerations on Liquids

The problem in understanding liquids is the lack of a simple model like the ones for solids and gases. Ideal solids can be modeled by the atoms that are regularly arranged at the lattice points. This regular arrangement of atoms is long-ranged and three-dimensional. Although thermal vibrations of the atoms are present the average positions are fixed. For the ideal gas the simplest model states that each atom can move freely throughout the volume, in which it is contained and the whole volume is taken by the gas. These simple models yield good results and can be extended to describe real substances. Unfortunately, there does not exist such a simple model for liquids. From a macroscopic point of view, the most characteristic feature of a liquid is its inability to support shearing. This is manifest in its capacity to flow. A liquid fills a container completely up to its own volume, whereas its compressibility is almost as low as for the corresponding solid. It is not possible to regard a liquid as a very dense gas nor a solid with atoms that are randomly oriented.

The simplest model for liquids assume the particles of the liquid as *hard spheres*. Their interaction is modeled by a complete repulsion when getting in contact and a weak attraction following a power law (e.g. Lennard-Jones type). This model proves useful for some aspects of liquid structures and

phase diagrams. It can be even applied to real liquids with some extensions to the model (e.g. [Jar69, vL75]). However, the simple model has its limits if one tries to do experiments with macroscopic hard balls and problems occur with container wall induced order [Ber59]. Liquids are densely packed, their packing fraction is almost as high as in the corresponding solid phase. The *packing fraction* η is defined as

$$\eta = \frac{N}{V} \cdot \frac{4}{3}\pi \left(\frac{\sigma}{2}\right)^3 = \frac{\pi}{6} n\sigma^3 \tag{2.1}$$

with σ the hard-sphere diameter and $n = N/V$ the number density, N being the number of spheres in Volume V. Liquids must be close packed with a lack of long range order though. This led to the concept of *random close packing* (RCP) [Tor00, Ell02]. Literature values are ranging from $\eta = 0.60$ to $\eta = 0.68$ of the maximum random packing fraction. One difficulty results from the fact that the packing fraction in experiments with randomly packed hard spheres depend on the method of reaching the packed state [Tor00]. The densest possible packing fraction for identical spheres is $\eta = \pi/\sqrt{18} \approx 0.741$, which is found in face-centered cubic (fcc) or hexagonal close packed (hcp) crystals.

It turned out that many aspects of the structure of real bulk fluids are nearly identical to those aspects of the bulk hard-sphere fluid [Sno77]. The bulk thermodynamics and structure factor of simple monatomic liquids, excluding transition and rare-earth metals, have been under considerable progress making it possible to calculate these properties independently from experiments. In this context structure refers to the structure factor of scattering experiments and the radial distribution function (s. Sec. 3.4). Interionic potentials can be calculated using pseudopotential theory and the effective pairwise potentials give a rather good description of the observed structure and several thermodynamic properties [Eva80]. Otherwise there are still open questions relating to the local structure of liquids.

It is useful to introduce the pair distribution function $g(r)$. It gives the probability of finding two atoms in the liquid at a distance r from each other. Then the quantity

$$4\pi\rho g(r) r^2 \mathrm{d}r \tag{2.2}$$

gives the mean number of atoms inside a spherical shell of radius r and thickness dr centered on an atom. Of course this relates to the average liquid atom. The pair distribution function is connected to the structure factor $S(q)$ of a liquid via a Fourier transformation. The structure factor measures the pair correlations within the liquid. A typical pair distribution function and

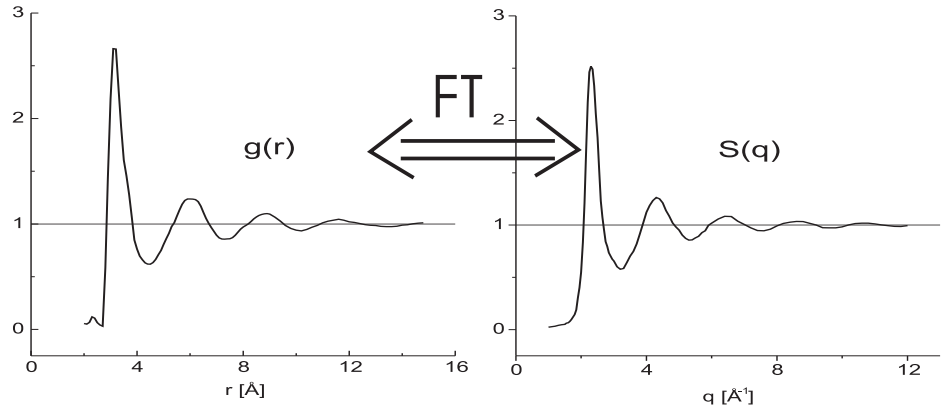

Figure 2.1: *Pair distribution function g(r) and structure factor S(q) of liquid indium. Temperature* 160°C. *Taken from [Was80]*

structure factor are illustrated in Fig. 2.1 for liquid indium slightly above its melting temperature. The mathematical details are discussed in Chap. 3.

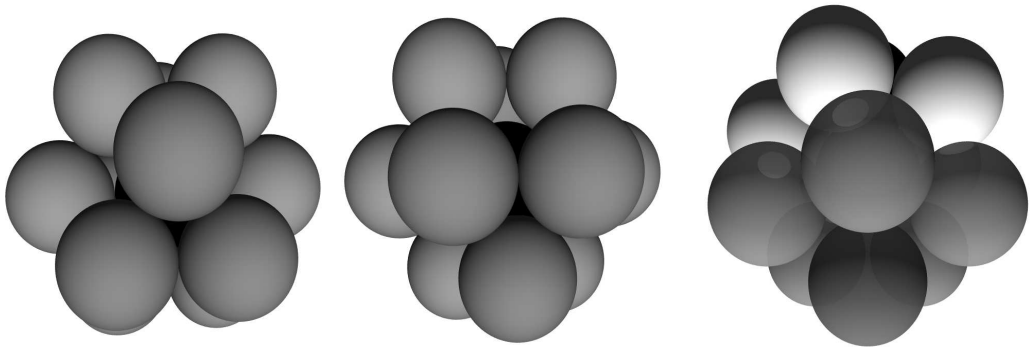

Figure 2.2: *Three different ways of dense packing of twelve atoms: hcp-cluster, fcc-cluster, icosahedral cluster.*

The integral over Eq. 2.2 gives the average number of atoms neighboring a central atom if the integration range is chosen appropriately. It gives only the average number and does not yield the short range order of the atoms in the liquids.

All liquids can be substantially supercooled by about 15%-25% of the absolute melting point [Fra52]. Surprisingly, even the simple monatomic liquids of metals can be supercooled, which leads directly to the assumption that the structure of liquids must be quite different than the long *and* short range order of solids: There are three ways of packing twelve balls as close

as possible around a centered one: the fcc and hcp configuration and an icosahedral formation showing five-fold symmetry. These three clusters are shown in Fig. 2.2. The icosahedral packing cannot be continuously extended in three dimensions. The surrounding balls of the icosahedron do not touch each other, they are only in contact with the center ball. If there are mutually attracting deformable spheres (like atoms), they will be a little closer to the center atom in the icosahedral building block. This allows the surrounding atoms to be in contact with each other resulting in a locally denser packing of the atoms. It has been conjectured for more than 50 years that liquids with centrosymmetric interactions are composed of icosahedral building blocks [Fra52]. Freezing of such a liquid will require a substantial rearrangement, which is an effective nucleation barrier and thus the solidification can be seriously supressed.

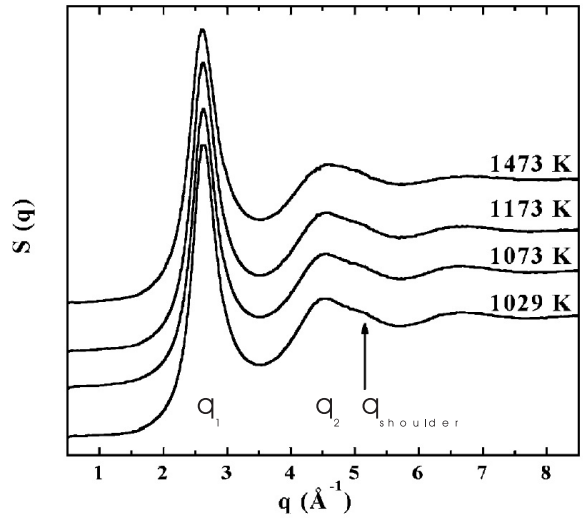

Figure 2.3: *Temperature dependent structure factor with increasing shoulder at the second peak indicating partial icosahedral order. Taken from [Kel03]*

Since the early aforementioned conjecture there has been vast theoretical and experimental work on the subject of the short-range order of liquids. Theoretical work was carried out with means of analytical mathematics (e.g. [Wer63]), geometrical calculations (e.g. [Ber59, Nel89]), Monte Carlo studies (e.g. [Sno77]) or molecular dynamics studies (e.g. [Ste83, UBn02]). On the experimental side the research with real liquids was mostly restricted to the precise determination of the structure factor in neutron and x-ray scattering (e.g. [Sha60]) or the consideration of model systems like macroscopic hard balls [Ber59] and colloids [And02]. Icosahedral order was mainly deduced

from integrations over parts of the pair distribution function $g(r)$ of liquids. The integral gives the averaged number of neighboring atoms in a certain range (e.g. next neighbor) and from this number conjectures about the local order were made. On the other hand for liquid mixtures the relative locations q_i of the first two peaks in $S(q_i)$ give a measure of the icosahedral order in the liquid. For a perfect icosahedron the theoretical ratio of the two positions is $q_1/q_2 = 1.71$. Furthermore, an additional shoulder on the high q-side of the second peak of the structure factor with a ratio of $q_{shoulder}/q_1 = 2.04$ indicates little distortions of the icosahedral order of the liquid [Kel03] (s. Fig. 2.3). The structure factor of bulk liquids can be routinely measured [Was72] and can be found tabulated on the internet [Was80].

The true short range order of liquids has still to be revealed. Only the progress of modern experimental techniques especially third generation synchrotrons and the upcoming free electron lasers as well as femtosecond laser pulses will allow to study the structural and dynamical properties of liquids in more details. One of the newest studies is about the huge structural change upon melting of crystalline aluminum, which was measured time resolved. The change is very rapid and after only a few picoseconds the Bragg peaks of the crystal are lost [Siw03].

2.2 Previous work on Solid-Liquid Interfaces

Solid-liquid interfaces are part of our everyday life. Many processes in life sciences appear at these interfaces. In technology it appears for example in the Czochralski method to grow silicon single crystals. For technical aspects it is growing in importance with the advancement of micro- and nano-technology. A fancy development is the chemical lab on an integrated circuit.

For research solid-liquid interfaces are split in different classes. It can be a solid material and its melt, it can consist of chemically non-interacting substances and the solid can be crystalline or amorphous. In models it is often a flat hard wall. The liquid can be simple monatomic, can consist of large and dipolar molecules, or even colloids. We will focus on crystalline surfaces in contact with simple monatomic liquids that do not chemically interact.

Another type of solid-liquid interfaces is the one between an electrode (electronic conductor / metal) and an electrolyte (ionic conductor). All electrochemical reactions take place at these interfaces. It was proposed by von Helmholtz [vH79] 125 years ago, that there exists an *electric double layer* at electrode-electrolyte interfaces. The existence of a double layer is not in doubt, yet, there is still a lack of *direct* experimental evidence. For a correct

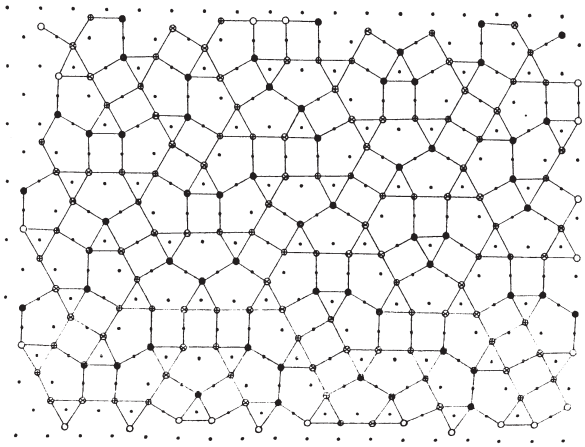

Figure 2.4: *Geometrical constructed solid-liquid interface based on three rules, the first layer. Taken from [Spa75]*

treatment the electronic properties of the metal electrode have to be taken into account, since there is a spill over of the electrons from the metal into the electrolyte [Sch96, Smo41].

A significant model for the structure of the liquid at a solid-liquid interface was proposed by F. Spaepen [Spa75]. It is developed on pure geometrical considerations of hard spheres. Only three rules are necessary to construct the interface as a random dense packed phase: first, tetrahedral symmetry is preferred, second, octahedral symmetry is forbidden, and third, the density is maximized. The first rule accounts for the assumed bulk structure of liquids (s. Sec. 2.1, [Fra52]), the second for the sign of crystalline symmetry, because the octahedron is the smallest possible 3D-building block in crystals, and the third rule accounts for experimental findings that liquids are only slightly less dense than the corresponding solids. Thus, an interface can be constructed, that shows five-fold symmetry at the scale of short-range order and no density defect. As an example construction see Fig. 2.4. The constructed interface of this model basically consists of just two altered layers until the bulk liquid is reached.

The structure of solid-liquid interfaces in perpendicular direction to the interface was first investigated with Monte Carlo studies of hard spheres near a flat wall. Parallel to the solid-liquid interface the spheres of the liquid arrange in separate well-defined layers with a decreasing order with increasing distance from the wall. The behavior is illustrated in Fig. 2.5 [Sno77], where the density perpendicular to the wall is plotted. The density shows an oscillating profile perpendicular to the wall. The layer to layer

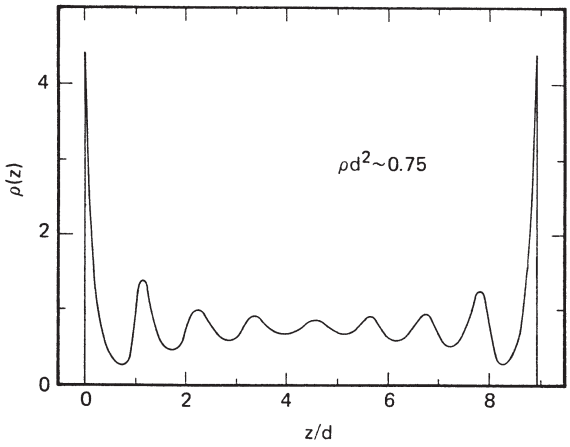

Figure 2.5: *Monte Carlo density profile for hard discs near a hard wall. Walls are on both sides. Taken from [Sno77].*

distance is slightly more than the hard sphere diameter. The spheres within the layers are disordered. The layering effect arises from the requirement that there must not be a density deficiency at the interface, therefore, a first close packed layer originates at the wall. The second layer has a less defined distance from the wall due to the lateral disorder of the first layer allowing the spheres to occupy a wider range in z-direction, which leads to a smearing of the layer. The third layer is even more smeared out and so on.

Layering perpendicular and the structure parallel to the fcc(111)-solid-liquid interface were investigated with molecular dynamics simulations, where a high degree of non-hexatic order was found in layers further away from the interface [Tal86]. Other studies applied the density-functional theory to argon having a Lennard-Jones potential on a substrate [Ebn77], to the hard-sphere fcc(100)-liquid interface [Cur87], to the structure factor perpendicular to a wall for hard spheres [Göt96], or the melt-crystal interface for silicon and germanium [Coo93]. These studies all showed a layering of the liquid perpendicular to the wall. In molecular dynamics simulations of microscopic thin films of a Lennard-Jones fluid to investigate the wetting behavior, layering was observed, too [Sik87].

For free surfaces the situation is quite different: Only hard sphere and metal-like liquids show surface layering, whereas liquids of atoms having a Lennard-Jones type potential do not show surface layering [Cha01].

The above mentioned research regarded the liquids mostly from their respective potential to deduce the interfacial structure. Another important quantity of solid-liquid interfaces is the interfacial tension. It is crucial for its

structure. In turn the interfacial energy will be affected by the short-range order of the liquid at the interface. A model for the interfacial energy that incorporates structural properties was introduced by Thomson, Spaepen, and Nelson [Nel89]. Its main result is that the interfacial energy is mostly due to configurational entropy [Spa76]. These concepts have been sucessfully applied to the silicon-melt interface [Uji01]. An icosahedral order, which is incompatible with the translational invariance of the crystalline phase, will increase the interfacial energy. Of course there is an anisotropy related to the crystallographic orientation of the solid surface [Hoy01].

The interfacial energy of metals in contact with their respective melt can be deduced from the nucleation rate in supercooling experiments. It was indirectly shown, that indeed a high fraction of icosahedral order in the melt and at the interface supresses crystallization [Sch02]. Moreover, supercooling experiments highlighted, that the nucleation behavior of solids can be dominated by the topological structure, while chemical effects are of minor importance as long as phases with the same topological structure nucleate [HM01]. More recent theoretical studies model more realistic models, e.g. a model for a liquid gold surface. Molecular dynamics simulations clearly show layering perpendicular to the free surface [Iar89]. This surface shows some degree of a hexatic order, which means that it is close packed [Cel97].

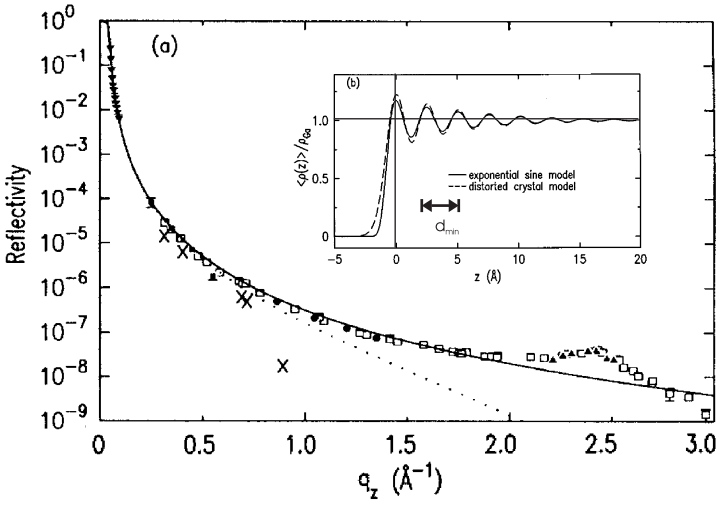

Figure 2.6: *Atomic layering at a free surface of liquid gallium. Taken from [Reg95, Reg97].*

The layering effect has been shown in various free surfaces of liquids. It was found that three to six layers are established. The decay of the layering amplitude is fast and follows some kind of exponential law. It was shown at

the surface of concentrated suspensions of colloidal particles that they are layered up to three layers and they did not have a lateral order [Mad01]. In liquid metal surfaces the layering effect is very strong with the complication that liquid metal surfaces are roughened by capillary waves. Capillary waves (CW) are thermal excitations of the surface that lead to an intrinsic correlated roughening of the surface [Bra88].

Using x-ray reflectivity surface layering of liquid metals has been found for several elements. For liquid mercury an exponential decay length of $3-3.5$Å was found [Mag95]. The example of liquid gallium is shown in Fig. 2.6. The x-ray reflectivity of the free surface is plotted with the corresponding electron density fit. At about 2.5Å^{-1} a clear deviation from the Fresnel reflectivity was detected manifesting in a broad hump[1]. This hump is called the *layering peak*. It is expected at around $q_z \approx 2\pi/d$, where d denotes the layer spacing. Therefore, to get atomic resolution from x-ray reflectivity the measurements have to be carried out to $q_z > 2\pi/d$, which is a difficult experimental task. Otherwise, the resolution of the fit will be limited to $d_{\min} = 2\pi/q_{z\max}$ [Reg95, Reg97]. The layering was shown, too, for liquid indium with a detailed study of the capillary waves [Tos99]. More recently studies of liquid alloy surfaces have been performed like for Ga-Bi [Tos00, Hub02], Bi-In [DiM01], and Pb-Sn-Ga [Li02]. For alloys not only layering can be found, but also surface segregation depending on the system investigated.

Until now there exists only one experiment where layering has been shown at a deeply buried solid-liquid metal interface [Hui97]. Huisman et al. showed a pronounced layering effect in liquid gallium in contact with a diamond crystal. Gallium has a dimer structure in the liquid, so that a layering of dimer occurs. These dimers are about twice as large as a single Ga atom, thus the layering peak of these dimers could be found at $q_z \approx 1.3$Å^{-1} enabling the experiment at all.

Water on Ag(111) was investigated with truncation rod measurements, were a layering of H_2O together with a tremendous density increase perpendicular to the interface was found [Ton94, Ton95]. However, these results are not supported by molecular dynamics simulations on this system [Sen00]. Otherwise reflectivity studies of water adjacent to a mica surface revealed a density enhancement of the oxygen electron distribution of more than 100% together with layering [Che01] and this is indeed supported by MD simulations [Par02].

Another group of experiments and simulations were carried out on confined liquids. In these investigations it is expected that the walls surrounding the liquid have a tremendous influence on its structure. For rubidium inter-

[1]The scattering theory is introduced in Chap. 3.

calated in graphite a clear six-fold modulation of the two-dimensional liquid was found [Rei86]. Thin films of organic liquids on silicon showed different density anomalies adjacent to the wall in comparison with the bulk liquid [Doe99, Doe00]. Reflectivity measurements of thin organic films that show layering and the ambiguity of these fits are presented in [Yu01]. Recently, thin films of stearic acid on liquid Hg have been investigated and additionally to layering of Hg atoms, monolayers of stearic acid have been identified [Kra02].

Other recent experiments were carried out on liquids confined by two walls on the lower and upper side of the liquid. The liquids are reduced to only two to five layers [Zwa00, See02, Bec03]. The confinement not only in two dimensions but in all three dimensions is investigated, too [Sch01a]. Thus molecular layering of inert gases could be detected with high resolution electron microscopy [Don02].

In the course of this work it will be seen that the following property of a liquid metal is not negligible in future experiments: a liquid metal is a two-component fluid, the ions form a (dense) classical liquid and the valence electrons form a (dense) Fermi liquid. At interfaces a highly inhomogeneous distribution of strongly interacting ions and electrons has to be considered. Both the ion and electron density profiles will vary extremely rapid at the interface. Additional complications arise from the fact that at a solid-liquid metal interface there must be a transition from metallic-like bonding to a more or less covalent bonding [Eva80].

2.3 Silicon Crystals and Surfaces

The semiconductor silicon makes up 27.5% of the earth's crust by weight and is the second most abundant element after oxygen. Due to its widespread applications in semiconductor electronics large bulk crystals of highest purity (up to 99.9999%) and quality are available. The silicon processing technology has been steadily improved for the last decades, e.g. [Ton99].

2.3.1 Silicon Crystals

Silicon is dark grey with a bluish tinge. Silicon belongs to group IV in the periodic table like carbon and germanium. It has diamond structure, which consists of two face-centered cubic unit cells that are shifted with respect to each other by ($^1/_4$, $^1/_4$, $^1/_4$). The unit cell is made up of tetrahedral building blocks (cp. Fig. 2.7). The lattice constant is 5.4309Å. The bonds in silicon are covalent and the Si-atoms are sp^3-hybridized, which leads to a

strong binding between the atoms. Silicon has a Debye temperature of 645K, which is one of the highest of all elements. Silicon is a semiconductor (specific resistivity: $\rho = 8 \cdot 10^7$ Ωm at ambient temperature) and has a static dielectric constant of 11.8[2]. The melting temperature is $T_m = 1687$K. This is fairly high compared with many metals that melt below 1000K and thus it can form a stable solid-liquid interface with a metal melt. The clear difference in melting temperature is a primary prerequisite for a binary system to qualify for our solid-liquid experiments.

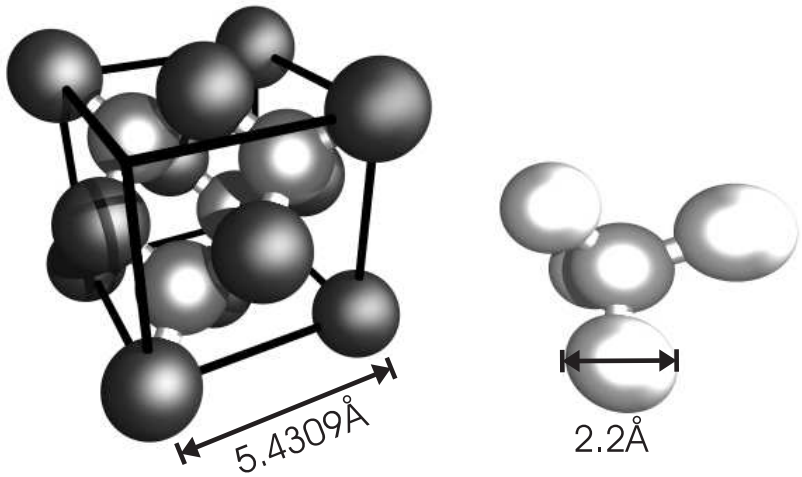

Figure 2.7: *The unit cell of silicon and the tetrahedral building block of silicon. The topmost Si-atom in front is removed for better view on the inner part of the cell. On the right a tetrahedron is shown, which is the simplest building block of silicon. The diameters and distances show the real proportions.*

The diamond structure of silicon has some advantages compared to other structures for our purposes as the number of allowed Bragg reflections determined by the crystal structure factor is reduced. The crystal structure factor is given as

$$F_{hkl} = \begin{cases} 8f_{\mathrm{Si}} & hkl \text{ all odd} \\ 4\sqrt{2}f_{\mathrm{Si}} & h+k+l = 4n, \quad n \text{ integer} \\ 0 & \text{all other cases} \end{cases} \tag{2.3}$$

h, k, l are the Miller indices and f_{Si} is the atomic form factor of silicon. Thus, the (200)-reflection is forbidden and there is only the low diffuse

[2]These values can be found at 'www.webelements.com', in 'Handbook of Chemistry and Physics' or in other books containing physical reference data.

scattering at the corresponding q-value. This is important for our interface sensitive measurements as will be seen in Chap. 6. Furthermore the strong directional bonding between the silicon atoms in combination with the few allowed Bragg reflections results in low thermal diffuse scattering (TDS) compared to metallic crystals.

2.3.2 Silicon Surfaces

The structure of free silicon surfaces and some of their properties are well-known. Silicon surfaces are of great interest since Si(100) surfaces are used extensively in integrated circuits and the (111)-surface is the natural cleavage face. Extensive reviews can be found in [Eas80, vdV85]. In this section the structure and properties important for this work are briefly discussed.

The ideal surfaces resulting from truncating a bulk crystal are not stable. The topmost atoms have one or two unsaturated bonds called *dangling bonds*, depending on the surface orientation. These surface atoms can reduce their energy by rearranging their positions and bonds. Therefore, surfaces of silicon always show reconstruction. The surface forms a new structure with a different unit cell than the bulk structure of the crystal. These reconstructions can be modified by adsorbates on the surface.

(100) surface

The ideal Si(100)-(1×1) surface is illustrated in Fig. 2.8. The atoms in the outermost surface layer are bonded in rows to second layer atoms along [110] directions and have two broken bonds in perpendicular direction. In reality, Si(100) is reconstructed with a (2×1) unit mesh. The accepted model for this reconstruction is a symmetric dimer model. In this model, adjacent rows of surface atoms are bonded and form dimers along the [110] and $[\bar{1}10]$ directions. The atoms below the surface up to the third layer remain almost in their bulk positions, especially keeping their bulk like bonds. They follow slightly the topmost surface layer, thus relaxing the strain, induced by the rearrangement of the top atoms.

It is possible to create almost defect free, reconstructed Si(100) surfaces, simply by annealing and flashing[3] under ultrahigh vacuum conditions (UHV) [Hat00]. The surface morphology changes if other atoms (mostly metal atoms) are deposited on the surface (e.g. [Li94, Don01]).

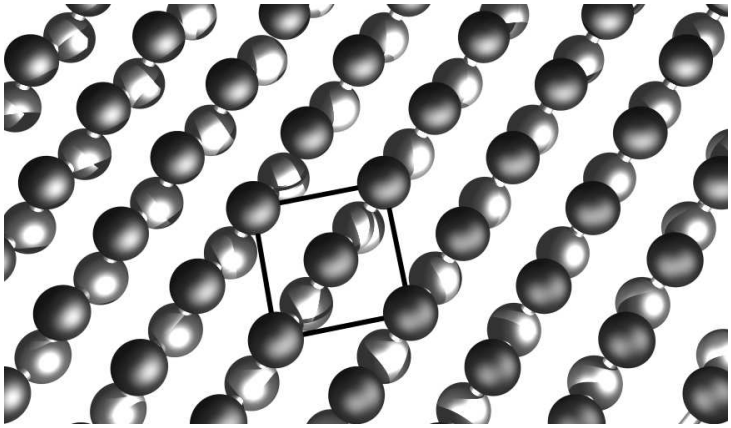

Figure 2.8: An ideal Si(100) surface. The black box marks the unit cell of the bulk crystal. The surface unit cell is rotated by 45° having a size of $(a/\sqrt{2} \times a/\sqrt{2})$. The dangling bonds of the topmost atoms are not shown, they are perpendicular to the rows in (110) direction.

(111) surface

In (111) direction the crystal consist of bilayers of atoms stacked in an ...ABCABC... sequence. The ideal (111)-surface is terminated with half a bilayer as illustrated in Fig. 2.9. A freshly cleaved silicon (111) surface shows a (2×1) reconstruction, which is metastable. The generally accepted model for this reconstruction is the π-bonded chain model [Pan81]. Fig. 2.9 shows a perspective view of an ideally cut Si(111) surface. Each topmost atom has a dangling bond that is pointing outwards. The Si(111)-(1×1) surface exists at temperatures above 1170K. At lower temperatures the free surface reconstructs in the two configurations, the metastable (2×1) reconstruction and the stable Si(111)-(7×7) reconstruction. The high temperature (1×1) structure can be stabilized by small amounts of adsorbates like Cl or Te [Eas80], such that it is stable at lower temperatures.

The structural models for these reconstructions are multilayer models as for the Si(100) surface. This means that not only the topmost atoms are rearranged but that the atoms in the layers underneath do not remain in their bulk positions as well. Fig. 2.10 shows the common model for the (2×1) reconstruction. It is called the *chain model*, since the topmost atoms form chains in a zig-zag structure. The atoms underneath are slightly displaced from their ideal bulk positions. The (2×1) reconstruction is irreversibly converted by annealing above 700K to the stable (7×7) reconstruction. The same

[3] flashing: rapidly heating to very high temperatures (s. Chap. 4)

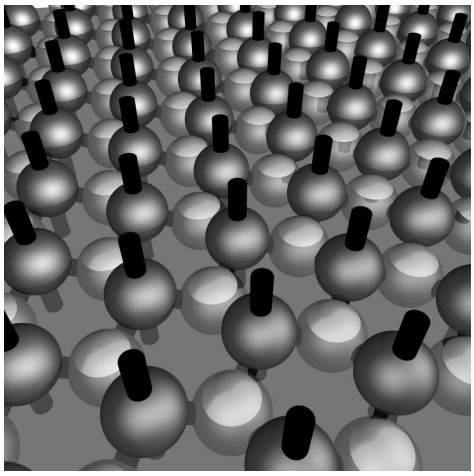

Figure 2.9: *A perspective view of an ideally terminated Si(111) surface. The outer atoms of the surface each have an unsaturated bond directed into the vacuum. These bonds are dangling bonds.*

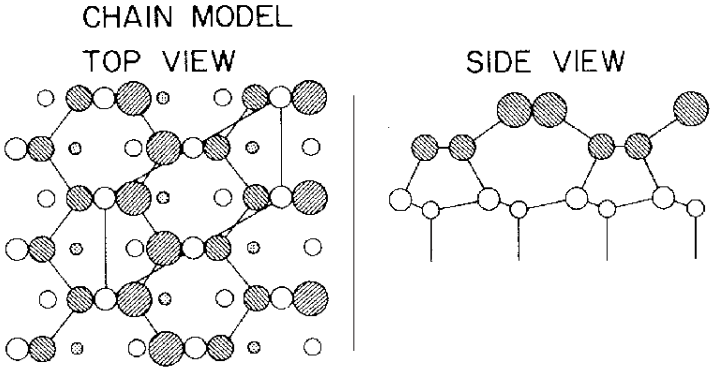

Figure 2.10: *Model of a Si(111)-(2 × 1) surface. The top two layers are the shaded circles. The topology of the zig-zag chain structure is similar to that of the ideal (110) surface. All bond lengths retain their ideal bulk values of 2.35Å, except the bonds along the chains in the top layer. They are contracted by 0.1Å. The parallelogram of the unit cell is also shown. Taken from [Pan81].*

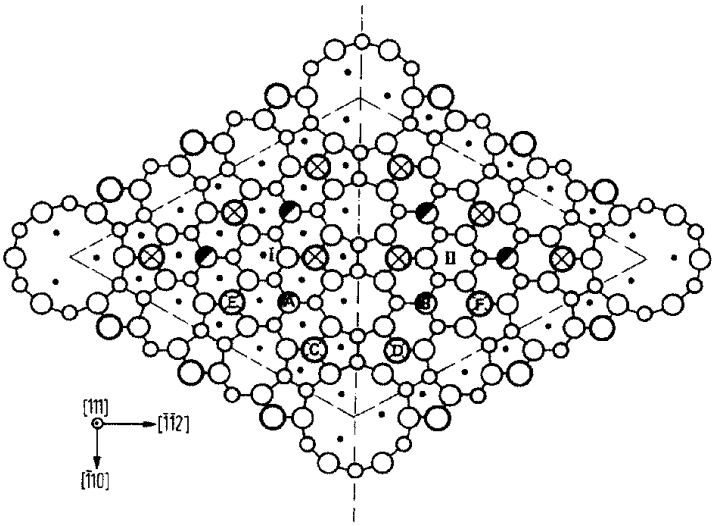

Figure 2.11: *Top view of a Si(111)-*(7×7) *surface. The unit cell is marked by the dashed rhombus. The topmost atoms are the large open circles with crosses inside. Taken from [Dev86].*

stable reconstruction is found on polished Si(111) surfaces after cleaning by ion bombardment or flash cleaning and successive annealing [Sch59, Pal67]. A top view is shown in Fig. 2.11.

2.4 Liquid Metals: Lead and Indium

The properties of liquid metals that are important for this work are introduced in this section. Extensive treatment of this subject can be found in e.g. [Dar53, Lüs80, Iid88]. Liquid metals are often treated as hard sphere fluids as introduced in Sec. 2.1 [Jar69]. The conduction electrons are neglected and the remaining ions are regarded as neutral hard spheres. This model yields good results for e.g. the volume change upon melting, self diffusivities, and pair distribution functions [Iid88]. More detailed studies of the structure factor take the conduction electrons into account [Chi87]. In this context the conduction electrons are regarded as a liquid having its own liquid structure factor rather than an electron gas [Ege74].

The core ions in metals have a Coulomb potential proportional to their charge. This potential is screened by the conduction electrons, which leads to a modified ion-ion-potential for metals that is oscillating

$$\phi(r) = \frac{A}{r^3} \cos(2k_F r), \tag{2.4}$$

where A is a parameter defining the strength and k_F is the radius of the Fermi sphere of the metal. The potential is the origin for long-ranged *Friedel oscillations* [Fri52]. Other potentials in liquids are the van-der-Waals-potential (e.g. in He, Ne) and dipolar potentials (e.g. in H_2O).

2.4.1 Lead

The metallic element lead is a group-IV element. Compared to other metals it has a high density and is ductile. It has a melting temperature of $T_m = 327.5°C$. The pure metal is oxidized rapidly in air. Off the shelf it is covered with an oxide layer that protects the metal from further oxidation. It has two oxidation steps of 2+ (the two $5p$-electrons) and 4+ (the additional two $6s$-electrons). The oxidation step of 2+ is preferred and all Pb(IV)-compounds are strong oxidants where Pb^{4+} is reduced to Pb^{2+}. Lead is not noble having a chemical normal potential of $Pb/Pb^{2+} = -0.13V$. Thus, it should be oxidized by all acids, however, with most acids it forms hardly soluble layers that protect the metal from further corrosion, except acetic acid. In addition Pb has an overvoltage of 0.4V with hydrogen. Furthermore, lead is amphoteric, which means that it is as well oxidized and solved in bases. With its 82 electrons it is a very good scatterer and absorbent for x-rays.

2.4.2 Indium

Indium has some macroscopic properties that are similar to those of lead. It is even softer and its melting temperature is about of the same order of magnitude ($T_m = 156.6°C$). Unlike lead it keeps its lustrous colour in air. It is dissolved by most anorganic acids but no bases. As a group III-element it has three valence electrons (two s- and one p-electron) and the only stable oxidation state is In^{3+}.

2.5 Pb and In interacting with Silicon: Bulk and Surface

The structures and properties of metals on semiconductor surfaces have been studied for a long time [Est64, Pal67]. These systems are important for applications in semiconductor manufacturing. In basic research they are used as model systems where the chemical interaction is small or negligible. A first insight on the chemical interaction is gained from the binary bulk phase diagrams of the corresponding metal-semiconductor systems.

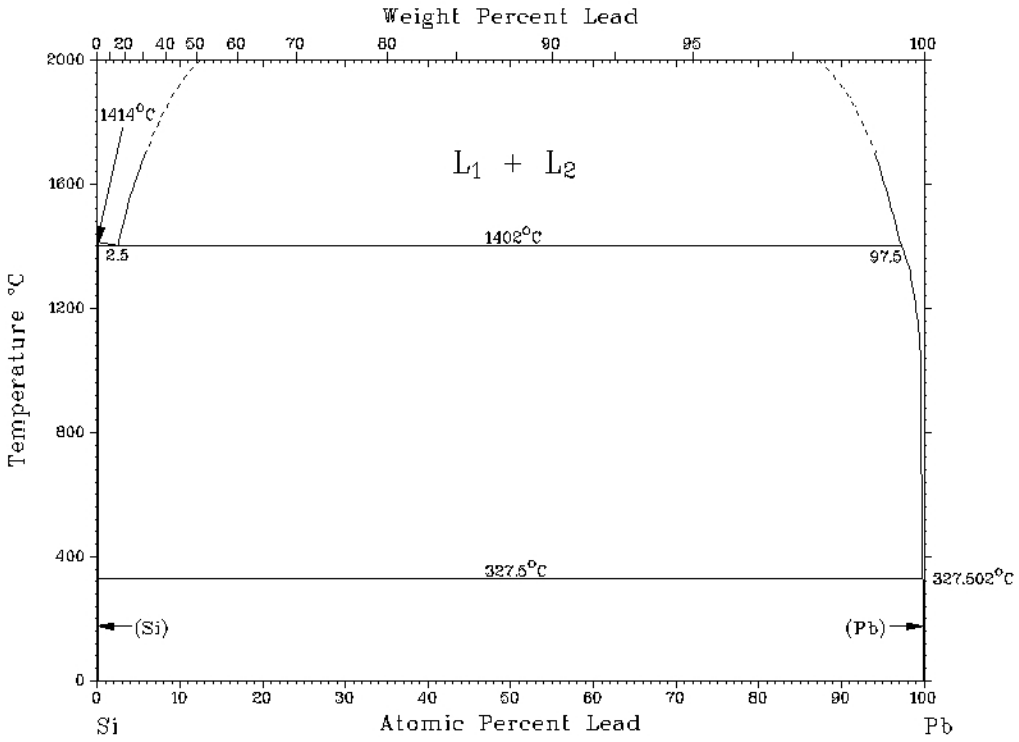

Figure 2.12: *The phase diagram of the lead-silicon-system. The two elements do not intermix, nor do they form any compounds. The liquids form separate phases. Taken from [Mas90]*

2.5.1 Bulk Interaction

Indium and Lead do not form compounds with silicon that consist only of these two elements, respectively. The solubility of silicon in liquid indium or liquid lead at the melting temperature of the metals is 4×10^{-3} atomic percent for indium and 9×10^{-8} atomic percent for lead. The solubility remains small up to the melting temperature of silicon at 1687K [Mas90, Bit70]. The phase diagram for Pb-Si is shown in Fig. 2.12 and for In-Si in Fig. 2.13. It can be seen that the phase diagrams are dominated by an almost complete miscibility gap for solid silicon.

A negligible bulk alloying behavior does not necessarily denote that a system is appropriate for structural interface studies as carried out in this work. There might be still a small but non-negligible chemical interaction present at an interface between the two elements. Therefore, it is important to consider surface studies on metal-semiconductor systems for monolayers

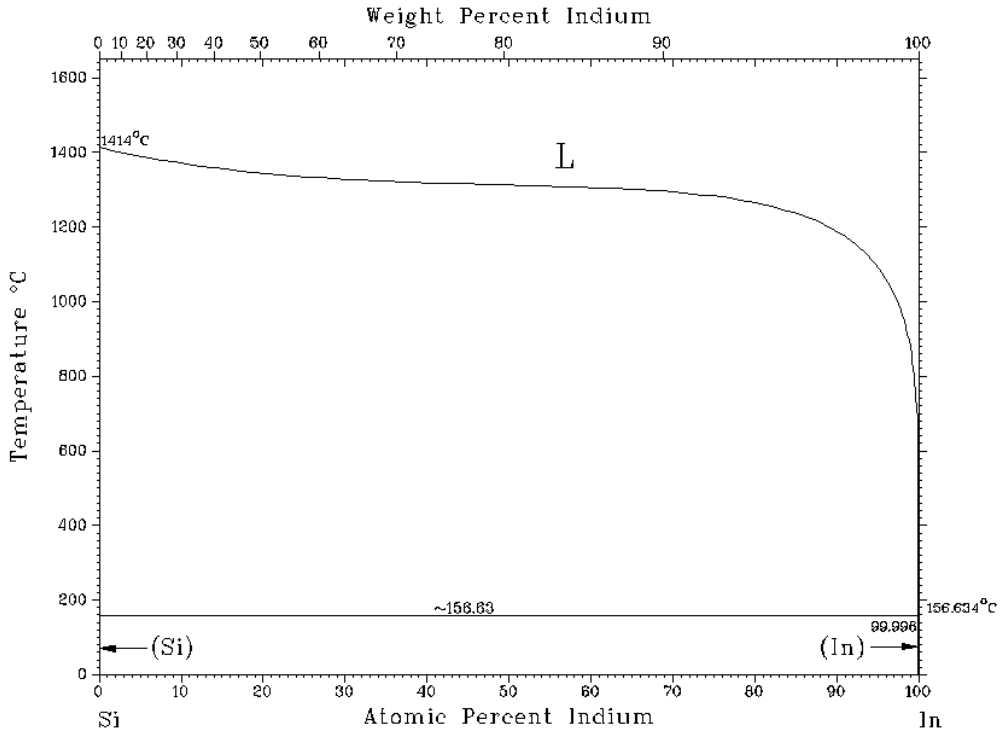

Figure 2.13: *The phase diagram of the indium-silicon-system. The two elements do not intermix, nor do they form any compounds. Taken from [Mas90]*

of metals on silicon surfaces as well.

2.5.2 Thin Metal Layers on Si Surfaces

At low coverages many metals form commensurate superstructures on silicon surfaces. For coverages exceeding a few monolayers (ML), most systems show a 3-dimensional (3D) island growth. This behavior is typical for the Stranski-Krastanov growth mode. The reconstructions of the surfaces are preserved at coverages up to two monolayers for many adsorbates. The coverage of one monolayer is the number of topmost atoms on an unreconstructed surface. For a Si(100) surface it is equivalent to $1\text{ML} = 6.8 \cdot 10^{18}\text{atoms/m}^2$ and for a Si(111) surface a monolayer amounts to $1\text{ML} = 7.8 \cdot 10^{18}\text{atoms/m}^2$.

An overview of the behavior and structure of small amounts of indium and lead on silicon surfaces is given in the following two sections. The structures of other metals on silicon and other surfaces are tabulated in appendix C.

The diffusion of single metal atoms on Si(100) is rapid at RT, which allows for the formation of well defined large scale structures. Most metals form rows of dimer adatoms on Si(100). The diffusion on Si(111) surfaces is slower resulting in more metastable structures.

The structure often depends on the temperature during or after deposition. Some other metals may change their structure strongly upon annealing, e.g. tin shows only gross rearrangement upon annealing and silver dewets to crystals with (111)-orientation on Si(100). In contrast to metals like gold that shows a layer by layer growth of up to three monolayers or germanium that grows up to five monolayers epitaxially. A different group of metals are the one that form stable compounds like nickel ($NiSi_2$).

Partly, the growth behavior can be understood taking into account the lattice mismatch, yet the electronic or chemical interactions determine the actual growth behavior [Zha98]. Quantum confinement, charge spilling, and interface-induced Friedel oscillations have to be taken into account for the understanding of the interfacial structure as will be seen in the course of this work [Czo03, Czo04, Upt04].

In on Si Surfaces

The structures of small amounts of indium on silicon surfaces and their respective temperature dependence are tabulated as they are reported in literature in Tab. 2.1. The reference for each system or phase is given in the table.

There is a two-dimensional (2D) growth for indium up to two ML on Si(100). Upon annealing, these layers dewet to one closed monolayer and 3D islands. Further deposition leads to a growth of the 3D islands. At a coverage of 0.5 monolayers the indium atoms form rows of ad-dimers that are perpendicular to the rows of silicon dimers existent on a Si(100)(2×1) reconstruction. Fig. 2.14 shows a sketch of the ad-dimer adsorption of In on a Si(100)(2×1) surface. The initial reconstruction of the Si surface is not lifted. The In dimers align parallel to the surface. This behavior is common to many metals on this surface. The rows are formed at room temperature and are stable even at elevated temperatures. At higher coverages the reconstruction changes gradually until 3D growth sets in. The prominent feature is always the dimer rows of adatoms with different surface periodicity. Most authors regard the metal adatom dimers as covalently bonded to the silicon surface. They conclude that due to the presence of silicon dangling bonds, most of the valence electrons from metal adsorbate atoms at submonolayer coverage are bound by the substrate through local covalent atomic bonding [Don01]. This will be important for the discussion of the results in Chap. 6-8.

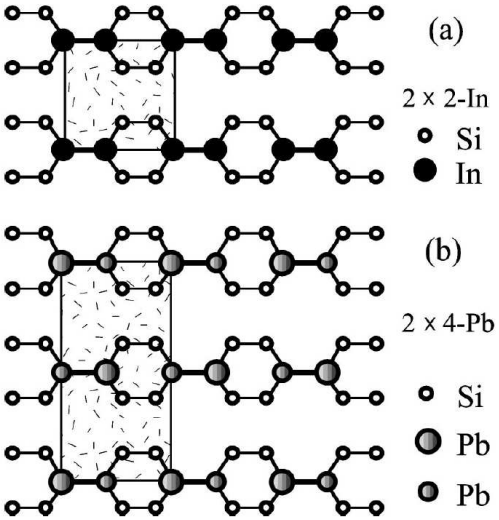

Figure 2.14: *Schematic models of the parallel ad-dimer adsorption structure and surface reconstruction of* 0.5ML, *(a) In on Si(100) with the square unit cell shaded for the* (2×2)*-In phase. The indium dimers are symmetric; (b) Pb on Si(100) with the rectangular unit cell shaded for the* (2×4)*-Pb phase. The lead dimers are asymmetric with the large shaded atoms buckled upward and the small shaded atoms buckled downward. Note that the* (2×1)*-reconstruction of the initial Si(100) surface is not lifted. Taken from [Don01].*

The complicated (7×7) reconstruction of Si(111) results in more complex reconstructions with metal adatoms. The situation gets even more complex if the initial reconstruction is lifted at high temperatures to (1×1) with a subsequent metal deposit. A model for the indium induced Si(111)(4×1) surface can be found in [Bun99].

Pb on Si Surfaces

The system Pb-Si(100) has been studied extensively. A complete phase diagram for monolayer coverages has been published for this system [Zha92].

For a coverage of about 0.5 ML the Pb atoms arrange in ad-dimers similar as for indium. Fig. 2.14 shows a sketch of the ad-dimer adsorption of Pb on a Si(100)(2×1) surface. The initial reconstruction is not lifted. The Pb dimers form a buckled structure contrary to the parallel dimers of In atoms. [Ito94] reports that the structure of Pb on Si(100) is independent of the growth rate. This indicates that the phase is in thermal equilibrium.

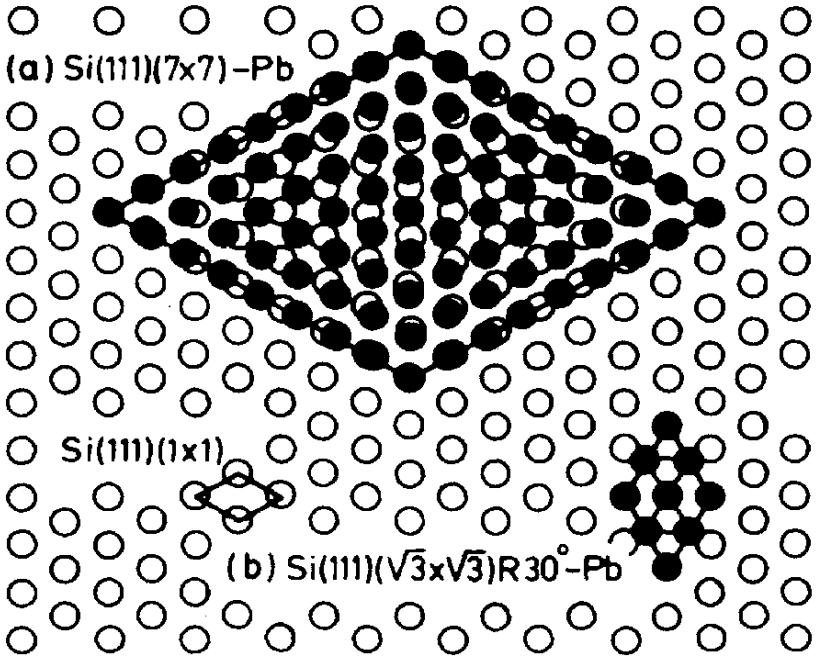

Figure 2.15: *Schematic surface structure of a Pb monolayer on Si(111). The upper part shows the Si(111)*(7×7)*-Pb structure the lower part shows the incommensurate Si(111)*$(\sqrt{3} \times \sqrt{3})R30° - Pb(\beta)$ *structure. Taken from [Wei92].*

Some authors claim a pronounced chemical interaction between lead and silicon in thin surface layers, which leads to a pronounced interfacial mixing between lead and Si(100) and Si(111) [Zha93]. Whereas Li et al. [Li94] report that they found no reactivity of Pb on Si at room temperature and above. The authors claim that it is possible to remove the lead by heating the silicon surface without damaging the surface, which is a strong indication that there is no covalent bonding between lead and silicon.

The other interface system investigated in this work is the Pb-Si(111) interface. Fig. 2.15 shows a model for a coverage of one monolayer Pb on a Si(111)(7×7) surface forming a (8×8) unit cell and the high temperature $\sqrt{3} \times \sqrt{3}R30°$-Pb$(\beta)$ structure.

In on Si surfaces

amount	surface	temp.	structure	source
0-0.5ML	Si(100) (2×1)	RT-150°C	dimer rows $\perp$ to underlying Si dimer rows (2×2) with (2×1) coexistent	[Bas91a], [Don97]
0-0.45ML		RT	streaks + (2×1)	[Nor91], [Yeo95]
-0.1ML		> 100°C	(2×1)	
0.1-0.3ML		> 100°C	(2×3)	
~ 0.5ML		RT-150°C	(2×2)	[Bas91a], [Nor91],
$0.5 - 1.0$ML		RT	(2×2)+ weak (4×3)	[Yeo95], [Don97]
> 1ML		> 100°C	(2×1)	[Bou88]
> 0.5ML		> 150°C	(4×3), disruption of Si dimers (stable transformation upon ann.)	[Bas91a], [Don97]
1ML	Si(111) (7×7)	RT	(4×1)	[Bun99],
		-200°C	(8×2)	[Kum00], [Yeo02]
$0.15 - 0.5$ML		$400 - 550$°C	$(\sqrt{3} \times \sqrt{3})R30°$	[Kra97]
$0.3 - 0.5$ML			$(\sqrt{31} \times \sqrt{31})$	
$0.4 - 0.8$ML			stripped	
$0.4 - 1.0$ML			(4×1)	
$0.8 - 1.2$ML	prob. (1×1)		(1×1), $(\sqrt{7} \times \sqrt{3})$, (4×4)	

Table 2.1: *Structure of indium adatoms on different silicon surfaces. ML: monolayer; RT: room temperature.*

Pb on Si surfaces

amount [ML]	surface	temp.	structure	source
$>$ 2ML	Si(100) (2×1)	$<$ 100°C	islands start	[Zha92], [Li94]
0.3-0.6; 0.5sc		RT	(2×2)	
0.3-0.6; 0.75sc		450°C	c(4×8)	
0.9-1.5		RT	(4×1)	
1.5-2.0; 1.0sc		RT	(2×1)	
2.1-7		RT	c(4×4)	
$>$ 2 and more		RT-300°C	trapezoidal, triangular, hexagonal islands	[Li94]
0.25-0.5		$-$200°C-RT	(2×4) buckled dimers similar to 2×2	[Don01], [GM98]
$>$3			Pb(111) islands on top of c(4×4)	[Ito94]
$\sim$ 0.5		RT	c(8×4)+(2×2) mixing (intermediate between (2×2) and (2×1))	
1-$^4/_3$ML	Si(111)	RT	(8×8) Pb atoms in a (7×7) Si unit cell. Pb-Pb distance 4% compressed	[Gre89], [Hon03]
$\sim$ 2ML	(7×7)	$>$ 250°C	$\sqrt{3} \times \sqrt{3}R30°$, incommensurate 2.3% compression compared to bulk Pb(111), sometimes referred as Si(111)$\sqrt{3} \times \sqrt{3}R30°$-Pb($\beta$) phase	[Wei92]
1-2ML		$>$ 300°C	Si(111)(1×1)P	[Wei92], [LL88]
1-2ML		$>$ 300°C	2D-liquid	[Ich84], [Gre90], [Wei92]

Table 2.2: *Structur of lead adatoms on a silicon surfaces. ML: monolayer; RT: room temperature; sc: saturation coverage*

2.5.3 Bulk Lead on Si(100)

Experiments at Pb(liq.)-Si(100)-interfaces were carried out previously in our group. This was Oliver Klein's Phd-thesis [Kle00] that was left unfinished after his tragic death in a car accident in year 2000. The structure factor of liquid lead parallel to the interface could be determined, and its azimuthal dependence at the interface with 20 peaks between 0° and 360°. This was explained by a convolution of the four-fold symmetry of the Si surface with the local five-fold symmetry of the liquid lead [Rei00].

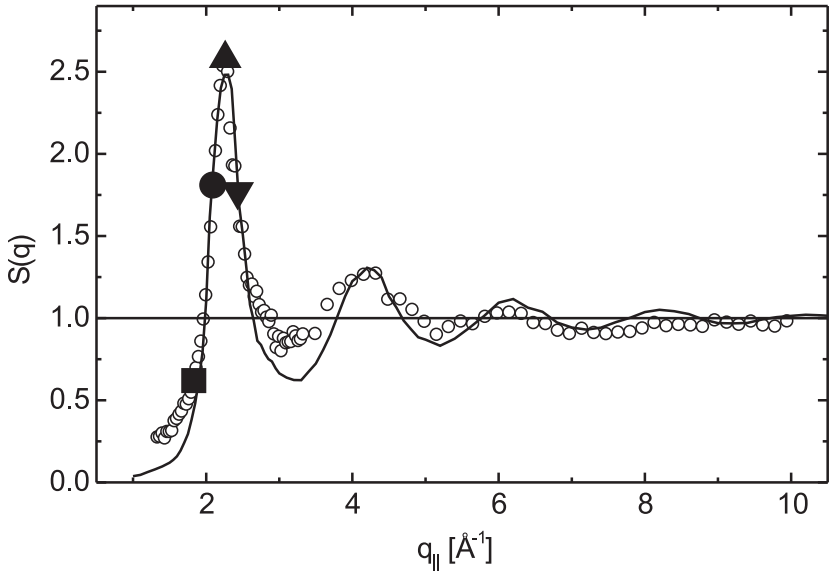

Figure 2.16: *The structure factor parallel to the interface (open circles). The solid line is the bulk structure factor [Was80]. The four large symbols around the first peak of the structure factor mark the positions, at which azimuthal scans of the structure factor parallel to the interface were performed (s. Fig. 2.17).*

The structure factor of liquid lead at the interface was measured parallel to the Si(100) surface. The depth resolution in the experiment was defined by the effective decay length of the evanescent x-ray wave to $\Lambda_{eff} = 55$Å. Fig. 2.16 shows the background subtracted and corrected data and the bulk liquid structure factor taken from [Was80]. Three peaks could be identified. Their q-values match exactly those of the corresponding bulk structure peaks. At higher q-values no more peaks could be distinguished. The width and the intensity of the first peak of the measured data is in excellent agreement with the bulk structure factor. The intensity of the second peak matches the

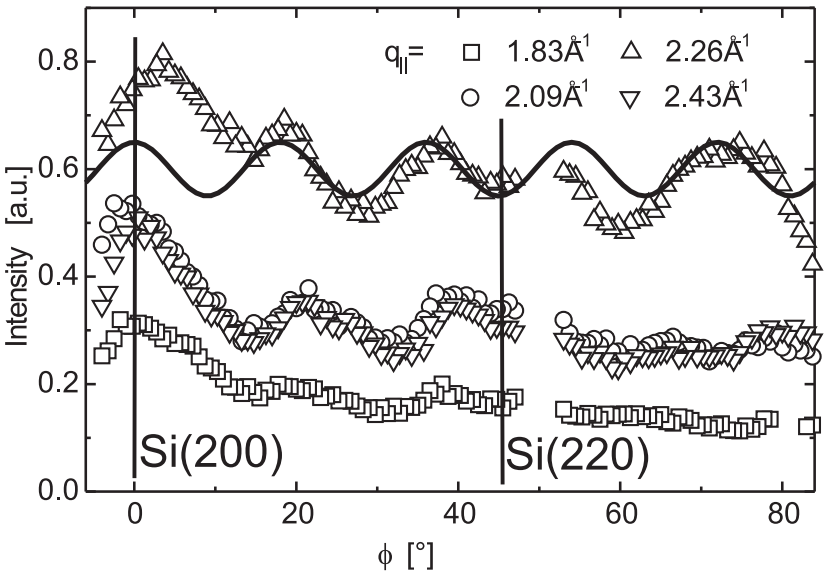

Figure 2.17: *The modulation of the first peak of the structure factor with respect to the crystallographic orientation of the interface. The strongest modulation can be seen on the curve measured at the maximum of the first peak of the structure factor. For the in plane momentum transfer of the measurements. Fig. 2.16. The solid line is an adaptation.*

corresponding peak of the bulk structure factor as well. It was concluded that the bulk liquid structure is essentially preserved parallel to the interface in the contact regime.

At certain positions around the first peak of the structure factor ($q_{||} = 2.3\text{Å}^{-1}$) the azimuthal dependence of the intensity was measured. The positions and their in plane momentum transfer are denoted by large filled symbols in Fig. 2.16. The scans with the azimuthal dependence are shown in Fig. 2.17. In a bulk liquid, this type of scan inevitably shows a constant intensity associated with the spherical symmetry of the bulk liquid structure factor.

The azimuthal ϕ scan measured at the interface of the non-reconstructed four-fold Si(100) wall, however, showed a pronounced modulation. Within a 90° segment five intensity maxima were observed that have a fixed epitaxial relationship to the substrate. The epitaxial relation to the silicon substrate is indicated by vertical lines and their corresponding Miller indices, respectively. This modulation is only found for in plane momentum transfer values close to the maximum of the liquid structure factor. At higher or lower $q_{||}$-

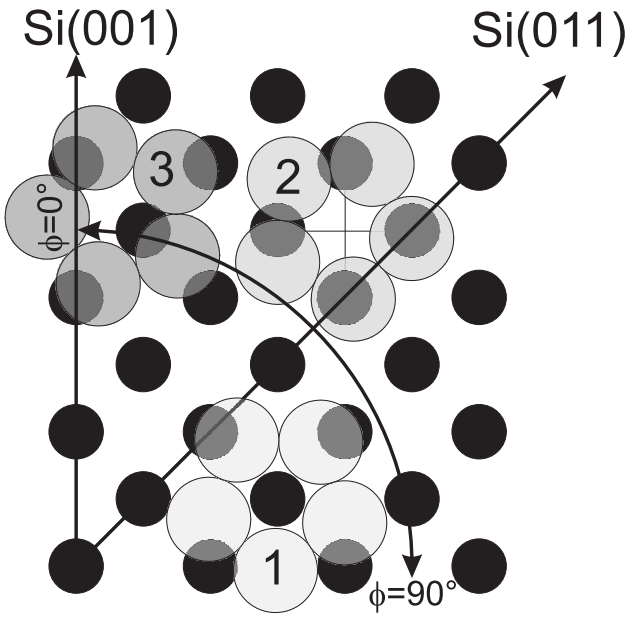

Figure 2.18: *Projection of Pb-pentagons (light circles) onto Si(100) (black circles) in different orientational relation sites. The bulk liquid forms clusters of five atoms that align parallel to the interface. From the modulation of the structure factor the position of the clusters can be determined. The correct site is the lowest cluster (1), see text.*

values the modulation is damped ($q_{||} = 2.09\text{Å}^{-1}$ and $q_{||} = 2.43\text{Å}^{-1}$) or gone ($q_{||} = 1.83\text{Å}^{-1}$). Extending these results of a 90° segment to a complete 360°-circle the modulation of the first peak of the structure factor shows 20 peaks along the ring. This intensity modulation can only be understood as a convolution of a four-fold and a five-fold symmetry. The four-fold symmetry is imposed by the Si(100) substrate and the orientational part of the associated Pb-Si interface interaction. The twenty-fold symmetry emerges when bulk liquid lead that contains clusters of five-fold symmetry, is brought in contact with the silicon wall, which means that the additional bulk Pb-Pb interaction is introduced. The observed bulk-like in plane liquid structure gives evidence that the Pb-Pb interaction $V_{\text{Pb-Pb}}$ is now dominating, while the Pb-Si interaction $V_{\text{Pb-Si}}$ is a two-dimensional perturbation leading to a preferred alignment of a certain fraction $n_{\text{align}}(z)$ of the liquid building blocks [Rei00]. The observed relative intensity modulation ($\Delta I_{\text{mod}}/I = 0.1 \pm 0.05$) is directly related to $n_{\text{align}}(z)$. The evanescent x-rays decay exponentially within a depth of 55Å, as set by the incidence angle. The relation between

$\Delta I_{\mathrm{mod}}/I$ and $n_{\mathrm{align}}(z)$ is given as [Dos92]

$$\frac{\Delta I_{\mathrm{mod}}}{I} = \frac{1}{\Lambda}\int_0^\infty n_{\mathrm{align}}(z)e^{-\frac{z}{\Lambda}}\mathrm{d}z \ . \tag{2.5}$$

The calculation and the intensity of the modulation yielded the value of the orientational part of the interface potential to $V_{\mathrm{Pb-Si}} = 50 - 90\mathrm{meV}$. It depends on the correlation length of liquid lead, which might be different at the interface and was estimated to $\xi = 5 - 8\mathring{\mathrm{A}}$.

It was a model proposed for the observed five-fold symmetry that the upper pentagonal half of the conjectured icosahedral building blocks [Fra52] of the liquid are captured at the wall and aligned parallel to the wall. Possible projections of the pentagonal Pb-cluster at the Si(100) surface are shown in Fig. 2.18. The position (1) gives the minimum overlap of the projected electron density for rotation angle $\phi_n = 360° \cdot n/20$, where n is an integer. The position (2) of the pentagon gives a minimum overlap for $\phi_n = 360° \cdot (n + \frac{1}{2})/20$. The total overlap is minimized for the upper site position (1) and it was concluded that it must be the preferred orientation. The off site position (3) of the pentagon can easily be excluded since it would not yield a 20-fold symmetry.

2.5.4 Metal-Semiconductor Contacts: Electronic View

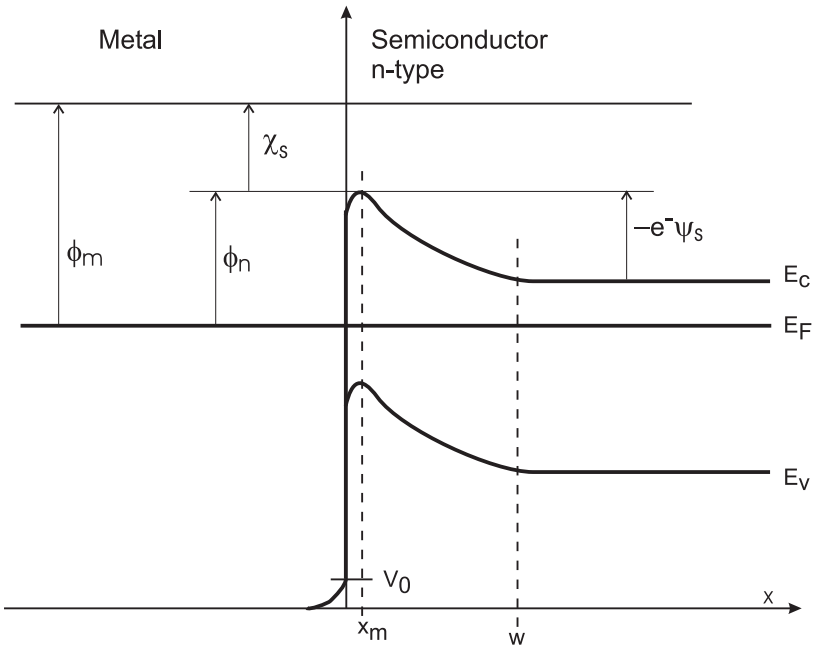

Figure 2.19: *Energy band scheme at a metal-semiconductor interface. For notation see text.*

A metal-semiconductor contact that is rectifying with respect to electric current is referred to as *Schottky contact* [Rho78, Rai92]. In general, a metal and a semiconductor that are separated exhibit different Fermi energies. Contacting both materials adjusts the Fermi energies. A region of width w of the semiconductor at the interface is depleted of its conduction electrons, which are transferred to the metal. On the other hand electrons from the Fermi edge of the metal penetrate into the forbidden semiconductor band gap. Thus, an electric space charge is created, which gives rise to a band structure illustrated in Fig. 2.19.

The metal has the work function ϕ_m and the semiconductor has the electron affinity χ_s. At the interface a potential barrier ϕ_n exists, which depends on the difference between the electron affinity of the semiconductor and the work function of the metal. v_0 is the energy corresponding to the electric potential at the surface. E_c is the energy of the conduction band and E_v is the energy of the valence band of the semiconductor, respectively, and E_F is the Fermi energy of the system. The bending of the conduction band decays up to a depth w, at which the semiconductor is depleted from its conduction electrons. The width w of the depletion layer is given by

$$w = \sqrt{\frac{2\epsilon_s\epsilon_0}{e^- N_D}\left(\frac{\phi_n}{e^-} - U\right)} f, \tag{2.6}$$

where ϵ_s is the dielectric constant of the semiconductor, N_D is the number density of the donors, U is an externally applied bias voltage, and e^- is the elementary charge. For typical semiconductor dopings of $10^{14}/\mathrm{cm}^3$ the depletion width is in the micrometer range.

From the charge density present at the depletion layer $Q_{\mathrm{sc}} = e^- N_D w$ a voltage dependent differential charge capacity can be calculated, which is given by

$$C(U) = \frac{\mathrm{d}Q_{\mathrm{sc}}}{\mathrm{d}U} = \sqrt{\frac{e^-\epsilon_s\epsilon_0 N_D}{2\left(\frac{\phi_n}{e^-} - U\right)}}. \tag{2.7}$$

The maximum of the valence and conduction band is shifted into the semiconductor to the depth x_m. At the interface it is reduced by the contact potential v_0, which is related to the Thomas-Fermi screening length.

The position x_m of the maximum of the conduction band fulfills the condition

$$x_m = \frac{1}{e^- N_D}\int_{x_m}^{w} q(x)\ \mathrm{d}x + \sqrt{\frac{2\epsilon_s\epsilon_0(v_b - U)}{e^- N_D}}, \tag{2.8}$$

where $q(x)$ is the charge density due to any cause in the semiconductor. $v_b = v_c + v_q - v_e - v_0$ is an interface related potential, where $v_c = E_{F_s} - E_{F_m}$ is the contact potential difference of the separated Fermi energies, $v_q = 1/\epsilon_s \int xq(x)\mathrm{d}x$ is a potential related to the charge density in the semiconductor, and v_e is the potential due to the electrons of the donor atoms. Note, that x_m is also the lower integration limit. For details see [Pel73]. Depending on the metal and the semiconductor x_m is in the range $7 - 25$Å [Pel73, Pel76, Rho78].

The previous discussion disregards additional surface states of the semiconductor and the metal. Especially the semiconductor may exhibit additional empty surface states due to dangling bonds that can be occupied by electrons of the metal [Mön93].

Chapter 3

X-ray Scattering from Interfaces

For this work x-ray scattering experiments have been performed to examine the structure of solid-liquid interfaces. The basic concepts will be introduced in this chapter. The derivations of these concepts can be found in [Gui63, War69, AN01, Suo02]. More advanced aspects of the scattering of liquids at interfaces, as well as scattering under grazing incidence will be evaluated in more detail in this chapter. Elaborate introduction to grazing incidence diffraction and scattering at interfaces can be found in [Dos92, Die95].

3.1 Optical Properties of Materials in the X-ray Regime

Similar to the scattering of visible light, x-ray scattering at materials can be described by introducing a complex index of refraction n. However, for x-rays the real part of n is always slightly smaller than unity ($Re(n) \approx 1 - 10^{-5}$) and the imaginary part is slightly larger than zero. It is defined as

$$n = 1 - \delta + i\beta, \tag{3.1}$$

with δ and β being the dispersion and absorption, respectively. Far from absorption edges the dispersion and absorption can be calculated using

$$\delta = \frac{\lambda^2}{2\pi} r_e \rho_{el}, \tag{3.2}$$

$$\beta = \frac{\lambda}{4\pi} \mu, \tag{3.3}$$

λ is the wavelength of the x-rays, $r_e = 2.818 \cdot 10^{-15}$m the classical electron radius, ρ_e is the average electron density of the material, and μ is the

linear absorption coefficient of the medium. δ and β can be calculated using tabulated values[1].

The scattering at a single interface, e.g. a surface to vacuum interface, is described by Snell's law of refraction. It relates the angle α_i of the incoming wave to the angle α_t of the transmitted wave in the medium without absorption

$$n = \frac{\cos \alpha_i}{\cos \alpha_t} \ . \tag{3.4}$$

Snell's law holds only for the real part of n. Because the refractive index is smaller than unity ($n < 1$), an incident angle α_i exists, at which $\alpha_t = 0$ applies. This angle is called the critical angle α_c of total external reflection. It can be deduced from Eq. 3.4 via a Taylor expansion of $\cos \alpha_i$

$$\alpha_c \simeq \sqrt{2\delta} = \lambda \sqrt{\frac{r_e \rho_e}{\pi}} \ . \tag{3.5}$$

For scattering at an interface of two different materials the refraction is determined by the combined index of refraction (s. Fig. 3.1):

$$n_{tot} = 1 - (\delta_2 - \delta_1) + i\beta_2 = 1 - \Delta\delta + i\beta_2 \tag{3.6}$$

with the incoming x-ray beam traveling through material 1. Note the important definition

$$\Delta\delta = \delta_2 - \delta_1 \ . \tag{3.7}$$

The absorption in material 1 only reduces the intensity of the primary beam, the scattered intensity has to be renormalized. The critical angle is calculated as

$$\alpha_c \simeq \sqrt{2(\delta_2 - \delta_1)} = \lambda \sqrt{\frac{r_e}{\pi}(\rho_{e2} - \rho_{e1})} = \lambda \sqrt{\frac{r_e}{\pi} \Delta\rho_e} \ . \tag{3.8}$$

Hence, there exists no critical angle if material 1 has a higher electron density than material 2. For x-ray energies of about 70keV the critical angle α_c is in the range of $0 \ldots 0.05°$. That holds for free surfaces as well as for the buried interfaces examined in this work. In the further discussion the interface will be treated as a free surface, with the critical angle calculated via Eq. 3.8.

For the reflected beam at given angles α_f, α_i the momentum transfer $\mathbf{q}$ is obtained via

[1] see e.g. http://physics.nist.gov/PhysRefData/FFast/html/form.html

$$|\mathbf{q}| = \frac{4\pi}{\lambda} \sin \frac{\alpha_i + \alpha_f}{2} \ . \tag{3.9}$$

A schematic drawing can be found in Fig. 3.1. The case $\alpha_i = \alpha_f$ with the momentum transfer $\mathbf{q} = (0, 0, q_z)$ is called *specular reflection*. In this case the plane of scattering is perpendicular to the interface. In Fig. 3.1 it can be seen that the beam gets refracted at two more interfaces: First upon entering the upper material 1 from vacuum and second upon leaving the upper material 1. These refractions can be neglected as can be easily calculated: for $\alpha_i = 1°$ and $\delta = 10^{-5}$ the deviation is $\Delta\alpha_i/\alpha_i \approx 10^{-7}$.

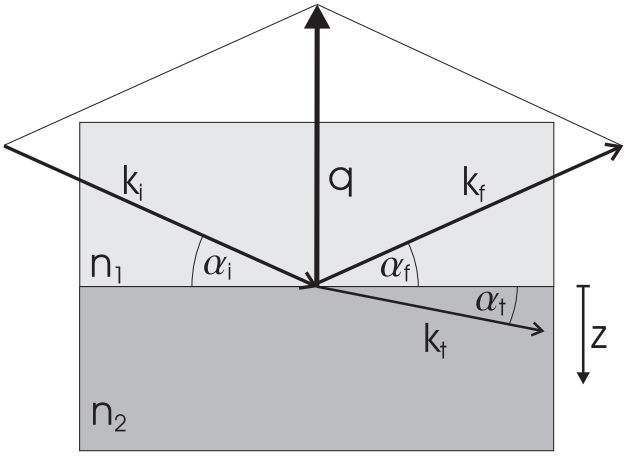

Figure 3.1: *Schematic drawing of reflection and refraction at a buried interface.* $\mathbf{k}_i, \mathbf{k}_f, \mathbf{k}_t$ *are the incident, reflected, and transmitted wave vector, respectively.* $\mathbf{q}$ *is the momentum transfer. The z-direction is marked at the right side of the sample.*

3.1.1 Fresnel coefficients

The Fresnel coefficients r_F and t_F are calculated according to classical electrodynamics, using the fact, that the tangential components of electric and magnetic fields are continuous at interfaces. This conditions determines the transmitted and reflected field amplitudes of a wave passing through an interface.

The z-direction is perpendicular to the interface with $z = 0$ at the position of the interface (s. Fig. 3.1). Using Snell's law (Eq. 3.4), the z-components of the incoming wave ($\mathbf{k_i}$) and transmitted wave ($\mathbf{k_t}$) are given by

$$k_{i,z} = \frac{2\pi}{\lambda}\sin\alpha_i \tag{3.10}$$

$$k_{t,z} = \frac{2\pi}{\lambda}\sqrt{n^2-\cos^2\alpha_i} \approx \frac{2\pi}{\lambda}\sqrt{\alpha_i^2-\alpha_c^2}\ . \tag{3.11}$$

For small angles and $\delta \ll 1$, the polarization of the incoming x-ray wave has no influence. The difference to in plane scattering will be discussed in Sec. 4.6.2. $R_F = r_F^2$ and $T_F = t_F^2$ can then be calculated

$$r_F = \frac{k_{i,z}-k_{t,z}}{k_{i,z}+k_{t,z}} \overset{\alpha_i \ll 1}{=} \frac{\alpha_i-\alpha_t}{\alpha_i+\alpha_t} \tag{3.12}$$

$$t_F = \frac{2k_{i,z}}{k_{i,z}+k_{t,z}} \overset{\alpha_i \ll 1}{=} \frac{2\alpha_i}{\alpha_i+\alpha_t}, \tag{3.13}$$

where α_t is the angle of the *refracted* beam

$$\alpha_t = \sqrt{\alpha_i^2-\alpha_c^2} = \alpha_i\sqrt{1-\frac{\alpha_c^2}{\alpha_i^2}}\ . \tag{3.14}$$

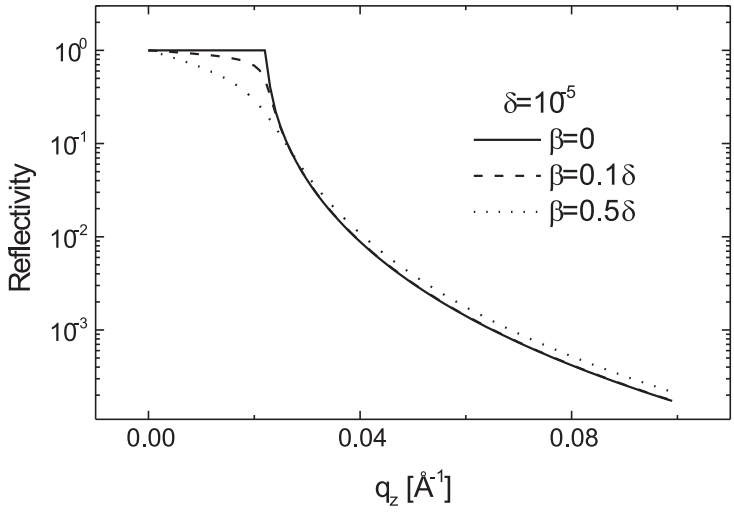

Figure 3.2: *Comparison of the region of total reflection for different values of absorption. Neglecting any absorption the reflectivity exhibits a sharp edge. Absorption of the reflecting material smoothens the sharp edge.*

For $\alpha_i \ll 1°$ the sine-function relating the wave vector to the angle can be neglected. Thus the k-components in Eq. 3.12 can be replaced by the

angles. Under the condition that $\alpha_i \gg \alpha_c$ two more approximations are helpful. First, the refraction angle α_t can be approximated by the first term of a Taylor series $\alpha_t \approx \alpha_i \left(1 + \left(\frac{\alpha_c}{2\alpha_i}\right)^2\right)$, and second, $\alpha_i^2 + \alpha_c^2 \approx 4\alpha_i^2$. The equation for $R_F = r_F^2$ (3.12) can then be reduced to

$$R_F \simeq \left(\frac{\alpha_c}{2\alpha_i}\right)^4 = \left(\frac{q_c}{2q_z}\right)^4, \tag{3.15}$$

where q_z is the momentum transfer perpendicular to the interface and the critical momentum transfer $q_c = \frac{4\pi}{\lambda}\sin\alpha_c$. For small angles the two scales α_c/α_i and q_c/q_z are identical. R_F is the so-called *Fresnel reflectivity* for a perfect interface. The deviation from the reflectivity calculated without any approximations is less than 3% for $q_z \geq 3q_c$. For an elaborate derivation see e.g. [Jac62].

Region of total reflectivity

If the incident angle is smaller than the critical angle ($\alpha_i < \alpha_c$), $k_{t,z}$ becomes imaginary (cp. Eq. 3.11) and reads $k_{t,z} = i\frac{2\pi}{\lambda}\sqrt{\alpha_c^2 - \alpha_i^2}$. This means that the whole intensity is reflected ($R = 1$) as long as absorption is neglected. Inserting $k_{t,z}$ into the expression for the electrical field in the medium, E reads:

$$E \propto e^{ik_{t,z}z} \propto e^{-z\frac{2\pi}{\lambda}\sqrt{\alpha_c^2-\alpha_i^2}} = e^{-\frac{z}{\Lambda}} \tag{3.16}$$

This implies an evanescent wave traveling parallel to the interface. The amplitude of the wave that penetrates the interface decreases exponentially with increasing depth. The penetration depth Λ of the wave is defined as the depth, at which the amplitude decays to $1/e$. For a realistic calculation of Λ the absorption β must be included

$$\begin{aligned} \Lambda^{-1} &= \frac{2\pi}{\lambda\sqrt{2}}\sqrt{\sqrt{(\alpha_c^2 - \alpha_i^2)^2 + 4\beta^2} + \alpha_c^2 - \alpha_i^2} \\ &\overset{\beta=0}{=} \frac{2\pi}{\lambda}\sqrt{\alpha_c^2 - \alpha_i^2}\,. \end{aligned} \tag{3.17}$$

The penetration depth as a function of the incidence angle α_i is shown in Fig. 3.3. Without absorption one would obtain $\Lambda \to \infty$ for $\alpha_i \geq \alpha_c$.

For $\alpha_i \to 0$, the penetration depth is independent of the wavelength and depends only on the dispersion difference (Eq. 3.7) of the materials at the interface. $\Lambda = \frac{\lambda}{2\pi\alpha_c} = \frac{1}{\sqrt{4\pi r_e \Delta\rho_{el}}}$. Neglecting absorption, the reflectivity is

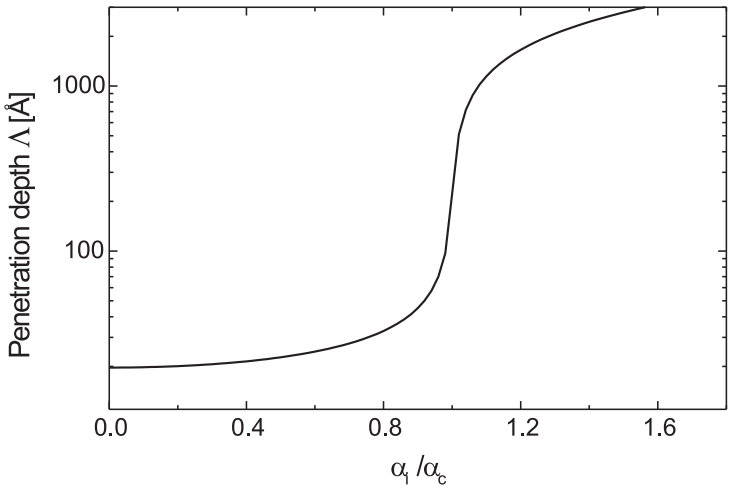

Figure 3.3: *Scattering depth Λ as a function of the incidence angle α_i. For the calculation $\alpha_f = \alpha_i$ was used. The scattering depth for angles larger than α_c is only limited by the absorption.*

unity for $0 < \alpha_i < \alpha_c$, which is called the region of total reflection. Taking into account the absorption the reflectivity is reduced even for $\alpha_i < \alpha_c$. This is further discussed in Sec. 3.2. The evanescent x-ray wave is a tool to reveal lateral structures at the interface with grazing incidence diffraction. This is further discussed in Sec. 3.3.

3.2 Evaluating Specular Scattering - Reflectivity

Specular scattering is the diffracted intensity appearing under the conditions that $\alpha_i = \alpha_f$ and that the plane of scattering is perpendicular to the scattering interface[2]. Thus, the momentum transfer $\mathbf{q}$ has only a component along the z-direction, namely q_z.

As already deduced in Sec. 3.1.1 the most prominent feature of x-ray reflectivity is the fast decay of the reflected intensity for momentum transfers $q_z > q_c$ (s. Eq. 3.15).

Up to this point we have considered only single interfaces without any roughness. In the following we include thin layers of different material and the roughness of the interfaces. A gradual change of the index of refraction at an interface or multiple layers of different index of refraction can be treated

[2]The *plane of scattering* is spanned by the incidence and exit wave vector.

with two different approaches.

3.2.1 Kinematical Approach - Master Formalism

A straightforward approach to calculate the specular scattered intensity based on semi-kinematic theory, i.e. only single scattering events are considered, is the so-called *Master formalism* [AN86].

The Master formula links the derivative of the electron density perpendicular to the interface to a value that is equal to the reflectivity of the interface divided by the Fresnel reflectivity (s. Eq. 3.15). The mathematical operation between the two values is a Fourier transformation. The reflected wave is a superposition of waves reflected from infinitesimally thin layers at different depth z. Each single reflectivity is much smaller than unity, thus, multiple reflections are neglected. The x-ray reflectivity of a thin layer of thickness $\delta z \ll \lambda$ is first calculated: A beam originating from a single source is scattered in the infinitesimal thin layer by the electrons. Then the scattered wave amplitude in a detector D is proportional to the scattering length r_0 of a single electron and to the density of electrons perpendicular to the beam ($\propto \rho_e \Delta z / \sin\theta$). The ratio of amplitudes of the incident and scattered ray E_D/E_S is dimensionless and, as argued above, it must be proportional to $r_0 \rho_e \Delta z / \sin\theta$. The dimension of this term is an inverse length and the ratio is written as

$$\frac{E_D}{E_S} = C \frac{r_0 \rho_e(z) \Delta z \lambda}{\sin\theta} \ , \tag{3.18}$$

$C = e^{i\pi/2} = i$ is a complex constant that results from integration over all beams of each area element of the layer with the appropriate phase factors (s. [War69], appendix A). For the next step beams reflected at a different depth z are superimposed. There is a phase factor $e^{iq_z z}$ incorporated and additionally the electron density as a function of z, which is $\rho_e = \rho_e(z)$. The electron density is calculated as the product of the bulk density ρ_{bulk} and the normalized density profile $\rho(z)$. Thus the reflectivity that includes the ratio of the *modulus squared* amplitudes reads

$$R(q_z) = \left| \frac{i4\pi}{q_z} \rho_{bulk} r_0 \int \rho_e(z) e^{iq_z z} \, \mathrm{d}z \right|^2 = \left(\frac{q_c}{2q_z} \right)^4 \left| \int \rho_e'(z) e^{iq_z z} \mathrm{d}z \right|^2 \ , \tag{3.19}$$

with the substitution $\lambda / \sin\theta = 4\pi/q_z$. The last term of Eq. 3.19 follows from partial integration and by using $q_c = 4\sqrt{\rho_{bulk} r_0 \pi}$. The prefactor $(q_c/2q_z)^4$ is the Fresnel reflectivity R_F from Eq. 3.15 for $q_z > q_c$. In summary the Master formula reads as

$$\frac{R(q_z)}{R_F(q_z)} = \left| \int_{-\infty}^{+\infty} \rho_e'(z) e^{iq_z z} \mathrm{d}z \right|^2 \quad . \tag{3.20}$$

The Master formula in the previous form holds good results for values of $q_z > 4q_c$. For smaller q-values there are significant deviations from the measured reflectivity curve. A semi-kinematic extension of the Master formula can be derived by taking into account refraction corrections at incident angles close to α_c. For this correction q_z is replaced by

$$q_z' = \frac{4\pi}{\lambda} \sin\left(\sqrt{\alpha_i^2 - \alpha_c^2}\right) = \frac{4\pi}{\lambda} \sin\left(\alpha_i'\right) \quad . \tag{3.21}$$

Using this approach the Master formula can be used for momentum transfers $q_z \gtrsim 3q_c$, however, the overall gain is small and depends furthermore on the specific sample parameters.

The mean square of the Fourier transform leads to a loss of the phase. Therefore, the electron density obtained from the Master formula is ambiguous (*phase problem*). The measured reflectivity has to be fitted with a model of the electron density. Known parameters of the system are helpful to build a physically reasonable model.

The Master formalism is well suited to describe the specularly scattered intensity for samples where the absorption of x-rays in the layers above the substrate plays only a minor role. This condition is fulfilled for x-ray scattering on all kinds of material with x-ray energies around 70keV that were used in our experiments. It is possible to tailor the required electron density by a sum of analytical functions, which is an advantage of the semi-kinematic theory. This tremendously reduces the number of free fitting parameters.

3.2.2 Parratt Formalism

The dynamical Parratt formalism was deduced by L.G. Parratt in 1954 [Par54]. It is a recursive algorithm to calculate the reflectivity of a sample consisting of N layers of thickness d_m having an index of refraction n_m on top of a substrate. Therefore we have to consider $N + 1$ interfaces. It is assumed that layer 1 is the medium above the sample (vacuum, air, or a light material) and the substrate is layer $N + 1$. For the reflected intensity not only the intensity reflected at each interface is considered but also the intensity transmitted and back reflected downwards in the direction of the substrate is taken into account (cp. Fig. 3.4). For each layer i the ratio between reflected and transmitted wave amplitudes is calculated

$$x_m = \frac{r_m}{t_m} = e^{-2ik_{z,m},z_m} \frac{r_{m,m+1} + x_{m+1}e^{2ik_{z,m+1}z_m}}{1 + r_{m,m+1}x_{m+1}e^{2ik_{z,m+1}z_m}} \ , \tag{3.22}$$

with

$$r_{m,m+1} = \frac{k_{z,m} - k_{z,m+1}}{k_{z,m} + k_{z,m+1}} \ . \tag{3.23}$$

This is the Fresnel coefficient (s. Eq. 3.12) of interface m and $k_{z,m} = \frac{2\pi}{\lambda}\sqrt{n_m^2 - \cos^2\alpha_i}$ is the z component of the wavevector in layer m (s. Eq. 3.11). For each interface the reflected intensity is calculated successively starting with the substrate and the assumption $r_{N+1} = x_{N+1} = 0$. Finally the reflected intensity is given by

$$R = |x_1|^2 = |r_1|^2 \ , \tag{3.24}$$

since the transmission coefficient for the topmost layer is taken as $t_1 = 1$. If the topmost layer is not vacuum, the incoming intensity at the interface is simply normalized in such a way that $t_1 = 1$ remains valid.

3.2.3 Roughness of Interfaces

Real interfaces are not flat, there is at least atomic roughness present. A single interface can be defined by a contour function $z(\mathbf{R}_{xy})$ with $\mathbf{R}_{xy} = (x, y)$ as the horizontal distance from the origin and z defining the local height of the interface. The mean height of the interface is defined as $\bar{z} = \langle z(\mathbf{R}_{xy})\rangle_{\mathbf{R}}$ where the brackets denote a spatial average. In the case of a homogeneous interface this corresponds to an ensemble average.

With the mean height the contour function can be rewritten as the height fluctuations $h(\mathbf{R}_{xy})$ around the mean height $\bar{z}$ (cp. Fig. 3.5)

$$h(\mathbf{R}_{xy}) = z(\mathbf{R}_{xy}) - \bar{z} \ . \tag{3.25}$$

The root mean square (rms) roughness σ of the interface is then given as

$$\sigma = \sqrt{\langle (h(\mathbf{R}_{xy}))^2 \rangle_{\mathbf{R}_{xy}}} \ . \tag{3.26}$$

The height-height correlation function is defined as

$$C(\mathbf{R}_{xy}) = \left\langle h(\mathbf{R}'_{xy}) \cdot h(\mathbf{R}'_{xy} + \mathbf{R}_{xy}) \right\rangle_{\mathbf{R}'_{xy}} \ . \tag{3.27}$$

Finally the height-difference correlation function is given as

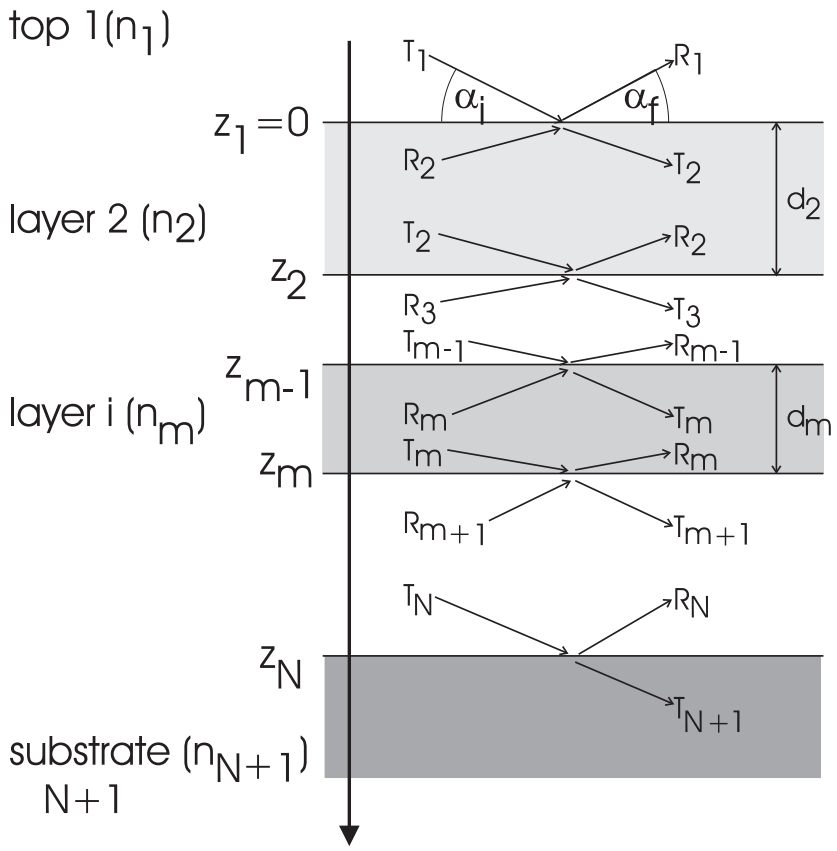

Figure 3.4: *Schematic representation to illustrate the different Fresnel coefficient in the sample consisting of N layers.*

$$g(\mathbf{R}_{xy}) = \left\langle (h(\mathbf{R}'_{xy}) - h(\mathbf{R}'_{xy} + \mathbf{R}_{xy}))^2 \right\rangle_{\mathbf{R}'_{xy}} = 2\sigma^2 - 2C(\mathbf{R}_{xy}) \ . \qquad (3.28)$$

It follows straightforward that $\sigma^2 = C(\mathbf{0})$. For isotropic surfaces, g and C only depend on the absolute value of $\mathbf{R}_{xy}$. Often the fluctuations around $\bar{z}$ can be described by a Gaussian probability distribution with the variance σ including 63.3% of all fluctuations in the interval $\bar{z} \pm \sigma$.

Roughness and Parratt

The Parratt formalism treats interfaces as ideally flat. In the original Parratt formalism roughness is not included. One way to incorporate it, consists of separating the sample in layers of tiny thickness with gradually changing

electron density. However, this may require hundreds of layers for modeling a given reflectivity data set. A more elegant way was developed by Névot and Croce [Név80]. They added a Gaussian roughness term to each interface.

The index of refraction $n(z)$ between layer m and $m+1$ follows then a continuous, error-function-like transition from n_m to n_{m+1} with a width σ_m. In the Parratt formalism it can be implemented by multiplying $r_{m,m+1}$ (cp. Eq. 3.23) by an exponential damping factor $e^{-2k_{z,m}k_{z,m+1}\sigma_m^2}$. The expanded Fresnel coefficient for the reflection at one of the interfaces reads then

$$\tilde{r}_{m,m+1} = r_{m,m+1} \cdot e^{-2k_{z,m}k_{z,m+1}\sigma_m^2} = \frac{k_{z,m} - k_{z,m+1}}{k_{z,m} + k_{z,m+1}} \cdot e^{-2k_{z,m}k_{z,m+1}\sigma_m^2} \ . \quad (3.29)$$

This expansion is only valid for roughness σ_m smaller than the thickness d_m and d_{m+1} of the corresponding layers: $\sigma_m \ll d_m$ and $\sigma_m \ll d_{m+1}$.

Roughness results in damping of the specularly reflected intensity. Further discussion can be found in [Dos92, Tol99]. The Parratt formalism for reflectivity at multiple interfaces takes into account all scattering contributions of all interfaces. Therefore it is correct for all momentum transfers q_z, especially for small momentum transfers. The drawback of the formalism is the limitation in the roughness as mentioned above and the potentially large number of layers required for a fit.

Roughness and the kinematical approximation

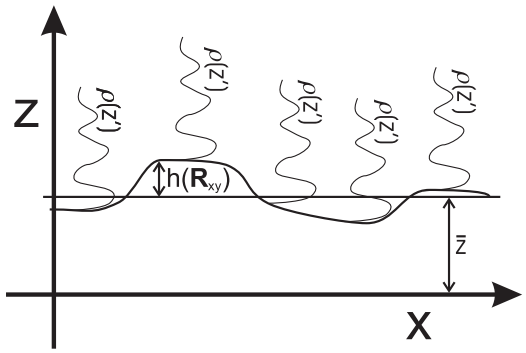

Figure 3.5: *Illustration of an interface with an electron density profile $\rho(z')$ independent of roughness projected along the x-axis. The roughness is described independently by $h(\mathbf{R}_{xy})$.*

The Master formalism is a kinematical approach to reflectivity. At first sight it does not distinguish between lateral roughness at an interface and

a gradient in the electron density profile. It assumes true specular reflected intensity ($\alpha_i \stackrel{!}{=} \alpha_f$) and does not consider diffuse scattered intensity. The Master formalism is extended to the case of roughness at an interface, the results are taken from [Rau05].

We consider the case of a rough interface. The interface is described by a height fluctuation function $h(\mathbf{R}_{xy})$ (s. prev. Sec. 3.2.3). Each height of the interface has the same density profile $\rho_l(z')$ with $z' = \bar{z} - h(\mathbf{R}_{xy})$. In this discussion the density ρ_l is linked to the electron density ρ_e as $\rho_l = \frac{k^2\lambda^2}{\pi} r_e \rho_e$. The absorption is neglected in this discussion. A sketch is shown in Fig. 3.5. An incident plane wave $E_i(\mathbf{r}) = e^{i\mathbf{kr}}$ is scattered at such an interface resulting in a scattered wave

$$E(\mathbf{r}) = -\frac{e^{i\mathbf{kr}}}{4\pi\mathbf{r}} \int e^{-i\mathbf{q}_{||}\mathbf{R}_{xy}} \int_{-\infty}^{\infty} e^{-iq_z z} \rho_l(z - h(\mathbf{R}_{xy}))\ \mathrm{d}z\ \mathrm{d}^2R\ , \tag{3.30}$$

where $\mathbf{q}_{||} = (q_x, q_y)$ is the momentum transfer parallel to the interface and $\mathbf{R}_{xy} = (x, y)$. By substituting $z' = z - h(\mathbf{R}_{xy})$, one obtains

$$\begin{aligned} E(\mathbf{r}) &= -\frac{e^{i\mathbf{kr}}}{4\pi\mathbf{r}} \int e^{-i\mathbf{q}_{||}\mathbf{R}_{xy} - iq_z h(\mathbf{R}_{xy})} \int_{-\infty}^{\infty} e^{-iq_z z'} \rho_l(z')\ \mathrm{d}z'\ \mathrm{d}^2R \\ &= -\frac{e^{i\mathbf{kr}}}{4\pi\mathbf{r}} \int e^{-i\mathbf{q}_{||}\mathbf{R}_{xy} - iq_z h(\mathbf{R}_{xy})} \tilde{\rho}_l(q_z)\ \mathrm{d}^2R\ , \end{aligned} \tag{3.31}$$

with

$$\tilde{\rho}_l(q_z) = \int_{-\infty}^{\infty} e^{-iq_z z'} \rho_l(z')\ \mathrm{d}z'\ , \tag{3.32}$$

being the Fourier transform of the density profile. The differential scattering cross section is then calculated as

$$\frac{\mathrm{d}\sigma}{\mathrm{d}\Omega} = \mathbf{r}^2 |E|^2 = \frac{1}{16\pi^2} \iint e^{-i\mathbf{q}_{||}(\mathbf{R}_{xy} - \mathbf{R}'_{xy})} e^{-iq_z(h(\mathbf{R}_{xy}) - h(\mathbf{R}'_{xy}))} |\tilde{\rho}_l(q_z)|^2\ \mathrm{d}^2R\ \mathrm{d}^2R'\ . \tag{3.33}$$

Under the assumption that the $(h(\mathbf{R}_{xy}) - h(\mathbf{R}'_{xy}))$-values are Gaussian distributed and that the projected x-ray coherence length parallel to the interface is large compared to the correlation length of $h(\mathbf{R}_{xy})$, Eq. 3.33 can be rewritten using the substitution $\mathbf{R}''_{xy} = \mathbf{R}_{xy} - \mathbf{R}'_{xy}$ and the height-difference correlation function $g(\mathbf{R}_{xy})$ and introducing the illuminated interface area $A(\mathbf{q})$

$$\frac{\mathrm{d}\sigma}{\mathrm{d}\Omega} = \frac{A(\mathbf{q})}{16\pi^2} \int e^{-i\mathbf{q}\mathbf{R}''_{xy}} e^{-q_z^2 g(\mathbf{R}''_{xy})/2} |\tilde{\rho}_l(q_z)|^2 \ \mathrm{d}^2 R''_{xy} \ . \tag{3.34}$$

In most cases $g(\mathbf{R}_{xy})$ reaches an upper limit of $2\sigma^2$ for $R_{xy} \to \infty$. Then the differential cross section can be split into a specular and a diffuse (off-specular) part

$$\begin{aligned} \left(\frac{\mathrm{d}\sigma}{\mathrm{d}\Omega}\right)_{\mathrm{spec}} &= \frac{A(\mathbf{q})}{16\pi^2} e^{-q_z^2\sigma^2} \delta(q_{||}) |\tilde{\rho}_l(q_z)|^2 \qquad (3.35) \\ \left(\frac{\mathrm{d}\sigma}{\mathrm{d}\Omega}\right)_{\mathrm{diff}} &= \frac{A(\mathbf{q})}{16\pi^2} e^{-q_z^2\sigma^2} \int e^{[C(\mathbf{R}''_{xy})q_z^2 - 1]} e^{\mathbf{q}\mathbf{R}''_{xy}} |\tilde{\rho}_l(q_z)|^2 \ \mathrm{d}^2 R'' \ . \end{aligned}$$

The measured intensity I is the integrated differential cross section over the solid angle that is covered by the detector

$$I = \int_{\substack{\mathrm{Solid} \\ \mathrm{Angle}}} \frac{\mathrm{d}\sigma}{\mathrm{d}\Omega} \ \mathrm{d}\Omega_{\mathrm{det}} \ . \tag{3.36}$$

Close to the specular condition and assuming that the full incident beam illuminates the interface the illuminated interface area is approximately given as $A(\mathbf{q}) \approx \frac{2kw_z w_y}{q_z}$ with w_z and w_y the beam height and width, respectively. The specular reflected intensity can then be written as

$$\int \left(\frac{\mathrm{d}\sigma}{\mathrm{d}\Omega}\right)_{\mathrm{spec}} \mathrm{d}\Omega = \frac{w_z w_y e^{-\sigma^2 q_z^2}}{2q_z^2} |\tilde{\rho}_l(q_z)|^2 \ . \tag{3.37}$$

The reflectivity is defined as the reflected intensity divided by the incident intensity. Thus the reflectivity is given from the above equation as

$$R_{\mathrm{spec}} = \frac{e^{-\sigma^2 q_z^2}}{q_z^2} |\tilde{\rho}_l(q_z)|^2 = \frac{e^{-\sigma^2 q_z^2}}{q_z^2} \frac{1}{q_z^2} \left| \left(\frac{\mathrm{d}\rho_l(z)}{\mathrm{d}z}\right)_{\mathrm{FT}} \right|^2 \ , \tag{3.38}$$

$\left(\frac{\mathrm{d}\rho_l(z)}{\mathrm{d}z}\right)_{\mathrm{FT}}$ denotes the Fourier transform of the derivative of the density profile. As a result the specular reflectivity is the same, if the interface is treated as smooth, but the laterally averaged density profile is taken. Assuming a Gaussian roughness of width σ this corresponds to a convolution of the density $\rho_l(z')$ with an error function of the same width. The reflectivity decays much faster with q_z due to the exponential damping factor in comparison with a perfectly sharp interface ($\sigma = 0$).

Inserting the definition of $\rho_l = \frac{k^2\lambda^2}{\pi} r_e \rho_e$ and the approximation of the Fresnel reflectivity for sufficiently large momentum transfers $R_F = \left(\frac{q_c}{2q_z}\right)^4$ one can rewrite Eq. 3.38

$$R_{\text{spec}}(q_z) = R_F(q_z) \left| \int \rho'_e(z) e^{iq_z z} \, \mathrm{d}z \right|^2 . \tag{3.39}$$

This is the Master formula (Eq. 3.20) introduced in Sec. 3.2.1. To deduce this result it does not make a difference whether the integration at the detector is done using open slits or with separate rocking scans.

Integrated diffuse intensity in the kinematical limit

In the previous section it was assumed that the specular intensity can be separated from the diffuse scattered intensity. Under certain conditions, especially if the roughness of the interface is large, this may be not the case. However, the integrated intensity from a rocking scan can be calculated for contributions from diffuse and specular reflected intensity. Eq. 3.34 contains the diffuse and specular reflected intensity. Using $A(\mathbf{q}) \approx \frac{2kw_z w_y}{q_z}$ with w_z and w_y the beam height and width, respectively as in the previous section and the appropriate integration limits one obtains

$$\int \frac{\mathrm{d}\sigma}{\mathrm{d}\Omega} \, \mathrm{d}\Omega = \frac{w_z w_y}{2q_z^2} \iint e^{-i\mathbf{q}_{||}\mathbf{R}''_{xy}} e^{-\frac{q_z^2}{2} g(\mathbf{R}''_{xy})} |\tilde{\rho}_l(q_z)|^2 \, \mathrm{d}^2q \mathrm{d}^2R'' = \frac{w_z w_y}{2q_z^2} |\tilde{\rho}_l(q_z)|^2 . \tag{3.40}$$

This is the same expression as for the specular part of the reflected intensity (Eq. 3.37), except for the exponential damping factor containing the roughness. This can be understood as reflected intensity that is off-specular scattered due to the roughness of the interface. It is regained via the integration of the rocking scan.

Minimum Details in the Electron Density Profile

Reflectivity measurements can usually only be recorded to an upper limit in momentum transfer, $q_{z_{max}}$. For larger momentum transfer the reflected signal cannot be distinguished from the diffuse scattered background. This limit is determined by the experimental setup and the sample properties like the roughness.

The maximum momentum transfer, at which the reflectivity was measured, determines the minimum features Δz_{min} that can be resolved in the fit of the electron density profile

$$\Delta z_{min} = \frac{2\pi}{q_{z_{max}}} , \tag{3.41}$$

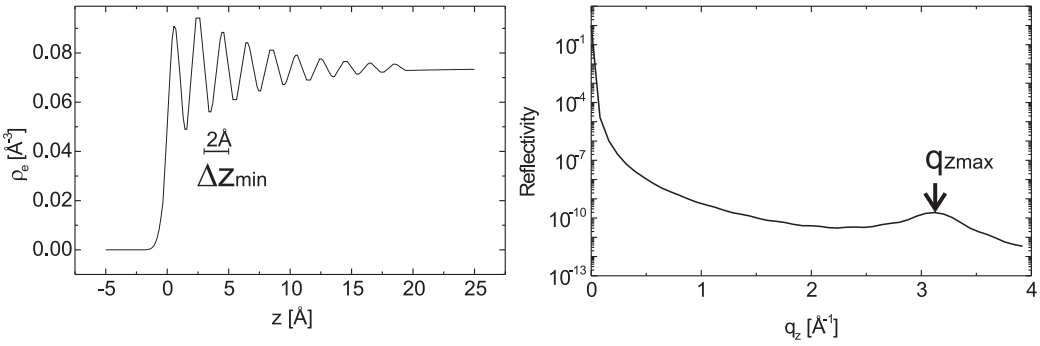

Figure 3.6: *Calculation of atomic layering at an interface (left side) and the correspondent reflectivity (right side) to illustrate the resolution limitations in fits. The layering effect was taken to be stronger than in real liquids [Reg95] (s. Fig. 2.6).*

which is given by the sampling theorem. In Fig. 3.6 this relationship is illustrated in a calculated reflectivity of a given electron density profile, where stratified atomic layers are supposed. To resolve features in the electron density profile smaller than 2Å, it is necessary to measure the reflectivity up to more than $q_z = 3\text{Å}^{-1}$. This has to be kept in mind for fitting reflectivities.

3.3 Grazing incidence diffraction

In the previous section it has been shown how structural information perpendicular to an interface can be obtained by analyzing specular reflection. To gain a comprehensive understanding about the structure of an extended interface, additional lateral structure information is mandatory. Grazing incidence diffraction (GID) is the perfect tool to resolve the lateral structure of an interface [Dos92].

We are interested in a diffuse signal from a liquid having a structure factor $S(\mathbf{q})$. For details about the liquid structure factor see Sec. 3.4. With grazing incidence diffraction we use the refraction properties of interfaces, which are denoted here as Y. The measured intensity is proportional to Y and to the liquid structure factor $S(\mathbf{q})$

$$I_{meas} \propto Y \cdot S(\mathbf{q}) \ . \tag{3.42}$$

A schematic drawing of the scattering process is shown in Figs. 3.7 and 3.8. The most important feature of grazing incidence diffraction is certainly

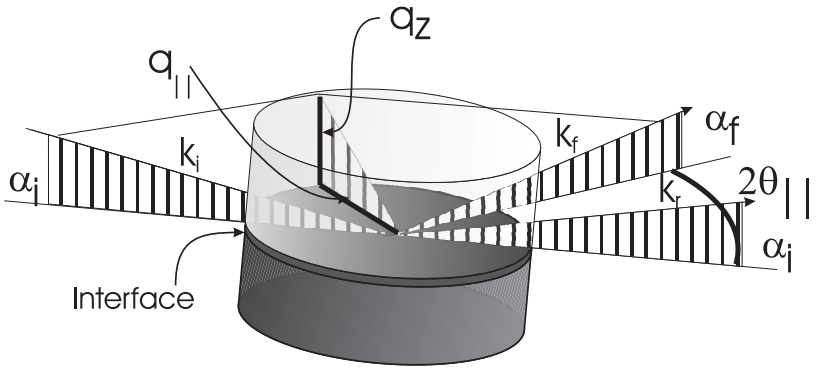

Figure 3.7: *Schematic of a GID setup in three dimensions. q_z is defined by the incident (α_i) and exit (α_f) angles. The in plane momentum transfer $q_{||}$ is defined by the angle $2\theta_{||}$.*

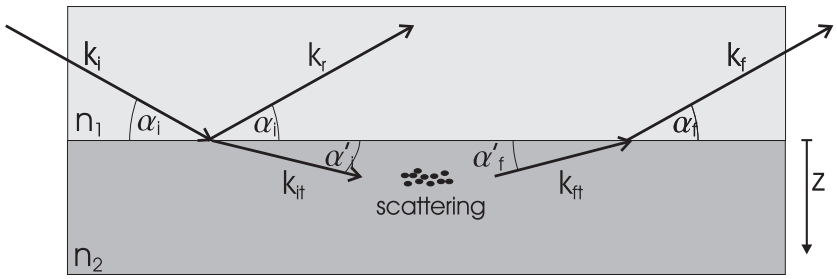

Figure 3.8: *Schematic of a GID setup in two dimensions. It emphasizes the separation of the refraction at the interface from the scattering inside the interface. The evanescent wave travels parallel to the interface and its amplitude is exponentially damped in deeper regions of the interface.*

the fact that the incidence angle α_i is kept below the critical angle α_c of the system. This results in a momentum transfer inside the interface, which has almost no specular component $q_z \simeq 0$. In this regime the structure factor of a liquid can be regarded as constant with respect to q_z. The structure factor can be separated in two parts $S(\mathbf{q}) = S(q_{||}) \cdot S(q_z)$, where $S(q_z)$ can be regarded as constant. Then the scattered intensity is proportional to the structure parallel to the interface. The other important feature are x-ray waves exponentially damped inside the interface for angles $\alpha_i \leq \alpha_c$ (cp. Eq. 3.16) with a penetration depth of $\Lambda(\alpha_i)$ (cp. Eq. 3.17). This allows for a very precise control of the depth, up to which the structural information is obtained, and thus permits a depth resolved structural analysis.

The z-components of the wave vectors k_i, k_f, k_{it}, and k_{ft} are given by

$$\begin{aligned} k_i &= \frac{2\pi}{\lambda}\sin\alpha_i \\ k_f &= -\frac{2\pi}{\lambda}\sin\alpha_f \\ k_{it} &= \frac{2\pi}{\lambda}\sqrt{\sin^2\alpha_i - 2\Delta\delta - 2i\beta_2} \\ k_{ft} &= \frac{2\pi}{\lambda}\sqrt{\sin^2\alpha_f - 2\Delta\delta - 2i\beta_2}\ . \end{aligned} \tag{3.43}$$

Normalizing the incident intensity at the interface to unity, the absorption of the upper material (β_1) is irrelevant. Note that the x- and y-components of the exiting wave vectors $\mathbf{k}_{ft}$ and $\mathbf{k}_f$ are different from the incidence wave vectors $\mathbf{k}_i$ and $\mathbf{k}_{it}$, depending on the momentum transfer parallel to the interface. The scattering depth is given by

$$\Lambda(\alpha_i, \alpha_f) = \left|\frac{1}{\mathrm{Im}(k_{it} - k_{ft})}\right|. \tag{3.44}$$

The result is symmetric in α_i and α_f. The depth of the scattering process can be limited either by the incidence or exit angle. This is illustrated in Fig. 3.9, where α_i is a parameter that limits effectively the scattering depth. The detected intensity can be increased by integrating over an exit angle interval, which is effectively done by opening the detector slits perpendicular to the interface, so that the detector covers a range larger than the critical angle α_c.

The transmission function t_i and t_f for the transmitted amplitudes through the interface are given as

$$t_i(\alpha_i) = \left|2\frac{k_i}{k_i + k_{it}} e^{\frac{\sigma^2}{2}(k_i - k_{it})^2}\right| \tag{3.45}$$

$$t_f(\alpha_f) = \left|2\frac{k_f}{k_f + k_{ft}} e^{\frac{\sigma^2}{2}(k_f - k_{ft})^2}\right|, \tag{3.46}$$

respectively. σ is a parameter for the roughness of the interface as introduced in Sec. 3.2. The roughness leads to a damping of the transmitted amplitudes. In Fig. 3.10 a set of transmission functions is shown. The transmission functions given in Eq. 3.45 and Eq. 3.46 yield the same result with respect to the angle, thus it is sufficient to plot t_i.

For the transmitted intensity $f(\alpha_i, \alpha_f, \mathbf{q})$ having linear polarisation and using GID-geometry it holds [Dos92]

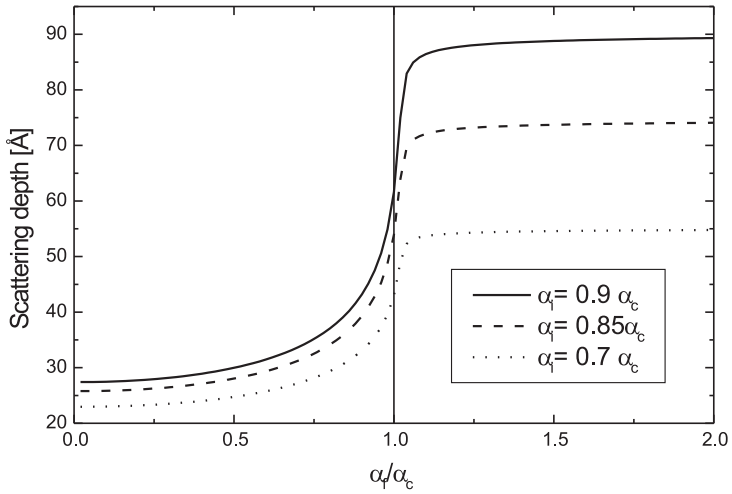

Figure 3.9: *Scattering depth Λ as a function of the exit angle α_f using the incidence angle α_i as a parameter. For a given incidence angle the scattering depth is restricted even for higher exit angles. Values were taken for a Pb(liq.)-Si(100) interface and $\lambda = 0.17\mathring{A}$.*

$$f(\alpha_i, \alpha_f, \mathbf{q}) \propto I_0 \cdot t_i(\alpha_i) \cdot t_f(\alpha_f) \cdot \Lambda(\alpha_i, \alpha_f) \cdot S(\mathbf{q}) \ . \tag{3.47}$$

I_0 is the incoming intensity and $S(\mathbf{q})$ is the liquid structure factor at the interface. The measured intensity as a function of α_f, using α_i as a parameter and setting the in plane momentum transfer $q_{||}$ to a fixed value is directly proportional to $f(\alpha_i = const, \alpha_f, \mathbf{q} = (q_z, q_{||} = const))$. The in plane momentum transfer is given as $q_{||} = \frac{4\pi}{\lambda} \sin\theta_{||}$ with respect to the in plane scattering angle $2\theta_{||}$. The maximum of f is at the critical angle α_c for $\alpha_i < \alpha_c$. This measurement can be used to check the precise position of the critical angle. Calculated examples for the term $T_i \cdot T_f \cdot \Lambda$ are plotted in Fig. 3.11 with different values for the incidence angle α_i. The transmitted intensity is higher for higher incidence angles, admittedly the penetration depth is increased as well. The function in dependence of α_f always peaks at the critical angle α_c for incidence angles smaller than the critical angle. For incidence angles larger than the critical angle there is only a steep increase of the signal at the critical angle. This signal is dominated by bulk scattering. As mentioned before for incidence angles $\alpha_i < \alpha_c$ the scattering depth Λ is limited even for scattering angles $\alpha_f > \alpha_c$. Moreover the structure factor is featureless in the region $q_z < q_c$. Therefore, it is useful to integrate the signal $f(\alpha_i, \alpha_f, q_{||})$ over an interval of the exit angle α_f simply by opening the

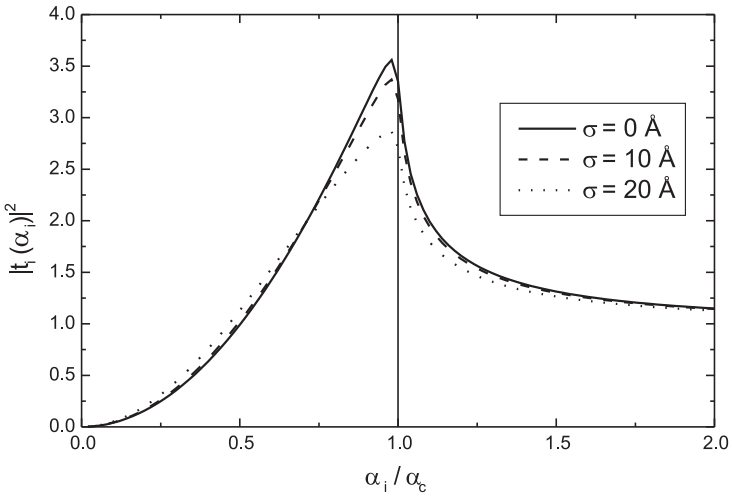

Figure 3.10: *The transmission function $t_i(\alpha_i)$ using σ as a Parameter. The maximum is slightly below the critical angle α_c.*

detector slits to a wider gap. The remaining free parameter of this function is the incidence angle α_i and $q_{||}$

$$I(\alpha_i, q_{||}) \propto \int_{\alpha_{\text{low}}}^{\alpha_{\text{high}}} f(\alpha_i, \alpha_f, q_{||})\ \mathrm{d}\alpha_f\ . \tag{3.48}$$

Calculated examples are shown in Fig. 3.12, with $\alpha_{\text{low}} = 0$ and $\alpha_{\text{high}} = n \cdot \alpha_c$. It can be seen that the intensity is increased, if the signal is integrated over a wider range of the exit angle α_f. However, for a larger integration area the background intensity from the whole sample increases in such a way that an intermediate value for the integration limit has to be chosen. In our experiments the integration range was usually set from zero to $3\alpha_c$.

The α_f-resolved scattering intensities can be converted into depth profiles depending on the setting of α_i and α_f. For the α_f-integrated data an effective scattering depth Λ_{eff} has to be calculated that depends on α_i

$$\Lambda_{eff}(\alpha_i) = \frac{\int_{\alpha_{\text{low}}}^{\alpha_{\text{high}}} f(\alpha_i, \alpha_f, q_{||})\Lambda(\alpha_i, \alpha_f)\ \mathrm{d}\alpha_f}{\int_{\alpha_{\text{low}}}^{\alpha_{\text{high}}} f(\alpha_i, \alpha_f, q_{||})\ \mathrm{d}\alpha_f}\ . \tag{3.49}$$

In conclusion, GID is a perfect tool to characterize the structure of buried interfaces. The roughness of the interface reduces the signal from the interface and increases diffuse scattering, which leads to a reduced signal to back-

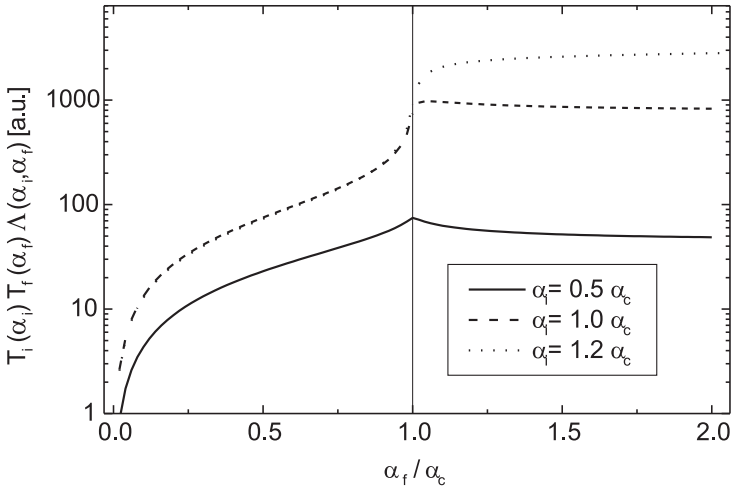

Figure 3.11: *The scattered intensity at the interface in grazing incidence geometry. The roughness σ is set to zero.*

ground ratio. In this work the roughness of the samples was always below 10Å. On the other hand the curvature of the interface can be a problem, since the angles are very small and therefore the angles can vary along the interface.

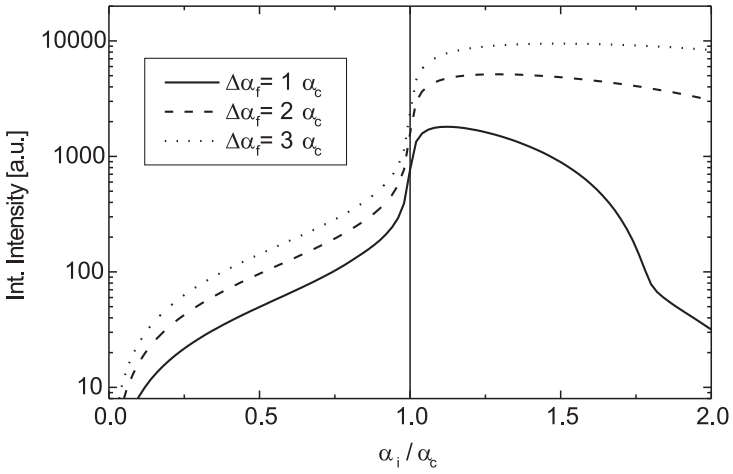

Figure 3.12: *Intensity scattered scanning the incidence angle α_i (α_i-Profile) and integrating over a range of α_f.*

3.4 Scattering from Liquids - Liquid Structure Factor

Liquids were investigated with x-rays almost from the very beginning of x-ray diffraction [Fri13]. The main principles are well understood and in parts further expanded, e.g. distinction of the nucleus and electronic structure factor [Chi87]. The structure factor $S(q)$ for a liquid is a continuous function unlike the one for a crystal. The relation to real space with its pair distribution function $g(r)$ is achieved via the 3-dimensional Fourier transform as already introduced in Sec. 2.1.

The coherently scattered intensity from a liquid is deduced following the discussions in [War69] and [Was81]. The amplitude of scattered x-rays from an arbitrary arrangement of atoms of one type is given as

$$u(\mathbf{q}) = \sum_m f(\mathbf{q}) e^{-i\mathbf{q}\mathbf{r}_m} \ , \tag{3.50}$$

$\mathbf{q}$ is the momentum transfer and f($\mathbf{q}$) the atomic form factor. The coherent scattering intensity is given by

$$\begin{aligned} I_{\mathrm{coh}}(\mathbf{q}) &= \langle u^*(\mathbf{q}) u(\mathbf{q}) \rangle = \left\langle |u(\mathbf{q})|^2 \right\rangle \\ &= \left\langle \sum_m \sum_n f^2(\mathbf{q}) e^{-\mathbf{q}(\mathbf{r}_m - \mathbf{r}_n)} \right\rangle \ . \end{aligned} \tag{3.51}$$

The brackets $\langle\rangle$ denote the statistical average. The relative positions of the atoms $(\mathbf{r}_m - \mathbf{r}_n)$ have no discrete values as for crystal structures. Thus, the summation in Eq. 3.51 may be expressed by the average value of the positional correlation over all orientations. Due to spherical symmetry, the function $f(\mathbf{q})$ and $I_{\mathrm{coh}}(\mathbf{q})$ depend only upon the magnitude q of the momentum transfer $\mathbf{q}$ for liquid systems.

Excluding the forward scattering term, the structure factor $S(q)$ is defined as follows

$$S(q) = \frac{1}{N} \left\langle \sum_m \sum_n e^{-iq(r_m - r_n)} \right\rangle - N\delta_{q,0} \ . \tag{3.52}$$

The term $N\delta_{q,0}$ corresponds to the intensity at $q = 0$. This term is frequently neglected in experiments because it has physical significance only near $q = 0$. It is related to the isothermal compressibility κ_T

$$S(q = 0) = \rho_0 k_B T \kappa_T \ , \tag{3.53}$$

$\rho_0 = N/V$ is the number density, k_B is the Boltzman constant, and T is the temperature [Mar02].

The pair distribution function $g(r)$ is defined by the following equation

$$g(r) = \frac{\rho(r)}{\rho_0} = \frac{1}{N\rho_0} \left\langle \sum_m \sum_n \delta(r - (r_m - r_n)) \right\rangle - \frac{\delta(r)}{\rho_0} \ , \tag{3.54}$$

$\rho(r)$ is the radial density function. Since the atomic correlation becomes blurred for large values of r the pair distribution function approaches unity, i.e. $g(r) \to 1$. Eq. 3.54 can then be rewritten to

$$\frac{1}{N} \left\langle \sum_m \sum_n \delta(r - (r_m - r_n)) \right\rangle - \rho_0 = \rho_0[g(r) - 1] + \delta(r) \ . \tag{3.55}$$

Using the Fourier transformation one obtains

$$\frac{1}{N} \left\langle \sum_m \sum_n e^{-iq(r_m - r_n)} \right\rangle - N\delta_{q,0} = 1 + \rho_0 \int [g(r) - 1] e^{-iqr} \mathrm{d}r \ . \tag{3.56}$$

Hence, the following relation between the structure factor and the pair distribution function is obtained

$$S(q) = 1 + \rho_0 \int [g(r) - 1] e^{-iqr} \mathrm{d}r \ . \tag{3.57}$$

The spherical symmetry of $g(r)$ and $S(q)$ allows to rewrite Eq. 3.57 as a Fourier-Sine transformation

$$\begin{aligned} S(q) - 1 &= \frac{4\pi\rho_0}{q} \int_0^\infty r[g(r) - 1] \sin qr \ \mathrm{d}r \\ g(r) - 1 &= \frac{1}{2\pi^2\rho_0 r} \int_0^\infty q[S(q) - 1] \sin qr \ \mathrm{d}q \ . \end{aligned} \tag{3.58}$$

The structure factor $S(q)$ can be measured in a scattering experiment. By definition $4\pi r^2 \rho(r) \mathrm{d}r$ is the average number of atom centers at a distance between r and $r + \mathrm{d}r$ from the center of an arbitrary atom. In a liquid this average is the average over all atoms *and* over the duration of the measurement.

The Fourier transformation can be evaluated under the pre-requisite that the structure factor is measured up to high enough q-values. The limit of the integrand is zero, because it holds $S(q) \rightarrow 1$ for $q \rightarrow \infty$. Possible artifacts from termination of the interval or the finite step size can arise for small values in r, more precisely for values smaller than the first peak of the pair distribution function. They can be eliminated by comparison with known structure factors.

3.4.1 Structure Factor for 2D-liquids

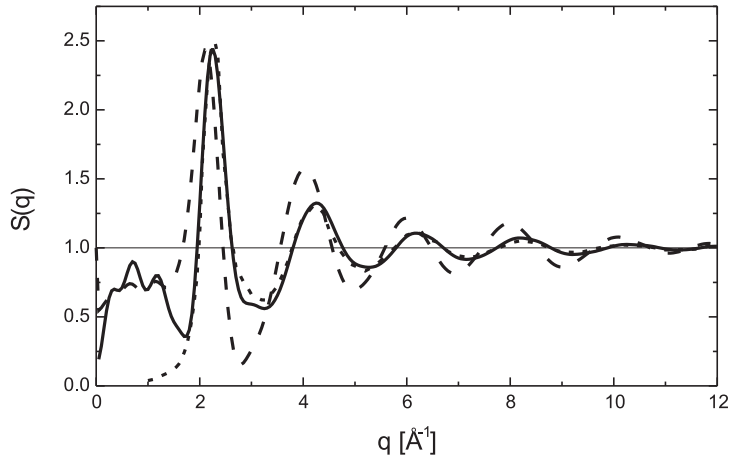

Figure 3.13: *Comparison of structure factors $S(q)$ of liquid lead. The long dashed line is the one calculated from $g(r)$ from [Was80] using cylindrical symmetry and the solid line is the one calculated assuming spherical symmetry. The short dashed line is taken from literature [Was80]. For q-values smaller than 2Å^{-1} one can see artifacts of the Fourier transformations.*

The Fourier-Sine transformation of Eqns 3.58 uses the spherical symmetry of the pair distribution function $g(r)$ in bulk liquids. In case that the scattered intensity originates from a two-dimensional liquid the pair distribution function has a cylindrical instead of a spherical symmetry. The Fourier transformation (cp. Eq. 3.57) can be displayed as a Fourier-Bessel transformation [Wri46, Gre90]

$$S(q) - 1 = 2\pi\rho_0 \int_0^\infty [g(r) - 1] r J_0(qr)\ \mathrm{d}r \tag{3.59}$$

$$g(r) - 1 = \frac{2\pi}{\rho_0} \int_0^\infty [S(q) - 1] q J_0(qr)\ \mathrm{d}q\ . \tag{3.60}$$

$J_0(qr)$ is the Bessel function of order zero[3]. In a direct comparison of the transform of a pair distribution function in spherical and cylindrical coordinates the difference in the structure factor can be seen. For a cylindrical symmetry the maxima of the structure factor are shifted to smaller values in q and the damping of the maxima is less for higher values in q. To illustrate these results calculated structure factors for liquid lead are shown in Fig. 3.13

[3] $J_0(x) = \sum_{\nu=0}^{\infty} \frac{(-1)^\nu}{\nu!\Gamma(\nu+1)} \left(\frac{x}{2}\right)^{2\nu}$

Chapter 4

X-ray Experiments

The measurements relevant for investigating deeply buried solid-liquid interfaces can only be performed at modern synchrotron radiation facilities. The required high energy photon flux of more than 10^{10} photons/s in a beam of micrometer size having almost no divergence is not achievable with conventional x-ray tubes. A high angular resolution is necessary since the critical angle of the interfaces investigated in this work is $\alpha_c = 0.03^\circ \ldots 0.04^\circ$ at $E \approx 70$keV. At the critical angle in GID it has to be measured with a resolution of $\Delta\alpha/\alpha \approx 10^{-2}$.

The experiments were exclusively performed at the European Synchrotron Radiation Facility (ESRF), which is a third generation synchrotron. The storage ring has a circumference of 844m and the electrons have an energy of 6GeV. The preferred operational modes for our experiments are 2/3 or uniform filling[1].

4.1 Beamline ID15A

For each of our experiments we built up a complete high precision diffractometer. A sketch of the beamline is shown in Fig. 4.1. The insertion device is an asymmetrical multipole wiggler consisting of seven periods. The critical energy is 44.1keV at a minimal distance of the poles of 20.3mm and a maximum magnetic field of 1.84T. Right after the wiggler the bending magnet is installed that separates the electron beam from the photons (not shown in Fig. 4.1). There is an aluminum filter of thickness 4mm installed that absorbs energies up to 40keV, which reduces the heat load on the downstream optical components. The source size is $200 \times 67\mu\text{m}^2$ in horizontal and vertical

[1]Details about operations modes can be found at www.esrf.fr

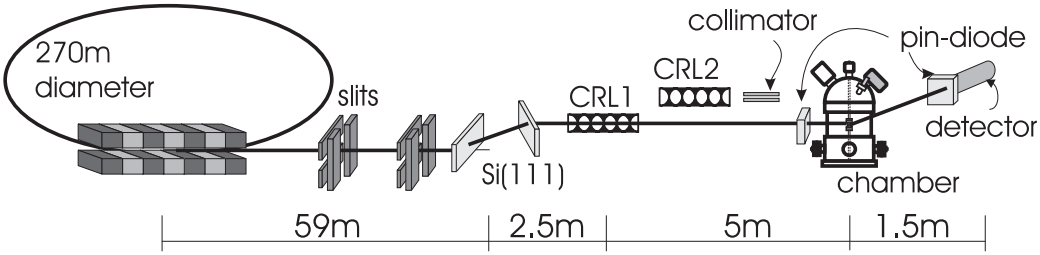

Figure 4.1: *Sketch of beamline ID15a from the storage ring to the detector. The photon producing element is a wiggler. All elements are computer controlled.* CRL1 *and* CRL2 *are compound refractive lenses, that focus either on the sample (1) or on the detector (2). The collimator defines a beam height of* 8μm*. Most of the measurements were done using the collimator.*

direction and the source divergence is $98 \times 4\mu\text{rad}^2$ in horizontal and vertical direction.

In Fig. 4.2 the diffractometer is shown. The three components collimator or CRLs, sample stage, and detector setup are mechanically separated, so that they do not influence each other. This increases the stability of the setup. A beam stop is installed at the detector table, which can be moved into the primary beam.

4.2 Beamline Optics

The monochromator consists of two bent silicon crystals in (111)-orientation with a miscut. The first crystal has a bending radius of about 60m. It produces a virtual source for the second crystal, thereby the intrinsic divergence of the primary beam in horizontal direction can be reduced. The absorption in the silicon crystals is very low at the high energies in use at ID15. Thus the heat load on the crystals is low and they can be installed in air with water cooling. For the initial experiment the first crystal had a miscut of 22° and the second one a miscut of 37.76°. Later we switched to a setup where both crystals had a miscut of 37.76°. At an energy of 71keV the first crystal had a bandpass of 300eV and later of 165eV corresponding to the miscut. The second crystal set the resolution to 165eV. Using this arrangement the fraction of higher harmonics in the photon spectrum can be neglected. The relative energy resolution was then $\Delta E \approx 2 \times 10^{-3}$.

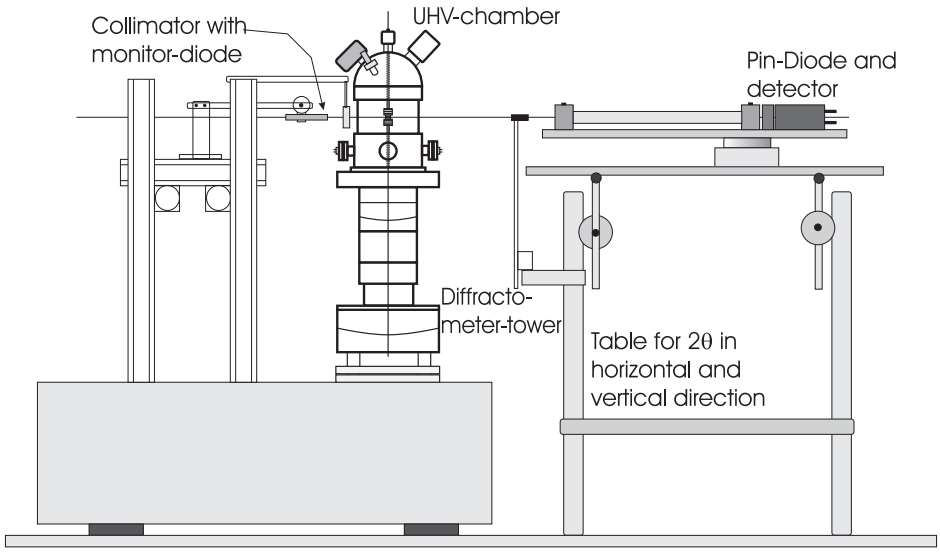

Figure 4.2: *Sketch of the diffractometer. The samples can be turned on four axes and translated on four axes.*

4.2.1 Special optical components

In the following section the additional components of the experiments are described. Some of them were especially acquired or even manufactured for the experiment.

Collimator

Most of the measurements were done using a collimator (s. Fig. 4.3). The incoming beam into the experimental hutch has a size of $0.5 \times 2\text{mm}^2$ (vertical $\times$ horizontal). It is defined by a set of slits in the optics hutch. The collimator reduces the beam size in vertical direction to a maximum of 8μm. The size can be chosen by different bars of the collimator that are drawn light grey in Fig. 4.3.

At a length of 128mm and a height of 8μm the accepted divergence of the collimator is $3.6 \cdot 10^{-3}$ degree. There is no collimation in horizontal direction. The acceptance in horizontal direction is 15mm, which means that the width of the beam is defined by the slits in the optics hutch. In Fig. 4.4 a knife edge scan is shown at the sample position in vertical direction. The derivative can be fitted by a gaussian and results in a FWHM of 5.7μm. The drift of the signal at smaller heights stems from the fact that the sample was not perfectly aligned horizontally and thus parts of the primary beam were transmitted.

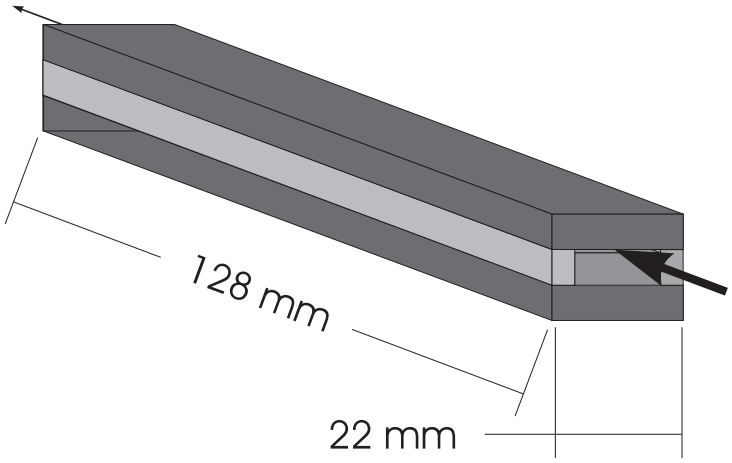

Figure 4.3: *Sketch of the collimator. It is* 12.8cm *long and its main material is densimet. The collimator reduces the beam in vertical direction to* 8μm*. In horizontal direction there is no collimation.*

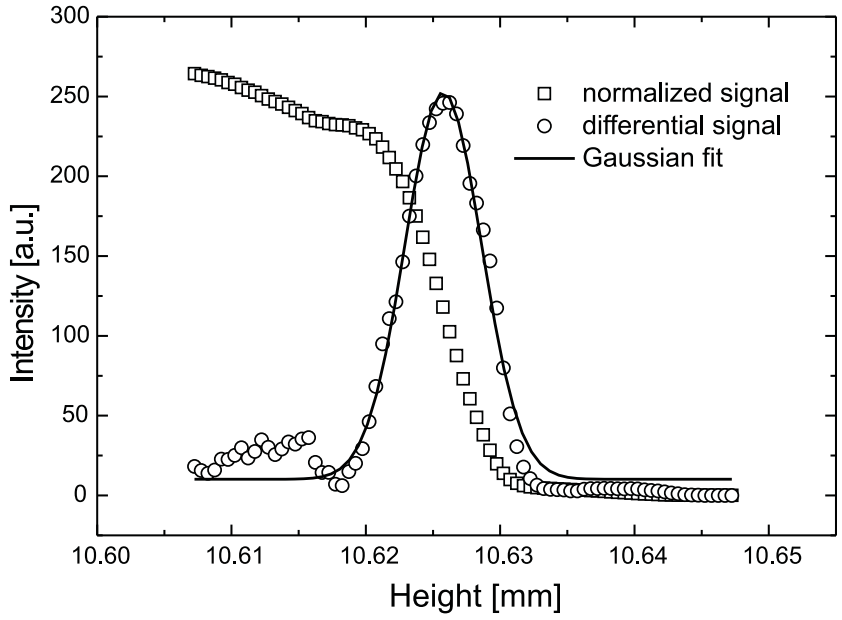

Figure 4.4: *Scan along the beam height at the sample position. The full width half maximum (FWHM) of the beam was* 5.7μm.

Compound refractive lenses, CRLs

A substantial advancement of the experiments involved the implementation of compound refractive lenses (CRLs). In the beginning these lenses were developed and used at significantly lower energies [Len99b, Sch01b, Len99a]. In the course of this work they were used for the very first time at energies above 70keV. The absorption of the lenses is much lower at high energies, so that there is an enormous increase of the flux density on the sample.

Since the refractive index for x-rays in matter is smaller than unity (cp. Chap. 3) we require concave lenses to achieve focusing. At high energies the index of refraction δ, is more than six orders of magnitude smaller than the one of visible light in glass. To achieve a reasonable focal length of about one meter one would require for a single less an extremely small radius of curvature R of about one micrometer. The trick is to use a stack of lenses with larger radius of curvature. By this close stacking the refraction power of each single lens is added up and the whole set of compound refractive lenses has a smaller focal length that is calculated as

$$f = \frac{R}{2N\delta} \ . \tag{4.1}$$

$R \approx 200\mu$m is the radius of curvature in the center of each lens, δ is the dispersion of the material of the lenses ($\delta = 1.506 \cdot 10^{-7}$ for aluminum at $E = 71.5$keV) and N is the number of lenses. The focal length of a single lense is $f \approx 1500$m. A stack of $N = 232$ lenses results in a focal length of the CRL of $f = 4.5$m. The effective aperture of the lenses lies in the range of 0.35mm.

The lens material is aluminum. Possible other materials under consideration are beryllium or nickel. The choice of material has to be made as a compromise between absorption and refraction power. For lower energies beryllium is more suitable as for higher energies it would be nickel.

Figs. 4.6 and 4.7 show knife edge scans (using a single blade of the slits) along the beam profile in the focal point at the detector position. The derivative and the corresponding Gaussian fit show a full width half maximum in vertical direction of 11μm. The lenses produce a very homogeneous beam, which has a Gaussian shape and no additional tails on the edges. The width of the beam in horizontal direction is 19μm as taken from the fit. The reason for the different size of the beam in horizontal and vertical direction is the divergence and the source size of the primary beam, which is different in the two directions.

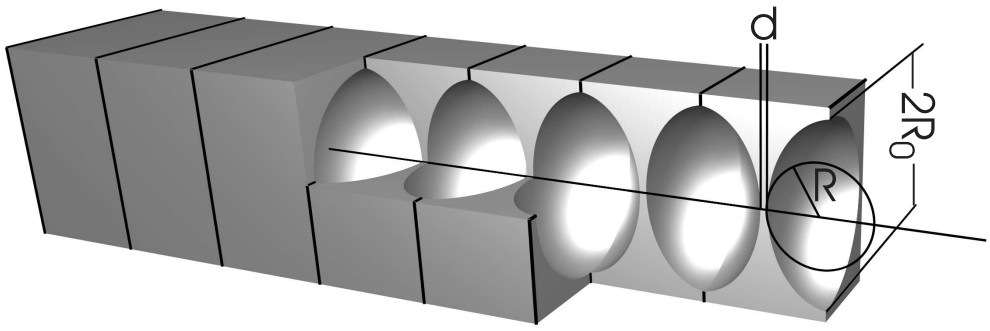

Figure 4.5: *Schematic of the parabolic compound refractive lenses. The thickness d of a single lens is about* 10μm. *The radius of curvature R in the center is* 200μm. *The total diameter of a lens is* $2R_0 = 1$mm. *For the experiment a stack of 200 to 300 lenses is used.*

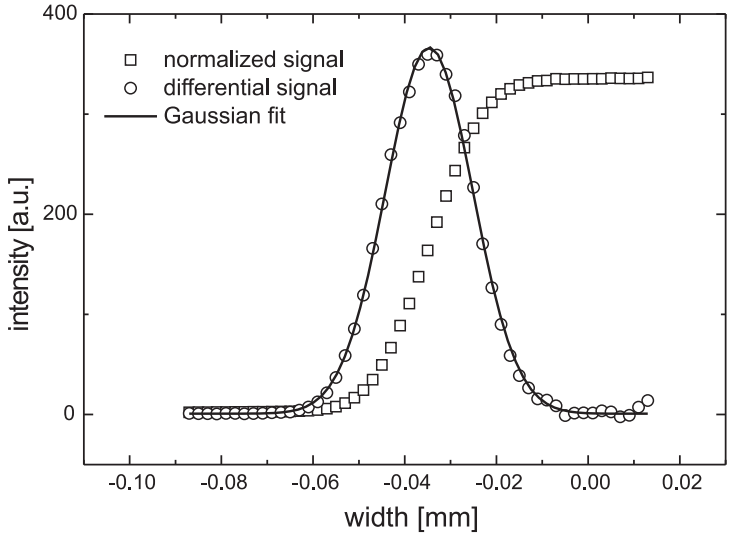

Figure 4.6: *Horizontal scan of the monochromatic primary beam in the focal point of the CRL. The Gaussian fit of the derivative shows a FWHM of the beam of* 19μm.

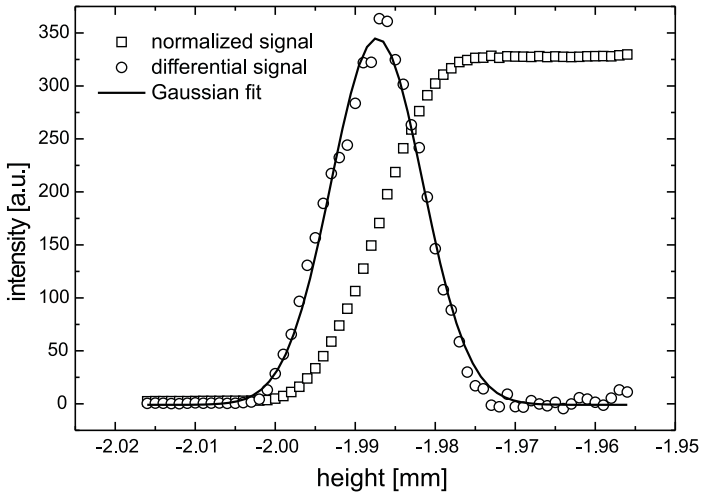

Figure 4.7: *Vertical scan of the monochromatic primary beam in the focal point of the CRL. The Gaussian fit of the derivative shows a FWHM of the beam of* 11μm.

4.3 Sample Manipulation

4.3.1 Chamber tower

The tower for the chamber is mounted on top of a heavy granite plate (1.5tons) to reduce oscillations from the bottom. A schematic is drawn in Fig. 4.8. A translation stage is mounted on top of the granite plate to align the sample tower in the x-ray beam. Located above the translation is a large cradle that defines the incidence angle (α_i-cradle). The position can be reached with a precision $< 0.001°$ and the absolute position is reproducible. The maximum range is $\pm 5°$ measured from the vertical direction. On top of the cradle a circle is mounted that turns the sample along a vertical axis. This circle is less precise and has a lower resolution ($0.01°$) than the α_i-cradle.

On top of the circle two translations are mounted to align the sample in horizontal direction. The precision of the translations stages is < 0.01mm. The most important part of the tower is the following z-translation in vertical direction. Using this stage the sample can be positioned relative and absolute with a precision of 0.1μm. The last motorized part is a double tilt stage to align the sample surface/interface perpendicular to the scattering plane with a precision better than $0.01°$. Just underneath the chamber is a simple circle installed that allows an easy installation and prealignment of the UHV-chamber.

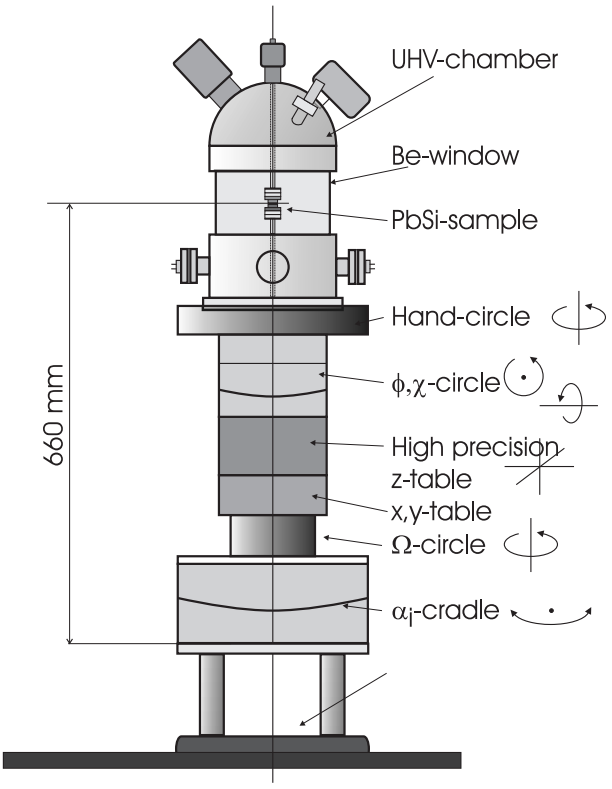

Figure 4.8: *The sample tower. The whole tower is assembled modular and separated from the other components. There are four motorized rotations and four translation stages. The α_i-cradle and the z-stage are manufactured with very high precision.*

4.3.2 UHV-chamber

Fig. 4.9 shows the mobile sample chamber. The final preparation of the sample is done *in situ*, after a bakeout of the chamber and after the chamber has reached a pressure of $p \approx 10^{-9}$mbar. The temperature of the metal is measured with a thermocouple of K-type (NiCr-Ni). The sample is heated by two boron nitride (BN) heaters that are mounted below the trough for the metal and above the silicon crystal. The heaters are powered by two separate power supplies, which allow to set the temperature of the liquid and the solid separately, this is important during the preparation process of the sample. In addition temperature gradients can be minimized. The two heaters are identical so that the same current through both heaters leads to the same temperature on both sides of the sample. Therefore, it is sufficient to measure the temperature only on one side of the sample. After the mounting of the silicon crystal and the metal the two materials are still separated.

The silicon crystal is protected with a tantalum shutter as long as the metal is ion sputter cleaned. There is an additional window in the chamber, which is not drawn in the figure. It is located in the top part of the chamber

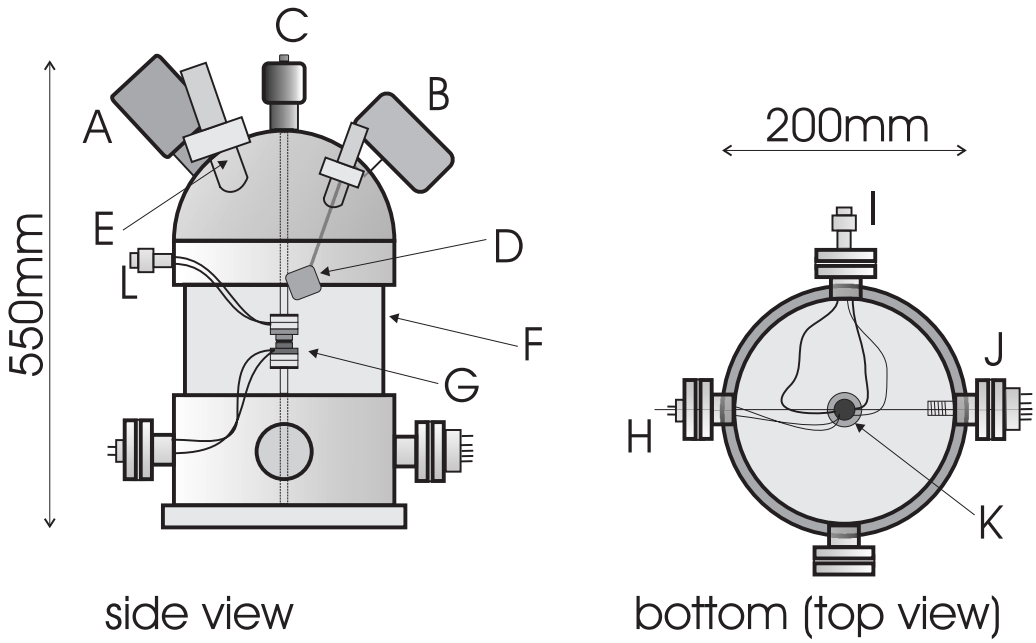

Figure 4.9: *Mobile sample chamber. A) turbo molecular pump, B) ion getter pump, C) translation that moves the silicon crystal, D) circular translation with Ta shutter to protect the silicon crystal as long as the metal is sputter cleaned, E)* Ar^+ *ion sputter gun, F) Be window, G) solid-liquid sample with heaters, H) thermocouple, K-type, I) feed through for the lower heater and to measure the ion current, J) pressure gauge (Bayard-Alpert), K) silicon trough for the metal, L) heater for silicon crystal*

on the opposite side of the ion sputter gun and allows the optical check of the oxide removal from the metal. The tantalum shutter can be moved from outside by a combined rotation and translation. Only directly before the silicon and the liquid metal are brought in contact the shutter is removed. The oxide layer of the metal is ablated with an Ar ion sputter gun. The acceleration voltage of the cold cathode sputter gun can be tuned from 0.5-5keV. On the sample we attain an ion current of $40 - 100\mu$A. The sputter current is measured via a tungsten wire that penetrates the metal and that is isolated from the chamber.

The trough for the metal and the silicon crystal are fixed with tantalum rods and nuts together with the heaters and some spacers that consist of

boron nitride on steel supports in the chamber. The boron nitride spacer together with thin tantalum sheets arrange for a thermal isolation of the sample against the chamber.

For the x-rays the sample is accessible through a beryllium window. Its height is 75mm and its diameter is 160mm. The thickness of the beryllium is 0.5mm. It is welded between two *CF160*-flanges and is supported by three steel rods (5×5mm) on the outside. Thus it is possible to have access to the sample in horizontal direction for almost 360°, except at the steel rods. In vertical direction the maximum scattering angle is 43°.

The pumping system consists of a turbo molecular pump with a rotary vane pump as prepump and an ion pump. The turbo pump can be separated from the chamber with a gate valve. During transport the valve is closed and the turbo pump is switched off. The ion pump keeps the vacuum of the chamber. It is permanently powered by a rechargeable battery pack and can be operated power-network-independent for about 48 hours. The pressure in the chamber stays in the range of 10^{-9}mbar.

4.4 Detector system

PIN-diodes

For the detection of very high beam intensities PIN-diodes were used. They consist of three layers: a p-conducting semiconductor layer, an isolating layer, and a n-conducting semiconductor layer. Using this diode a current is measured that is directly proportional to the number of photons passing through the diode. The enormous advantage is their linearity at all intensities occurring in our experiments. At an energy of 71keV they absorb only about 10% of the intensity and the remaining intensity is transmitted. Therefore a PIN-diode can be placed directly in the beam in front of the chamber without reducing the number of photons noticeable at the sample position. This PIN-diode is mounted after all optical elements and serves as a monitor to normalize the measured intensities. The advantage of this setup is that intensity fluctuations of the beam arising from fluctuations in the optical elements are eliminated.

A second PIN-diode is used for the detection of the scattered intensity on the detector arm in front of the scintillation counter (s. following section). It is used for alignment in the primary beam and for measuring the reflectivity near the critical angle.

Scintillation counter

To measure low intensities we used a NaJ-scintillation counter. The electronic background was less than one count per second. The maximum count rate is more than 50000cts/s. However, the dead time increases rapidly for more than 10000cts/s, which makes a correction mandatory. The more convenient way of handling higher count rates are lead absorbers in front of the detector arm, with a thickness of up to 2mm. The control software SPEC[2] records the signals of all detectors and motors.

Mechanical setup

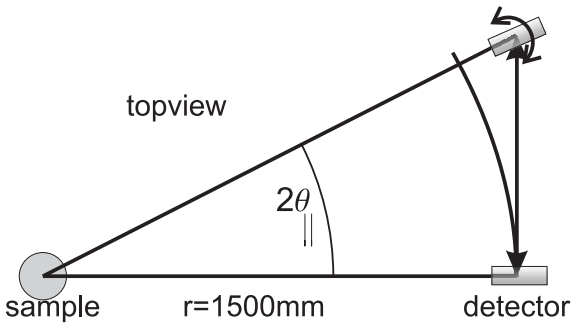

Figure 4.10: *The detector is moved perpendicular to the direction of the primary beam and additionally rotated. The distance between the rotation centre and the detector changes by a factor of* $1/\cos(2\theta)$.

The detector can be rotated horizontally and vertically around the interface position. The vertical rotation is realized by the combination of two translation stages and the horizontal rotation is realized by the combination of a translation stage and a rotation stage. In front of the detector there are two sets of slits each having four blades installed. The scatter slits define the field of view and reduce the diffuse background. The detector slits are mounted in the nominal position of the detector. They define the exact momentum transfer and the angular resolution of the instrument. The distance between the detector slits and the sample position (rotation center) is 1.5m. Using a slit size of $0.1 \times 2\text{mm}^2$ (vertical $\times$ horizontal) gives a resolution in vertical direction of $0.0019°$ ($\Delta q_z = 1.3 \cdot 10^{-3}\text{Å}^{-1}$) and in horizontal direction

[2]for further information about the software see:
www.esrf.fr/Infrastructure/Computing/ and www.certif.com

of 0.038° ($\Delta q_{||} = 0.25\text{Å}^{-1}$). The absolute accuracy of positioning is given as 0.001° in vertical direction and 0.01° in horizontal direction.

The detector does not move on a real circle, yet the $2\theta_{||}$-angle is precisely defined and the momentum transfer can be calculated (s. Fig. 4.10). The distance between the detector and the centre of rotation is a function of $2\theta_{||}$. In turn the solid angle that is detected by the detector has to be corrected by a factor of $1/\cos^2 2\theta_{||}$. For a momentum transfer of $q_{||} = 6\text{Å}^{-1}$ (at $\lambda = 0.17\text{Å}$) the correction factor is 3%.

For the vertical momentum transfer q_z, a correction is not necessary, since the maximum vertical angle used is 1.2° and thus the error amounts to 0.04%, which is less than the statistical error.

4.5 In situ sample preparation

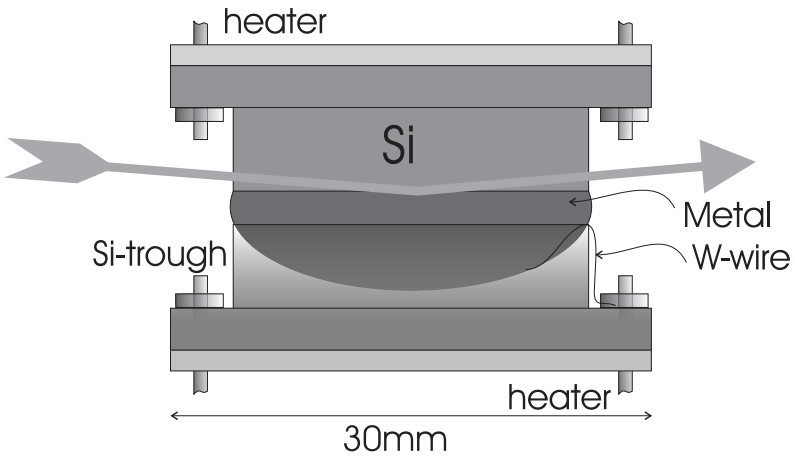

Figure 4.11: *The sample with the solid-liquid interface. The silicon sample and the trough are cylindrically. The interface itself has a diameter of* 20mm. *The path of the beam is indicated. The trough has a volume of about* 1cm^3 *of liquid metal. The tungsten wire is for measuring the ion current when it is sputter cleaned. The thermocouple and the cabling to the heaters are not shown.*

One cubic centimeter of metal is needed for the experiments ($1\text{cm}^3 \hat{=}$ 11.3g Pb or 7.3g In). There are two ways to treat the metal before it is put in the chamber: either it is etched in an adequate acid (Pb: acetic acid, In: hydrochloric acid) or it is molten and poured into the trough in such a way

that the dirt and initial oxide remains in the crucible. After this treatment the metal is still in air and rapidly covered with a new oxide layer. However, this layer is rather thin and it consists only of the natural oxide of the metal. Even with the thin oxide layer the sputter process takes a couple of days. It is done at the liquid and the solid phase of the metal in an alternate state. After a while the oxide skin on top of the liquid metal is very thin and it breaks up to small chunks that drift on top of the liquid metal. The oxide chunks often stick to the edge of the trough. To move the oxide chunks back into the ion beam, which is smaller than the liquid metal surface, it is necessary to knock on the chamber and to solidifiy the metal without sputtering. The trough consists of polycrystalline silicon. The solubility of silicon in lead and indium is negligible (s. Sec. 2.5.1).

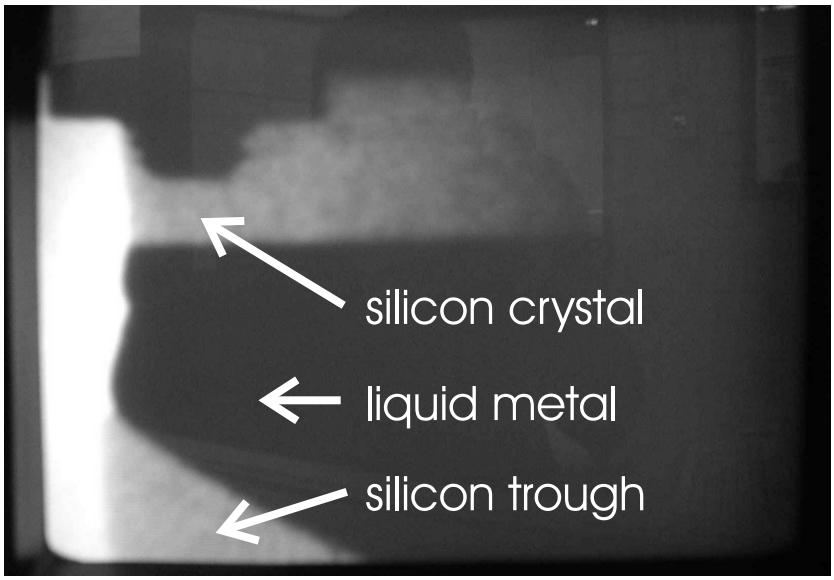

Figure 4.12: *X-ray image of a solid-liquid interface about ten times magnified. The sample was illuminated with the white beam from a tungsten x-ray tube. The silicon crystal and the trough are transparent. In the upper part a screw with a nut can be seen.*

The polished silicon crystal is cleaned and etched in an elaborate treatment (s. App. A.1) directly before mounting it in the chamber. After the preparation the silicon crystal is covered with a very thin well defined oxide layer.

After the liquid metal is sputter cleaned the silicon crystal is treated with a *flash process*. This treatment removes the oxide layer from the silicon. The

procedure starts by outgassing the silicon crystal and the sample stage at 600°C for about one hour. Then the crystal is rapidly heated to 1200°C for five minutes. In doing so the oxide layer sublimates and one gets an atomically clean surface. This process works only if the vacuum in the chamber is very good and the silicon is only covered with the oxide layer with no other adsorbates. The pumping power of the chamber is comparably small due to the fact that the chamber itself is small and mobile. Therefore, the pressure increases during the heating up to 10^{-7}mbar. The studies of the flash process of silicon were done in large MBE-systems. These large UHV-clusters are built in such a way that even at sample temperatures above 1000°C the pressure stays in the range of 10^{-10}mbar [Sch98, Ton99]. In our experiments we must expect that the sublimation of the silicon oxide was not always complete and there remained some oxide islands on the surface. It is clear that in these spots we did not achieve an atomically clean surface, which might influence some experiments (s. Sec. 6.2.1).

Finally, the liquid metal and the silicon crystal are prepared to get in contact with each other. This has to be done very carefully since the liquid can easily spill out from the shallow trough or up at the side of the silicon sample crystal. The chamber is mounted on a diffractometer and illuminated with a white x-ray beam in such a way that the liquid metal can be monitored with an x-ray eye. The silicon crystal and the metal are heated to the same temperature. The surfaces can be contacted while the sample is observed with the x-ray eye. It is mandatory to avoid to lower the crystal too far into the liquid metal since the metal might migrate at the side of the crystal, producing bulk liquid scattering upon penetration by the incoming x-ray beam. Fig. 4.12 shows a picture of the sample after the contact has been made. The metal is pushed a bit outwards. It does not drop or move up at the side due to the surface tension of the liquid metal. Pure lead does not wet silicon.

4.6 Data collection and treatment

The photon beam entering the experimental hutch is scattered in numerous ways. We separate the scattering in three different contributions. The first is regarded as background scattering. The source of background scattering is scattering from air, backscattering from walls, and the beryllium windows in the beam path. It can be reduced by carefully shielding of the beam path and slits defining the field of view.

The second contribution is bulk scattering from the liquid and from the silicon crystal. The bulk scattering from the liquid is minimized by the special

properties of GID. The scattering from the silicon crystal can be measured separately and subtracted from the interface measurement. For reflectivity measurements off-specular measurements reveal the background signal.

The third scattering contribution is the interface signal. Several corrections have to be applied to this signal that are discussed in the following sections.

4.6.1 Reflectivity measurements

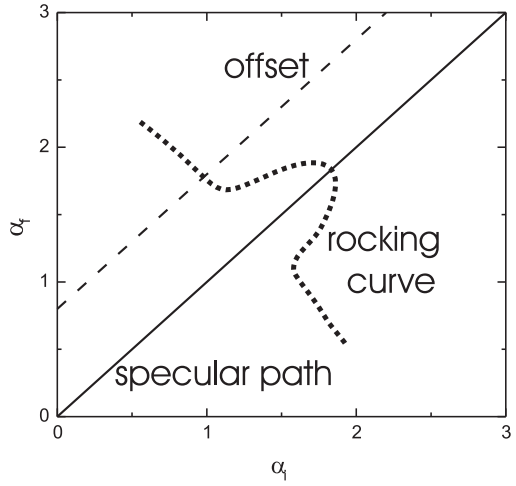

Figure 4.13: *Measuring reflectivity at the specular condition $\alpha_i = \alpha_f$. The diffuse background is measured with an offset in α_f. The required offset is determined by rocking scans as shown.*

Measuring along the specular rod in an experiment ($\alpha_i = \alpha_f$) records a superposition of the amplitude of the specular intensity I_s and the diffuse scattered intensity I_d thus $I_{\mathrm{tot}} = I_s + I_d$ (cp. Fig. 4.13). I_d can be measured solely by doing an offset-scan with the condition $\alpha_f = \alpha_i + \alpha_{\mathrm{offset}}$. The offset angle α_{offset} is chosen such that the signal does not contain any signal from the specular rod. Then it can be easily subtracted from I_{tot} to receive the amplitude of the specular reflectivity.

The specular reflectivity as a function of $q_{||}$ is a peak of certain width (FWHM) and height in reciprocal space. As reflectivity the integrated intensity of the peak has to be taken. The reflectivity can be determined by a linear scan along the specular path and a background scan with an offset from the specular path.

If the peak shape and width is q_z-dependent, either the integrated intensity has to be measured or the q_z-dependence has to be determined and the reflectivity curve has to be corrected with respect to the integrated intensity.

Geometrical correction

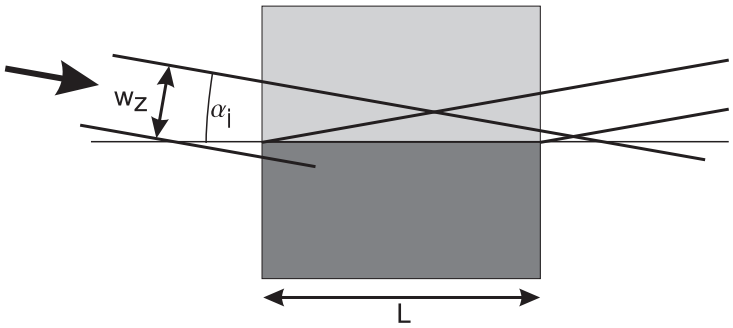

Figure 4.14: *Sketch of the geometrical correction of reflectivity for small incidence angles α_i.*

The *illumination correction* has to be applied to receive the reflected intensity for small angles. The illuminated area A at the sample position *(footprint)* is given by $A = w_y \cdot w_z / \sin\alpha_i$ with w_y the width and w_z the height of the beam. For angles $\alpha_i < \arcsin(w_z/L)$ with L the length of the sample, the illuminated area is larger than the sample and therefore the scattered intensity is reduced by the ratio between the footprint and the projected area of the sample. The correction is done by

$$I_{\mathrm{corr}}(\alpha_i) = I_{\mathrm{meas}}(\alpha_i) \cdot \frac{\frac{w_z}{L}}{\sin\alpha_i} \qquad \text{for} \quad \alpha_i < \arcsin\frac{w_z}{L} \tag{4.2}$$

4.6.2 In plane Data treatment

Diffuse Background Subtraction

The diffuse scattering of the silicon crystal is part of the in plane measurements. It can be measured separately as shown in Fig. 4.15. The sketch shows a side view of the sample. The angle parallel to the interface cannot be seen. After a scan in GID geometry (left sketch, I_{tot}) the sample is moved vertically, such that the incoming x-ray beam only transmits the silicon crystal (right sketch, I_{diffuse}). From the geometrical point of view, both scans contain a signal from the same silicon scattering volume. However, the reflectivity of the interface is less than unity and therefore, the silicon signal

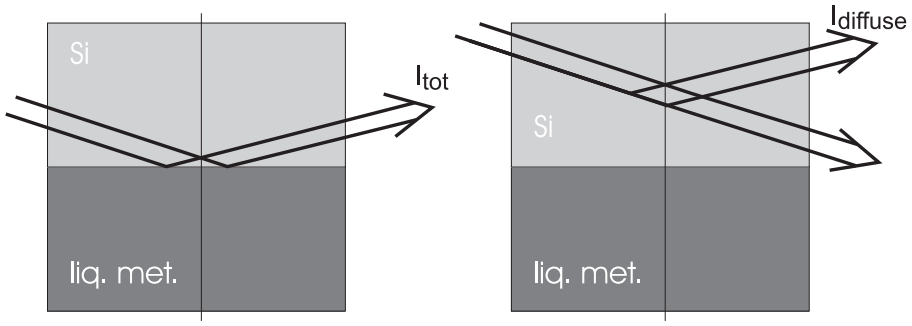

Figure 4.15: *Left picture: measuring intensity from the interface and diffuse background of silicon. Right picture: measuring solely the diffuse scattered signal from the silicon crystal.*

is reduced in the interface scan compared to the background scan. It is not possible to give a fixed factor x that has to be multiplied to the background scan. The correction factor depends on sample shape and the geometrical conditions of the x-ray measurements. In the experiments x varied between 0.29 and 0.95. The interface signal is then given as

$$I_{\text{interface}} = I_{\text{tot}} - x \cdot I_{\text{diffuse}} \ . \tag{4.3}$$

An example is shown in Fig. 4.16. The final result is shown in Chap. 6.

Footprint Correction

The illuminated area A depends on the scattering angle $2\theta_{||}$, the width of the incoming beam w_i, and the accepted width w_f of the detector (cp. Fig. 4.17)

$$A = \frac{w_i \cdot w_f}{\sin 2\theta_{||}} \ . \tag{4.4}$$

Thus, the intensity $I_{\text{interface}}$ has to be corrected for the footprint of the interface. Depending on the settings there is an offset angle $2\theta^*$ involved, which shifts the correction angle $2\theta_{||}$, for details see [Dos92]

$$I_{\text{corr}} = I_{\text{interface}} \cdot \frac{1}{\sin(2\theta_{||} - 2\theta^*)} \ . \tag{4.5}$$

Polarization

Synchrotron radiation is almost completely polarized in the horizontal plane [AN01]. Thus in vertical direction for $2\theta_{\text{vert}} \lesssim 2^\circ$ no correction has to be

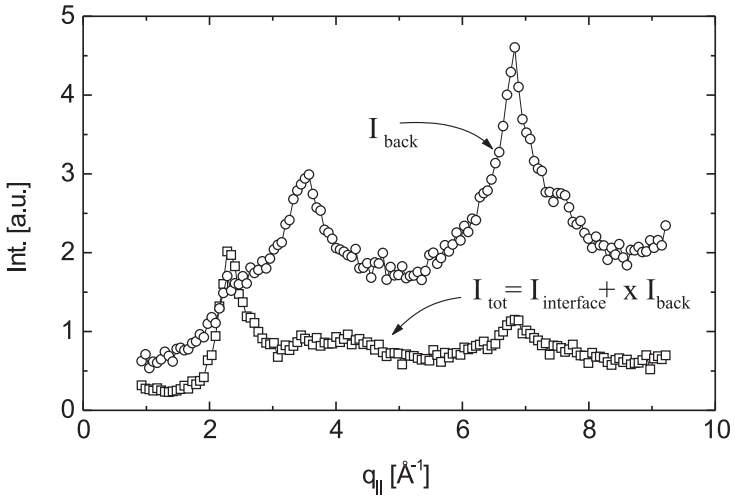

Figure 4.16: *Scan that shows the interface indium signal and the background of the silicon crystal (squares) and a scan that shows only the background of the silicon crystal (circles). The two peaks in the background data are thermal diffuse scattering from the Si. Example for a In(liq.)-Si(100) interface. The data is normalized to the monitor intensity.*

applied since the polarization factor P equals unity. This was important for the reflectivity measurements.

In horizontal direction the polarization has to be considered. The polarization factor P gives the projection of the electrical polarization of the incoming beam onto the plane perpendicular to the exiting beam. Parallel to the interface the polarization factor is $P = \cos^2 2\theta_{||}$ for the component parallel to the interface. $2\theta_{||}$ is the scattering angle parallel to the interface (s. Fig. 3.7 and Fig. 4.17). The correction is given by

$$I_{\text{corr}} = I_{\text{uncorr}} \cdot \frac{1}{\cos^2 2\theta_{||}} \ . \tag{4.6}$$

Atomic form factor

The atomic form factor $f(\mathbf{q})$ introduced in Eq. 3.50 is a function of the magnitude of the momentum transfer $\mathbf{q}$. It is tabulated for all elements and can be found in public sources[3]. The measured intensity is divided by the function in order to retrieve the structure factor

[3] e.g. http://www-cxro.lbl.gov/optical_constants/

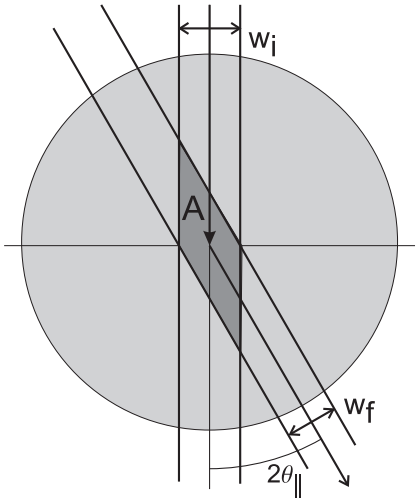

Figure 4.17: *Top view of the interface. The footprint A is shown as dark grey. w_i and w_f are defined by horizontal slits.*

$$S(q) \propto \frac{I_{corr}}{f^2(q)} \ . \tag{4.7}$$

Compton scattering

Compton scattering is an incoherent scattering contribution, which is part of all scattering experiments [War69, AN01]. In a compton scattering event the photon transfers parts of its energy to the electron, at which it is scattered. The Compton scattered photons must be eliminated in the measured intensity. Although the detector we used is energy dispersive, its sensitivity is not high enough to eliminate Compton scattered photons. The scattering cross section ratio between coherent scattering ($\propto f^2(q)$) and Compton scattering $S_c(q)$ is well known (s. previous footnote). Therefore, it is possible to calculate the fraction of the coherently scattered intensity from a sum of both intensities

$$I_{\mathrm{coh}} = I_{\mathrm{tot}} \cdot \frac{f^2(q)}{f^2(q) + S_c(q)} \ . \tag{4.8}$$

The correction factors are summarized in Fig. 4.18. It can be seen that they partly compensate each other. For the calculation tabulated data for lead have been used.

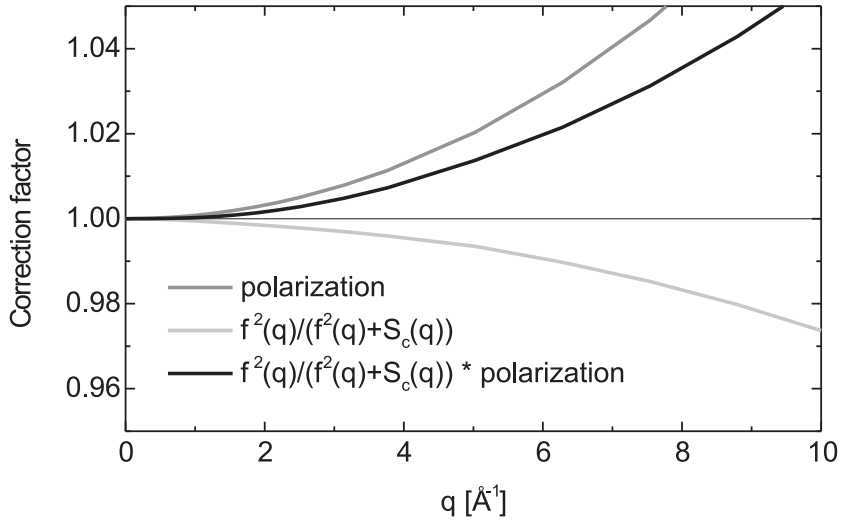

Figure 4.18: *Correction factors for incoherent scattering and polarization*

Chapter 5

Characterization of the free Silicon Surface

Prior to the investigation of the solid-liquid interfaces, the silicon samples were characterized in advance. The quality of the surface was investigated with a particular emphasis on the x-ray optical properties. For the atomic structure of the surface itself and its final flash preparation, we relied on the recipes reported in literature (s. Sec. 2.3).

The silicon samples were cut and manufactured from large preoriented silicon blocks. Two different types of silicon crystals were employed in this work, one was undoped and the other one was n-doped (phosphorous-doped). In the following step the crystals were oriented with respect to the surface better than 0.1% using an x-ray beam. Then the samples were lapped and afterwards polished with a Siton solution as described in [Pie94]. The subsequent etching steps were done prior to mounting the sample in the chamber (s. App. A.1).

5.1 Macroscopic Morphology

Contrary to the needs of typical MBE or AFM experiments, our samples are large with a diameter of 20mm (s. Fig. 5.1). The incidence angle in high energy x-ray grazing incidence experiments is kept well below 0.1° and has to be controlled with a precision better than 0.001°. Curvature of the surface leads to a variation of the incidence angle along the x-ray beam direction (cp. Fig. 5.2). Therefore, the samples have to be smooth on a macroscopic length scale. As long as the variation is small enough, it can be accounted for in the data analysis by the resolution function.

Since it is impossible to get samples that are absolutely flat, it is preferable

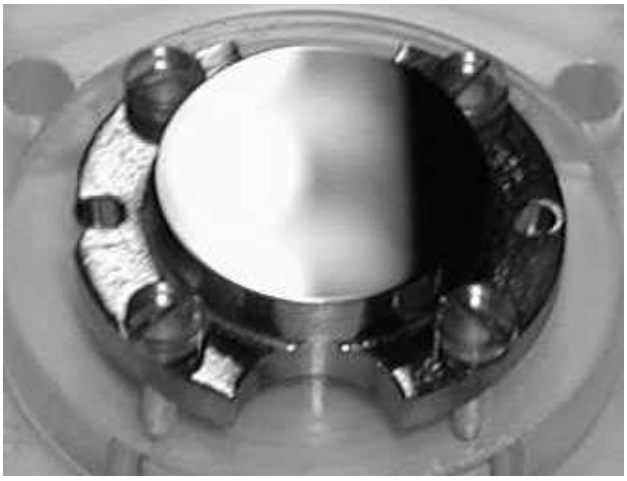

Figure 5.1: *A typical silicon substrate for the solid-liquid experiments. By eye the surface is perfect and only the edges are slightly rounded.*

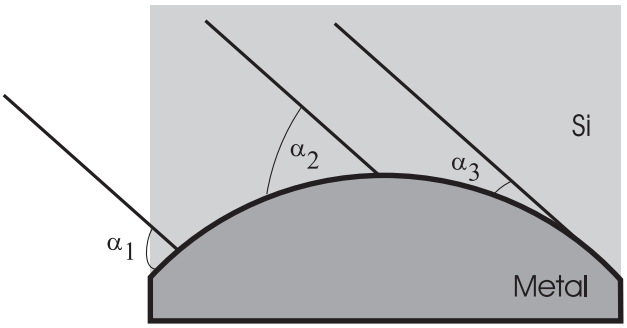

Figure 5.2: *Curvature of the surface sample leads to a varying incidence angle along the surface. The curvature of the liquid metal is determined by the solid silicon.*

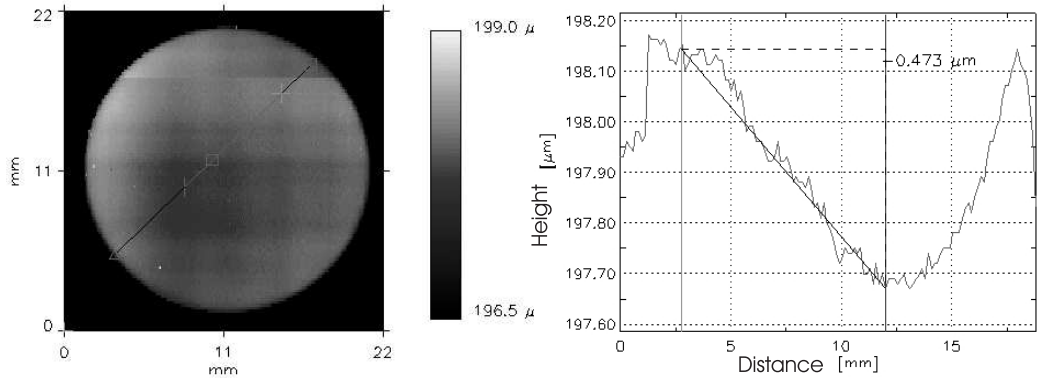

Figure 5.3: *Interferometric characterization of a silicon surface. The vertical resolution is* 10nm *and the lateral resolution is* 20μm. *On the right side a diagonal trace is shown along the line on the left side. The maximum height deviation is* 500nm. *The sample is slightly concave and ideally suited for the preparation of solid-liquid interfaces.*

to prepare sample surfaces that are slightly concave rather than convex. Pb blocks x-ray energies below 100keV almost completely, thus the solid-liquid interface is investigated from the silicon side. At a convex silicon surface the liquid metal might creep up at the side of the sample. In this case bulk liquid metal is located in the beam path. Therefore, it is better that the silicon surface is rather concave than convex (cp. Fig. 5.2).

A reliable way to quantify the surface morphology of the silicon sample is an interferometric surface scan with a special device *Jurca CHR150E* by Precitec Optronic. This device maps the surface height with lateral resolution. It gives a complete overview of the sample. In Fig. 5.3 a typical result is shown. The depth profile (segment length 20mm, height 0.473μm) gives a bending radius of 106m. Since this perpendicular cross section is taken at the maximum deviation, the radius of curvature is even larger in other regions of the sample. At a bending radius of 106m the incidence angle varies across the sample by $\pm 0.005°$. This is already a small value, but smaller values should be achieved in future experiments.

Surfaces with larger radius of curvature may be obtained by polishing larger samples. The origin of the curvature of the surface is the polishing process where the samples are rotated around several axis. The rotations have to be applied to eliminate the scratches across the surface. Tests with

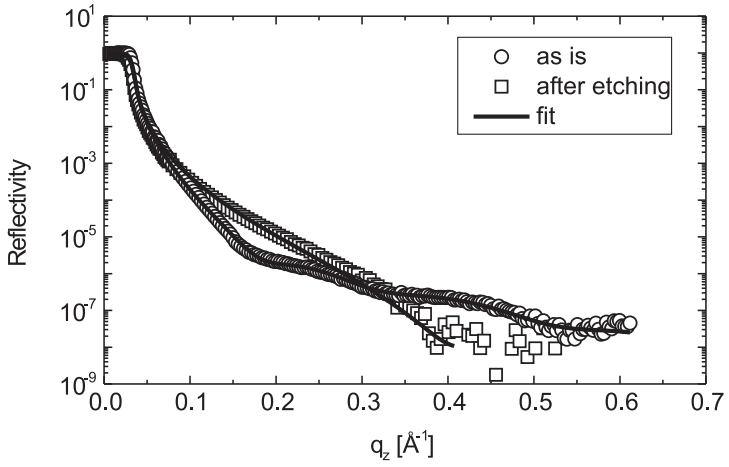

Figure 5.4: *Reflectivity measurements at a Si(111) surface in air. The first measurement was done after the polishing process. The second measurement was done after the subsequent cleaning process described in App. A.1.*

a larger sample, where the sample was cut after the final polishing, did not provide better samples, since the edges of the samples were jarred.

5.2 X-ray reflectivity measurements

Besides its macroscopic smoothness, the silicon surfaces should be flat on an atomic length scale. Microscopic roughness at or below the scale of the coherence length of the x-ray beam leads to an exponential damping of the reflected intensity (s. Chap. 3). At first sight, the in plane measurements are less sensitive to the roughness than the reflectivity measurements. However, it is clear that the in plane order cannot be precisely determined without a sufficiently low roughness.

The roughness of the silicon substrates was routinely checked by reflectivity measurements at laboratory x-ray sources. Samples were measured shortly after polishing (up to four weeks). It is known that it takes more than a year for silicon surfaces to degrade markedly. The presence of correlated roughness was checked by rocking scans at different perpendicular momentum transfers q_z. In all samples no correlated roughness was found. The width of the specular rod was resolution limited.

The reflectivity measurements presented in Fig. 5.4 were performed at a Cu-K_α sealed tube ($\lambda = 1.54$Å). After the first measurement (as is) the

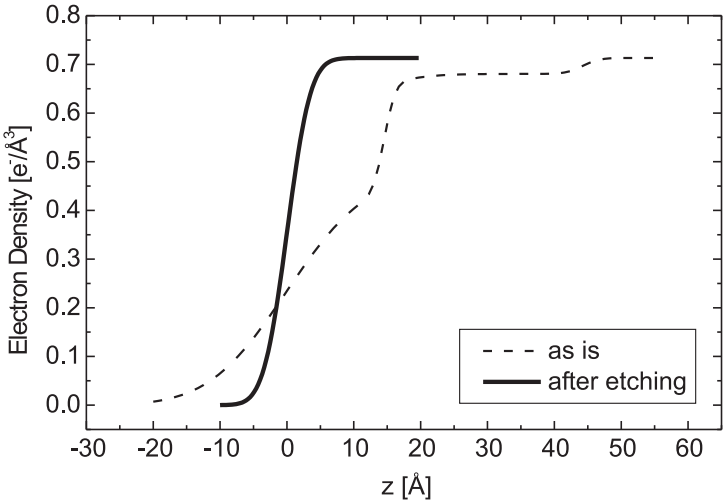

Figure 5.5: *The electron density profiles for the reflectivity measurements shown in Fig. 5.4. After the cleaning the sample exhibits a smooth surface with an RMS roughness of* $\sigma = 5.5$Å

sample was cleaned and etched as described in appendix A.1. After the etching, the silicon surface is hydrogen terminated, which is only stable for a short time (minutes) [Dit03]. Then, oxidation starts again and after an hour the surface is covered by a thin oxide layer. Since reflectivity measurements at laboratory sources take at least 24 hours, the measurements examine the oxide covered surface.

The first reflectivity measurement on a Si(111) surface (as is) shows already by eye a deviation from Fresnel reflectivity (cp. Fig. 5.4). The specular rod was detectable up to $q_z = 0.6\text{Å}^{-1}$. The corresponding electron density profile determined by the fit, is shown in Fig 5.5. In general, we find two layers on top of the silicon substrate. The first layer is a 28Å thick layer of SiO_2 on top of the substrate. The second layer does not have sharp boundaries in the sense of a well-defined layer. It exhibits a more gradual decrease of the electron density from the electron density of the SiO_2 layer to zero across 30Å. This layer is attributed to remaining adsorbants after the polishing procedure.

The roughness between the SiO_2-layer and the Si(111)-substrate is only 2Å. The reflectivity measurement after the etching procedure shows no sign of a layer on top of the substrate. At q_z-values larger than the corresponding critical angle the reflected intensity follows the Fresnel curve damped by roughness until it drops below the background of the instrument. The electron density extracted from the fit provides an estimate for the roughness of

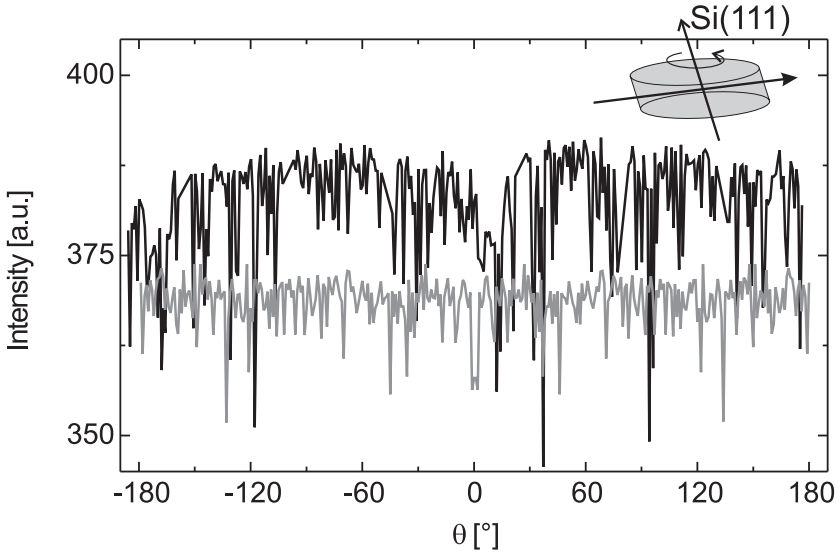

Figure 5.6: *Transmission of a high energy x-ray beam through a 20*mm *disk of a Si(111) crystal. The sample is rotated around the Si(111)-surface normal. The sharp dips are caused by excitation of Bragg reflections in the silicon (black line: measurement; grey line: calculation).*

the substrate. The oxide on top of the substrate is too thin to be detected in the measurement and its fit. The fit cannot be reasonably improved by applying an additional SiO_2-layer. The RMS roughness of the substrate is $\sigma = 5.5$Å.

The roughness did not increase significantly by the etching procedure. This is important to verify since it is known that etching of Si(111) surfaces may result in facets, wich increase the roughness. This is not the case for Si(100) surfaces [Hig90].

Using thin wafers we were able to prepare surfaces with smaller roughness, however, at the cost of an increased curvature.

5.3 Excitation of Bragg Reflections

In the high energy x-ray experiments the silicon is penetrated by two x-ray beams: First the incoming x-ray beam, and second the diffracted beam from the interface. Due to the high x-ray energy the Ewald sphere is large ($r_{\mathrm{Ewald}} = 1/\lambda$). The Bragg reflections with the smallest d-spacing or the maximum h, k, l values are given by $h_{\mathrm{max}} = 2r_{\mathrm{Ewald}}a_{\mathrm{Si}}, k = 0, l = 0$, where h, k, l are the Miller indices that denote a point in reciprocal space (s. e.g.

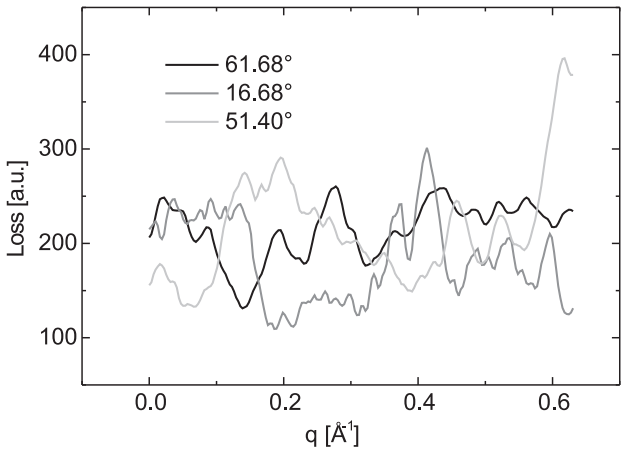

Figure 5.7: *Comparison of loss due to Bragg reflections in the q-range of typical reflectivity measurements. The three curves are different directions perpendicular Si(100). The Si(001) axis is at* 0°.

[War69, Ash76]). Exciting Bragg reflections in Si leads to a loss of intensity in one of the beams, since part of the incoming or outgoing beam is diffracted in other directions. Therefore, it is mandatory to check whether this loss in intensity might produce secondary features in the x-ray measurements.

All reflectivities and structure factor measurements presented in this work were performed in such a way that the diffuse scattering of the silicon was subtracted. The raw data of the structure factors show TDS streaks of silicon reflections (s. Fig. 4.16). They can be eliminated by subtracting carefully weighted background scans in the pure Si substrate (s. Sec. 4.6.2). In contrast to the in plane structure factor measurements, the reflectivity measurements are performed at small momentum transfers ($q < 1\text{Å}^{-1}$), thus no intensity from Bragg reflections or TDS of Bragg reflections is recorded. However, with a large Ewald sphere at all incidence angles Si Bragg reflections are excited and lead to a loss of intensity in the transmitted x-ray beam, which is calculated and measured in the following.

All Bragg reflections that fulfill the Laue condition (s. e.g. [War69, Ash76])

$$\mathbf{H}_{hkl} = \frac{1}{\lambda}(\mathbf{s} - \mathbf{s}_0) \ , \tag{5.1}$$

are excited. $\mathbf{H}_{hkl}$ is a reciprocal lattice vector, and $\mathbf{s}$ and $\mathbf{s}_0$ denote the unit vector of the exiting and incoming x-ray beam, respectively. For a cubic structure like the diamond structure of silicon the reciprocal lattice vector is

defined as $\mathbf{H}_{hkl} = \sqrt{h^2 + k^2 + l^2}/a$, with the lattice constant a. Additionally, the selection rules for the allowed Bragg reflections have to be obeyed, which are for silicon

$$\begin{aligned} h, k, l \quad & \text{all odd, or} \\ h + k + l = 4n \quad & \text{all even and } n \in \mathbf{N} \ . \end{aligned} \tag{5.2}$$

Not all intensity is diffracted by an excited Bragg reflection. The power of the Bragg reflection depends on the atomic form factor, which is a function of the momentum transfer. Tabulated values for the atomic structure factor are available in literature [Gul04]. For incidence angles with respect to the orientation of the silicon crystal the excited Bragg reflections were calculated by applying numerically the construction of the Ewald sphere. The number of excited Bragg reflections crucially depends on the energy resolution of the monochromator used at the synchrotron, since it defines the width of the Ewald sphere. For the calculation the energy resolution of the later reflectivity measurements, which was $2.2 \cdot 10^{-3}$, was taken. The calculation shows that at all incidence angles between zero and 25 Bragg reflections are excited.

The relative loss in intensity can be directly measured by measuring the intensity of the primary beam after the silicon crystal with the incident angle to the crystal as parameter. Fig. 5.6 shows a measurement and a calculation where a disk shaped silicon crystal was rotated parallel to the Si(111) axis and the x-ray beam hit the crystal perpendicular to the Si(111) axis. The measurement shows resolution limitation that accounts for the lack of the expected symmetry. The maximal loss is about 10%. Even the calculation shows resolution effects since the loss is calculated at discrete values.

To quantify possible effects on reflectivity measurements Fig. 5.7 shows calculated losses of the transmitted intensity in reflectivity measurement in three different directions with respect to the Si(100) axis. The loss is calculated as a function of the momentum transfer parallel to the Si(100) axis. The loss was calculated by adding the incoming and outgoing x-ray beam from the Si(100) surface. The transmission changes by a factor of two. The curves do not show specific features and no correlation with respect to each other.

In summary the influence of excited Bragg reflections can be precisely determined and eliminated in the experiments at solid-liquid interfaces. Possible effects can be detected in reflectivity measurements and it can be accounted for.

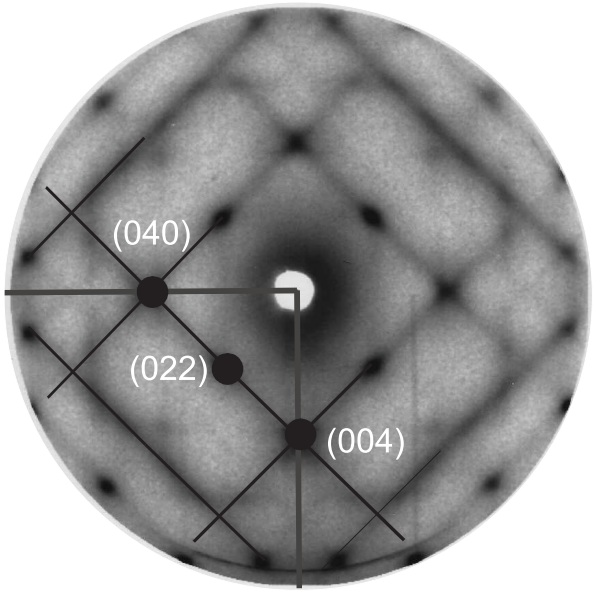

Figure 5.8: *TDS of Si perpendicular Si(100) axis. Courtesy of H. Reichert [Rei99].*

TDS of Silicon

For the measurements of the liquid structure factor parallel to the interface it is necessary to know the position of the thermal diffuse scattering (TDS) streaks of the Si crystal. To identify the peaks in the in plane measurements, reference data was taken, which is shown in Fig. 5.8 for measurements at Si(100) interfaces and in Fig. 5.9 for measurements at Si(111) interfaces. For details about the method of these experiments see [Sch03].

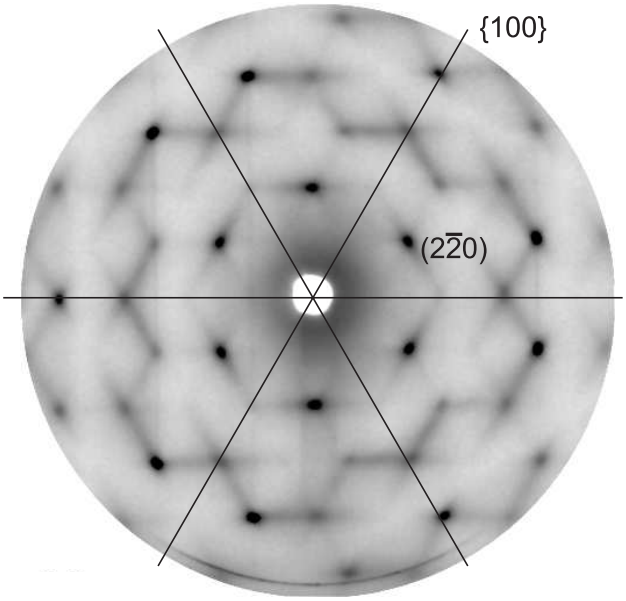

Figure 5.9: *TDS of Si perpendicluar to the Si(111) axis. Courtesy of H. Reichert [Rei99]*

Chapter 6

The Interface In(liq.)-Si(100)

In this chapter the experiments at the indium-silicon interface are presented and the results are discussed. The data sets were obtained from two different samples during two separate beam times. The chapter is separated into three sections: First GID measurements of the in plane structure are presented, followed by the reflectivity experiments in the second section. Finally, the results are discussed in a common framework.

The samples were heated to a constant temperature 10K above the melting temperature of indium. After 30 hours thermal equilibrium of the whole setup was reached.

6.1 In Plane Structure

6.1.1 Characterization and Alignment of the Interface

In the following the characterization and alignment of the sample in the beam is discussed in detail. All the experiments presented at the different interfaces follow this procedure. GID measurements require a precise characterization of the interface prior to the actual diffraction measurements. This is especially important for a deeply buried interface in order to ensure that the measured signal truly originates from the interface.

As discussed in Chap. 3 interfaces carry clear refraction signatures. In the GID geometry the intensity distribution as a function of α_i and α_f is dominated by refraction effects. In order to characterize the optical properties of the interface and determine its location we adopt the following procedure:

1. The sample is placed such that it cuts the incoming intensity I_0 in half.
2. The in plane momentum transfer $q_{||}$, the incidence angle α_i, and the exit angle α_f are fixed and the sample height z is scanned.

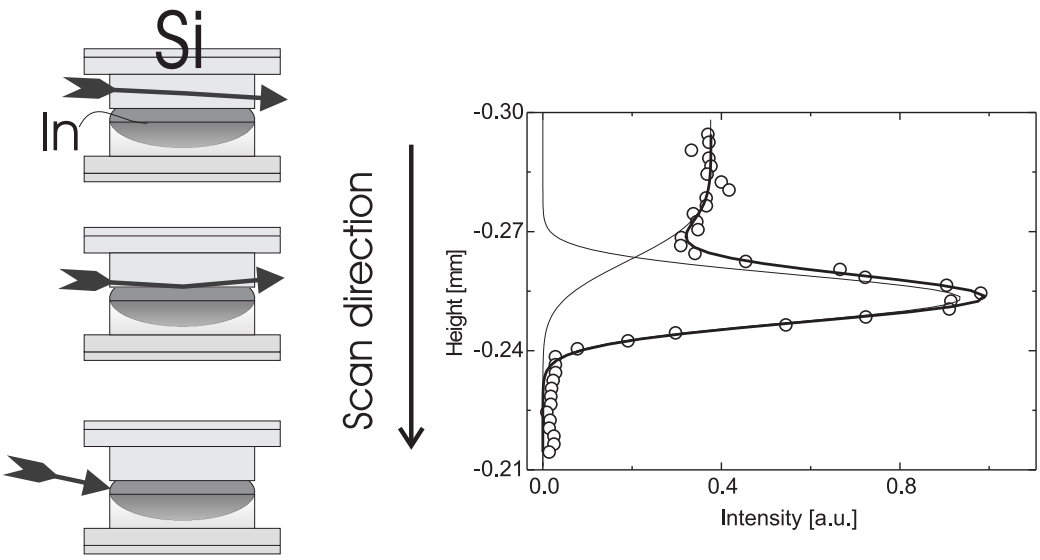

Figure 6.1: *Vertical translation of the sample at* $q_{||} = 2.3\mathring{A}^{-1}$. *The fit (thick line) is the sum of a Gaussian and an error function (thin lines). The width of the error function is* $12\mu m$. *The width of the Gaussian is* $\sigma = 8.4\mu m$. *The incidence and exit angle were kept at the specular condition near the critical angle.* $\alpha_i = \alpha_f \approx \alpha_c = 0.03°$.

3. Then $q_{||}$, z, and α_f are fixed and α_i is scanned.

4. Finally, $q_{||}$, z, and α_i are fixed and α_f is scanned.

$q_{||}$ is fixed at the value corresponding to the maximum of $S(q_{||})$. The bulk structure factor of liquid indium exhibits its maximum at $q(1^{st}peak) = 2.3\mathring{A}^{-1}$ [Was80]. At an x-ray wavelength of $\Lambda = 0.178\mathring{A}$ this corresponds to a scattering angle of $2\theta_{||} = 3.73°$.

Alignment in z-direction

The exit angle α_f is set to the specular condition ($\alpha_i \approx \alpha_f \approx \alpha_c$). A translation of the sample perpendicular to the interface moves the interface through the beam as illustrated in Fig. 6.1. At first the x-ray beam penetrates the weakly absorbing silicon sample and only diffuse structureless scattering from the bulk silicon (Compton and TDS) is recorded. When crossing the interface, a distinguished peak indicates interface scattering from the indium. The width of the peak is a convolution of the projected interface width and

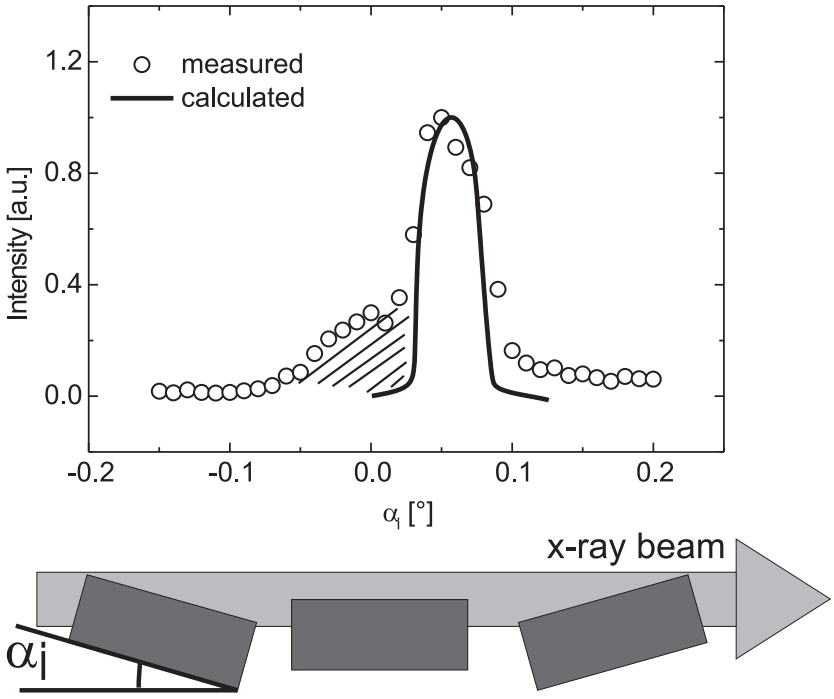

Figure 6.2: *Rocking scan of the sample at a fixed detector angle. The liquid metal is sketched as a dark grey block.*
The solid lines are calculations to the measured data where the transmitted intensity from the edge of the sample (shaded region) is disregarded.

the beam profile. For smaller z-values the beam is blocked by the strong absorption of the bulk liquid indium. The interface-related peak displays a Gaussian width of 8.4μm. In the following experiments the sample height was kept at the value corresponding to the maximum of the interfacial peak.

Alignment with respect to α_i

The next important step for the alignement of the sample in the x-ray beam is a scan of the incidence angle α_i at a fixed total momentum transfer. This allows to align α_i precisely to the critical angle of the system (s. Fig. 6.2). At the critical angle a sharp rise of the scattered signal is observed. For angles smaller than zero the scattered intensity should be zero since the x-rays are absorbed by the indium (s. Sec. 3.3). The attenuation length of liquid indium is small at the wavelength used (330μm for $\lambda = 0.178$Å). Some bulk liquid scattering, however, is transmitted through the edge of the sample

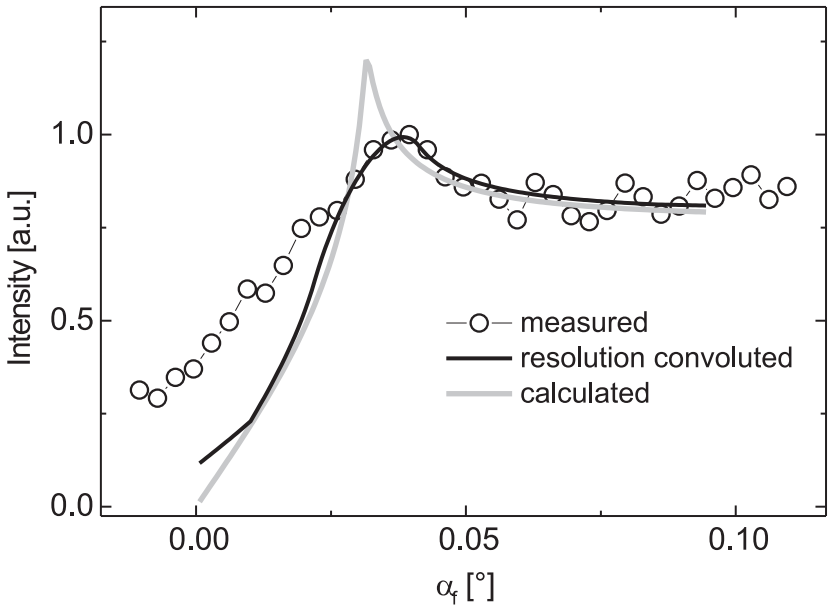

Figure 6.3: *Scan of the exit angle α_f at an in plane momentum transfer corresponding to the first maximum of the structure factor of liquid indium ($q_{||} = 2.3\text{Å}^{-1}$). The grey line is calculated for high resolution and the black line with a resolution adjusted to that of the actual measurement.*

for negative α_i.

The detector integrated from $q_z = 0.085\text{Å}^{-1}$ to $q_z = 0.092\text{Å}^{-1}$, which was defined by the detector slits. The calculation (solid line in Fig. 6.3), includes no free parameters except a scaling factor. The parameters used are all set by the measurement: the detector angle $\alpha_D = 0.14°$, the slits at the detector (lower edge $-0.05\text{mm}\hat{=}0.002°$, upper edge $0.25\text{mm}\hat{=}0.0097°$).

Alignment with respect to α_f

Fig. 6.3 shows a scan of the exit angle α_f with the incidence angle below the critical angle α_c and the same in plane momentum transfer as in the previous two scans. The signal increases to a peak at the position of the critical angle. At larger exit angles the intensity shows a constant value. This indicates that the origin of the signal is diffuse scattering (s. Eq. 3.47) contrary to Bragg scattering from a crystalline interface [Dos92]. The line shape carries the signature of a transmission function and is a direct confirmation that the scattering signal originates from the interface. At small exit angles the

signal does not drop to zero due to bulk scattering at the edge of the interface, similar to the scan shown in Fig. 6.2 ($\alpha_i = 0.021°$). The peak at the critical angle of $\alpha_c = 0.0315°$ is broadened by the angular resolution of 0.008°.

The measurement presented in Fig. 6.3 exhibits the peak at the critical angle of the interface In(liq.)-Si(100). The sharp peak in the calculated curve (grey line) is broadened by the resolution function. The black line shows the calculated diffuse interface scattering convoluted with the resolution function. The bulk scattered intensity from the edge of the sample at low scattering angles is not accounted for in the calculation.

The procedure lined out above allows to locate and characterize the interface. The detailed measurement of the shape of the diffraction signal confirms the existence of a clearly separated interfacial liquid structure factor. The structure factor parallel to the interface can now be measured and compared with the bulk liquid structure factor.

6.1.2 Structure Factor parallel to the Interface

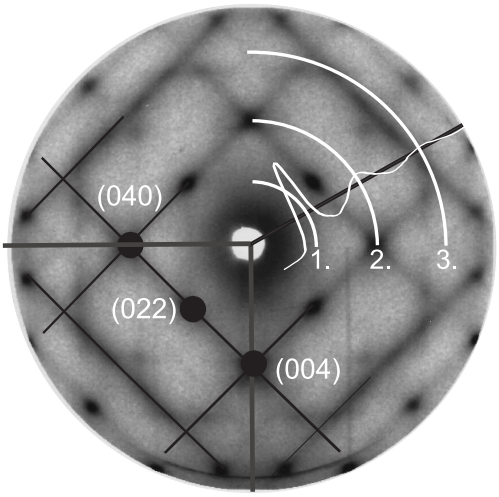

Figure 6.4: *Sketch of the measurement of the in plane structure factor parallel to the interface in a detector scan. The quarter circles denote the maxima of the liquid structure factor.*

Fig. 6.4 shows a sketch of the detector scan at the interface. The measured structure factor is superimposed by the TDS of the silicon crystal. In contrast to the liquid structure factor, the $q_{||}$-position of the TDS streaks of Si depends on the azimuthal angle (s. Chap. 5). The azimuthal angle θ of the

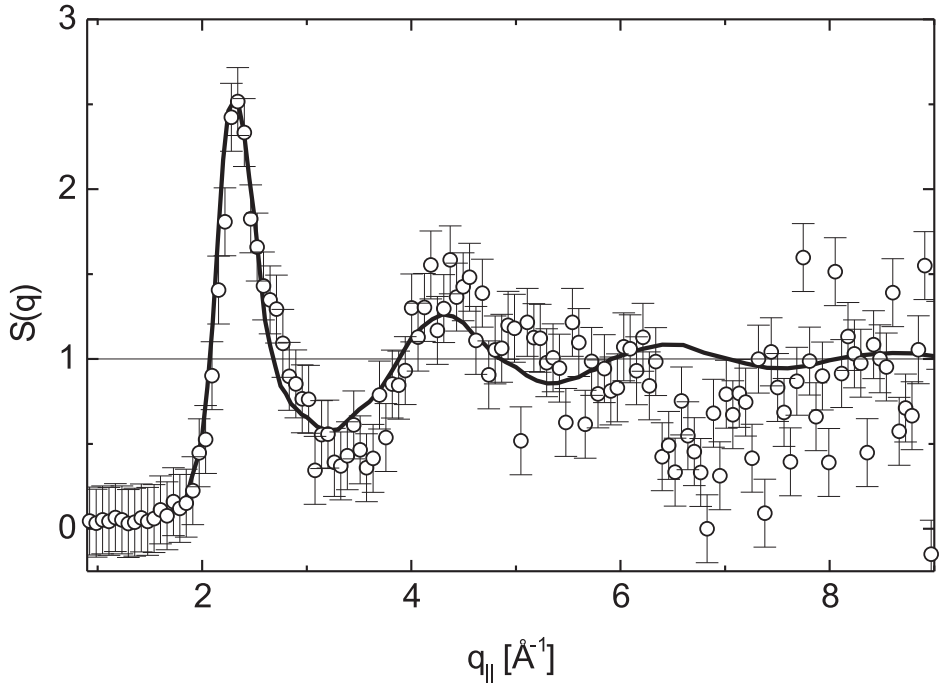

Figure 6.5: *Liquid structure factor of indium at the Si(100) interface. The open circles represent the measured structure factor. The thick solid line is the bulk structure factor taken from [Was80].*

silicon crystal is chosen in such a way that the TDS peaks are at different $q_{||}$-values than the expected peaks of the liquid structure factor. In Fig. 6.5 the structure factor of liquid indium in contact with a Si(100) surface is shown. The diffuse scattering of the silicon crystal was subtracted. The corrections described in Sec. 4.6.2 were applied and the first peak was normalized to the peak of the bulk structure factor reference. The magnitude of the error bars is mainly determined by the counting statistics. The scattering depth is given by the incidence and exit angle to $\Lambda_{\text{eff}} = 68.4$Å. The data presented up to $q_{||} = 9\text{Å}^{-1}$ parallel to the interface include the first four maxima of the bulk structure factor.

The width and the position of the first peak of the structure factor matches the reference of the bulk structure factor taken from literature [Was80]. The position, the width, and the peak height of the second peak also matches the one of the bulk structure factor within the error bars. Additional peaks are not distinguishable in the measured data. No signal indicating the presence of crystalline indium is identified.

For momentum transfer values $q_{||} \gtrsim 5.5\text{Å}^{-1}$ the data is increasingly noisy.

The TDS peak of the silicon substrate is located at 6.8Å^{-1}, which could not be eliminated completely. It was not possible to measure the structure factor with better statistics in order to improve the data. With the current setup after some hours the position of the interface in the beam is lost and a complete realignment of the sample is necessary.

6.2 Out of plane structure

The structure perpendicular to the interface is referred to as the out of plane structure. Reflectivity measurements were performed to explore the density profile across the In(liq.)-Si(100) interface.

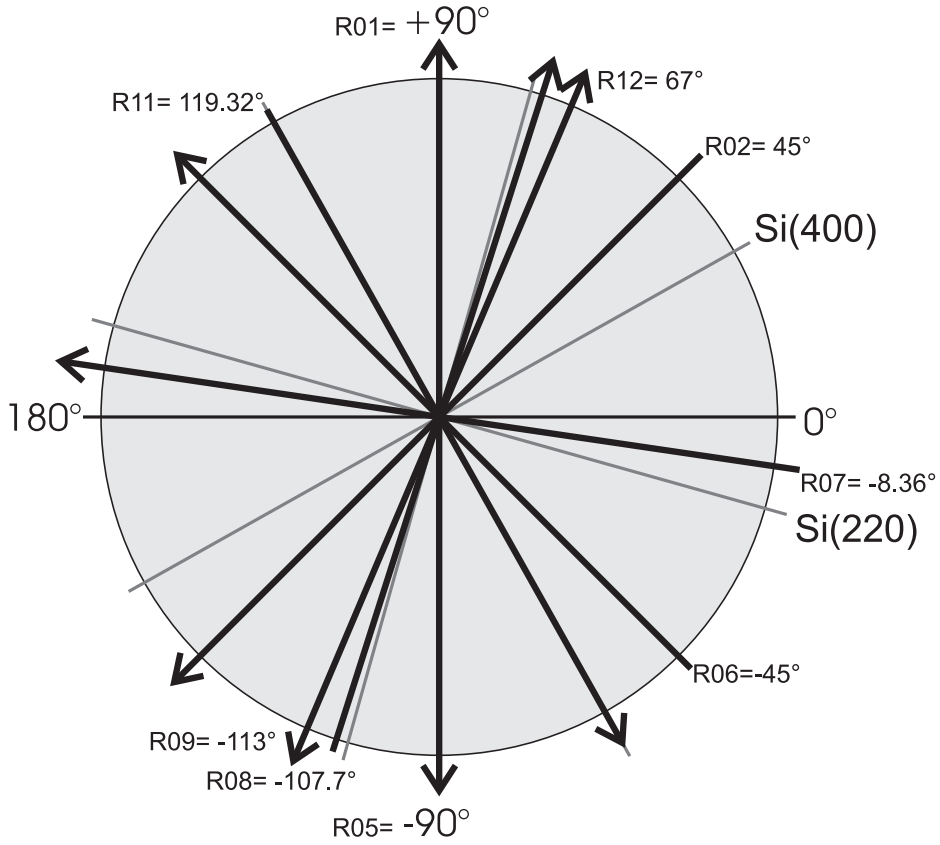

Figure 6.6: *Top view onto the interface. Illustration of the different directions at which the reflectivity was measured depicted by the arrows. The crystallographic orientation of the silicon is also marked.*

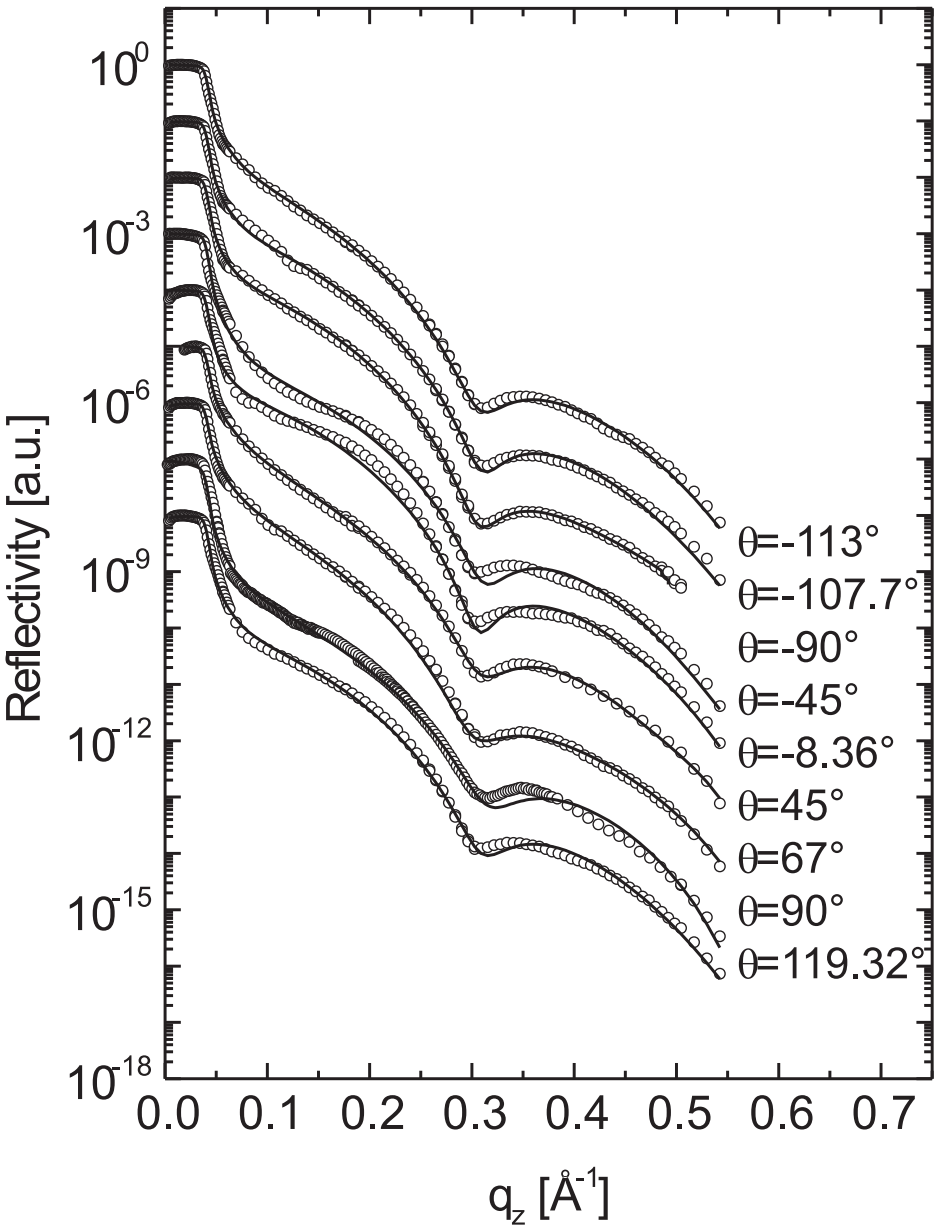

Figure 6.7: *Nine reflectivity measurements at the In(liq.)-Si(100) interface at different azimuthal angles. The measurements are shown as open circles and the fits are the solid lines. The curves are shifted by a factor of ten with respect to each other. The dip at about* 0.3Å^{-1} *is independent of the azimuthal angle.*

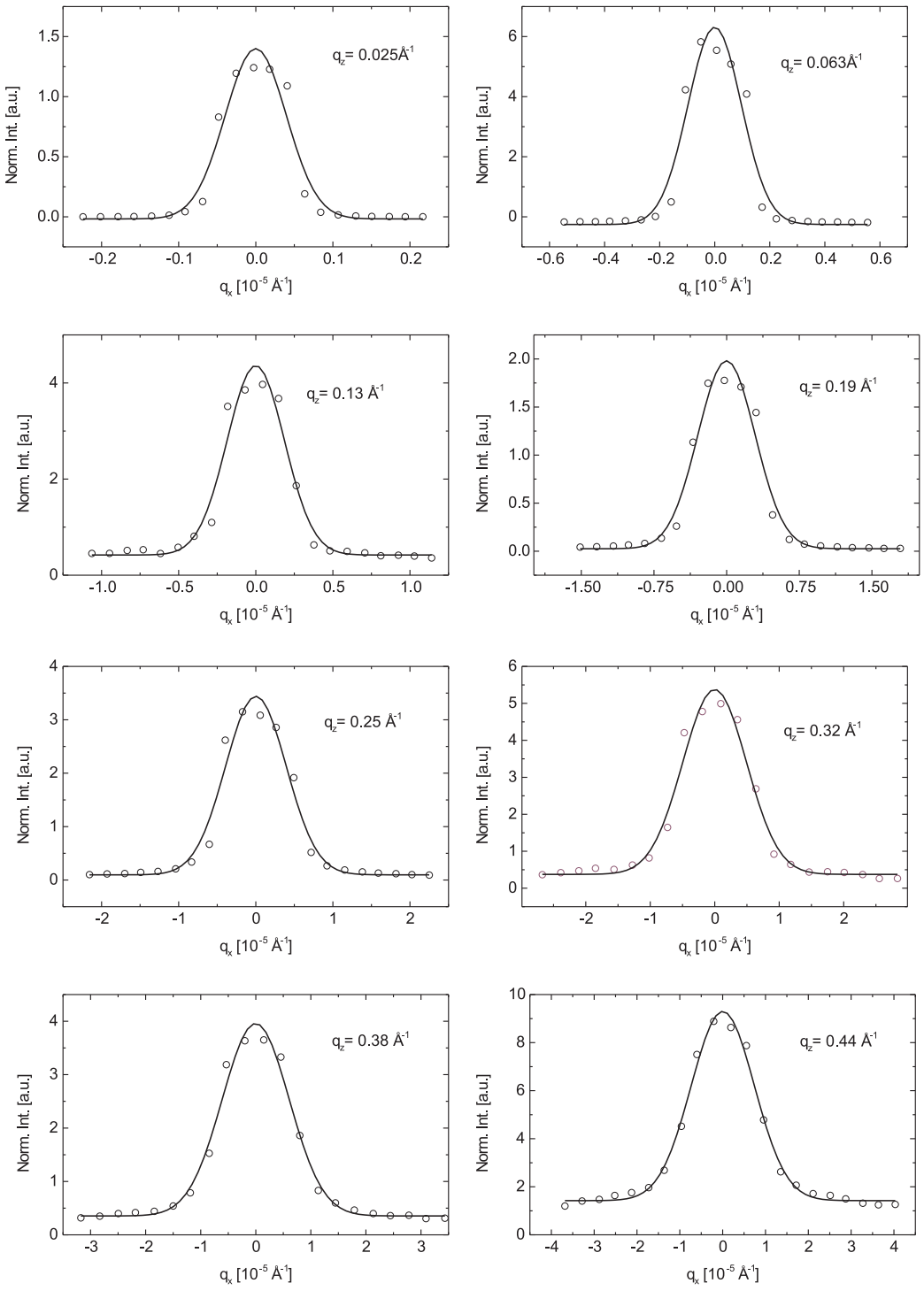

Figure 6.8: *Transverse scans of the specular rod at different vertical momentum transfers q_z.*

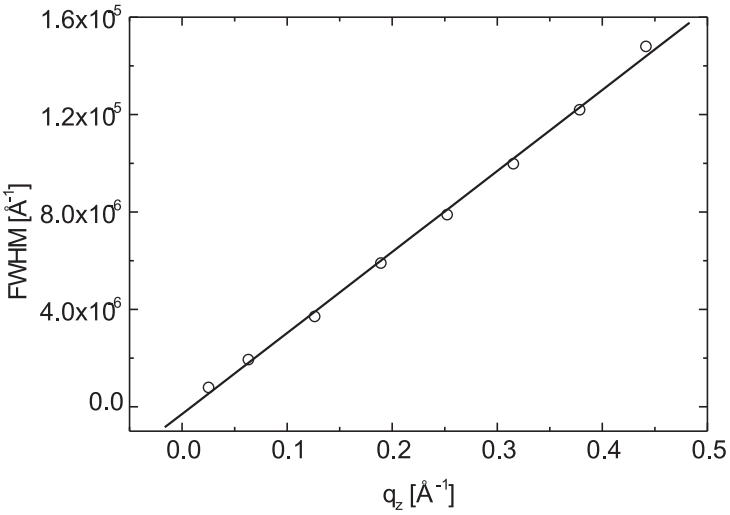

Figure 6.9: *Linear increase of the peak width with respect to q_z. Data denotes the width of the peaks shown in figure 6.8.*

6.2.1 Azimuthal dependence

Reflectivity measurements are more straightforward to perform than GID measurements. The alignment of the sample is less elaborate and it is easy to identify the specular reflection.

One important question is whether the density profile deduced from the reflectivity measurements is homogeneous over the whole surface area. The second and even more important questions is whether there are distinct density changes as a function of the crystallographic orientation of the silicon crystal. In order to answer these questions a set of reflectivity measurements has been performed at different azimuthal angles, changing the illuminated spot on the interface at moderate incidence angles.

In Fig. 6.7 a set of nine reflectivities is shown. The sample was rotated along the axis perpendicular to the interface changing the azimuthal angle between the measurements. The exact azimuthal position of each reflectivity measurement is shown in Fig. 6.6. The directions are denoted by the arrows. The crystallographic orientation of the silicon crystal is also marked. The rocking scans perpendicular to the specular rod exhibit a Gaussian line shape for all reflectivities and at all perpendicular momentum transfers q_z. The FWHM of the Gaussian was $0.003° \pm 0.002°$ ($E = 71.3\mathrm{k}eV$). A set of scans across the specular rod (rocking scans) is shown in Fig. 6.8. The width of the specular rod is resolution limited as can be seen from the linear increase of the width with respect to the perpendicular momentum transfer in Fig. 6.9.

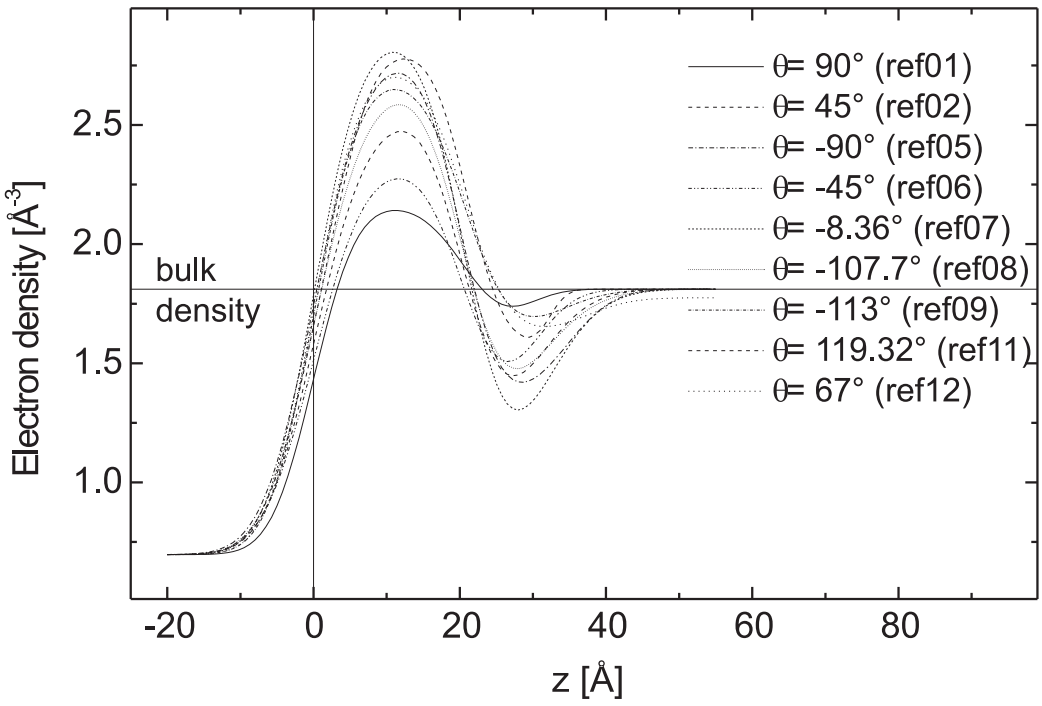

Figure 6.10: *Electron density profiles perpendicular to the interface obtained from the reflectivity measurements shown in Fig. 6.7.*

At first sight the reflectivities in Fig. 6.7 exhibit the same generic features, which indicates that the electron density profile is independent of the crystallographic orientation of the silicon. Minor variations are due to statistical and geometrical variations of the sample. The variations of the reflectivities as a function of q_z are less than one order of magnitude with respect to each other. The reflectivity could be measured up to $q_z = 0.55\text{Å}^{-1}$. The maximum value, at which the specular rod could be identified at this sample was 0.6Å^{-1}, the background was too large, however, to be subtracted unambiguously at large perpendicular momentum transfer values. The maximum momentum transfer of defines the spatial resolution in the electron density profile. With $q_{z_{max}} = 0.55\text{Å}^{-1}$ it is not possible to derive electron density profiles with atomic resolution from the measured reflectivities.

The electron density profiles were determined as described in Chap. 3. A two layer model including roughness at each layer and the substrate (bulk liquid indium) is necessary to describe all the features in the measured reflectivity curves. For some curves it was necessary to introduce a third layer

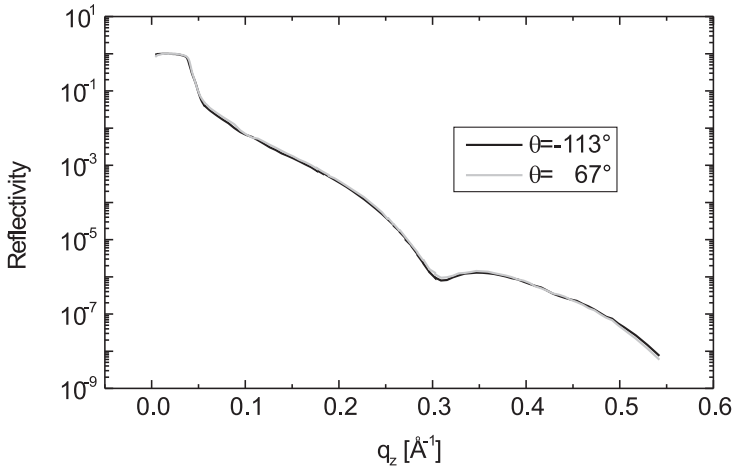

Figure 6.11: *Comparison of two reflectivities in reverse directions. The measurements were recorded with a time lag of nine hours. No deviations of the two curves are visible.*

in order to model the transition at the interface to the silicon surface with a smaller gradient. The electron density and absorption of the silicon and bulk liquid indium were calculated from tabulated values and fixed during the fitting process. Each layer was described with four parameters: density, thickness, roughness and absorption. The absorption has the smallest influence on the reflectivity.

This is necessary, because reflectivity curves are not uniquely related to an electron density profile due to the well-known phase problem in x-ray diffraction [Siv91]. The deviations from the measurements was quantified by

$$\chi^2 = \frac{1}{n-1} \sum_i \left(\frac{R^i_{exp} - R^i_{calc}}{R^i_{exp}} \right)^2 \tag{6.1}$$

and minimized in the fits. n denotes the number of data points, R^i_{exp} and R^i_{calc} are the measured and calculated reflectivity points, respectively. The weighting of χ^2 by relative deviations ($\propto 1/R^i_{exp}$) ensures, that the reflectivity is for all q_z equally weighted. The resulting χ^2 was ranging from $\chi^2 = 1.23 \cdot 10^{-2}$ to $5.56 \cdot 10^{-2}$.

The fits were obtained with the following constraints:

- The fit should consist of as few free parameters as possible, such that the features of the measurement are reproduced. The number of parameters N_p multiplied with $\chi^2_{N_p}$ has to be smaller than a fit with less parameters N_{p1} multiplied with its corresponding $\chi^2_{N_{p1}}$:
  $N_p \cdot \chi^2_{N_p} < N_{p1} \cdot \chi^2_{N_{p1}}$ with $N_p > N_{p1}$.

- The fitted electron density profile must have a physical meaning. The scattering length density for x-rays cannot be negative and the roughness between the layers cannot be zero, there must be at least atomic roughness.

Fig. 6.10 shows the electron density profiles resulting from the fits. In all cases a first layer of increased density with a thickness of about 22Å is followed by a layer of decreased density and thickness of about 12Å. The bulk liquid density is marked by a horizontal line. The thickness of the layers varies only slightly by ±2Å in all fits. The electron density of the first layer varies from $2.14/\text{Å}^3$ to $2.81/\text{Å}^3$. In relation to the bulk electron density of $1.81/\text{Å}^3$ the density increase is 18% to 55%. The density of the second layer varies from $1.31/\text{Å}^3$ to $1.74/\text{Å}^3$, which corresponds to an electron density decrease of −28% to −4% compared to the bulk liquid.

The thickness of the layers and the roughness directly at the silicon interface are similar in all fits. For a qualitative discussion we will concentrate on a more specific electron density profile. First we consider in more detail the origin of the deviations. Fig. 6.11 shows two reflectivities that were measured with a time lag of nine hours in the exact opposite directions at $\theta = 67°$ (Ref12) and $\theta = -113°$ (Ref09). The two curves are equal except for the statistical count rate fluctuations. Rocking scans of the specular rod at the same perpendicular momentum transfer q_z in both directions exhibit an equal width (s. Fig. 6.12). Therefore, the deviations in consecutive measurements are not due to a drift of the setup or the sample. The alignment of the sample was reproducible in different directions and is not the origin of the deviations in the measured reflectivity curves.

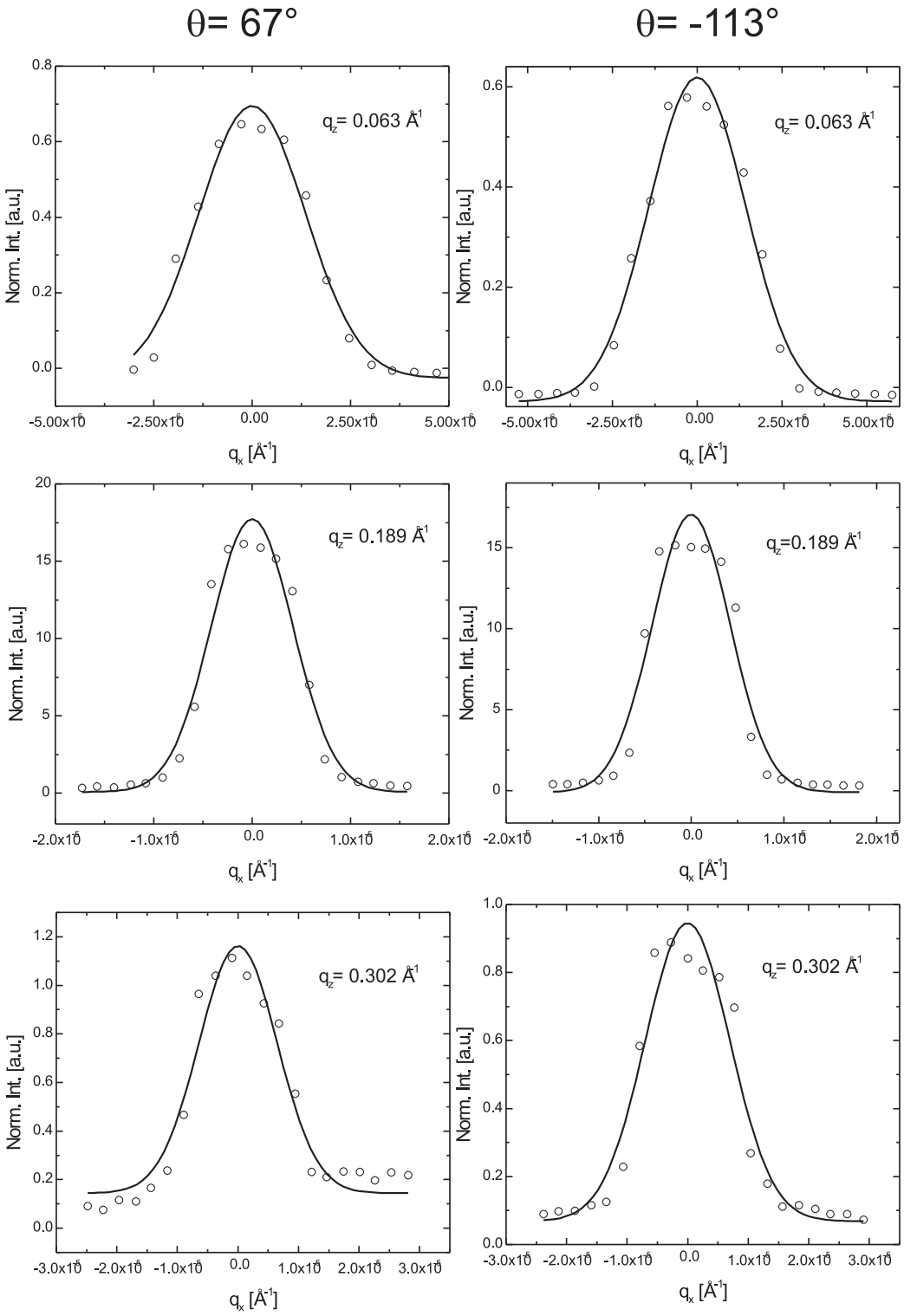

Figure 6.12: *Rocking scans for the reflectivity curves shown in Fig. 6.11. The two curves have been measured with a time lag of several hours.*

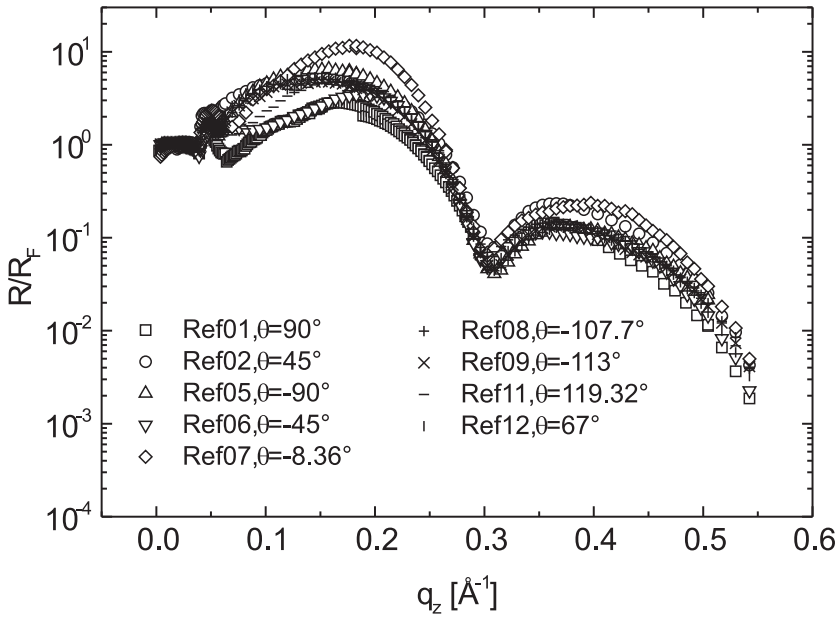

Figure 6.13: *Reflectivity measurements at the In(liq.)-Si(100) interface. The reflectivities shown in Fig. 6.7 normalized by the Fresnel reflectivity of an ideal In(liq.)-Si interface. The dip at* $0.31\mathring{A}^{-1}$ *is independent of the azimuthal angle.*

Fig. 6.13 shows the reflectivities divided by the Fresnel reflectivity of an ideal indium-silicon interface with bulk densities. Roughness results in a monotonic decay of the signal. The modulations of the monotonic decay indicate the presence of additional structural features at the interface.

The differences between the reflectivities in the different directions are maximum between the critical angle at $q_c = 0.038\text{Å}^{-1}$ and $q_z = 0.2\text{Å}^{-1}$. This behavior shows that the origin of the deviations are geometrical differences near the edges of the sample. These are probed for small momentum transfers when the incidence and exit angles are small. The main feature, which is the dip at $q_z = (0.31 \pm 0.01)\text{Å}^{-1}$, is identical in all measurements.

To compare the measured reflectivities, the quality of the respective fits, and the found electron density profile the least square χ^2 (s. Eq. 6.1) of these curves are calculated with respect to a reference. The description of the input numbers is summarized in Tab. 6.1. In Fig. 6.14 the obtained numbers are illustrated for each reflectivity. The first column that quantifies the deviation from Fresnel reflectivity is scaled by a factor of 1/1000. Since roughness and structural features both influence the deviation from Fresnel reflectivity, this is not a sufficient characteristic of the measured curves to

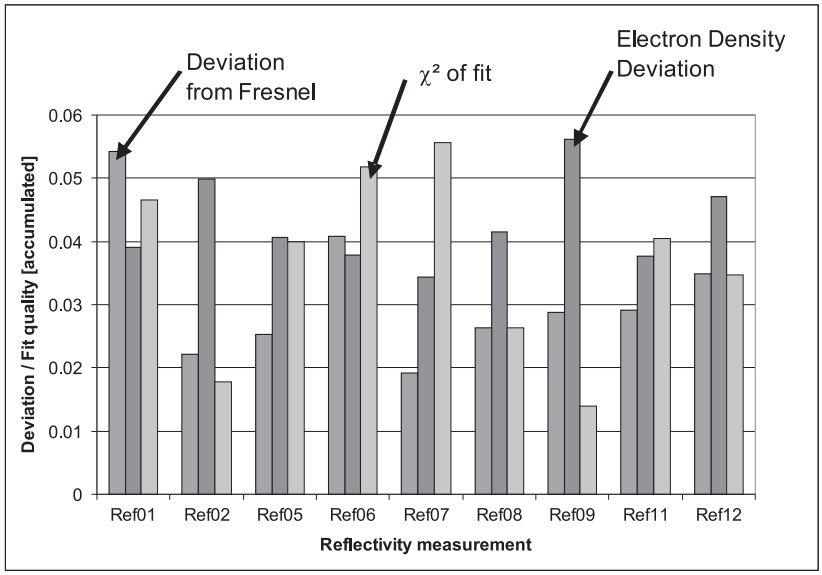

Figure 6.14: *Deviation of the reflectivity from the Fresnel reflectivity in various directions across the sample.*

Data points for	Column 1	Column 2	Column 3
R_{calc}	Measured reflectivity	Electron density from fit	Fitted reflectivity
R_{exp}	Fresnel reflectivity	Electron density from Fresnel ref.	Measured reflectivity

Table 6.1: *Input numbers for the calculation of the different χ^2 using Eq. 6.1. The results are displayed in Fig. 6.14.*

determine the most reliable reflectivity. The least square between the electron density profile and the one of the Fresnel reflectivity completes the graph. There is no correlation between the calculated numbers. The other important insight from the graph is that there is no distinctive correlation between the deviation from Fresnel reflectivity and the azimuthal angle of the respective reflectivity measurement. It cannot be concluded that a larger deviation of the electron density profile results in a smaller χ^2 of the fit and vice versa.

It is known that the flashing process (s. Sec. 4.5) might not be complete and that there are remaining silicon oxide patches on the silicon surface [Fal98] and it is impossible to decide, which reflectivity measurement was performed on the spot of the interface with the fewest silicon oxide patches.

As a reference we take the most carefully measured reflectivity Ref09 measured at $\theta = -113°$ for the following reasons: The measurement was

additionally verified in the opposite direction. The quality of the fit, denoted by χ^2, is the best for Ref09 with $\chi^2 = 0.014$, which is the smallest value of all reflectivity fits and a two layer fit was sufficient to model this reflectivity.

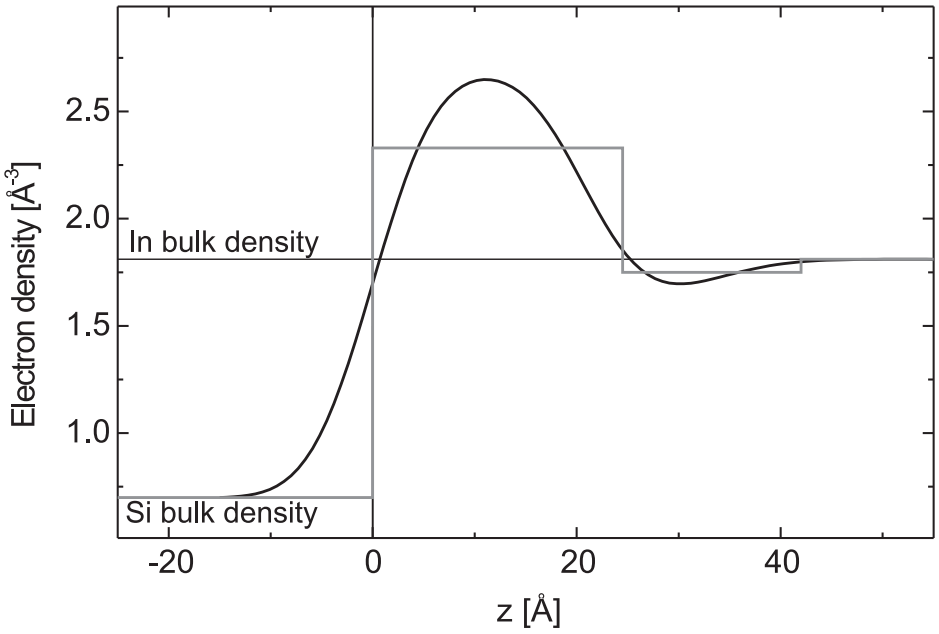

Figure 6.15: *Electron density profile determined from the measurement at* $\theta = -113°$ *(Ref09). The maximum electron density excess is* $2.69\mathring{A}^{-3}$ *compared to the bulk density of* $1.81\mathring{A}^{-3}$*. The width of the first layer is* $24.5\mathring{A}$*, which is denoted by the grey line that shows the box model of the interface.*

We propose an out of plane electron density profile at the In(liq.)-Si(100) interface with the features shown in Fig. 6.15. The roughness between the silicon and the first layer for this sample was 5.3Å. The first layer exhibits an electron density of $(2.33 \pm 0.36)\text{Å}^{-3}$ and a thickness of (24.5 ± 3)Å, the second layer exhibits an electron density of $(1.75 \pm 0.4)\text{Å}^{-3}$ and a thickness of (17.5 ± 5)Å.

6.3 Discussion

X-ray scattering experiments were performed to investigate the structure of liquid indium close to a Si(100) surface. Parallel to the interface, the structure factor was measured with an effective scattering depth of $\Lambda_{\text{eff}} = 68.4$Å. Perpendicular to the interface reflectivity measurements were carried out up to $q_z = 0.55\text{Å}^{-1}$.

Perpendicular to the interface we found a density profile of the liquid that has not been reported in literature before. Neither the thickness of the altered layers nor the density increase has been expected. The structure factor parallel to the interface remains almost unchanged with the scattering depth that was accessible in the experiments.

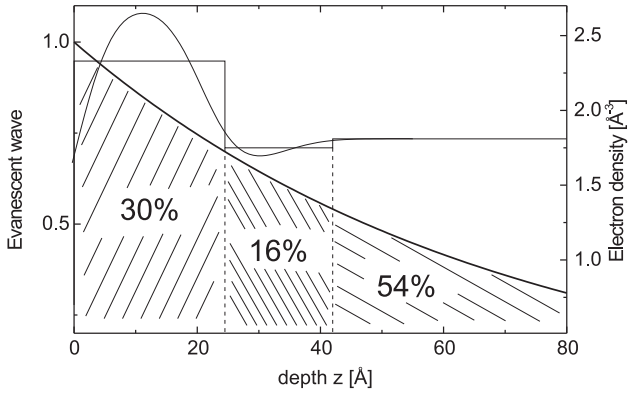

Figure 6.16: *Illustration of the fraction of the scattering contributions from different depth and its relation to the box model of the interface. The effective scattering depth was* 68.4Å.

At first sight these two results contradict each other. Let us consider the structure factor in more detail. The measured structure factor parallel to the interface is a sum of contributions from layers in different depth. The sum is incoherent, which is confirmed by the characteristics of the exit angle profile shown in Fig. 6.3 [Dos92]. The actual contribution of each layer to the total signal depends on the effective scattering depth Λ_{eff} of the evanescent wave, which was in our case $\Lambda_{\text{eff}} = 68.4$Å. Scattering contributions in a distance d from the interface will be exponentially damped by $e^{-d/\Lambda_{eff}}$. The fraction of the signal from each layer is calculated accordingly and shown in Fig. 6.16 together with the intrinsic density profile approximated by rectangular boxes. The fractional contribution of each layer is given as the hatched area below the exponential decay. It can be seen that 30% of the total signal emanates from the region with an increased electron density close to the interface.

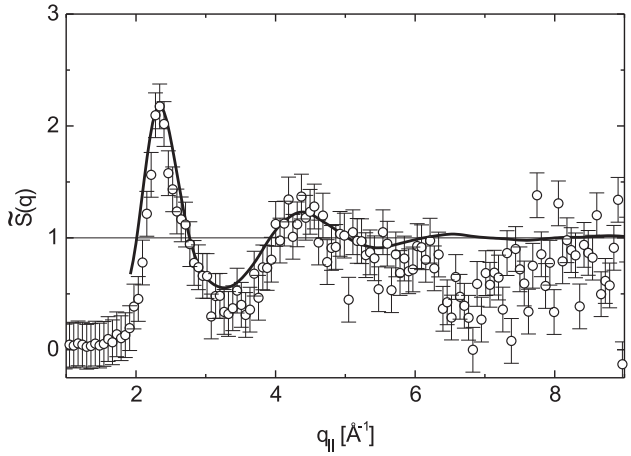

Figure 6.17: *Comparison of the measured structure factor with a calculated structure factor that has been constructed from compressed and stretched pair distribution functions $g(r)$.*

If we assume that the pair distribution function $g(r)$ must be compressed or stretched in the two layers, respectively, in order to account for the density modifications, we can calculate a partial structure factor $\tilde{S}(q)$ for each layer. The modification of the pair distribution function will be discussed later in this chapter. This treatment is in accordance with the theoretically and experimentally deduced behavior of compressed liquid metals. This was shown in experiments and calculations for rubidium [Tsu96, Chi99] and caesium [Fal05], and the transition metals copper [Zha05] up to 25GPa and iron [She04] up to 58GPa.

The interfacial structure factor is calculated by assuming that the density increase/depletion $\tilde{\rho} = x{\cdot}\rho$ (e.g. $x = 1.29$ for the first layer) can be described by a change in the atomic radius $\tilde{r} = 1/\sqrt[3]{x}$. The pair distribution function $g(r)$ is then compressed/expanded to $\tilde{g}(r) = g(\tilde{r}{\cdot}r)$. The structure factor $\tilde{S}(q)$ can then be calculated as described in Chap. 3. The different structure factors $\tilde{S}_i(q)$ are weighted by the scattering contribution and summed up. The average $\tilde{S}(q)$ is depicted in Fig. 6.17 (solid line). The only change compared to the bulk structure factor is a slight broadening of the peaks and a decrease of the intensity of the first peak. The measured structure factor is normalized to the intensity of the first peak of the calculated $\tilde{S}(q)$. The measured and the calculated structure factor $\tilde{S}(q)$ coincide well. This confirms that the strongly modified density profile is not accompanied by large changes in the measured in plane structure factor under the geometrical constraints of our GID measurements.

The density profile of the liquid metal exhibits a first layer at the interface with a maximum density that is 28.7% increased with respect to the bulk liquid and a thickness of 24.5Å. It is followed by a second layer of reduced density (-3.3% with respect to the bulk). Its thickness is 17.5Å. Only then appears the regular bulk liquid. The transition from layer to layer is not sharp but very smooth, due to the roughness of the silicon substrate, which has been determined independently at the free silicon sample.

Some cases of increased density of liquids close to solids are reported in literature. These findings were either not discussed [Hui97, Hen02, Reg95] or they were explained by an increased packing fraction of the corresponding liquid [Ton94, Doe00]. Even recent studies on density fluctuations in liquid metals do not show such a density increase [Sco00].

The density increase deduced from the reflectivity curves slightly varies at different regions of the interface. It can be attributed to geometrical inhomogeneities of the silicon substrate, since it is known that the flashing procedure of silicon might leave some surface defects and remaining silicon oxide patches [Fal98]. We thus deduce that the interfacial structure crucially depends on the quality of the silicon surface.

Up to date, the length scale for the density oscillations found in our experiments has not been reported in literature for liquid metals at a hard wall. The bulk correlation length of simple liquid metals is known to be in the range of $5 - 8$Å, which is a factor of two to four smaller than the length scale that we found.

In the following we will discuss the two major features of the interfacial density profiles, the length scale and the amount of the density increase in more detail.

Applying the hard sphere model

The simplest approach to the density profile of a liquid at an interface is the application of a hard sphere model. The liquid atoms are considered as hard spheres having a fixed radius and a uniform electron density inside. The aim is to model the electron density profile obtained from the experiments using these assumptions.

The most important question is whether it is possible to arrange the hard spheres in such a way that the electron density is increased by more than 20% compared to the bulk density on a length of more than 10Å. For the atomic radius of the indium atoms we use half of the bond length of crystalline indium ($r_{In} = 1.63$Å) [Win05]. This results in an electron density of 2.70Å^{-3} within the hard spheres. Since the electron density at the interface is averaged along slabs parallel to the interface, the average density depends

state	density	packing fraction η	electron density
solid In	7310 kg/m^3	0.70	1.88Å^{-3}
liquid In	7030 kg/m^3	0.67	1.81Å^{-3}
hard sphere (theoretical In)	–	–	2.7Å^{-3}
fcc (theoretical)	–	0.74	2.0Å^{-3}
max fcc (theoretical) (111)-direction	–	0.91 ($FWHM$= 0.6r)	2.46Å^{-3}

Table 6.2: *Packing fractions for different hard sphere models of Indium (r_{In} = 1.63Å). Molar mass:* 114.818*g/mol. For a detailed explanation of the last row see text.*

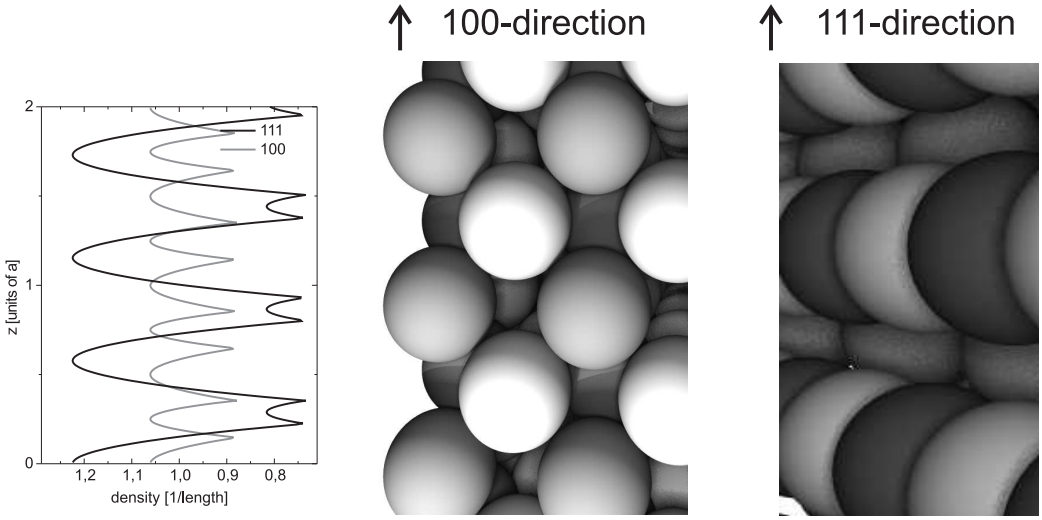

Figure 6.18: *Density profile of an fcc lattice of hard spheres in (100)- and (111)-direction. The maximum density variation occurs for hard sphere layers perpendicular to the (111)-direction.*

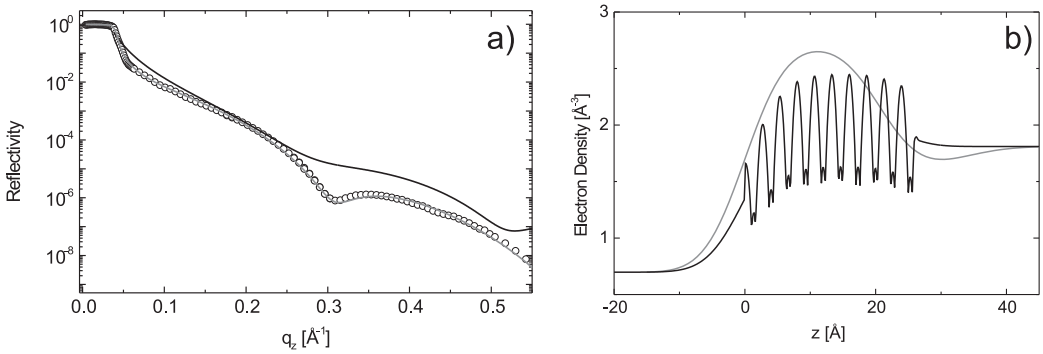

Figure 6.19: *Calculated density profile and reflectivity for an fcc-like layer of In atoms between the silicon crystal and the liquid indium (solid black line). The grey line shows the electron density fit to the measured data (small circles).*

on the packing fraction of hard spheres. Tab. 6.2 summarizes the packing fractions of In hard spheres in its native tetragonal structure and in other structures not found in indium. The fcc packing comprises the maximum packing of hard spheres.

Upon melting the packing fraction and density decrease by 3.8%. This rules out a quasi-solid layer of indium at the interface, since the measured density increase is approximately a factor of five larger than that. In addition, the bulk occurrence of a structure factor parallel to the interface rules out the presence of a solid layer of indium. Even a fcc or hcp layer of indium at the interface could not explain the observed density increase.

The local density in a hard sphere model varies between the uniform density within the hard spheres and the empty space in between. The average density is given by the product of the packing fraction η and the hard sphere density. In a crystalline structure the density of layers along a high-symmetry direction of a crystal varies with the periodicity of the crystal. The most extreme variation is found along the (111)-axis of the fcc-structure, as shown in Fig. 6.18.

The local packing fraction reaches $\eta = 0.91$ at the maximum, which is a density increase of 23%. However, this large local density occurs only within a thin slab of $FWHM = 0.6r$.

Assuming a fcc-like layer at the interface to the silicon surface, the graph b) of Fig. 6.19 shows a theoretical electron density profile. It was constructed by introducing a (111)-fcc indium layer between the two homogeneous densities of the silicon crystal and the liquid indium, replacing the fitted layer

of increased density. Applying the master formalism to the modeled electron density (s. Eq. 3.20), graph a) of Fig. 6.19 is obtained. The reflectivity of the modeled electron density has a $\chi^2 = 1500$ to the measured reflectivity and is five orders of magnitude worse than the simple two layer electron density fit obtained in Sec. 6.2. It can be concluded that geometrical packing effects are not sufficient to explain the measured reflectivity at the In(liq.)-Si(100) interface.

Electronic effects

Since geometric models are not sufficient to explain the measured reflectivity and the electron density profile deduced from the reflectivity, we will focus on electronic effects that might occur at the interface and influence the electron density at the interface. Since the atomic radius is sensitive to charge transfer effects, they can influence the electron density substantially.

The properties of Schottky-contacts focusing on the semiconductor has been studied extensively (e.g. [Mön93]). There are charge displacements and energy band bending in the semiconductor up to a depth of more than a micrometer. In the case of an undoped semiconductor, the depth of the bending is even increased, since there are less conduction electrons for screening the interface. The maximum of the conduction band that is shifted by x_m into the semiconductor (s. Fig. 2.19), might be defined arbitrarily as an interface width. For In-Si the value is expected to be in the range of 20Å, which is typical for many other systems [Pel76]. No specific value could be found in literature for the In-Si system. Inside the metal the decay of the interface effect is much faster, and according to the theory of Schottky-contacts, governed by the Thomas-Fermi screening length. It is given as $x_{\mathrm{TF}} = \frac{1}{k_F}\left(\frac{3\pi^2}{16}\right)^{1/3}\left(\frac{r_s}{a_0}\right)^{-1/2}$, with the Fermi vector k_F and a dimensionless number (r_s/a_0) denoting the radius of a sphere with a volume equal to the volume per conduction electron [Ash76]. For indium we find $x_{\mathrm{TF}} = 0.52$Å, a value far from the thickness of the interface layer obtained from the reflectivity of Sec. 6.2.

Another important length scale within metals is the mean free path length of the conduction electrons, which is not directly related to the crystal structure of metals. Following the Sommerfeld theory of metals, the mean free path length of electrons in a metal between two collisions is given as $l = \frac{(r_s/a_0)^2}{\rho_\mu} \times 92$Å, with ρ_μ as the conductivity of the metal in $\mu\Omega$cm [Ash76]. For indium the conductivity in the liquid state at 427K is $33.1\mu\Omega$cm [Iid88]. This results in a mean free path length of $l = 16.1$Å. The value is of the same order of magnitude as the thickness of the interfacial layer (24.5Å). Thus, it

is worthwhile to consider how the mean free path length might be related to the interfacial layer and the electron density profile.

A free silicon (100) surface exhibits a (2×1) reconstruction to lower the surface energy of the topmost silicon bonds. In the presence of metallic adatoms this reconstruction is lifted. Each topmost silicon atom exposes two dangling bonds that must be saturated by electrons from the liquid metal side. The saturated dangling bonds comprise a thin charged layer at the interface. In the following we assume that the liquid responds to this charged surface. The response will be balanced by a screening effect within the liquid metal that is limited by the charge transferred to the silicon surface.

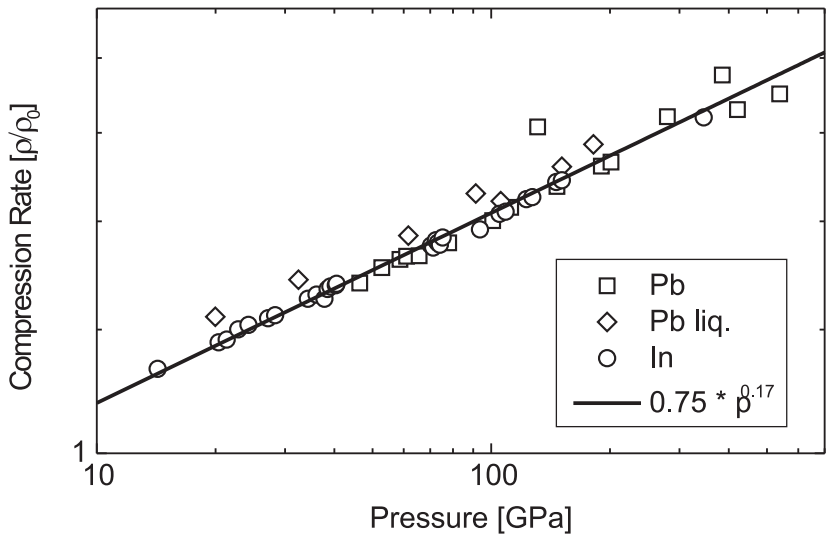

Figure 6.20: *Compression ratio of indium and lead as a function of the pressure. Double logarithmic representation. Data taken from [For03]*

A phenomenological model that may partly account for the measured density profile includes several features:

1. In contact with a liquid metal the reconstruction of silicon surfaces is fully or partially lifted. Dangling bonds evolve at the surface.

2. The dangling bonds are saturated by conduction electrons of the liquid metal. The interface gets negatively charged due to the saturation of the dangling bonds. The charged surface might be considered as one side of a parallel plate capacitor.

3. The other plate of the capacitor is represented by the positively charged ions of the liquid metal. The ions are distributed in a layer within a certain width perpendicular to the surface of the silicon crystal.

4. The coulomb force compresses the layer of liquid atoms. Thus, the overall electron density is increased in the layer of liquid atoms at the interface.

5. The compression is determined by the charge transfer to the dangling bonds, the resulting Coulomb forces and the compressibility of the liquid indium. The compression results in a reduction of the effective radius of the liquid atoms.

The number of dangling bonds for a Si(100) surface is given as $4/a_{\mathrm{Si}}^2$ with $a_{\mathrm{Si}} = 5.43\text{Å}$ the lattice constant of silicon. The surface charge density is then given as

$$\sigma = \frac{4e^-}{a_{\mathrm{Si}}^2} = 2.173 \frac{\mathrm{C}}{\mathrm{m}^2} \ . \tag{6.2}$$

The magnitude of the force per area, corresponding to a pressure, between two plates with the surface charge σ is given as

$$p = \frac{\sigma^2}{2\epsilon_0} = 2.67 \cdot 10^{11} \frac{\mathrm{N}}{\mathrm{m}^2} = 267\mathrm{GPa} \ . \tag{6.3}$$

The compression ratio of metals follows a power law as illustrated in Fig. 6.20 using tabulated values of indium, lead, and liquid lead [For03]. We obtain a compression law

$$\frac{\rho}{\rho_0} = 0.75 \cdot p^{0.17} \qquad \text{with the pressure } p \text{ in GPa.} \tag{6.4}$$

A pressure of 267GPa results in a compression ratio of $\rho/\rho_0 = 1.94$. This value is very large and the observed density increase is significantly smaller. Thus, the force is obviously overestimated. On the other hand the maximum pressure can be calculated from the maximum electron density of the layer. The measured compression ratio is given as

$$\frac{2.69\text{Å}^{-3}}{1.81\text{Å}^{-3}} = 1.49 = \frac{\rho}{\rho_0}. \tag{6.5}$$

This corresponds to a pressure of

$$\left(\frac{1.49}{0.75}\right)^{\frac{1}{0.17}} = 56\mathrm{Gpa}. \tag{6.6}$$

It can be assumed that for this calculated pressure the liquid metal behaves like a close-packed hard-sphere liquid [She04]. Apparently, the induced surface charge of the dangling bonds is continuously screened perpendicular to the layer of increased density.

Apart from the Coulomb pressure one may also argue that the charge transfer of the liquid atoms leads to a decrease in the effective radius of the atoms close to the interface. Phenomenologically, the radius of the liquid atoms depends on the number of electrons per atom. In other words, if electrons are localized at the interface to saturate the dangling bonds of the Si surface, the atoms will decrease in size. The radius of the neutral indium atom is (1.58±0.03)Å and the radius of the In^{3+}-ion is (0.92±0.12)Å [Sha76]. The error accounts for the dependence of the radius on the coordination number of the atom or ion [Pau38]. More extensive data available for other elements like lead indicate that the radius changes linearly with the oxidation number. This holds exactly only for ionic bonds and the values are used here as a reference. Each atom contributes a number of electrons to the conduction band, their number per atom is not necessarily an integer. Therefore, the mean radius of the atoms can be calculated as $r_{ox} = (1.58 - 0.22\ ox)$Å, where ox denotes the oxidation state. Since the deviation of the radius will be small in our case, we extrapolate the linear fit to atomic radii larger than the neutral radius for the case of additional electrons in a layer of the liquid metal.

The model incorporates the density and thickness of the two layers, one layer of increased density at the interface, which is followed by a second layer of reduced density. The model relates the ratio of the dangling bonds to the number of excess electrons of the two layers. From the fact that the structure factor parallel to the wall is in accordance with the density variations in z-direction, we assume that the packing fraction is similar to the one of bulk liquid indium ($\eta_{\mathrm{In}} = 0.67$).

The fractional oxidation number ox of the atoms within a layer is calculated as

$$ox = \frac{1}{b}\left(r_0 - \sqrt[3]{\frac{Z\eta}{\frac{4}{3}\pi\rho_l}}\right) \ . \tag{6.7}$$

The number N of atoms in a layer is given as the specific volume per area of the layer times the packing fraction divided by the volume of a single atom

$$N = la^2 \frac{\eta}{\frac{4}{3}\pi r_{ox}} \ . \tag{6.8}$$

Once the packing fraction, the thickness, and the density is known the number of excess electrons ec in a given volume $a^2 l$ can be calculated as

$$ec(l, \rho_l) = Nox = \frac{a^2 l \rho_l \left(2r_0 - \sqrt[3]{\frac{6Z\eta}{\pi\rho_l}}\right)}{2bZ} \ . \tag{6.9}$$

It is convenient to use the size of the unit cell a and the thickness of the layer l as the volume. N is the number of atoms in this volume and ox their fractional oxidation state. r_0 is the radius of the neutral atom, Z is the atomic number, ρ_l is the electron density of the layer, η is the packing fraction, and b is the negative slope of the dependence of the atomic radius on its oxidation state. The formula is based on the assumption that the atomic radius depends linearly on the number of valence electrons and on the approximation that the number of excess electrons is small compared to the atomic number Z.

The density profile is approximated by two boxes excluding roughness. The layer density is averaged for each layer. For the In(liq.)-Si(100) electron density profile we find (cp. Fig. 6.16):

layer i	l_i	ρ_i	ec
1	24.5Å	2.33 Å^{-3}	12.8
2	17.5Å	1.75 Å^{-3}	-5.7

The number of excess electrons is $12.8 - 5.7 = 7.1$. This is the number of electrons per a_{Si}^2 that can be transferred to the Si surface to saturate the dangling bonds. This calculated result deduced from the electron density profile is compared to the area density of dangling bonds. There are two Si atoms present per surface unit cell (a_{Si}^2). Each has a maximum of two dangling bonds in the case of a (100)-surface, which equals $4db/a_{Si}^2$. For our model we calculate a number of 7.1 electrons/a_{Si}^2. The uncertainty of the result depends on the uncertainty of the reflectivity fit, the parameters of the calculation, and the quality of the measured interface. The quality of the interface is the dominating parameter of the uncertainty. There is no way to estimate or quantify the area of remaining oxide patches on a sample surface of 30mm in diameter [Fal98]. The uncertainty from the reflectivity fit is 10% for the layer thickness and its density, respectively. The uncertainty of the packing fraction is the difference between solid and liquid indium, which is $\Delta\eta = 4.5\%$. The radius of the atoms at the interface has an error of at least 4.7%, which is the uncertainty of the ion radius. From the known factors, the total error of the number of excess electrons is then 37%, fixing the number

of electrons for the saturation of the dangling bonds to $(7.1 \pm 2.6)/a_{Si}^2$. The calculated value is too large to match with the expected number of $4db/a_{Si}^2$, even if the error is taken into account. This is not surprising considering the qualitative nature of the model derived above.

In summary the models presented in this section provide phenomenological explanations for the observed electron density profile at the In(liq.)-Si(100) interface. On the other hand there is still a lack of fundamental understanding. A model that describes the behavior of the interface exactly *and* that gives a microscopic or even quantum mechanical insight to the interfacial structure of a liquid metal in contact with a semiconductor surface is still missing.

Chapter 7

The Interface Pb(liq.)-Si(100)

In this chapter the experiments and results for the interface between liquid lead and silicon(100) are presented and discussed. The investigation of different systems enables us to work out the generic features of solid-liquid Schottky interfaces. In this spirit, one alternative to the In-Si system is the Pb-Si system, as it features a different size mismatch. Lead has a larger atomic radius than indium and four valence electrons, one more than indium. The electron density is 41% higher, leading to a larger scattering power and an increased critical angle of $\alpha_c = 0.04°$ at $E = 71.5$keV. This improves counting statistics, which renders the experiments less time consuming and less demanding with respect to stability in the experimental setup.

7.1 Out of plane structure

To explore the atomic arrangement perpendicular to the interface, reflectivity measurements were performed at the Pb(liq.)-Si(100) interface in a similar way to the In(liq.)-Si(100) interface (s. Sec. 6.2). Since the reliability of the setup was extensively checked at the aforementioned system, we proceeded in a straightforward manner and measured the reflectivity completely on a single spot on the sample. The position of the specular rod with respect to the incidence and exit angle was carefully checked by rocking scans at different scattering angles (s. Fig. 7.1). The width of the Gaussian fits increases linearly with respect to the perpendicular momentum transfer q_z indicating the resolution limited width of the specular rod (s. Fig. 7.2).

Fig. 7.3 shows the reflectivity measured at the Pb(liq.)-Si(100) interface (open circles) and the fit to the measurement (black line). For comparison the Fresnel reflectivity of a sharp Pb(liq.)-Si interface (light gray line) and the reflectivity of the In(liq.)-Si(100) interface (s. Sec. 6.2) (dark grey line)

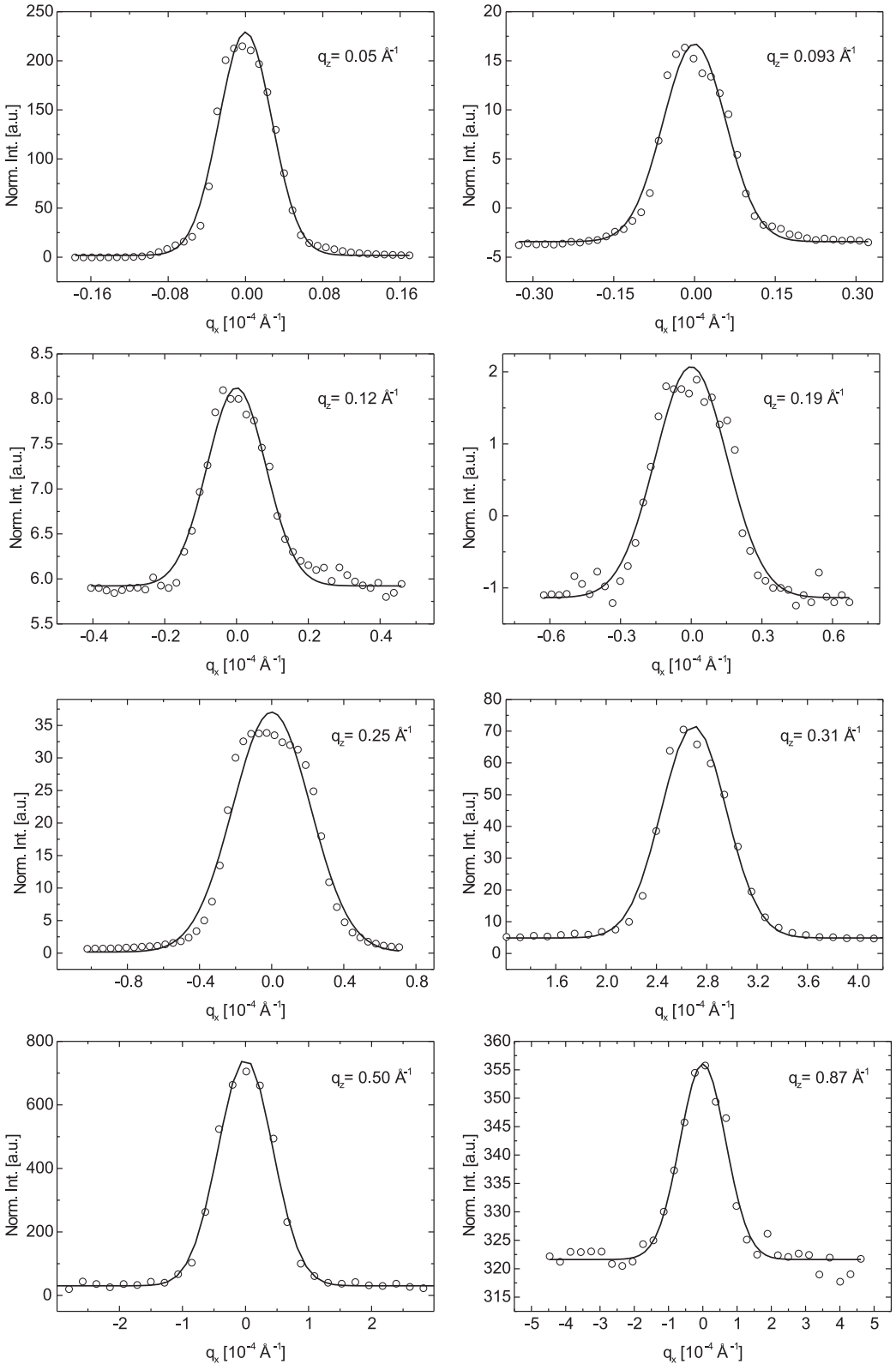

Figure 7.1: *Rocking scans on the specular rod at different momentum transfers q_z.*

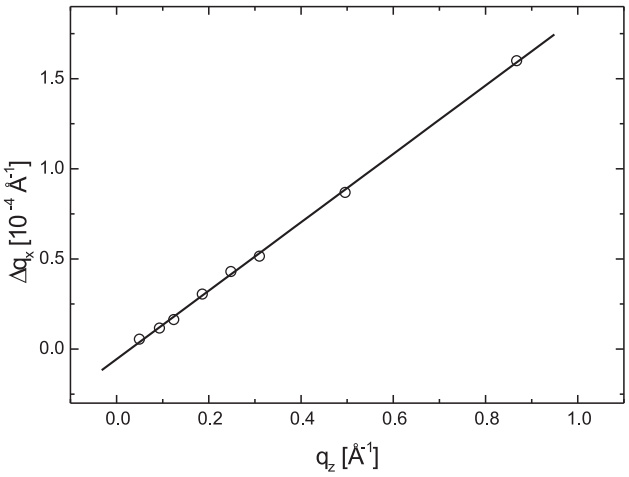

Figure 7.2: *Linear increase of the peak width with respect to q_z. Data denotes the width of the peaks shown in Fig. 7.1.*

are added.

The specular reflectivity could be separated from the diffuse background with reliable statistics up to $q_z = 0.9\text{Å}^{-1}$, corresponding to a dynamic range of eight orders of magnitude. At first glance, clear deviations from the Fresnel reflectivity of a sharp Pb-Si interface are apparent, indicating that the electron density profile perpendicular to the interface is complex and cannot be modeled by a single roughness parameter. It is obvious that additional layers with modified density are present at the interface. A similar behavior was found at the In-Si interface. A detailed comparison of the respective reflectivities of the Pb(liq.)-Si(100) and the In(liq.)-Si(100) interfaces is given below.

- The larger jump in electron density at the Pb-Si interface leads to a shift of the critical momentum transfer q_c. The shift is small but noticeable in Fig. 7.3.

- The overall roughness of the In(liq.)-Si(100) interface was larger since the reflectivity decayed much faster. This results in a different maximum value of q_z, at which the reflectivity could be separated from the background. This value was $q_z = 0.55\text{Å}^{-1}$ for In and $q_z = 0.9\text{Å}^{-1}$ for Pb.

- The length scale of the layers in z-direction must be smaller at the Pb(liq.)-Si(100) interface, since the dip in the reflectivity curve appears at a higher q_z-value compared to the In(liq.)-Si(100) interface.

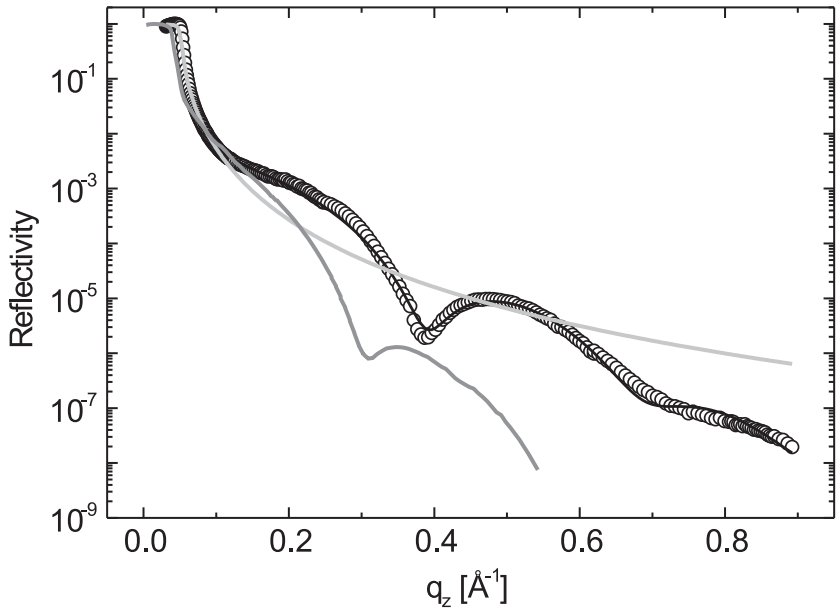

Figure 7.3: *Reflectivity measurement of the Pb(liq.)-Si(100) interface. The specular rod was identifiable up to* $q_z = 0.9\mathring{A}^{-1}$. *The black line corresponds to a two layer fit. The light grey line denotes the Fresnel reflectivity of the sharp interface and the dark grey line the reflectivity of the In-Si interface presented in Sec. 6.2.*

- There is an additional broad and weak dip at $q_z = 0.7\text{Å}^{-1}$ in the Pb(liq.)-Si(100) interface data.
- Nevertheless, the generic shape of both curves is the same.

Based on the maximum momentum transfer measured ($q_{z_{max}} = 0.9\text{Å}^{-1}$), the experiment is sensitive to features in the electron density with a minimum z-resolution of $\Delta z = \frac{2\pi}{0.9}\text{Å} = 7\text{Å}$. The fit does not show atomic resolution.

Fig. 7.4 shows the electron density profile obtained from the fit of the measured reflectivity. The dashed curve is a more detailed fit that matches exactly the measured reflectivity data of Fig. 7.3 at the expense of an additional number of parameters. The model assumes six layers and gives $\chi^2 = 1.4705 \cdot 10^{-2}$.[1] The first and more generic fit consists of only two layers and yields $\chi^2 = 2.9170 \cdot 10^{-2}$. Weighting χ^2 with the number of layers gives a better value for the two-layer fit compared to the six layer fit: $\chi^2(2\text{-}layer) = 5.834 \cdot 10^{-2}$ and $\chi^2(6\text{-}layer) = 8.823 \cdot 10^{-2}$. Since the deviations of the two density profiles and their corresponding reflectivities are small and, even more important, the features of the measured reflectivity are well reproduced by the two layer model, the following discussion will be based on the two-layer-model. In Fig. 7.4 the electron density profile of the In(liq.)-Si(100) interface is shown for comparison.

The bulk electron density of the liquid metal is larger for the Pb-Si interface than for the In-Si interface. Apart from that, the generic features of the electron density models are identical. A first layer of increased density is followed by a second layer of decreased density compared to the bulk liquid. Let us consider this in a more detailed way: The first layer has a RMS roughness of 3.2Å imposed by the silicon side. Its electron density is increased by 28.8%. The interface between the first and second layer has a width of 2.8Å. The width of the interface to the bulk liquid is 1.8Å. The electron density of the second layer is decreased by 37%. The thickness of the first layer is 17Å and the one of the second layer is 6Å.

The main difference to the In(liq.)-Si(100) electron density profile is, that the roughness of the profile at the edge to the silicon substrate is smaller for the lead data. This leads to reduced roughness in all subsequent layers and the whole profile is more pronounced. Whereas this can be attributed to the initial roughness of the silicon substrate, the change of the thickness and its density deviations from the bulk liquid of the two layers must be due to the different properties of the liquid metals.

In summary the structure perpendicular to the Si surface is as follows: The electron density profile exhibits an oscillatory modulation. The average

[1] for definition s. Sec. 6.2.1

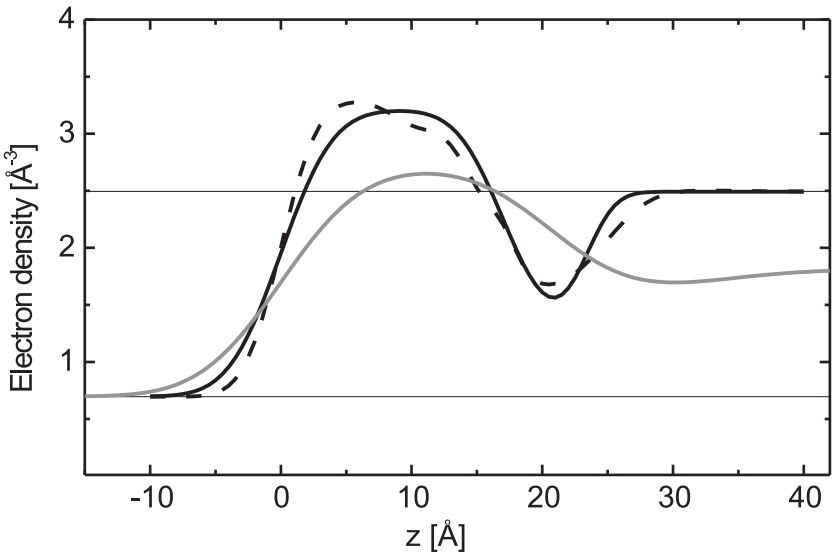

Figure 7.4: *Electron density profile deduced from the fits shown in Fig. 7.3. The solid line is a two box model with gaussian roughness at each interface. The dashed line denotes a more complicated model that allows deviations of the two layer model. The grey line shows the electron density profile of the In(liq.)-Si(100) interface for comparison.*

density calculated in the two layers is increased by 3.0% compared to the bulk liquid. The density is locally increased up to 28.8% and the average density increase in the first layer is 15.1%.

7.2 Discussion

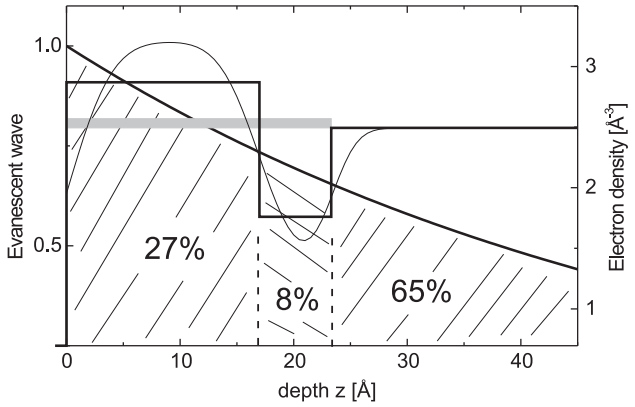

Figure 7.5: *Illustration of the fraction of the scattering contributions of layers at different depth and its relation to the box model of the interface. The grey area shows the averaged density increase between the silicon and the bulk liquid lead. The effective scattering depth was* $\Lambda_{\text{eff}} = 55\mathring{A}$.

As can be seen in Fig. 2.16 in Sec. 2.5.3 the structure of the liquid seems not to be altered close to the wall, except for the azimuthal modulation of the intensity of the first peak of the structure factor. Its origin has been discussed in detail [Rei00]. Perpendicular to the interface we found a strong deviation from the bulk electron density with similar results to the In(liq.)-Si(100) interface. Since these two results seem to be contradicting, the structure factor will be analyzed in more detail. The measured structure factor parallel to the interface is a superposition of structure factors layered parallel to the interface. The description follows the one presented in Sec. 6.3. The contribution of the layers depends on the effective scattering depth Λ_{eff} of the evanescent wave, which was $\Lambda_{eff} = 55\text{Å}$ in the structure factor measurement. All atoms perpendicular to the interface will contribute to the observed scattering signal decaying exponentially. Fig. 7.5 shows the density profile approximated by rectangular boxes together with the electron density profile smoothed by roughness. The fractional contribution of each box to the scattered signal is

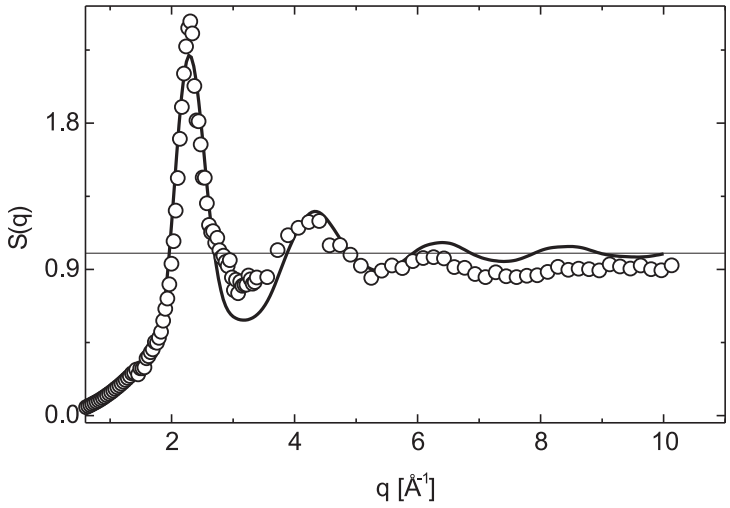

Figure 7.6: *Comparison of the measured structure factor with a calculated structure factor $\tilde{S}(q)$ that has been constructed from compressed and stretched pair distribution functions $g(r)$.*

denoted in the area below the exponential decay. 27% of the signal emanates from the first layer with increased electron density close to the interface.

If we assume that the pair distribution function $g(r)$ must be compressed or stretched in the two layers in order to account for the change in the density, we can calculate a partial structure factor $\tilde{S}(q)$ for each layer.

The partial structure factors are calculated as follows: For a change in the density by a factor x, i.e. $\tilde{\rho} = x \cdot \rho$ (e.g. $x = 1.15$ (first layer)). Then the stretching factor $\tilde{r}$ is given as $\tilde{r} = 1/\sqrt[3]{x}$. The pair distribution function $g(r)$ is then compressed to $\tilde{g}(r) = g(\tilde{r} \cdot r)$. The structure factor $\tilde{S}(q)$ is determined as described in Chap. 3. The different structure factors $\tilde{S}_i(q)$ are weighted by their respective scattering contribution and summed up. The total $\tilde{S}(q)$ is shown in Fig. 7.6. The only change compared to the bulk structure factor is a slight broadening of the peaks and a decrease of the intensity of the first peak. The measured structure factor is in good agreement with the calculated structure factor. We conclude therefore, that there is no contradiction between the measured structure of the liquid parallel and the observed density profile perpendicular to it.

Charge transfer effects at the interface offer the most promising way towards an explanation of the observed interfacial electron density profile. The silicon crystal was a n-conducting phosphorus-doped semiconductor with a resistivity between 12.4Ωcm and 14.4Ωcm. In this case the conduction band

of the silicon crystal is bent upwards at the interface on a length in the micrometer range (s. Fig. 2.19) [Mön93]. On the metal side of the interface perturbations are screened on the Thomas-Fermi screening length $x_{\mathrm{TF}} = 0.51$Å [Ash76] for lead. This value is far too small to explain the length scale of 24Å for the density modulation at the Pb(liq.)-Si(100) interface.

The mean free path length l of the conduction electrons following the Sommerfeld theory of metals [Ash76] is 5Å for liquid lead at 600K, calculated from the conductivity of $95\mu\Omega$cm [Iid88]. The mean free path length is of the same order of magnitude as the thickness of the first layer, however it is too small to be identified with the thickness directly.

As discussed in Chap. 2, a free silicon (100) surface exhibits a (2×1) reconstruction. This reconstruction is lifted in the presence of bulk lead. Each topmost silicon atom has two dangling bonds that can be saturated by electrons from the liquid. The saturated dangling bonds correspond to a thin charged layer at the interface. Applying the phenomenological model introduced in Sec. 6.3 the following results are obtained: The maximum possible surface charge with completely saturated dangling bonds is $\sigma = 2.173\mathrm{C/m}^2$. This gives rise to a maximum pressure of $p = 267$GPa. According to Fig. 6.20, this corresponds to a compression ratio of $\rho/\rho_0 = 1.94$. Indeed the maximum electron density deduced from the fit of the reflectivity and the maximum compression ratio is

$$\frac{3.20\text{Å}^{-3}}{2.49\text{Å}^{-3}} = 1.29 = \frac{\rho}{\rho_0}. \tag{7.1}$$

This corresponds to a pressure of

$$\left(\frac{1.29}{0.75}\right)^{\frac{1}{0.17}} = 24\text{GPa}. \tag{7.2}$$

At this pressure the liquid metal is expected to behave like a close-packed hard-sphere liquid [She04]. The pressure calculated from the electron density is about a factor of eleven smaller than the maximum possible pressure calculated from the density of the dangling bonds.

The charge transfer from the liquid leads to a reduction of the effective radius of the atoms, which can be calculated and gives the number of excess electrons of the interfacial layer (cp. Sec. 6.3). There are two oxidation states known for lead (Pb^{2+}, Pb^{4+}). The linear dependence of the radius r_{ox} on the oxidation state ox is demonstrated in Fig. 7.7. The data is taken from [Sha76] and the error bars account for the dependence of the radius on the coordination number of the ions [Pau38]. The linear fit gives $r_{ox} = (1.75 - 0.24ox)$Å for the radius as a function of the oxidation state, with a

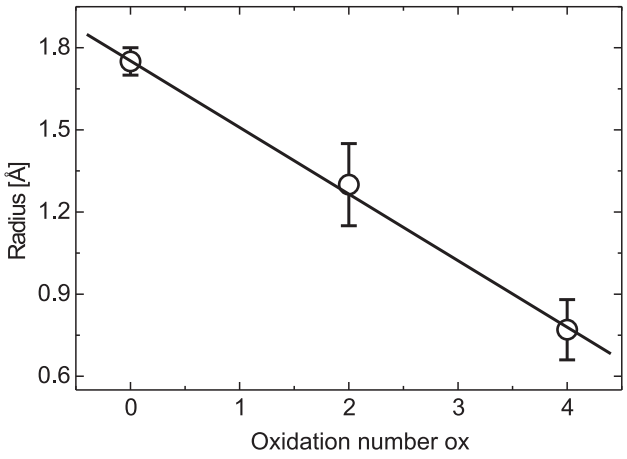

Figure 7.7: *The atomic radius of Pb as a function of the oxidation state. Data taken from [Sha76].*

neutral radius of 1.75Å. Assuming a packing fraction similar to the bulk liquid ($\eta = 0.696$) one can calculate the number of excess electrons of the respective layer using Eq. 6.9. The size of the silicon unit cell is taken ($a^2_{\mathrm{Si}} = 29.5\text{Å}^2$) as reference area.

layer i	l_i	ρ_i	ec
1	17.5Å	2.87 Å^{-3}	5.1
2	6.3Å	1.76 Å^{-3}	-3.8

Table 7.1: *Excess electrons in the respective layer of the electron density profile. l_i gives the thickness of the layer, ρ_i the electron density and ec the number of electron excess in each layer calculated from Eq. 6.9.*

The density profile is approximated by two boxes excluding roughness and smearing due to the liquid properties. The layer density is averaged for each layer. For the Pb(liq.)-Si(100) electron density profile we find the results given in Tab. 7.1. The total number of excess electrons is $5.1 - 3.8 = 1.3$. This is the number of electrons per a^2_{Si} that are transferred to the Si(100) surface to saturate the four dangling bonds per surface unit cell (a^2_{Si}). It has been reported that the breaking of the surface reconstruction may be only partial [Don01]. For an estimation of the error bar, we take into account the uncertainty of the reflectivity fit and the systematic errors for all parameters. The packing fraction might be increased close to the wall and reach partially the solid packing fraction, thus $\Delta\eta = 6.4\%$. The radius of the atoms at the

interface has an error of 5.8% extracted from the linear fit (cp. Fig. 7.7). The largest uncertainty arises from the fit of the reflectivity, with 5% for the layer thickness and its density, respectively. The uncertainty of the number of excess electrons sums up to 23%. The number of electrons to saturate the dangling bonds is thus $(1.3 \pm 0.3)/a_{\mathrm{Si}}^2$. This is in qualitative agreement with the expected number of $4/a_{\mathrm{Si}}^2$ with the assumption that the reconstruction is not lifted completely.

Comparison of the Pb(liq.)-Si(100) and In(liq.)-Si(100) interface

Tab. 7.2 summarizes the main features of the electron density profiles of the two systems. For both systems we find the same generic features. At the interface to the silicon a layer of increased density exists, which exhibits a thickness of about five times the lattice constant ($\approx 5d_{100}$) or about five atomic diameters. The density of this layer cannot be explained by an enhanced packing fraction of the liquid atoms. A second layer of decreased density appears between the layer of increased density and the bulk liquid. The transition between all layers is smooth and the roughness of the silicon surface is superimposed. The roughness of the silicon substrates is comparable for the two samples and it was verified at several silicon substrates that the roughness was reproducible.

System -Si(100)	roughness at interface	thickness of layer 1	$\rho/\rho_{\mathrm{bulk}}$ layer 1	thickness of layer 2	$\rho/\rho_{\mathrm{bulk}}$ layer 2
In(liq.)	5Å	24.5Å	28.7%	17.5Å	-3.3%
Pb(liq.)	3.2Å	17Å	28.8%	6Å	-37%

Table 7.2: *Comparison of the results of the model calculations for the two interfaces.*

The relative thickness of the first layers corresponds to 4.9 atomic diameters of lead and 7.8 atomic diameters of indium, based on the ambient atomic diameter. The relative density increase in the first lead and indium layer is the same within the calculated error. The thickness of the second layer corresponds to 1.7 atomic diameters for lead and 5.5 atomic diameters for indium. The reduced density differs by an order of magnitude between the two systems. While there is only a slight density decrease at the indium interface, the density of lead is decreased even more than it is increased in the first layer of the lead profile. Thus, although there are common features in both systems, there are noticeable quantitative differences. The relative density increase given in Tab. 7.2 is calculated from the average density in

the layer, the maximum density increase in the indium layer is indeed much higher compared to lead (s. Tab. 7.3). The interfacial influence of the Si(100) surface on the density of the liquid lead is smaller than on the liquid indium. This is reflected in the length scale, over which the density is varied compared to the bulk density and in the maximum density deviation of the layers: For the Pb(liq.)-Si(100) interface the length scale and the density deviation are smaller.

System -Si(100)	max. calc. pressure from fit	maximum compression ratio ρ/ρ_0	calculated electron transfer
In(liq.)	56GPa	1.49	$7.1/a_{\mathrm{Si}}^2$
Pb(liq.)	24GPa	1.29	$1.3/a_{\mathrm{Si}}^2$

Table 7.3: *Comparison of the results of the charge transfer model for the interfaces In(liq.)-Si(100) and Pb(liq.)-Si(100).*

Tab. 7.3 summarizes the results from the model calculations of Secs. 6.3 and 7.2. The non linear dependence of the pressure on the compression ratio results in a maximum pressure for indium, which is about twice as much as for lead. This indicates that the screening of the saturated dangling bonds is less effective for indium than for lead. The properties of the second layer fit well to this behavior, the lead shows a thin layer of strongly decreased density compared to the indium that shows a shallow layer, which is far more extended and which again indicates that the indium is less capable of screening the dangling bonds of the silicon surface.

The two silicon samples were not identical either. For the indium an undoped silicon crystal was used and for the lead a n-doped silicon crystal was prepared. Thus, there are more free electrons in the doped crystal present, which might be trapped at dangling bonds and saturate the bonds. As a consequence the surface is less charged and less electrons are transferred from the liquid to the silicon surface, which leads to a smaller pressure. This is supported by the observation that the liquid lead is less altered at the silicon surface than the liquid indium.

An effect that cannot be considered qualitatively is the state of the free silicon surface after the flashing procedure. It is known that for single flashing there remain oxide patches on the silicon surface [Fal98]. If the fraction of oxide patches on the Si surface differed for the In-Si and Pb-Si sample, it might influence the reflectivity in a way as it was measured.

Chapter 8

The Interface Pb(liq.)-Si(111)

In the previous two chapters we have investigated two different solid-liquid metal-semiconductor interfaces, where the liquid side of the interface has been changed. In order to investigate the influence of the structure of the solid wall we now discuss a third solid-liquid interface, where the solid substrate was changed.

As the most straightforward step we changed the silicon surface from (100)- to (111)-orientation. The chemical properties of the bulk solid are the same, as well as the x-ray properties given as the critical angle. The most important change is the symmetry of the solid substrate. The primitive Si(100) surface has a four-fold symmetry, whereas the primitive Si(111) surface features a three-fold symmetry. In addition, each Si atom in the topmost layer extends only one dangling bond. Therefore, the area density of dangling bonds is $(4/\sqrt{3})/a_{\mathrm{Si}}^2 \approx 2.3/a_{\mathrm{Si}}^2$, which is almost a factor of two smaller than for the Si(100) surface $(4/a_{\mathrm{Si}}^2)$.

The chapter is separated into three sections. The first section focuses on the structure parallel to the Si(111) surface. In the second section the results for the density profiles perpendicular to the interface are presented. In the third section the combined results are discussed.

8.1 In plane structure

The sample was aligned and characterized in the same way as described in Sec. 6.1. The in plane momentum transfer $q_{||}$ was set to the first peak of the structure factor of liquid lead ($q_{||} = 2.3\mathrm{\AA}^{-1}$). The exact position of the interface in vertical direction was found by a vertical scan of the sample (z-scan). In Fig. 8.1 the projection of the interface is shown together with a fit using the model that was introduced in Sec. 6.1. The x-ray wave

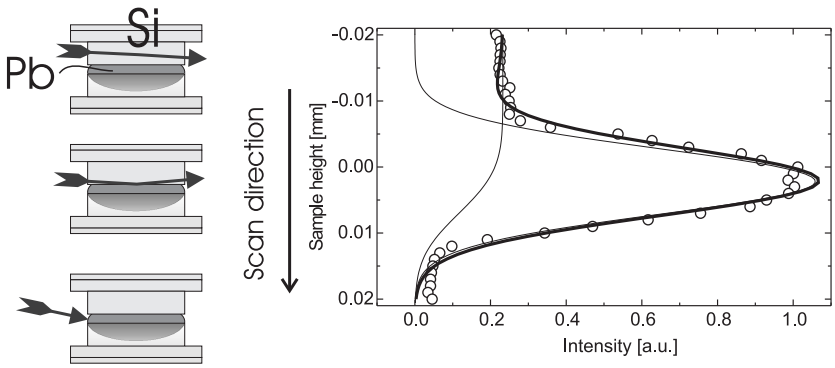

Figure 8.1: *Scan of the interface through the x-ray beam at the first maximum of the structure factor of liquid lead ($q_{||} = 2.3\mathring{A}^{-1}$). The fit (thick line) is the sum of a Gaussian and an error function (thin lines).*

length was $\lambda = 0.174$Å ($E = 71.4$keV). The width of the interface was 7.1μm. The incidence and the exit angle were kept at the specular condition ($\alpha_i = \alpha_f = \alpha_c = 0.04°$). The intensity scattering from the interfacial liquid lead is five times larger than the diffuse scattering intensity of the silicon, compared to a factor of 2.5 in the case of liquid indium (s. Fig. 6.1).

The exit angle profile features the typical form of a transmission function with a maximum at $\alpha_f = \alpha_c$ (see Fig. 8.2). The calculated curve is convoluted with the resolution function. The calculated profile is scaled to the measured intensity, no other free parameters are used. The resolution was $\Delta\alpha_f = 0.0085°$. The intensity drops almost to zero at $\alpha_f = 0$, however, there is some remaining bulk scattering emanating from the edges of the sample. Again, the resolution and statistics are better than for the In-Si sample (cp. Fig. 6.3). The peak in the measured intensity is exactly at $\alpha_f = \alpha_c = 0.0395°$, as expected for an interfacial scattering signal feature.

For a further characterization of the interface the slits of the detector were opened to integrate the signal on a wider range of scattering angles α_f. Fig. 8.3 shows a scan of the incidence angle α_i with the detector angle set to $\alpha_D = 0.04° = \alpha_i + \alpha_f$. The detector slits were set to integrate from $\alpha_{D_{\text{low}}} = 0.036°$ to $\alpha_{D_{\text{upper}}} = 0.167°$. The calculated curve is free of parameters except for a scaling factor and a constant background. As in the case of the exit angle profile (cp. Fig. 8.2), we find bulk scattering from the edges of the sample, which was suppressed by a proper slit setting for the subsequent measurements. For further details see Fig. 6.2 and the discussion in Sec. 6.1.1. The profiles confirm that refraction effects at the interface can be used to isolate the scattering from a thin liquid metal layer adjacent to a deeply

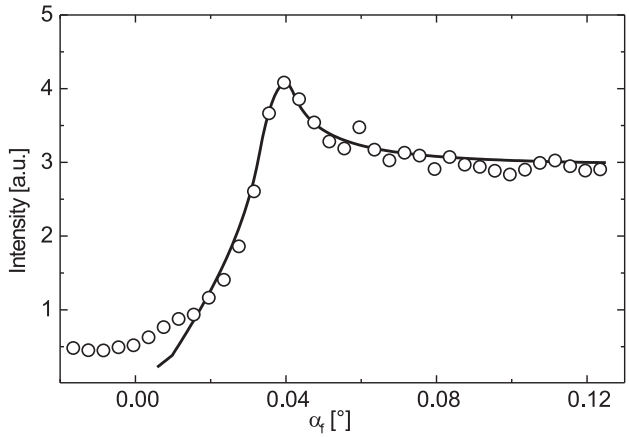

Figure 8.2: *Scan of the exit angle α_f at the first maximum of the structure factor of liquid lead ($q_{||} = 2.3\mathring{A}^{-1}$), together with a model calculation (black line). The incidence angle was set to $\alpha_i = 0.0365°$.*

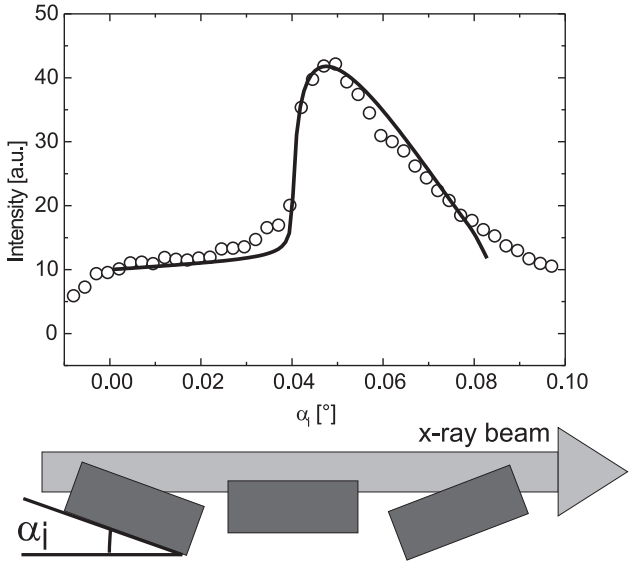

Figure 8.3: *Tilt scan of the interface in the beam at the first maximum of the liquid structure factor of lead ($q_{||} = 2.3\mathring{A}^{-1}$), together with a model calculation (solid line). The highly absorbing liquid Pb is sketched as a block.*

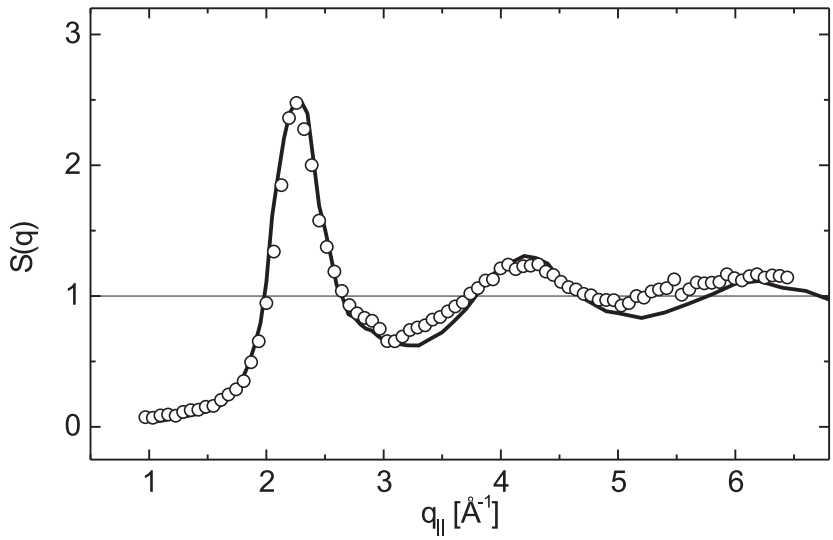

Figure 8.4: *Liquid structure factor of lead parallel to the Si(111) wall. The open circles represent the measured structure factor. The solid line is the bulk structure factor taken from [Was80].*

buried wall.

The bulk reference structure factor was measured parallel to the interface with the effective scattering depth set to $\Lambda_{eff} = 88$Å. The diffuse scattered background from the silicon was subtracted and the corrections of Sec. 4.6.2 were applied. The result is presented in Fig. 8.4. For comparison the bulk structure factor is also shown [Was80]. The first two peaks are clearly identified and match in size and position the bulk structure factor. The third peak is visible, but not as clear as the first two peaks.

In order to answer the question whether the interfacial liquid structure factor is affected by the Si(111) surface, we concentrated on the maximum of the structure factor at $q_{||} = 2.3\text{Å}^{-1}$. This is the most sensitive position in order to detect the influence of the solid substrate on the liquid structure factor (see Sec. 2.5.3). The structural substrate may impose its symmetry on the liquid structure, therefore, the static structure factor $S(q_{||})$ is measured at fixed $q_{||}$ and constant scattering depth at different azimuthal angles ϕ. To allow for the separation from statistical variations the intensity was measured using the incidence angle α_i as an additional parameter. In Fig. 8.5 a complete set of 73 scans ($\Delta\phi = 5°$) at different azimuthal angles covering a full circle of 360° is shown in a three-dimensional projection. There are six small sections with a width of $\Delta\phi = 3°$ where either the incident or the

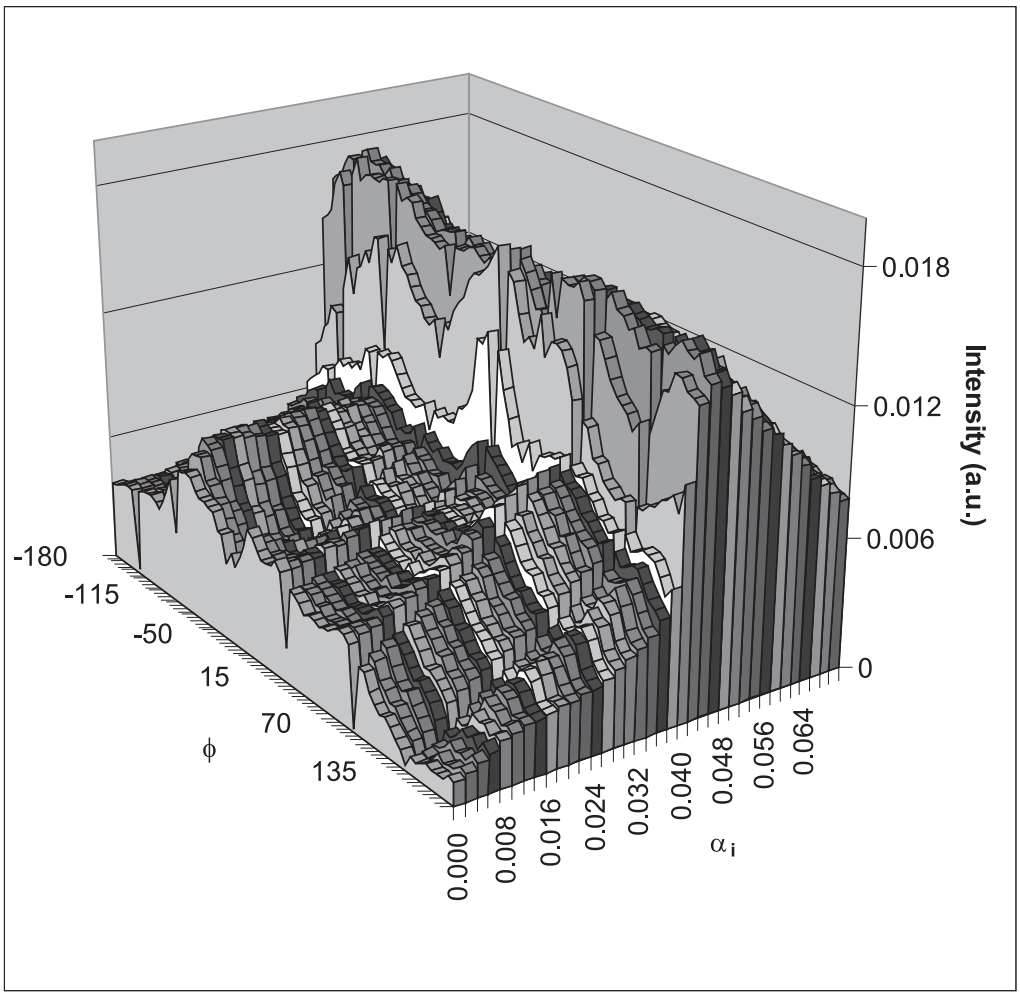

Figure 8.5: *A set of 73 scans of the incidence angle α_i at different azimuthal angles ϕ. In order to demonstrate azimuthal modulations of the in plane structure factor, data points taken at a fixed azimuthal angle are depicted on the same grey scale. The in plane momentum transfer was kept at $q_{||} = 2.3\mathring{A}^{-1}$.*

scattered beam is blocked by supporting steel rods of the chamber.

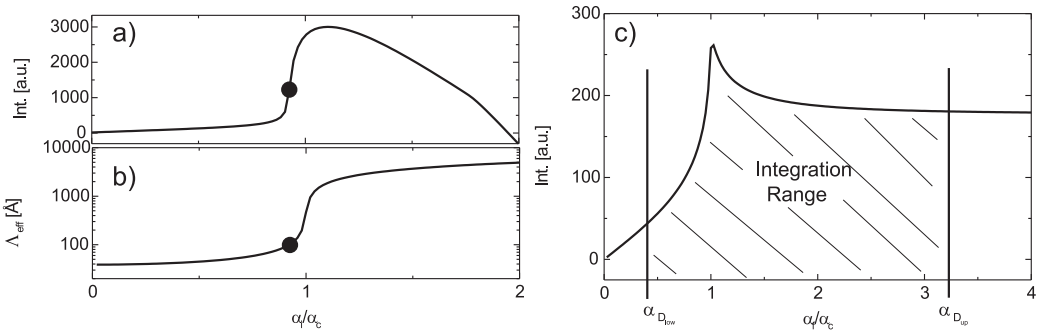

Figure 8.6: *Measuring the structure factor interface sensitive using GID. a) the scattered intensity of a tilt scan. b) the effective scattering depth* Λ_{eff}*. The dots give the best angle for measuring the modulation of the structure factor. Graph c) shows an exit angle profile and a typical range for* α_f*, over which the intensity was integrated by opening the detector slits.*

The incidence angle profile is most sensitive to the interfacial structure at angles well below the critical angle with the disadvantage of a low signal intensity. In our case there is the additional implication of bulk scattering at the edges for small angles as discussed in Sec. 6.1.1. An extraction of data points at a fixed incidence angle α_i and at different azimuthal angles shows the ϕ-dependence of the in plane structure factor at a fixed $S(q_{||})$. Fig. 8.6 illustrates the measuring method to detect the modulation of the structure factor with respect to the azimuthal angle ϕ. Keeping the incidence angle α_i fixed (s. Fig. 8.6.a) and integrating the exit angle α_f over a range $\alpha_{D_{\text{low}}}$ to $\alpha_{D_{\text{up}}}$ (s. Fig. 8.6.c) limits the effective scattering depth Λ_{eff} (s. Fig. 8.6.b) independent of the azimuthal angle ϕ. Due to the experimental constraints the incidence angle and integration range has to be chosen appropriately. The detector angle was set to $\alpha_D = 0.04° = \alpha_i + \alpha_f$. The detector slits were set to an integration range of $\alpha_{D_{\text{low}}} = 0.036°$ to $\alpha_{D_{\text{upper}}} = 0.167°$.

Fig. 8.7 shows a set of four scans at fixed incidence angles α_i at an azimuthal circle of 360°. The silicon crystal orientation is marked by vertical lines that denote the Si$\langle 2\bar{2}0\rangle$ directions determined by an independent measurement. The scan at $\alpha_i = 0.056° > \alpha_c$ (open triangles) shows only bulk signal with an effective scattering depth $\Lambda_{eff} > 300$nm. The scan at $\alpha_i = 0 \ll \alpha_c$ (open squares) with $\Lambda_{eff} = 39$Å is dominated by edge effects of the sample (cp. Fig. 5.3). The two scans at $\alpha_i = 0.036° < \alpha_c$ (black circles) and $\alpha_i = 0.038° < \alpha_c$ (black triangles), respectively, show a modulation of

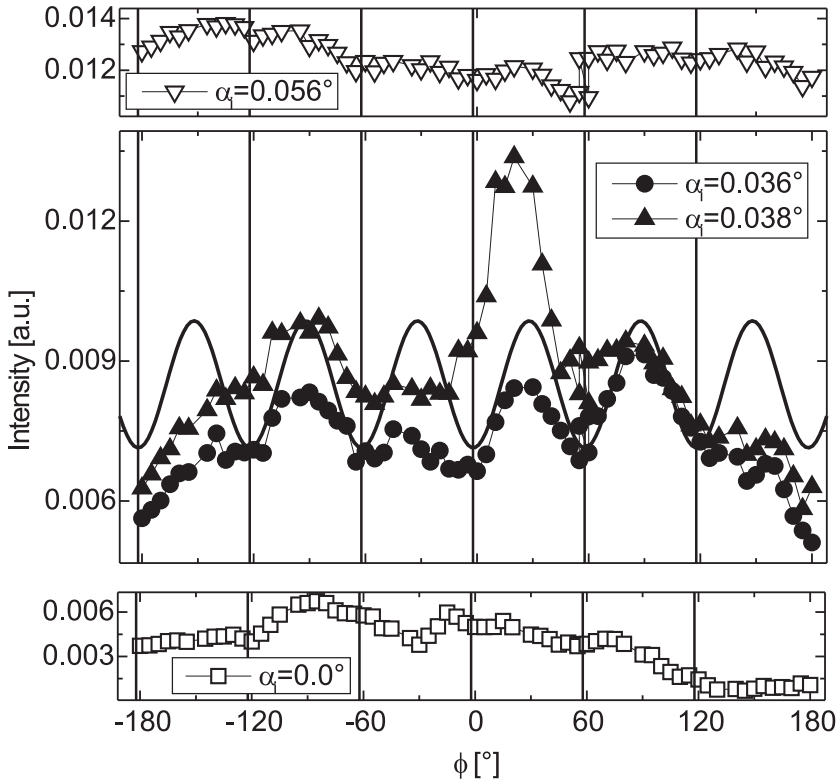

Figure 8.7: *Extraction of points at fixed incidence angles α_i from Fig. 8.5 along the azimuthal angle ϕ. The six positions of the Si$\langle 2\bar{2}0\rangle$ reflections are denoted by vertical lines. A sine-function emphasizes the six-fold modulation of the in plane structure factor. Its phase minima match the Bragg positions of the silicon substrate.*

the liquid structure factor close to the wall. The modulation is connected to the substrate orientation of the Si(111). The minima of the intensity match the $\langle 2\bar{2}0\rangle$-direction of the Si(111). The straight line is a sinusoidal adaptation to the measured data having a six-fold symmetry. The effective scattering depth at $\alpha_i = 0.036°$ and $\alpha_i = 0.038°$ was $\Lambda_{eff} = 80.4$Å and $\Lambda_{eff} = 109$Å, respectively.

8.2 Out of plane structure

To explore the electron density profile perpendicular to the interface, reflectivity measurements were carried out. The optical properties are the same as for the Pb(liq.)-Si(100) interface with $q_c = 0.05$Å^{-1}. Although the crystal orientation itself does not influence the reflectivity, there might be one complication: For a Si(100) surface the first specular Bragg reflection appears at $q_{400} = 4.62$Å^{-1}. For the Si(111) surface the first specular Bragg reflection appears at $q_{111} = 2.0$Å^{-1}. The Bragg reflections are several orders of magnitude more intense than the reflectivity at these q-values. Due to the presence of an interface the Bragg reflections are connected by *truncation rods* perpendicular to the surface (For a detailed explanation see e.g. [Hol99]). If the miscut of the surface is sufficiently small, the truncation rod of a specular Bragg reflection is superimposed to the reflectivity. For a Si(111) surface with a typical roughness of several Ångström, the contribution might be significant at 1Å^{-1}. For a Si(100) surface this is unlikely.

An atomic layering peak is expected at a momentum transfer close to the (111) reflection of crystalline lead ($q_{111} = 2.20$Å^{-1}). Thus, the layering peak would appear as a shoulder or asymmetry on the Si(111) truncation rod. On the other hand, truncation rods can be precisely calculated and it is possible to detect tiny deviations of the ideal surface, allowing to separate it from the reflectivity (see e.g. [Str03]).

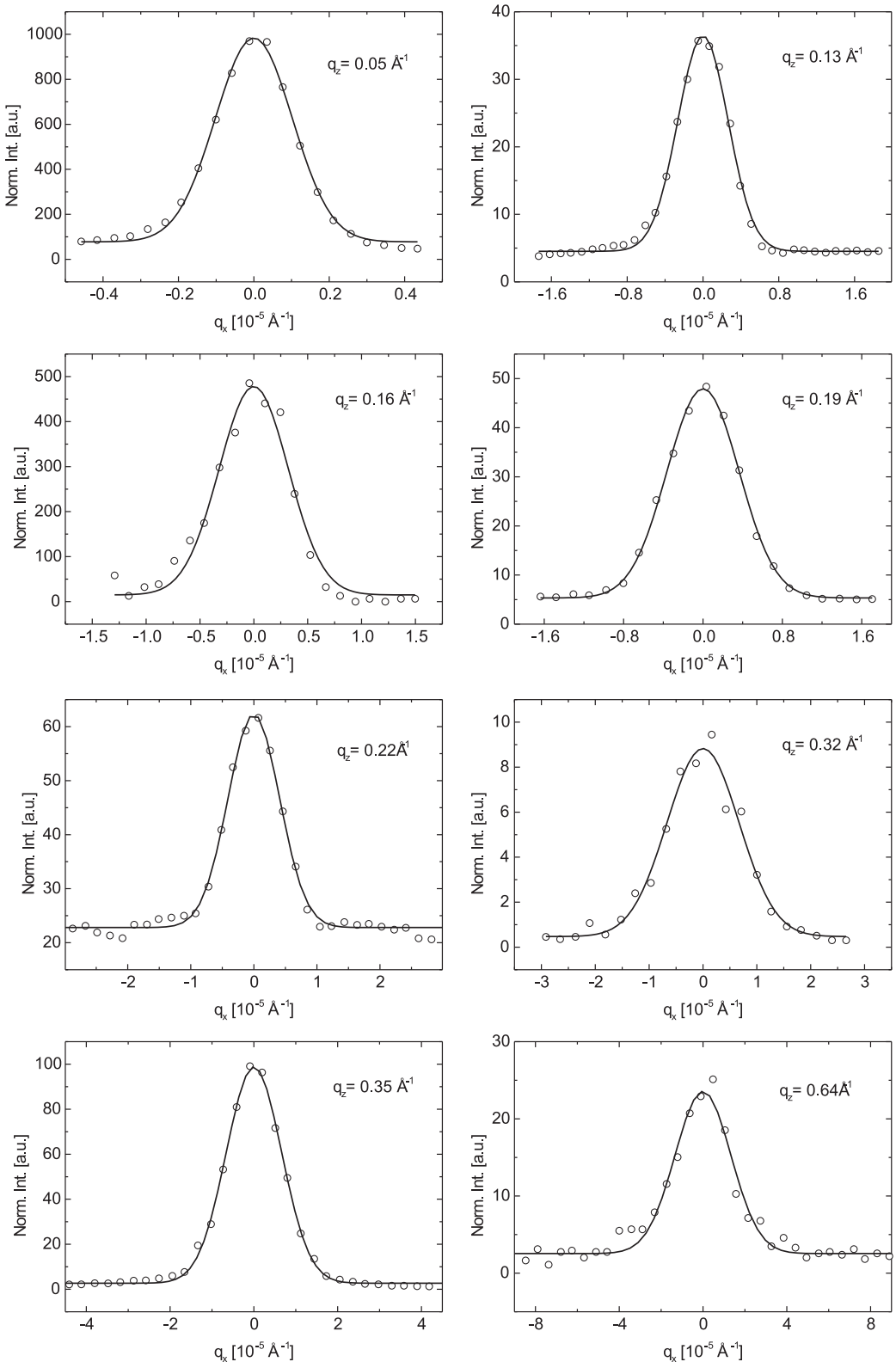

Figure 8.8: *Rocking scans of the specular rod at different momentum transfers q_z.*

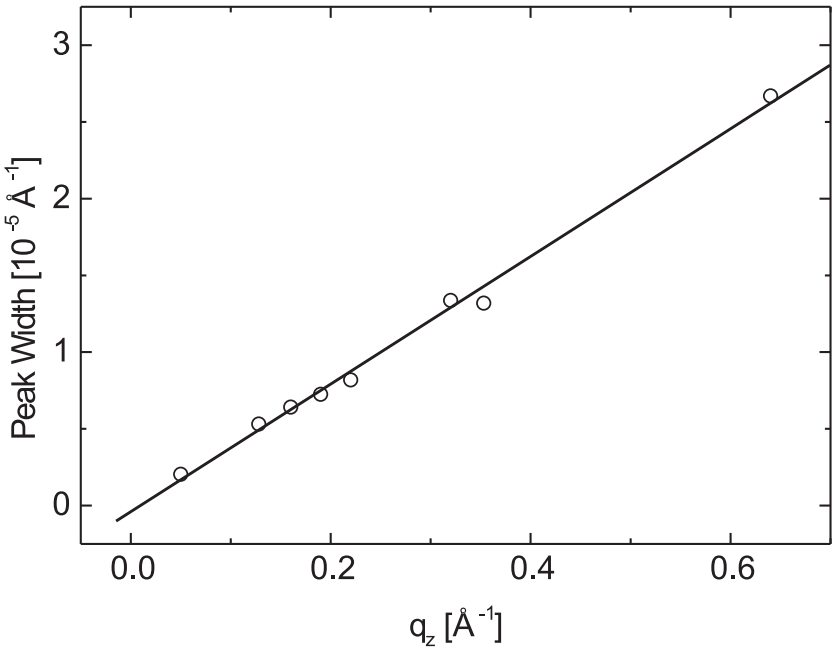

Figure 8.9: *Linear increase of the peak width with respect to q_z. Data points denote the width of the peaks presented in Fig. 8.8.*

Experimentally, the reflectivity can be separated from the truncation rod by a slight miscut of the surface, which was always present at silicon surfaces in this work. The Si surface exhibits still large Si(111) terraces, but the crystal truncation rod is slightly tilted in reciprocal space and does not overlap with the reflectivity curve.

Fig. 8.8 shows a set of eight rocking scans perpendicular to the specular rod at different momentum transfers q_z. The x-ray energy was $E = 72.33$keV ($\lambda = 0.171$Å). The width of the specular rod is resolution limited, which can be seen from the linear increase of the FWHM of the Gaussian fits with respect to q_x shown in Fig. 8.9. There was no diffuse scattering from roughness correlations detectable, emphasizing the high quality of the interface. Note the improved quality in comparison with the Pb(liq.)-Si(100) interface (s. Sec. 7.1) owing improvements in the Si surface preparation and the experimental setup (CRL).

Fig. 8.10 shows the reflectivity of the Pb(liq.)-Si(111) interface. The specular rod could be measured up to $q_z = 0.77\text{Å}^{-1}$. The reflectivity again deviates strongly from the Fresnel reflectivity and resembles the reflectivity of the Pb(liq.)-Si(100) interface. The critical momentum transfer q_c is identical for both systems as expected. Both reflectivities could be measured over eight

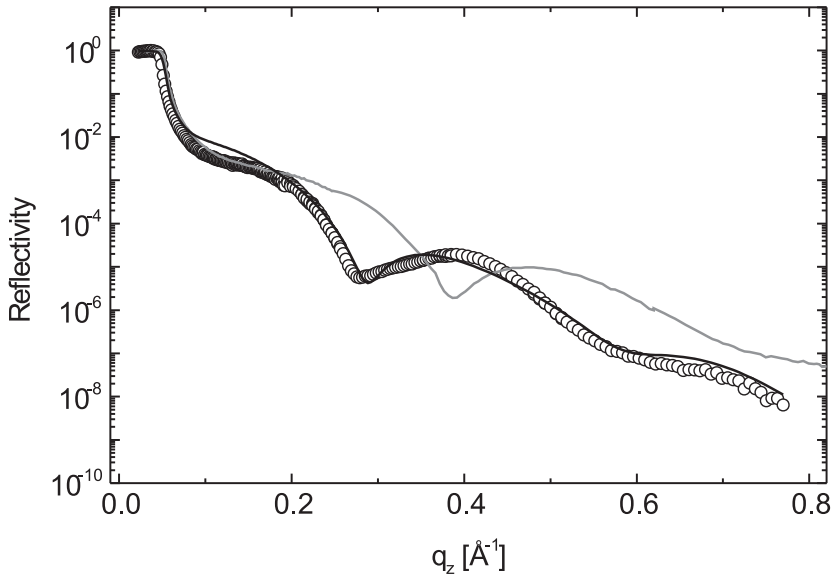

Figure 8.10: *Reflectivity of the Pb(liq.)-Si(111) interface (circles) and fit to the data (black line). For comparison the measured reflectivity from Pb(liq.)-Si(100) data is also shown (grey line).*

orders of magnitude. For the Si(100) surface this corresponds to $q_z \lesssim 0.9\text{Å}^{-1}$ and for the Si(111) surface to $q_z \lesssim 0.77\text{Å}^{-1}$. We observe the same number of oscillations in both cases. The electron density modulation appears on a larger length scale at the Si(111) surface, since the dip in the reflectivity curve appears at a smaller q_z-value ($q_{\text{Dip}} = 0.28\text{Å}^{-1}$ for Si(111) compared to $q_{\text{Dip}} = 0.39\text{Å}^{-1}$ for Si(100)).

Fig. 8.11 shows the electron density profile obtained from a fit to the measured reflectivity. As for the Pb(liq.)-Si(100) interface the fit can be improved to match the measured data perfectly at the cost of several additional layers and many more free parameters. The increased layer thickness deduced directly from the reflectivity curve can be seen in the electron density profile. The generic features of the electron density profiles are similar to the other interfaces with only quantitative differences. The profile at the Pb(liq.)-Si(111) interface appears to be stretched in comparison with the profile at the Pb(liq.)-Si(100) interface. The density deviations from the bulk density are smaller and the interface between the layers is less sharp. Tab. 8.1 summarizes the parameters for both Pb-Si interfaces.

We did not find excess electron density at the Pb(liq.)-Si(111) interface. The exact calculation gives even a slight depletion of -0.8%, which is smaller

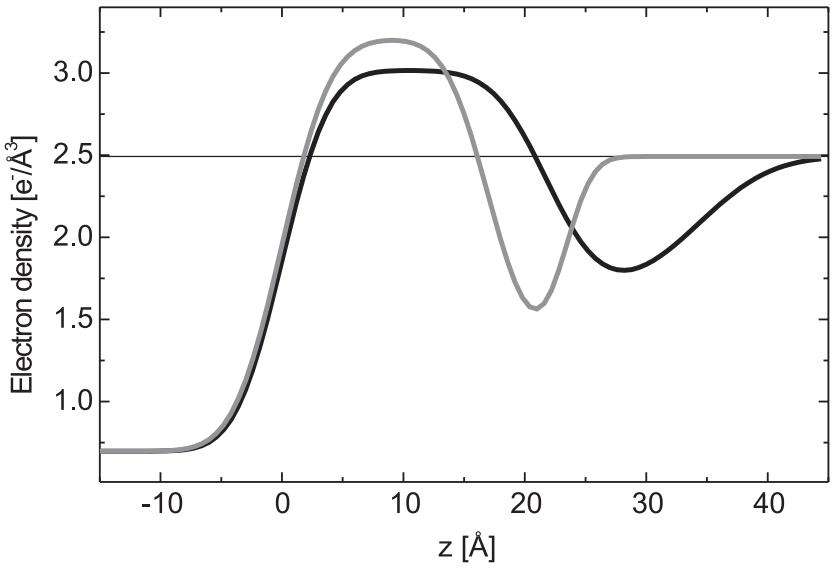

Figure 8.11: *Electron density profile of the Pb(liq.)-Si(111) intensity deduced from the reflectivity using a two layer model with Gaussian roughness at all interfaces (black line). The grey line is the fit to the Pb(liq.)-Si(100) reflectivity.*

E.-Density-	Profile	Pb(liq.)-Si(111)	Pb(liq.)-Si(100)
layer 1	roughness	3.0Å	3.2Å
	thickness	21.8Å	17.0Å
	density	3.02 $Å^{-3}$ (21.3%)	3.21 $Å^{-3}$ (28.8%)
layer 2	roughness	3.5Å	2.8Å
	thickness	12.4Å	6Å
	density	1.80 $Å^{-3}$ (-27.7%)	1.57 $Å^{-3}$ (-37%)
bulk	roughness	4.8Å	1.8Å
	density	2.49$Å^{-3}$	2.49$Å^{-3}$
	excess density	-0.8%	3%

Table 8.1: *Parameters of the density profiles of liquid lead in contact with two differently oriented Si surfaces. The excess density denotes the integrated electron density normalized to the bulk electron density.*

than the error of the calculation, dominated by the uncertainty of the layer thickness.

8.3 Discussion

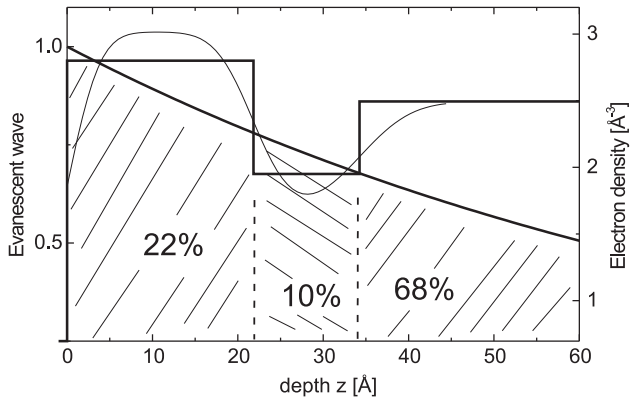

Figure 8.12: *Illustration of the fraction of the scattering contributions from each layer and its relation to the box model of the interface. The effective scattering depth was* $\Lambda_{\text{eff}} = 88\text{Å}$.

The effective scattering depth for the in plane measurements was $\Lambda_{eff} = 88$Å. The recorded intensity is a sum of scattering contributions, which are exponentially decaying perpendicular to the interface. Fig. 8.12 shows the electron density profile approximated by rectangular boxes and the smooth electron density profile. The fractional contribution to the scattered signal corresponds to the hatched area below the exponential decay. 22% of the measured structure factor emanates from the layer with increased electron density close to the interface.

The expected structure factor $\tilde{S}(q)$ is calculated as described in Sec. 6.3 and shown in Fig. 8.13 (solid line). The measured structure factor is in good agreement with the calculation. This demonstrates again that the liquid structure factor is not sensitive to the structural changes in the interfacial liquid layer. In order to detect such changes, the scattering depth must be smaller than the thickness of the layer with increased density ($\Lambda_{eff} \leq 20$Å).

In Plane Modulation of Liquid Lead at Si(111)

The first peak of the structure factor shows a modulation with respect to the azimuthal angle. The relative intensity modulation $\Delta I_{\text{mod}}/I$ is estimated

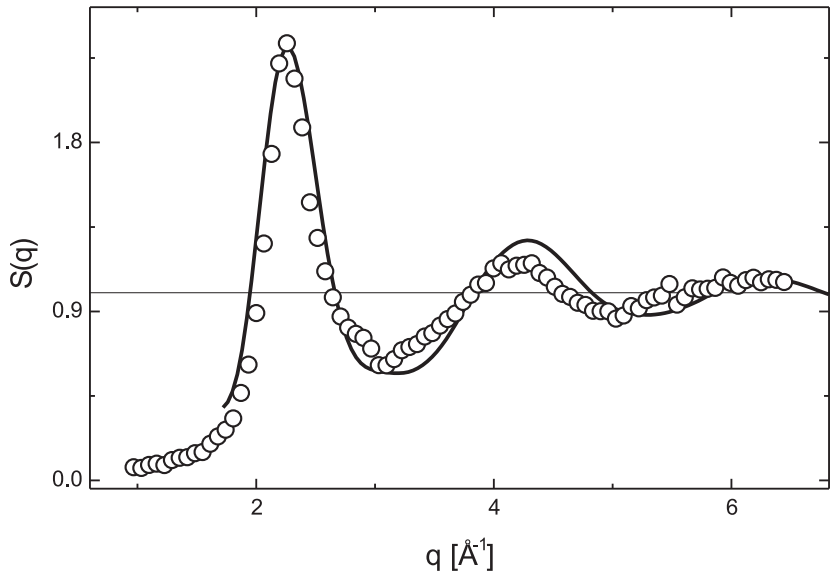

Figure 8.13: *Comparison of the measured structure factor (open circles) with a calculated structure factor (solid line) constructed from a sum of compressed and stretched pair distribution functions $g(r)$.*

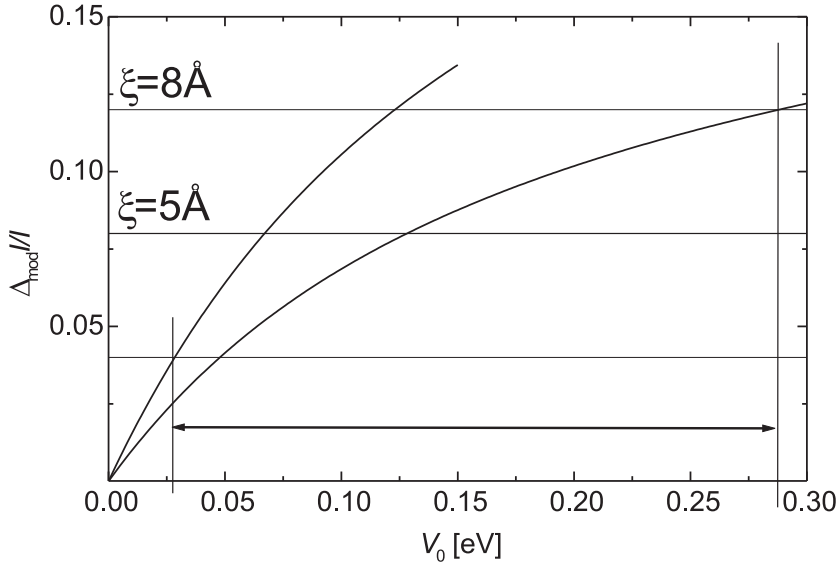

Figure 8.14: *Estimation of the Pb-Si interface potential V_0 from the amplitude of the azimuthal relative intensity modulation $\Delta I_{\mathrm{mod}}/I$ assuming a bulk like correlation length ξ in the range of 5Å-8Å.*

to $8\% \pm 4\%$ based on the sinusoidal model (cp. Fig. 8.7). This neglects non-periodic, systematic deviations.

Following [Rei00], the intensity modulation is related to the alignment potential of the interface $V_0^{\mathrm{Pb-Si}}$, which influences a certain fraction $n_{\mathrm{align}}(z)$ of the liquid building blocks. The bulk correlation length for liquid lead is $\xi_{\mathrm{Pb}} = 5 - 8\text{Å}$. We assume an exponential decay for the depth-dependent alignment potential

$$V^{\mathrm{Pb-Si}}(z) = V_0^{\mathrm{Pb-Si}} e^{-\frac{z}{\xi_{\mathrm{Pb}}}} \ . \tag{8.1}$$

The fraction of aligned structural motifs on the liquid side of the interface liquid is then given as

$$n_{\mathrm{align}}(z) = 1 - e^{-\frac{-V^{\mathrm{Pb-Si}}(z)}{k_B T}} \ . \tag{8.2}$$

The relative intensity modulation is a function of the effective scattering depth Λ_{eff} and the distribution of aligned structural motifs

$$\frac{\Delta I_{\mathrm{mod}}}{I} = \frac{1}{\Lambda_{eff}} \int_0^\infty n_{\mathrm{align}}(z) e^{-\frac{z}{\Lambda_{eff}}} \mathrm{d}z \ . \tag{8.3}$$

From Eq. 8.3 the value of the interaction potential $V_0^{\mathrm{Pb-Si}}$ can be estimated numerically, which is shown in Fig. 8.14. The result is $V_0^{\mathrm{Pb-Si}} = 30 - 280\text{meV}$ for the orientational part of the interface potential. The uncertainty arises from the assumption of the interface-related value of ξ_{Pb}, which is 25% and the uncertainty of the modulation $\Delta I_{\mathrm{mod}}/I$, which is 50%. The observed interface energy is in the range of the thermal energy $k_B T_M = 52\text{meV}$ at the melting temperature of lead.

The origin of the modulation can be visualized by a structural model of the liquid lead parallel to the Si(111) wall. The unreconstructed Si(111) surface exhibits a six-fold symmetry. At low temperatures it shows a 7×7 reconstruction that is lifted at temperatures above 300°C to Si(111)1×1 [Wei92]. Lead melts above 330°C and all measurements were done above this temperature, thus, the Si(111) was unreconstructed.

There are three different high symmetry positions for a single atom on an unreconstructed Si(111) surface. First, the *on top site* (T_4), which refers to the position on top of a second layer Si atom. Second, the *hollow site* (H_3) that has no atom directly below in the lower part of the Si(111) surface double layer. Third, the position on top of the topmost Si atom. It is generally accepted that adatoms sit on the T_4-site [Har77, LL88, Pat89]. Thus, the adatom replaces three dangling bonds by one and three badly bent bonds in the case of four valences of the adatom [Rob88].

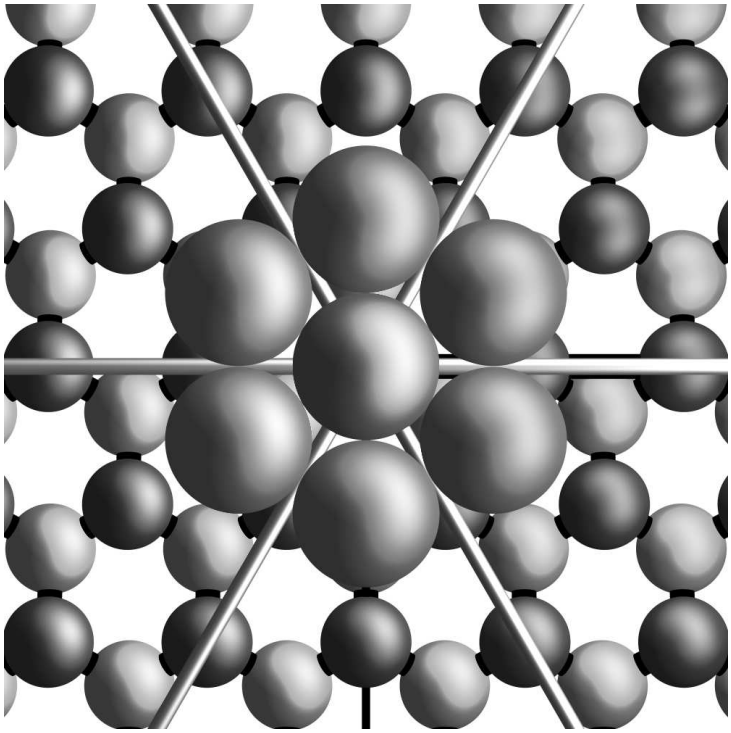

Figure 8.15: *Model for bulk Pb on Si(111) showing six fold symmetry. Large spheres are Pb atoms, small spheres are Si atoms. Si<220> directions are marked as grey lines.*

Previous experiments suggest the formation of a 2D-liquid in the case of Ge(111)1 × 1-Pb [Wei92, Gre90] for a coverage above 1ML of lead and a temperature above 300°C. Our results suggest, that for a complete coverage of the surface with liquid lead close packed rings of six Pb atoms are grouped around a top layer Si atom (s. Fig. 8.15). On the very top position there is a center Pb atom. This structure is not commensurate with the Si(111) surface, it can form only *locally*. The orientation of the six-atom building block with respect to the orientation of the Si(111) substrate corresponds to the Si(111)$(\sqrt{3}\times\sqrt{3})R30°$-Pb, whereas the Si(111)$(7\times7)$-Pb is rotated by 30° (s. Fig. 2.15) [Wei92]. This is in good agreement with the temperature dependence of these two low-coverage structures. The Si(111)$(\sqrt{3}\times\sqrt{3})R30°$-Pb structure exhibits a larger area density than the Si(111)(7×7)-Pb structure, which is, of course, preferred in the case of a bulk liquid on top of the silicon surface.

For the Pb(liq.)-Si(100) interface an interaction potential between silicon and lead was estimated to $V_0^{Pb-Si} = 50 - 90$meV (s. Sec. 2.5.3 and [Rei00]),

while for the system Pb(liq.)-Si(111) we find $V_0^{Pb-Si} = 30-280$meV including the uncertainty of the modulation.

The Electron Density Profile at the Pb(liq.)-Si(111) Interface

At the beginning of the chapter we have discussed the generic features and the differences between the Pb(liq.)-Si(100) (s. Chap. 7) and the Pb(liq.)-Si(111) interface: The electronic bulk properties are identical, for both experiments a n-type (phosphorus doped) semiconductor was used. The surface properties depend on the crystal orientation. The clean (100)- and (111)-surface of Si do reconstruct and the reconstruction is lifted with the adsorption of metal adatoms. The difference is that each Si-atom has two dangling bonds in a (100)-surface and only one in a (111)-surface. The density of atoms in the surface layer is different for the two crystal orientations, resulting in four dangling bonds per (1×1) unit cell ($a_{\mathrm{Si}}^2 = (5.4309\ \text{Å})^2$) for Si(100) and in 2.309 dangling bonds per (1×1) unit cell for the Si(111) surface. This leads to a substantial difference of the possible charge located at the surface and the possible pressure perpendicular to the surface (s. Sec. 6.3), summarized in Tab. 8.2.

Surface	dangling bonds	pressure
Si(100)	$4/a_{\mathrm{Si}}^2 = 0.136\text{Å}^{-2}$	267GPa
Si(111)	$2.309/a_{\mathrm{Si}}^2 = 0.078\text{Å}^{-2}$	88.2GPa

Table 8.2: *Maximum possible Coulomb force from charged Si surfaces in the (100)- and (111)-orientations.*

If we assume, that the maximum achievable Coulomb pressure is related to the measured maximum density increase, this should be reflected in the experimental data. The measured maximum electron density increase for the Pb(liq.)-Si(111) system is 3.01Å^{-3}, this corresponds to a density ratio of $\rho/\rho_0 = 3.01/2.49 = 1.21$. The resulting pressure is $p = 16.7$GPa (cp. Eq. 6.6). In order to compare this with the Pb(liq.)-Si(100) results, the data is collected in Tab. 8.3.

The decreased density of dangling bonds at the Si(111) surface compared to the Si(100) surface is mirrored in the decreased maximum possible Coulomb pressure. The calculation shows that the smaller increase of electron density in the first interfacial lead layer at the Pb(liq.)-Si(111) interface may indeed point to a substantially decreased pressure inside the layer. The maximum possible pressure is reduced to about one third, whereas the measurement yields a reduction of about one third of the calculated pressure of

system	ρ/ρ_0	p
Pb(liq.)-Si(100)	1.29	24GPa
Pb(liq.)-Si(111)	1.21	16.7GPa

Table 8.3: *Specific density enhancement and the pressure p calculated from the fitted maximum electron density increase ρ/ρ_0.*

the lead layer in the Pb(liq.)-Si(111) system compared to the lead layer in the Pb(liq.)-Si(100) system. For a calculation of the number of excess electrons, the electron density profile is approximated by two layers with no adjacent roughness. The number of excess electrons in each layer is shown in Tab. 8.4 for the Pb(liq.)-Si(111) interface.

layer i	l_i	ρ_i	ec
1	21.8Å	2.80 Å^{-3}	5.1
2	12.4Å	1.95 Å^{-3}	-5.9

Table 8.4: *Number of excess electrons per layer at the Pb(liq.)-Si(111)-interface.*

The number of excess electrons is $5.1-5.9=-0.8$. The uncertainty of the value is 28% (s. Sec. 6.3). The number of transferred electrons is then given as $(-0.8\pm0.2)/a_{\mathrm{Si}}^2$. The negative value implies that effectively electrons are transferred from the silicon surface to the liquid metal. The origin of this result is the broad second layer that gives a large contribution to the number of excess electrons and effectively accepts more electrons that are transferred by the first layer. The result is consistent with the result obtained at the Pb(liq.)-Si(100) interface, which is shown in Tab. 8.5.

system	dangling bonds	calculated transferred electrons	difference (deficiency)
Pb(liq.)-Si(100)	$4/a_{\mathrm{Si}}^2$	$1.3\pm0.3/a_{\mathrm{Si}}^2$	$-2.7/a_{\mathrm{Si}}^2$
Pb(liq.)-Si(111)	$2.309/a_{\mathrm{Si}}^2$	$-0.8\pm0.2/a_{\mathrm{Si}}^2$	$-3.1/a_{\mathrm{Si}}^2$

Table 8.5: *Comparison of the number of excess electrons to the number of dangling bonds per surface area.*

In both systems the number of excess electrons to saturate the dangling bonds of the silicon surface is equally deficient within the uncertainty of

the calculation. The increased length scale of the density variation and the decreased absolute value of the density deviation from the bulk value supports the assumption that the pressure induced by Coulomb forces due to the charge transfer, plays an important role in the density profile of the liquid metal. The transferred charge is smaller in the case of the Si(111) surface, because the number of dangling bonds per surface area is decreased. Thus, the Coulomb pressure is smaller and the liquid is less compressed, which leads to an increased length, over which the effects of the dangling bonds are screened. This picture is consistend with our results for the Pb-Si(111) interface and the Pb-Si(100) interface.

It is apparent that the behavior of the liquid metal depends on the electronic surface properties of the solid wall.

Chapter 9

The System Pb(bulk)-PbO-Si(111)

So far we have considered interfaces that show no chemical interactions. In the following we discuss a buried interface where the interface itself changes its structure with time. For this we prepared an interface with an intervening lead-oxide layer between the liquid metal (Pb) and the solid crystal Si(111). The system is more complex, since it involves more than two elements. Most important, the Pb-O-Si system is chemically not inert in contrast to the Pb-Si system.

This interface may serve as a model for internal corrosion processes, since many processes of corrosion appear deeply buried in bulk material at interfaces. Up to now it was very difficult to investigate these interfaces in situ. Our high energy diffraction method allows us not only to investigate the structure of buried oxide layers on atomic length scales, but also to observe structural changes time-resolved.

9.1 The Chemical System Pb-O-Si

Lead and oxygen form several compounds where Pb_1O_1 has the lowest oxygen content and is the only stable oxide above 1149K. PbO melts at 1149K and the density of PbO is 17.5% smaller than the density of pure liquid lead. Other Pb_xO_y compounds decompose at lower temperatures. The solubility of molecular oxygen is extremely small ($\approx 10^{-4}$ at.-%) in solid lead up to the melting temperature of 600K. In liquid lead the solubility increases slowly with temperature. For these reasons one expects that at temperatures up to 600K the only compound formed in an oxygen atmosphere will be a layer of PbO on top of liquid lead.

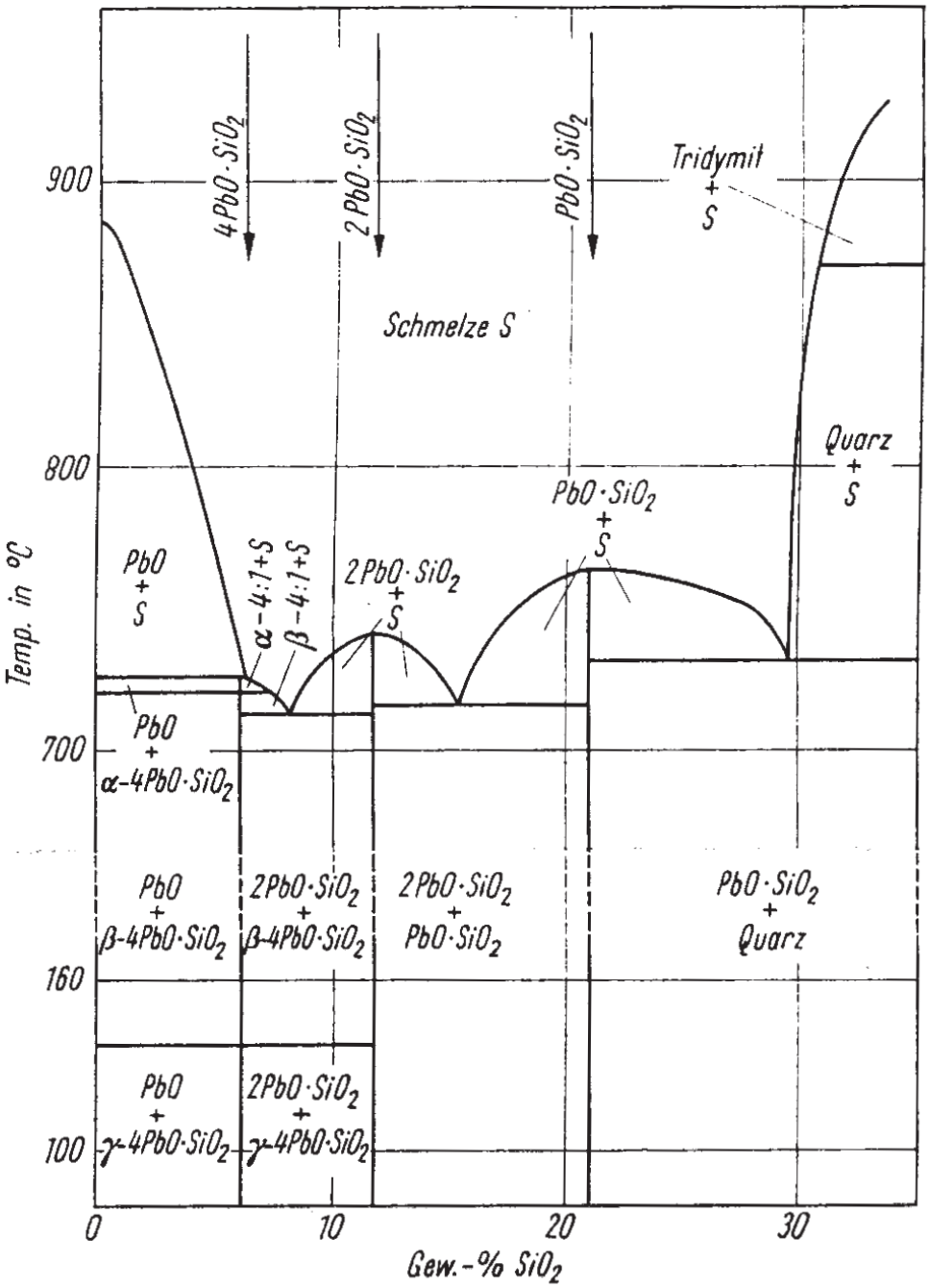

Figure 9.1: *PbO-SiO phase diagram. Taken from [Bit70].*

Si forms only one chemical compound with oxygen, which is silicon dioxide. The solubility of Si in SiO_2 is below 2×10^{-7} at.-% at 600K. Its melting temperature is higher than that of Si ($T_m(SiO_2) = 2000$K). The Pb-O and Si-O phase diagrams are shown in appendix B.

PbO and SiO_2 form the stochiometric compounds Pb_2SiO_4 and $PbSiO_3$ [Bit70]. For other concentrations a number of well defined mixtures exist between quartz and $PbO{\cdot}SiO_2$. However, these compounds can only be formed from the melts of SiO_2 and PbO. At temperatures up to 1000K a phase separation is expected with no intermixing of the existing solid phases of SiO_2 and PbO. This is summarized in the phase diagram of PbO and SiO_2 shown in Fig. 9.1.

The energy gain for oxidising a single Pb atom to Pb^{2+} is 0.54eV, for oxidising a Si atom to Si^{4+} it is as large as 1.69eV. Reducing Pb and oxidising Si results in an overall energy gain of

$$2\mathrm{PbO} + \mathrm{Si} \longrightarrow 2\mathrm{Pb} + \mathrm{SiO_2} \quad +0.61\mathrm{eV}\ . \tag{9.1}$$

The preparation of the interface was similar to the clean Pb-Si interfaces. A few minutes in air after the etching process are sufficient to coat the lead with a thin PbO-layer. Melting the lead under UHV condition ($p < 5 \cdot 10^{-9}$ mbar), the oxide is visible as a floating layer on top of the liquid lead. In the previously reported experiments the oxide was removed by subsequent steps of sputtering with Ar^+ ions (4keV, 50μA), solidifying, and melting. In this case however, the oxide layer was not completely removed, but thinned and homogenized. The silicon crystal was prepared in the same way as before (s. Sec. 4.5). The Si crystal and the lead in the trough were heated to 600K, before the crystal was brought in contact with the molten lead covered by the PbO-layer. Immediately after contact the temperature was reduced to room temperature for the transport to the synchrotron.

9.2 In plane structure

All the measurements shown in this section were performed above 600K, where bulk lead is liquid. The x-ray wavelength was $\lambda = 0.174$Å ($E = 71.3$keV). The PbO-layer was expected to be amorphous or at least polycrystalline with no preferential orientation of the individual grains. Therefore, one does not expect an azimuthal modulation of the PbO structure factor with respect to the interface normal. Furthermore, no fixed orientational correlation between the silicon crystal and the PbO-layer is expected. Thus,

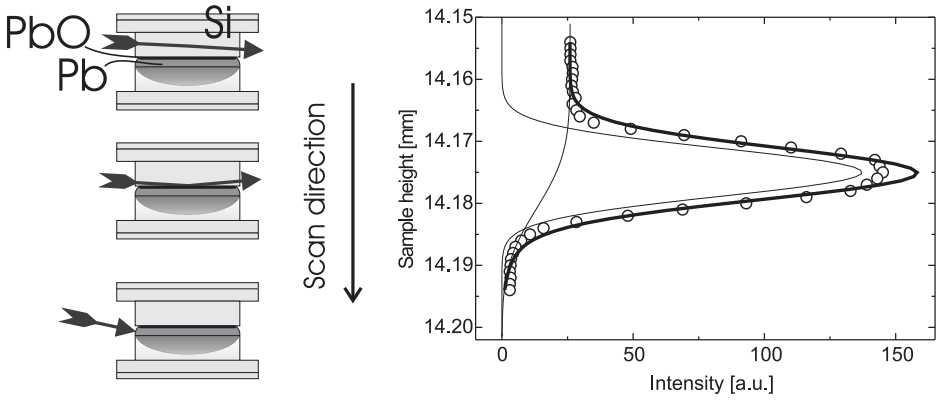

Figure 9.2: *Scan perpendicular to the interface at an in plane momentum transfer* $q_{||} = 2.3\mathring{A}^{-1}$ *(open circles). The solid line is a fit to the data using a Gaussian and an error function, which are displayed individually (thin solid line).*

structural measurements parallel to the silicon surface where only performed to confirm the presence of the intervening PbO-layer.

The exact position of the interface in vertical direction is found via a vertical scan of the sample (z-scan). In Fig. 9.2 the result is shown with the fit using the model that was introduced in Chap. 6 (for details of this scan type and the model see Sec. 6.1). The interface can be identified at the peak position. The width of the error function is 10.2μm and the width of the Gaussian is 5.5μm. The width of the peak is a convolution of the projected interface and the beam profile. The incidence angle was kept at $\alpha_i = 0.042°$, while the exit angle profile was integrated from $\alpha_f = 0°$ to $\alpha_f = 0.043°$. The oxide layer itself cannot be identified in this scan.

Scans of the exit angle α_f using the incidence angle α_i as a parameter reveal the presence of two separate interfaces. A set of four scans is shown in Fig. 9.3. The in plane momentum transfer for all four scans was set to $q_{||} = 2.3\mathring{A}^{-1}$, corresponding to the maximum of the structure factor of liquid lead. At an incidence angle $\alpha_i = -0.02°$ the measured intensity increases linearly with the exit angle α_f. Its origin is bulk scattering from the edge of the sample. At $\alpha_i = 0.026°$ the α_f-profile displays the typical shape of a transmission function with a critical angle of $\alpha_c = 0.022°$. This value corresponds to the critical angle of the interfacial PbO-layer. At $\alpha_i = 0.038° \approx \alpha_c(\mathrm{Pb})$ the measured intensity displays the presence of a second interface to the liquid lead as seen at the pure Pb(liq.)-Si(111) interface (cp. Fig. 8.2). At $\alpha_i = 0.06° = 1.5 \cdot \alpha_c$ the peak of the transmission function has vanished. The α_f-profile shows only a kink at $\alpha_f = \alpha_c$. For larger exit angles the intensity

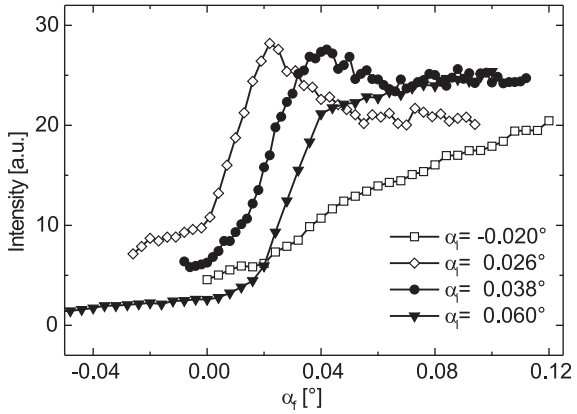

Figure 9.3: *Scan of the exit angle α_f at $q_{||} = 2.3\mathring{A}^{-1}$. The incidence angle α_i was set to different values.*

increases slowly, indicating the signature of a bulk signal.

Opening the slits at the detector to integrate the signal on a wider range of scattering angles increases the detected intensity from the interface. Fig. 9.4 shows a scan of the incidence angle α_i with the detector angle set to $\alpha_D = \alpha_i + \alpha_f = 0.035°$. The slits were set in such a way that the detector integrated from $\alpha_{D_{\text{low}}} = 0.035°$ to $\alpha_{D_{\text{upper}}} = 0.15°$. The in plane momentum transfer was kept at $q_{||} = 2.3\text{Å}^{-1}$, as before. In contrast to the clean Pb(liq.)-Si(111) interface (cp. Fig. 8.3), the scan features a second (smaller) peak below the critical angle α_c at $\alpha_i = 0.026°$. The broad peak at negative incidence angles α_i originates from the previously discussed bulk scattering from the edge. The second peak at $\alpha_i = 0.026°$ is attributed to the PbO-layer, which exhibits a lower electron density than the liquid lead, and consequently a smaller critical angle.

The structure factor parallel to the interface was measured as a function of the scattering depth. This reveals the contributions to the structure factor at a certain depth. In Fig. 9.5 two prominent measurements are shown. The incidence angle of the measurements were $\alpha_i = 0.026°$ and $\alpha_i = 0.04°$, respectively. This corresponds to an effective scattering depth of $\Lambda_{eff} = (40 \pm 5)\text{Å}$ and $\Lambda_{eff} = 360\text{Å}$. The measurement at small scattering depth can be completely attributed to a signal arising from the oxide layer. A first peak in the structure factor is visible, which matches the peak of the bulk structure factor of liquid lead. The additional shoulder to the high q-side of the first peak points to the presence of the oxide. The structure factor is dominated by the lead-lead correlations, since the oxygen ions cannot be detected from the two different materials due to their weak scattering cross section. The

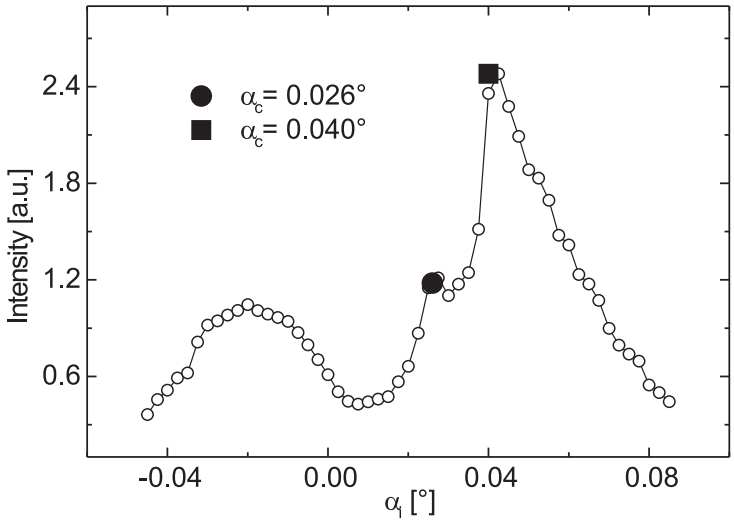

Figure 9.4: *Incidence angle scan at in plane momentum transfer of* $q_{||} = 2.3\mathring{A}^{-1}$. *Two positions are marked that correspond to two different critical angles.*

second measurement at large scattering depth exhibits the features of pure liquid lead. The first and the second peak of the structure factor can be identified. Thus, the inplane measurements of the structure factor confirm the presence of a second layer at the interface.

9.3 Out of plane structure

The Pb(liq./sol.)-PbO-Si(111) system was characterized by several reflectivity measurements. The first measurement was carried out while the bulk lead was solid at ambient temperature. After melting the bulk lead, 20h later, a second measurement was performed. The last measurement was recorded after 140 hours. The reflectivity curves are shown in Fig. 9.6. The symbols denote the measured data points and the solid lines the corresponding fits. The specular rod exhibits Gaussian line shape at all times and at all momentum transfers q_z. Scans at different momentum transfers q_z and at different conditions are shown in Figs. 9.8 and 9.9. The FWHM was resolution limited and it increased linearlly with respect to q_z (s. Fig. 9.10).

The thick oxide layer is immediately identified by the existence of the pronounced Kiessig fringes in the reflectivity curves. From their width ($\Delta q_{\text{Kiessig}} \approx 0.024\text{Å}^{-1}$) the approximate thickness of the layer can be determined to

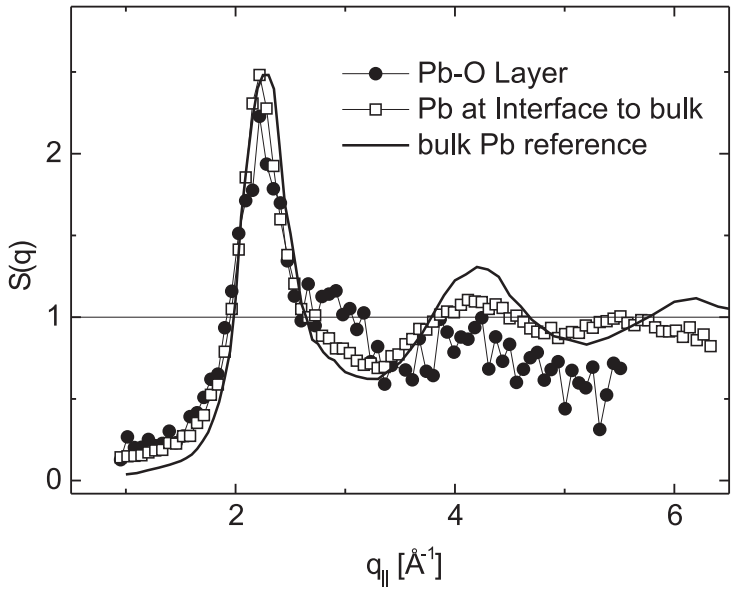

Figure 9.5: *Structure parallel to the Pb(liq.)-PbO-Si(111) interface measured at two different incidence angles α_i (the positions are marked in Fig. 9.4). The solid line is the bulk reference [Was80].*

$2\pi/0.024\text{Å}^{-1} \approx 260\text{Å}$. The intervening layer is of lower electron density. This produces a second critical angle in the reflectivity at $q_z \approx 0.03\text{Å}^{-1}$, which is smaller than the value for the Pb(liq./sol.)-Si(111) interface ($q_z = 0.05\text{Å}^{-1}$). The three reflectivity curves deviate from each other and correspond to different electron density profiles.

A two layer model is sufficient to fit the measured reflectivities. The weighted χ^2 are optimized and all features of the reflectivity curves are reproduced in the fit. The corresponding electron density profiles are shown in Fig. 9.7. The fits confirm the presence of the oxide layer with a thickness ranging from 257.8Å to 268.3Å. The interface between the PbO-layer and the bulk lead is rather inhomogeneous, requiring an additional layer to mimic the gradient between the two phases. The density of the PbO-layer is small compared to the density of bulk lead oxide. PbO has a bulk electron density of 1.94Å^{-3}. In our fits we find 1.16Å^{-3} as the largest density for the layer, which corresponds to 60% of the bulk density. The amorphous layer must, therefore, be very loosely packed. The details of the fits are summarized in Tab. 9.1.

The most pronounced change of the electron density profile is found upon increasing the temperature and melting the bulk lead, which increases the

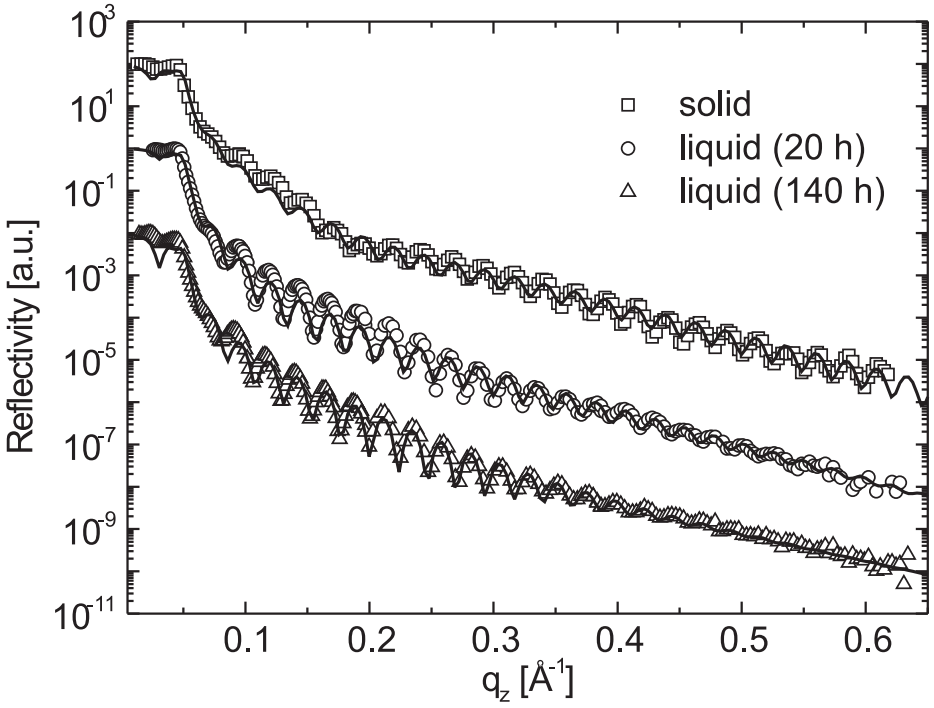

Figure 9.6: *Reflectivity of a Pb(liq./sol.)-PbO-Si(111) interface and its evolution with time. Fits of the reflectivities are the solid lines, respectively.*

thermal energy by $\Delta E = k_B(T_{m(\mathrm{Pb})} - T_{RT}) = k_B(600\mathrm{K} - 290\mathrm{K}) = 27\mathrm{meV}$ per atom.

The oxide layer is well defined at the interface to the silicon. At the interface to the bulk lead it is more diffuse. The density of the PbO-layer increases upon melting the bulk lead. After melting the process slows down and progresses in the course of several days. Upon melting the bulk lead the roughness at the interface to the silicon increases by 88% and decreases slowly to the starting value, when the lead was solid. In the final stage we find only a small increase of the roughness (4%). The interface between the PbO-layer and the lead exhibits an initial width of 18.6Å. The width increases first by 36.6% and then by another 67%, which adds up to 16% of the total layer thickness. The thickness of the PbO-layer increases by 2.0% and after 140h by 4.1%. The electron density of the PbO-layer increases by 20.2% upon melting. After 140h it increases by another 2.7%.

The density increase of the PbO-layer upon melting is the most remarkable effect after increasing the temperature. The additional effects on the

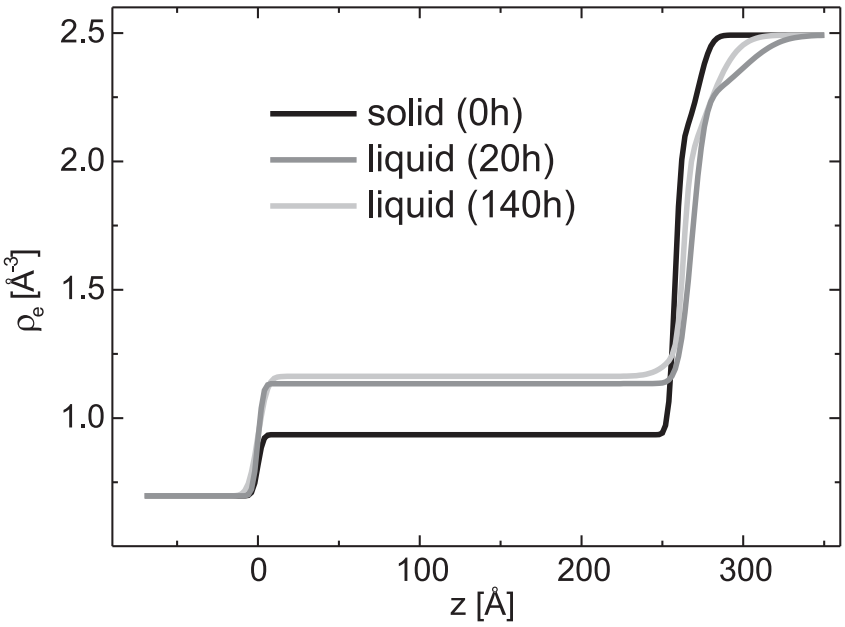

Figure 9.7: *Electron density profiles to the fits shown in Fig. 9.6. The parameter solid/liquid denote the state of the bulk lead. $z = 0$ marks the interface between silicon and the lead-oxide.*

interfacial width at both sides of the PbO-layer as well as the small increase in thickness can be regarded as secondary effects. In order to change the density of the PbO-layer by 20% interdiffusion is required.

		solid (0h)	liquid (20h)	liquid (140h)
PbO-layer	thickness	257.8Å	263.0Å	268.3Å
	density	0.94Å^{-3}	1.13Å^{-3}	1.16Å^{-3}
	roughness PbO-Si	2.5Å	4.7Å	2.6Å
PbO-Pb	interface width	18.6Å	25.4Å	42.4Å
bulk	density	2.49Å^{-3}	2.49Å^{-3}	2.49Å^{-3}

Table 9.1: *Evolution of the PbO-layer upon melting and time.*

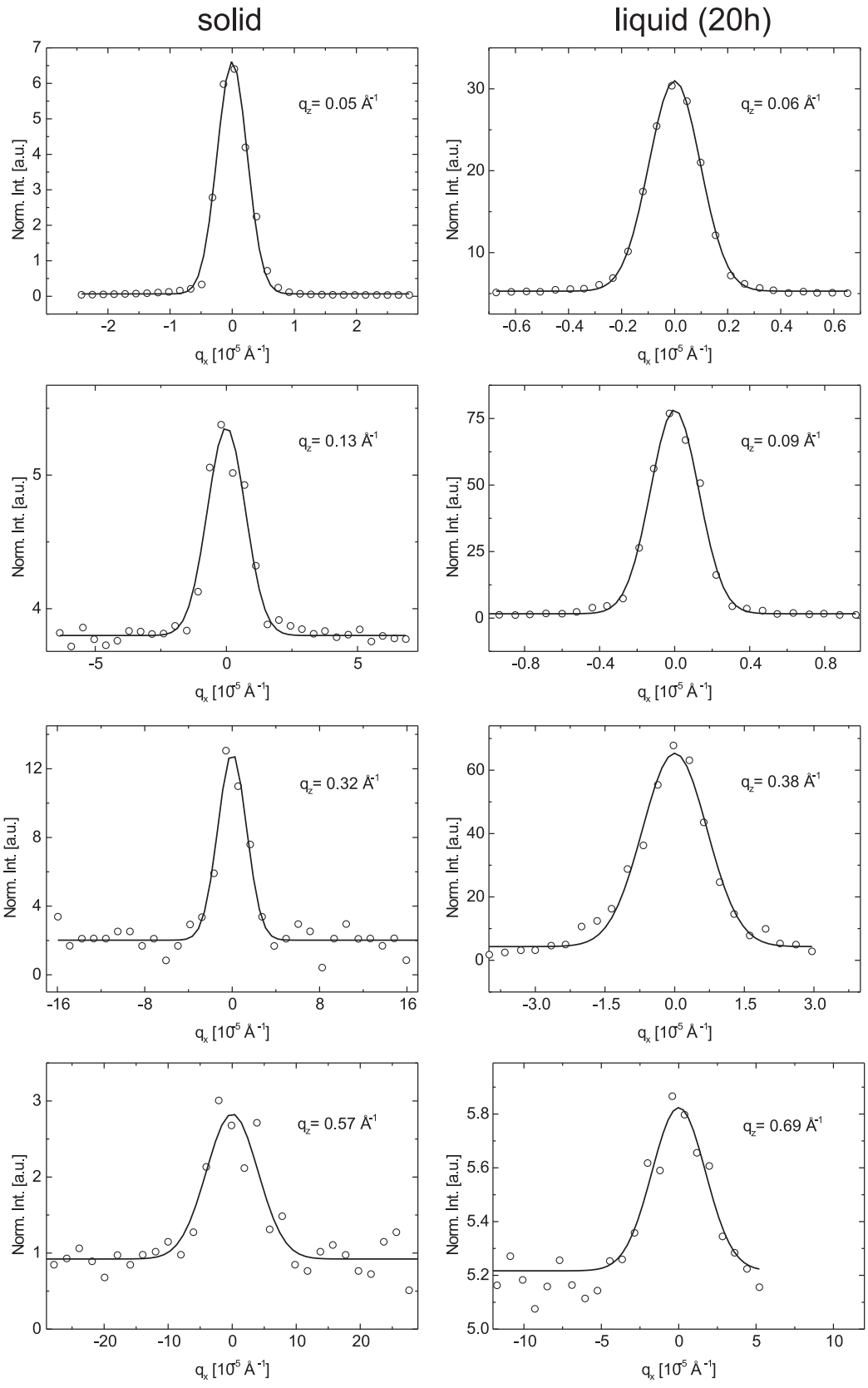

Figure 9.8: *Transverse scans of the specular rod at different vertical momentum transfers q_z at two different times.*

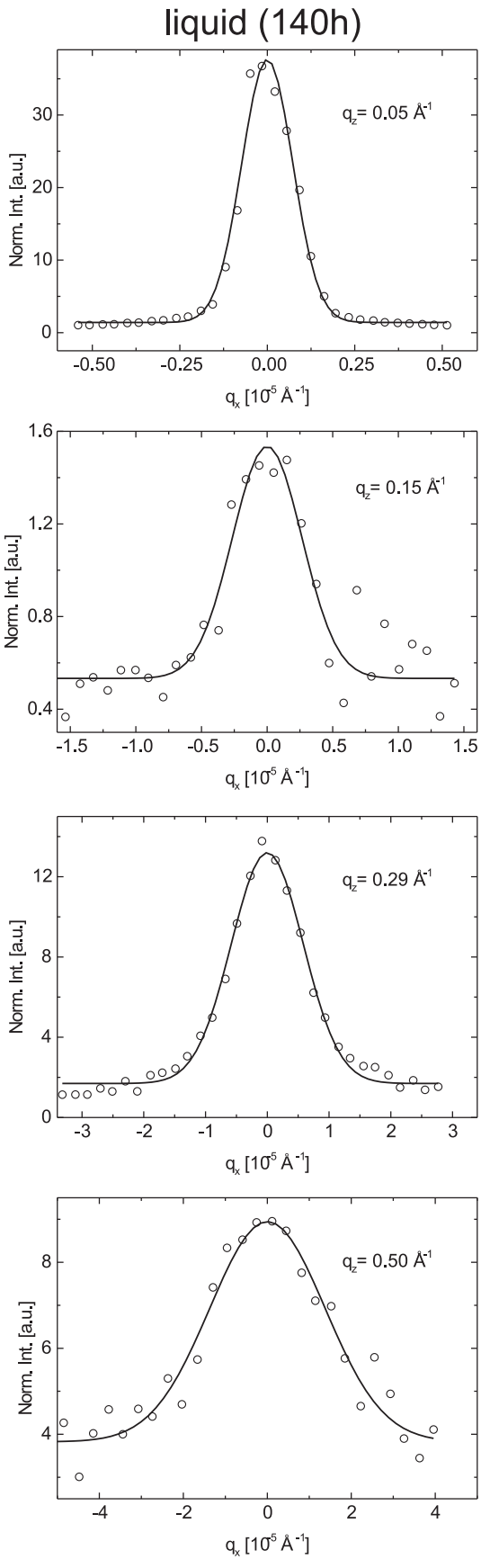

Figure 9.9: *Transverse scans of the specular rod at different vertical momentum transfers q_z after 140h.*

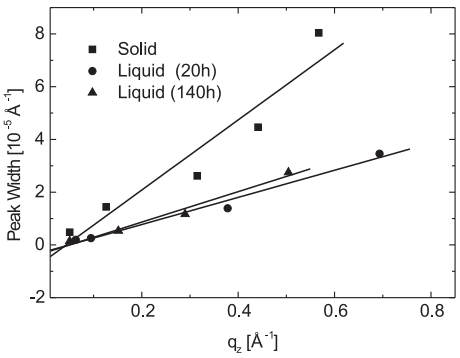

Figure 9.10: *Linear increase of the peak width with respect to q_z. The data points denote the width of the peaks shown in Figs. 9.8 and 9.9.*

9.4 Discussion

The in plane measurements were carried out to verify the presence of an additional layer between the silicon crystal and the bulk lead with a structure different from pure bulk lead. The GID measurements confirmed the presence of lead-lead correlations of the intervening layer between the Si(111) crystal and the bulk lead. The measurements and the phase diagram suggest the presence of a thick PbO-layer ($d \approx 260$Å). The structure factor of the PbO revealed an amorphous structure, which was expected from the preparation method.

Most interestingly we found an evolution of the PbO-density in time and after increasing the temperature. The reflectivity measurement at ambient temperature revealed a well defined layer of thickness 260Å with a density only half as large as the density of bulk PbO. The stable bulk crystal structure of PbO below 810K is a tetragonal structure of type $B10$. Pb and PbO are almost immiscible at the temperatures we applied (see the phase diagram of lead and oxygen in App. B).

We propose the following mechanism for the evolution of the PbO-layer: The Pb^{2+}-ions are reduced to Pb atoms by Si atoms, which are oxidized to Si^{4+}-ions and form SiO_2. Only at elevated temperatures (>600K) diffusion in the PbO-layer and at its interfaces is sufficiently large to enable a noticeable reduction of the lead in the PbO-layer. The mixing energy is reduced and Pb atoms from the liquid intermix with the PbO at the PbO-Pb interface in the range of 25Å to 42Å. After a certain time ($\sim$ 20h) a passivating SiO_2-layer has formed on top of the Si(111). The reduction-oxidation process slows down and stops finally. At this stage the low density amorphous PbO-layer is enriched with Pb-atoms reduced from PbO.

The temperature is not high enough to allow for noticeable silicon diffusion. The SiO_2 layer cannot be detected in the reflectivity measurement due to its small thickness. In addition, the electron density differs not enough from the silicon substrate in comparison with the PbO-layer. The low density of the amorphous PbO-layer is necessary for the diffusion of the metallic Pb atoms into the layer. The process is driven by an exothermic reaction (s. Eq. 9.1).

The measurements discussed in this section demonstrate that high energy microdiffraction is well suited to study reactions at deeply buried interfaces. Here we performed first studies of an internal oxidation-reduction reaction. For a more quantitative analysis of the diffusion and reaction rates more measurements at different temperatures and times are necessary. The process as discussed above is basically finished after one day at the temperatures that we applied.

Chapter 10

Conclusions and Outlook

This work reports on experiments, where established x-ray surface and interface scattering techniques (GID, XR) were extended to x-ray energies above 70keV.

Measurements were performed at four different deeply buried interfaces, three liquid metal-semiconductor systems and one metal-metaloxide-semiconductor system. The semiconductor substrates were silicon single crystals of different doping and orientation. The interfaces with its different parameters are listed in Tab. 10.1.

System	1	2	3	4
Metal	In	Pb	Pb	Pb-PbO
Surface	Si(100)	Si(100)	Si(111)	Si(111)
doping	undoped	n-doped (P)	n-doped (P)	n-doped (P)

Table 10.1: *Investigated deeply buried interfaces.*

The interfaces were prepared in situ in a portable UHV chamber. Before being mounted in the chamber the silicon samples were polished and chemically etched with a special HF-procedure. Inside the chamber the persistent SiO_2 was removed by flash heating the silicon crystal to about 1500K. The metal was molten in the chamber and the metal-oxide was removed (except for the oxide interface) by Ar^+-sputter cleaning.

After contacting the silicon with the liquid metal the chamber was transported to beamline ID15A (ESRF, Grenoble) and mounted on a specially designed high precision diffractometer.

The results of the x-ray scattering experiments are recapitulated with respect to their structure parallel and perpendicular to the interface. The results on the oxide interface are summarized separately.

Modulation of the Liquid Structure Factor

Scattering experiments in grazing angle geometry were carried out to reveal a modulation of the liquid metal structure factor parallel to the silicon surface. In all cases the presence of a well-defined deeply buried interface was verified. The position of the critical angle was found precisely at the predicted values. For the In(liq.)-Si(100) system the stability of the set up has not been sufficient to reveal a modulation of the liquid structure factor, since the measurements require long-term stability in the submicrometer and microradian range. For liquid Pb a modulation of the structure factor was found on a Si(100) [Rei00] and a Si(111) surface.

The Si(100) surface exhibits a four-fold symmetry and the Si(111) surface a three-fold symmetry. Measuring at the maximum of the liquid structure factor a modulation was discovered, which is a convolution of the surface symmetry with the preferred symmetry of the liquid building blocks close to the wall. For the lead at the Si(100) surface 20 maxima were found and six maxima at the Si(111) surface. At the Si(100) surface this corresponds to a five-fold symmetry of the liquid Pb, and to a six-fold symmetry of the liquid Pb at the Si(111) surface. In both cases the liquid building blocks of Pb arrange around a topmost Si atom. In the case of the Si(100) these are rings of five Pb atoms and in the case of Si(111) these are six Pb atoms with a center Pb atom. The different modulation is attributed to the different interface symmetry. Different clusters of liquid metal atoms are selected at each interface according to the symmetry of the solid substrate. Applying a simple model the alignment potential at the Si(100) interface was estimated to (50-90)meV and to (30-280)meV for the Si(111) interface.

Electron Density Perpendicular to the Interface

X-ray reflectivity measurements were carried out to probe the electron density perpendicular to the interface. At the liquid metal-semiconductor interface a strong deviation of the electron density of the metal from the bulk electron density on a new length scale was found. The phenomenon is not restricted to a specific interface, but was found in all liquid metal-silicon systems under investigation.

For all systems the electron density profile can be summarized qualitatively as follows: The electron density between the silicon surface and the liquid metal increases smoothly. The width of the interface is determined by the roughness of the silicon surface. An oscillatory profile is found with an increase of the density of at least 20% above the bulk density of the respective liquid metal followed by a depletion below the bulk density. The width of

the increased density is about five atomic diameters. The width of the depletion is thinner than the width of the increased density. This generic profile describes all distinctive features of the measured reflectivities (s. Fig. 10.1).

Tab. 10.2 summarizes the most important features of the electron density profiles normalized to the system specific parameters as the bulk electron density ρ_0 and the atomic radius r_0. The ratio of the maximum density increase to the bulk density $\rho_{\max}/\rho_0$ is given. And the ratios of various length scales denoted in Fig. 10.1 of the respective electron density profiles. r_0 denotes the atomic radius, which is 1.58Å for In and 1.75Å for Pb. The bulk electron density is 1.81Å^{-3} for In and 2.49Å^{-3} for Pb.

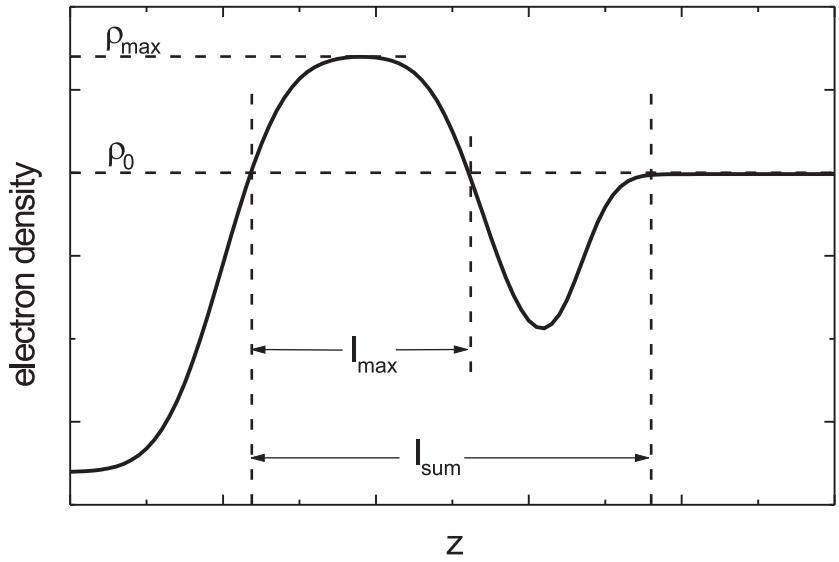

Figure 10.1: *Generic electron density profile at metal-silicon-semiconductor-interfaces.*

System	In(liq.)-Si(100)	Pb(liq.)-Si(100)	Pb(liq.)-Si(111)
$\rho_{\max}/\rho_0$	1.48	1.29	1.21
l_{sum}/r_0	25.9 (41Å)	12.5 (21.8Å)	18.4 (32.2Å)
$l_{\max}/r_0$	15.5 (24.5Å)	8.0 (14Å)	10.9 (19Å)
$l_{\text{sum}}/l_{\max}$	1.67 ± 0.22	1.56 ± 0.18	1.69 ± 0.14

Table 10.2: *Comparison of generic numbers at the different metal-silicon-semiconductor interfaces*

The maximum density increase is found for indium at an undoped Si(100) surface. It is minimal for lead at a p-doped Si(111) surface.

The ratio of the length scales with respect to the atomic radius differs by a factor of two. The In(liq.)-Si(100) system shows the largest length scale. The Pb(liq.)-Si(100) system shows the smallest length scale. The ratio between the overall length and the length of the maximum density increase is equal within the uncertainty for all systems.

This leads to the conclusion that this is a universal behavior of the electron density profile of liquid metals at silicon interfaces. A phenomenological model of the behavior attributes the finding to the saturation of the dangling bonds that emerge at a reconstructed Si-surface in contact with a metal.

Assuming that the saturated dangling bonds correspond to a charged interface, it attracts the atom cores of the liquid metal. This charged interface can be regarded as one plate of a capacitor. If it is assumed that the other plate of the capacitor of opposite charge is established somewhere in the bulk liquid, a force between the two plates emerges related to the amount of charge at the interface. This force can cause a pressure on the atom cores in the liquid metal.

The pressure induced by a completely charged Si-surface, which is one electron per dangling bond, would be fairly large: It is 267GPa for the Si(100) surface and 88.2GPa for the Si(111) surface. The density of a liquid metal is related to the pressure by $\rho/\rho_0 = 0.75 \cdot p^{0.17}$. If the density is given, the pressure in the liquid metal can be calculated. For the three systems from the maximum density increase found in the electron density fit, the results are summarized in Tab. 10.3.

	In(liq.)-Si(100)	Pb(liq.)-Si(100)	Pb(liq.)-Si(111)
$p_{\max}$	56GPa	24GPa	16.7GPa

Table 10.3: *Maximum pressure in the liquid metal calculated from the maximum density increase.*

The values are lower than the maximum possible pressure by a factor of 5-10. This can be interpreted as a continuous screening effect of the charge at the surface and in the liquid.

System specific parameters that influence the density profile of a given interface are the surface orientation, which determines the surface density of dangling bonds, the doping of the silicon crystal, and the number of valence electrons of the liquid metal.

The Pb-PbO-Si(111) Interface

Between bulk lead and a Si(111) crystal a PbO-layer of initial thickness 260Å was prepared. The initial roughness of the Si(111) surface was 2.5Å.

In comparison to the roughness at the silicon surface the roughness between the PbO-layer and the bulk Pb was large (18.6Å).

The partial structure factor of the Pb fraction of the PbO-layer showed that the layer was amorphous. The liquid structure factor of Pb was measured at the interface between the PbO-layer and the bulk Pb. Two separated critical angles were found for the oxide layer and the bulk lead, respectively.

Upon melting the bulk lead the density of the PbO-layer increased by 20.2%, the roughness at the interface to the silicon crystal increased by 88%, and the width of the interface to the bulk lead increased by 36.6%. After six days at 600K the density of the PbO-layer increased by 23.4% compared to the initial density, the thickness increased by 4.1% compared to the initial thickness. The interface width PbO-Pb(liq.) was more than doubled to 128%.

The Pb^{2+}-ions are reduced to Pb atoms by Si atoms, which are oxidized to Si^{4+}-ions and form SiO_2. For this reaction elevated temperatures (>600K) are necessary. After a certain time ($\sim$ 20h) a passivating SiO_2-layer emerged on top of the Si(111). The reduction-oxidation process stops. The loose packed amorphous PbO-layer is filled with Pb-atoms that were reduced from PbO, and the density does not increase further.

10.1 Outlook

In 2005 a new permanent high energy surface and interface diffraction end station has been set up at ID15A. This new instrument provides long-term stability for structural studies of deeply buried interfaces.

In order to advance the understanding of the liquid structure perpendicular to solid-liquid Schottky contacts a set of experiments should be carried out that systematically vary single parameters of the interface. Since the surface preparation of silicon is well established, it is straightforward to use silicon crystals in other orientations than the ones used in this work. Another important parameter is the doping level of the silicon crystal. To determine the influence of the electronic structure of the silicon crystal the doping should be varied from n-type to p-type.

In addition, electric fields can be applied across the interface. This would provide an in situ method for the reflectivity measurements at a single system with a tunable parameter.

Appendix A

Experimental tricks and Beamtimes

A.1 Cleaning of Silicon

The silicon samples were cleanded in several steps immediately before mounting them in the UHV chamber. The cleaning avoids any mechanical impact onto the samples. The single steps consist only of chemical interactions, it follows roughly the process described by Ishizaka [Ish86].

Piranha cleaning

- A mixture of sulphuric acid and hydrogen peroxide (H_2SO_4 (80%) : H_2O_2 (30%) in mixing ratio: 3 : 1) is called *Piranha acid*. Upon mixing it gets hot. The silicon sample is put into the acid as a long as it is hot (about 5 minutes). By this treatment the silicon surface gets covered by a thick oxide layer [Hig90].

- Then the sample is rinsed in purified H_2O for 3 minutes.

- The SiO_2 on the silicon sample is removed by a dip of the sample in hydrofluoric acid (HF, 5% solution) for 2 minutes.

- The remains of the acid are removed in a second rinse of the sample in purified H_2O. Only if the H_2O drains completely the previous cleaning steps were successful.

Modified RCA cleaning

The RCA cleaning[1] is the industry standard for removing contaminants from wafers.

- Heat purified H_2O in a beaker to (70°C) then add an ammonia solution (NH_3, 25%) and a hydrogen peroxide solution (H_2O_2, 30%) at a mixing ratio of 4 : 1 : 1. Keeping the mixture heated the silicon sample is put into it for 10 minutes. This step is intended to dissolve organic compounds.

- Afterwards the sample is rinsed in purified H_2O for 2 minutes.

- It follows a dip of the sample in hydrofluoric acid (HF, 5% solution) for 1 minute.

- Again the sample is rinsed in purified H_2O for 2 minutes.

- Another beaker with H_2O is heated to (70°C) then hydrochloric acid (HCl, 30%) and a hydrogen peroxide solution ($H_2O_2, 30\%$) are added at a mixing ratio of 8 : 1 : 1. Keeping the mixture heated the silicon sample is put into if for 10 minutes. This treatment dissolves inorganic compounds and it leads to an oxidation of the silicon surface.

- Afterwards the sample is rinsed in purified H_2O for 2 minutes.

- With a dip of the sample in hydrofluoric acid (HF, 5%) for 1 minute the oxide grown in the previous step is removed.

- In the last step the sample is dipped for 1 minute in a solution of pH 9-10 consisting of HF that is buffered with ammonium fluoride (NH_4F). The mixing ratio is 1:7. The required pH of 9-10 is adjusted with ammonium hydroxide (NH_4OH).

This treatment produces a sample surface that is ideally terminated with hydrogen ($\equiv Si - H$) and stable in air for minutes [Dit03, Hig90]

[1] Developed by Werner Kern in 1965 who worked for RCA (Radio Corporation of America).

A.2 Cleaning of Lead

Lead oxide on metallic lead is very resistant against many acids. A suitable acid for etching lead oxide is acetic acid in low concentration. Immersing lead in this solution is accompanied by bubble formation and a greenish luster appears on the lead. Afterwards, the surface appears blank and clean. After exposing lead again to air, it takes only seconds to form a new oxide layer.

A.3 Cleaning of Indium

A solution of HCl in low concentration is sufficient to remove indium oxide. Exposing the cleaned indium to air, it is rapidly covered again with an oxide.

A.4 Beamtimes at ID15A

Beamtime	Date	Measured Data
Apr 2000	17.04.-27.04.00	Pb(liq.)-Si(100) Reflectivity
Mar 2001	17.03.-27.03.01	In(liq.)-Si(100) Reflectivity
Jun 2001	24.06.-02.07.01	In(liq.)-Si(100) in plane
Nov 2001	13.11.-20.11.01	Pb-PbO-Si(111)
Feb 2002	14.02.-22.02.02	Pb(liq.)-Si(111) in plane
Dec 2002	10.12.-19.12.02	Pb(liq.)-Si(111) Reflectivity

Appendix B

Phase Diagrams

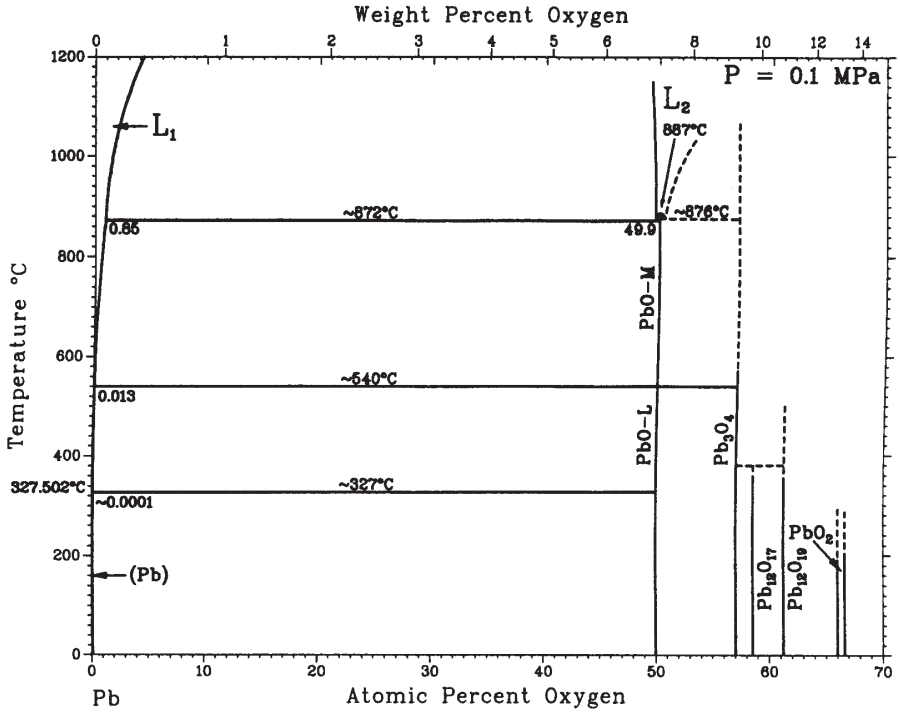

Figure B.1: *The binary Pb-O phase diagram. Taken from [Mas90].*

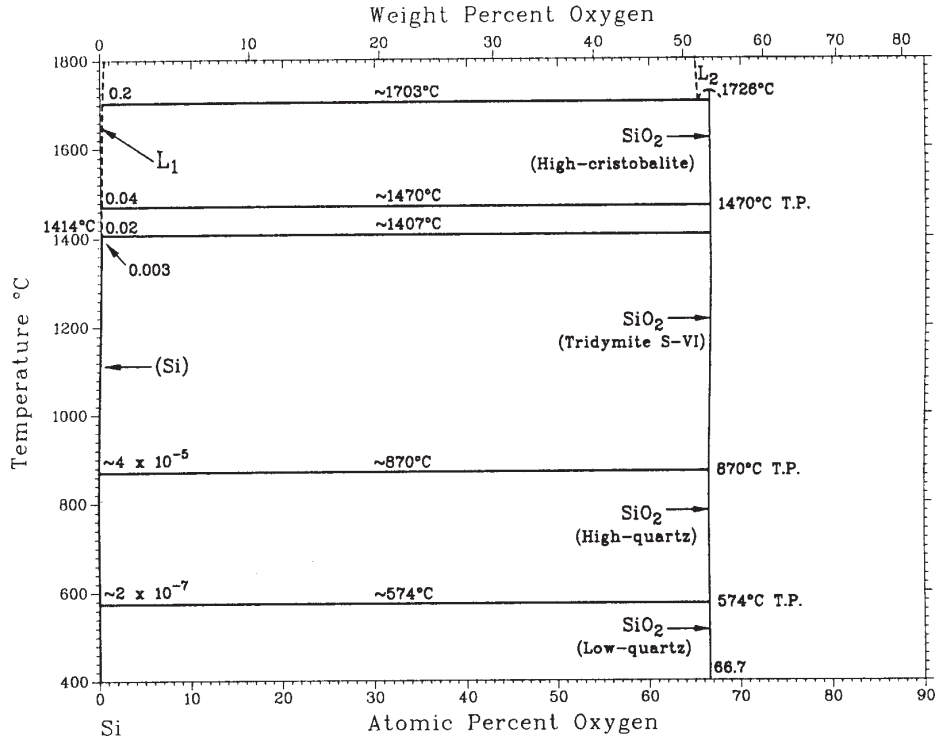

Figure B.2: *The binary Si-O phase diagram. Taken from [Mas90].*

Appendix C

Structure of Metal Adsorbates on Semiconductor Surfaces

Pb on different surfaces

amount	surface	temp.	structure	source
$\sim$ 1ML	Ge(111)	223°C	2D-liquid	[Gre90]
$\sim$ 4ML	(1×1)	> 302°C	3D-liquid	
$\sim$ 1ML	c(2×8)	250°C	$\sqrt{3} \times \sqrt{3}R30°$	[Fei86]
$\sim$ 1ML	Ge(111)	> 250°C	2D-liquid	[Ich84]
$\sim$ 1ML	Cu(110)	120°C	$p(5 \times 1)$	[Mar82]
		> 320°C	2D-liquid with anisotropy, solid $\rightarrow$ incomensurate	

Table C.1: *Structures of lead adatoms on different substrates.*

Different metals on Si surfaces

metal	amount	surface	temp.	structure	source
Al	low coverage	Si(100)		long 1D-strings of atoms, like In dimers	[Nor91], [Bro93]
	increased coverage			$p(2\times n)$ n from 5 to 2	[Yeo95]
	~ 0.5ML			$p(2\times 2)$	
Sn	low coverage	Si(100)	RT$-$150°C	dimers as for In	[Bas91b]
	0.5ML			(2×2)	
	< 0.5ML		500°C	$c(4\times 4)$, (2×6)	
	$0.5-1.0$ML			$c(4\times 8)$	
	$1.0-1.5$ML			(1×5)	
	> 2.0ML		ann.	gross rearrangement, {311} facets	
Ni $NiSi_2$	0.1ML	Si(100)	$450-500$°C ann.	$NiSi_2$ $(2\times n)$ mainly (2×8) and (2×1) dimer rows	[Kha94]
	> 0.1ML				
Ga	0.07Ml	Si(100)	$450-500$°C ann.	(2×1) dimer rows	[Nog88], [Bou88],
	-5ML		RT$-$300°C	epitaxial growth, covalent Ga-Si bonding	[Nor91]
Bi	~ 0.5ML	Si(100)	RT	(1×2) dimer rows	[Noh94]
Ag	~ 0.3ML	Si(100)	500°C	(1×2) dimer rows	[Win94]
	1ML		RT	(2×1) strong dewetting	
	10ML			only 70% covered Ag(111)||Si(100)	
	~ 1ML	Si(111)	200°C	$(\sqrt{3}\times\sqrt{3})$	
Au	1ML	Si(100)	RT	(2×2) dimer rows	[Lin94]
	-3ML			layer by layer growth	

Table C.2: *Structures of metal adatoms on different surfaces. ML: monolayer; RT: room temperature; ann.: annealing*

Akronyms

2D	2-dimensional
3D	3-dimensional
AES	Auger Electron Spectroscopy
AFM	Atomic Force Microscopy
CRL	Compound Refractive Lense
CTM	Charge Transfer Model
CW	Capillary Wave
ESRF	European Synchrotron Radiation Facility
fcc	face centered cubic
FWHM	Full Width Half Maximum
GID	Grazing / Glancing Incidence Diffraction
Hasylab	Hamburger Synchrotron Strahlungslabor
hcp	hexagonal centered cubic
HF	Hydrofluoric Acid
LEED	Low Energy Electron Diffraction
liq.	liquid
ML	Monolayer
RBS	Rutherford Back Scattering
ref	reflectivity
RHEED	Reflecting High Energy Electron Diffraction
SEM	Scanning Electron Microscopy
SLD	Scattering Length Density
STM	Scanning Tunneling Microscopy
TDS	Thermal Diffuse Scattering
TESLA	Tera Electron Volt Energy Superconducting Linear Accelerator
UHV	Ultra High Vacuum
XPS	X-ray Photo electron Spectroscopy
XR	X-ray Reflectivity

Bibliography

[AN86] J. Als-Nielsen. Handbook on synchrotron radiation, *X-ray reflectivity studies of liquid surfaces*, volume 3, chapter 12, 471–503. Elsevier Science Pub. (1986).

[AN01] J. Als-Nielsen and D. McMorrow. *Elements of modern x-ray physics*. John Wiley & Sons, Ltd. (2001).

[And02] V. Anderson and H. Lekkerkerker. *Insights into phase transition kinetics from colloid science*. Nature **416**, 811 (2002).

[Ash76] N. Ashcroft and N. Mermin. *Solid State Physics*. Holt, Rinehart and Winston, New York (1976).

[Bas91a] A. Baski, J. Nogami, and C. Quate. *Indium-induced reconstructions of the Si(100) surface*. Phys. Rev. B. **43** (11), 9316 (1991).

[Bas91b] A. Baski and C. Quate. *Tin-induced reconstructions of the Si(100) surface*. Phys. Rev. B **44** (20), 11167 (1991).

[Bec03] T. Becker and F. Mugele. *Nanofluidics: viscous dissipation in layered liquid films*. Phys. Rev. Lett. **91** (16), 166104 (2003).

[Ber59] J. Bernal. *A geometrical approach to the structure of liquids*. Nature **183** (4655), 141 (1959).

[Bit70] H. Bitterer et al. *Gmelins Handbuch der Anorganischen Chemie*, volume Blei Teil C3. Verlag Chemie, Weinheim, 8th edition (1970).

[Bou88] B. Bourguignon, K. Carleton, and S. Leone. *Surface structures and growth mechanism of Ga on Si(100) determined by LEED and Auger electron spectroscopy*. Surf. Sci. **204**, 455 (1988).

[Bra88] A. Braslau, P. Pershan, G. Swislow, B. Ocko, and J. Als-Nielsen. *Capillary waves on the surface of simple liquids measured by X-ray reflectivity*. Phys. Rev. A **38** (5), 2457 (1988).

[Bro93] G. Brocks, P. Kelly, and R. Car. *Adsorption of Al on Si(100): a surface polymerization reaction*. Phys. Rev. Lett. **70** (18), 2786 (1993).

[Bun99] O. Bunk, G. Falkenberg, J. Zeysing, L. Lottermoser, and R. Johnson. *Structure determination of the indiuminduced Si(111)-*(4×1) *reconstruction by surface x-ray diffraction*. Phys. Rev. B. **59** (19), 12228 (1999).

[Cel97] F. Celestini, F. Ercolessi, and E. Tosatti. *Can liquid metal surfaces have hexatic order*. Phys. Rev. Lett. **78** (16), 3153 (1997).

[Cha01] E. Chacón, M. Reinaldo-Falagán, E. Velasco, and P. Tarazona. *Layering at free liquid surfaces*. Phys. Rev. Lett. **87** (16), 166101 (2001).

[Che01] L. Cheng, P. Fenter, K. Nagy, M. Schlegel, and N. Sturchio. *Molecular-scale density oscillations in water adjacent to a mica surface*. Phys. Rev. Lett. **87** (15), 156103 (2001).

[Chi87] J. Chihara. *Difference in x-ray scattering between metallic and nonmetallic liquids due to conduction electrons*. J. Phys. F: Met. Phys. **17**, 295 (1987).

[Chi99] J. Chihara and G. Kahl. *Pressure-variation of structure factor of liquid Rb*. Jpn. J. Appl. Phys. **38_1**, 492 (1999).

[Coo93] S. Cook and P. Clancy. *Comparison of semi-empirical potential functions for silicon and germanium*. Phys. Rev. B **47** (13), 7686 (1993).

[Cur87] W. Curtin. *Density-functional theory of the solid-liquid interface*. Phys. Rev. Lett. **59** (11), 1228 (1987).

[Czo03] P. Czoschke, H. Hawoong, L. Basile, and T.-C. Chiang. *Quantum oscillations in the layer structure of thin metal films*. Phys. Rev. Lett. **92** (22), 226801 (2003).

[Czo04] P. Czoschke, H. Hawoong, L. Basile, and T.-C. Chiang. *Quantum beating patterns observed in the energetics of Pb film nanostructures*. Phys. Rev. Lett. **93** (3), 036103 (2004).

[Dar53] L. Darken and R. Gurry. *Physical Chemistry of Metals*. International student edition. McGraw-Hill Book company, New York (1953).

[Dev86] B. Dev, G. Materlik, F. Grey, R. Johnson, and M. Clausnitzer. *Geometrical structures of the Ge/Si(111) interface and the Si(111)* (7×7) *surface*. Phys. Rev. Lett. **57** (24), 3058 (1986).

[Die95] S. Dietrich and A. Haase. *Scattering of x-rays and neutrons at interfaces*. Phys. Rep. **260**, 1 (1995).

[DiM01] E. DiMasi, H. Tostmann, O. Shpyrko, P. Huber, B. Ocko, P. Pershan, M. Deutsch, and L. Berman. *Pairing interactions and Gibbs adsorption at the liquid Bi-In surface: a resonant x-ray reflectivity study*. Phys. Rev. Lett. **86** (8), 1538 (2001).

[Dit03] T. Dittrich. *private communication* (2003).

[Doe99] A. Doerr, M. Tolan, J.-P. Schlomka, W. Press, D. Smilgies, and W. Press. *Observation of capillary waves on liquid thin films from mesoscopic to atomic length scales*. Phys. Rev. Lett. **83** (17), 3470 (1999).

[Doe00] A. Doerr, M. Tolan, J.-P. Schlomka, and W. Press. *Evidence for density anomalies of liquids at the solid/liquid interface*. Europhys. Lett. **52** (3), 330 (2000).

[Don97] Z.-C. Dong, T. Yakabe, D. Fujita, Q. Jiang, and H. Nejo. *STM studies of initial In growth on Si(100)-*(2×1)*: the In ad-dimer chain and its I-V characteristics*. Surf. Sci. **380**, 23 (1997).

[Don01] Z.-C. Dong, D. Fujita, and H. Nejoh. *Adsorption and tunneling of atomic scale lines of indium and lead on Si(100)*. Phys. Rev. B **63** (11), 115402 (2001).

[Don02] S. Donnelly, R. Birtcher, C. Allen, I. Morrison, K. Furuya, M. Song, K. Mitsuishi, and U. Dahmen. *Ordering in a fluid inert gas confined by flat surfaces*. Science **296**, 507 (2002).

[Dos92] H. Dosch. *Critical phenomena at surfaces and interfaces*, volume 126 of *Springer Tracts in Modern Physics*. Springer Verlag, Berlin, Heidelberg (1992).

[Dra89] B. Drake, C. Prater, A. Weisenhorn, S. Gould, T. Albrecht, C. Quate, D. Cannell, H. Hansma, and P. Hansma. *Imaging crystals, polymers, and processes in water with the atomic force microscope*. Science **243** (4898), 1586 (1989).

[Eas80] D. Eastman. *Geometrical and electronic structure of Si(001) and Si(111) surfaces: A status report*. J. Vac. Sci. Technol. **17** (1), 492 (1980).

[Ebn77] C. Ebner and W. Saam. *New phase-transition phenomena in thin argon films*. Phys. Rev. Lett. **38** (25), 1486 (1977).

[Ege74] P. Egelstaff, N. March, and N. McGill. *Electron correlation functions in liquids from scattering data*. Can. J. Phys. **52**, 1651 (1974).

[Ell02] J. Elliott, A. Kelly, and A. Windle. *Recursive packing of dense particle mixtures*. J. Mat. Sci. Lett. **21**, 1249 (2002).

[Est64] P. Estrup and J. Morrison. *Studies of monolayers of lead and tin on Si(111) surfaces*. Surf. Sci. **2**, 465 (1964).

[Eva80] R. Evans. *The surface properties of liquid metals*. J. de Phys. Coll. **8** (8), 775 (1980).

[Fal98] G. Falkenberg. *STM-Untersuchungen zur Rekonstruktion und Facettierung reiner und adsorbatbedeckter Elementhalbleiteroberflächen mit (001)- und (103)-Orientierungen*. Ph.D. thesis, Universität Hamburg, DESY (1998).

[Fal05] S. Falconi, L. Lundegaard, C. Hejny, and M. McMahon. *X-ray diffraction study of liquid Cs up to 9.8GPa*. Phys. Rev. Lett. **94**, 125507 (2005).

[Fei86] R. Feidenhans'l, J. Pedersen, M. Nielsen, F. Grey, and R. Johnson. *Ge(111)$\sqrt{3} \times \sqrt{3}$-Pb: the atomic geometry*. Surf. Sci. **204**, 927 (1986).

[For03] V. Fortov. *Institute for Chemical Physics Research, Chernogolovka Russia*. http://teos.ficp.ac.ru/ (2003).

[Fra52] F. Frank. *Supercooling of liquids*. Proc. Roy. Soc. London, Ser. A **215** (1120), 43 (1952).

[Fri13] W. Friedrich. *Eine neue Interferenzerscheinung bei Röntgenstrahlen*. Physik. Zeits. **14**, 317 (1913).

[Fri52] J. Friedel. *The distribution of electrons round impurities in monovalent metals*. Phil. Mag. **43** (337), 153 (1952).

[Gin43] N. Gingrich. *The diffraction of x-rays by liquid elements*. Rev. Mod. Phys. **15** (1), 90 (1943).

[GM98] M. González-Méndez and N. Takeuchi. *First-principles calculations of the initial growth of Pb on Si(100)*. Phys. Rev. B **58** (24), 16172 (1998).

[Gre89] F. Grey, R. Feidenhans'l, M. Nielsen, and R. Johnson. *The relationship between the metastable and stable phases of Pb/Si(111)*. J. Phys. Coll. **C-7**, 181 (1989).

[Gre90] F. Grey, R. Feidenhans'l, J. Skov Pedersen, M. Nielsen, and R. Johnson. *Pb/Ge(111)1x1: An anisotropic two-dimensional liquid*. Phys. Rev. B **41** (13), 9519 (1990).

[Göt96] B. Götzelmann, A. Haase, and S. Dietrich. *Structure factor of hard spheres near a wall*. Phys. Rev. E **53** (4), 3456 (1996).

[Gui63] A. Guinier. *X-ray Diffraction*. Freeman, San Francisco (1963).

[Gul04] E. Gullikson. *www-cxro.lbl.gov/optical_constants* (2004).

[Har77] W. Harrison. *Abstract: Surface reconstruction*. J. Vac. Sci. Technol. **133** (14), 883 (1977).

[Hat00] K. Hata, T. Kimura, S. Ozawa, and H. Shigekawa. *How to fabricate a defect free Si(001) surface*. J. Vac. Sci. Technol. A **18** (4), 1933 (2000).

[Hen02] M. Heni and H. Löwen. *Do liquids exhibit local fivefold symmetry at interfaces*. Phys. Rev. E **65** (2), 021501 (2002).

[Hig90] G. Higashi, Y. Chabal, G. Trucks, and K. Raghavachari. *Ideal hydrogen termination of the Si (111) surface*. Appl. Phys. Lett. **56** (7), 656 (1990).

[HM01] D. Holland-Moritz. *Short-range order and solid-liquid interfaces in undercooled metallic melts*. Mat. Sci. Eng. A **304-306**, 108 (2001).

[Hol99] V. Holý, U. Pietsch, and T. Baumbach. *High-Resolution x-rayscattering from thin films and multilayers*, volume 149 of *Springer Tracts in Modern Physics*. Springer Verlag, Berlin, Heidelberg (1999).

[Hon03] H. Hong, C.-M. Wei, M. Chou, Z. Wu, L. Basile, H. Chen, M. Holt, and T.-C. Chiang. *Alternating layer and island growth of Pb on Si by spontaneous quantum phase separation*. Phys. Rev. Lett. **90** (7), 076104 (2003).

[Hoy01] J. Hoyt, M. Asta, and A. Karma. *Method for computing the anisotropy of the solid-liquid interfacial free energy*. Phys. Rev. Lett. **86** (24), 5530 (2001).

[Hub02] P. Huber, O. Shpyrko, P. Pershan, B. Ocko, E. DiMasi, and M. Deutsch. *Tetra point wetting at the free surface of liquid Ga-Bi*. Phys. Rev. Lett. **89** (3), 035502 (2002).

[Hui97] W. Huisman, J. Peters, M. Zwanenburg, S. de Vries, T. Derry, D. Abernathy, and J. van der Veen. *Layering of a liquid metal in contact with a hard wall*. Nature **390**, 379 (1997).

[Iar89] S. Iarlori, P. Carnevali, F. Ercolessi, and E. Tosatti. *Structure and correlations of a liquid metal surface: gold*. Surf. Sci. **211/212**, 55 (1989).

[Ich84] T. Ichikawa. *On the structure of monolayer liquid Pb on Ge(111) surfaces*. Sol. Stat. Communic. **49** (1), 59 (1984).

[Iid88] T. Iida and R. Guthrie. *The Physical Properties of Liquid Metals*. Oxford Science Publications. Clarendon Press, Oxford, 1st edition (1988).

[Ish86] A. Ishizaka and Y. Shiraki. *Low temperature surface cleaning of silicon and its application to silicon MBE*. J. Electrochem. Soc. **133** (4), 666 (1986).

[Ito94] H. Itoh, H. Tanabe, D. Winau, A. Schmid, and T. Ichinokawa. *Growth mode and surface structure of the Pb/Si(001) system observed by scanning tunneling microscopy*. J. Vac. Sci. Technol. B **12** (3), 2086 (1994).

[Jac62] J. Jackson. *Classical electrodynamics*. John Wiley & Sons, Inc., New York, 1990, 2nd edition (1962).

[Jar69] J. Jarzynski, J. Smirnow, and C. Davis. *Isothermal compressibility and the structure factor of liquid alkali metals*. Phys. Rev. **178** (1), 288 (1969).

[Kel03] K. Kelton, G. Lee, A. Gangopadhyay, R. Hyers, T. Rathz, J. Rogers, M. Robinson, and D. Robinson. *First x-ray scattering studies on electrostatically levitated metallic liquids: demonstrated influence of local icosahedral order on the nucleation barrier*. Phys. Rev. Lett. **90** (19), 195504 (2003).

[Kha94] Y. Khang, S. Kahng, K. Mang, D. Jeon, J. Lee, and Y. Kim, Y.N. Kuk. *Structure of nickel silicide on Si(001): an atomic view*. J. Vac. Sci. Technol. B **12** (3), 2094 (1994).

[Kle00] O. Klein. *unpublished*. Ph.D. thesis, Max-Planck-Institut für Metallforschung, Stuttgart (2000).

[Kra97] J. Kraft, M. Ramsey, and F. Netzer. *Surface reconstructions of In on Si(111)*. Phys. Rev. B. **55** (8), 5384 (1997).

[Kra02] H. Kraack, B. Ocko, P. Pershan, E. Sloutskin, and M. Deutsch. *Structure of a Langmuir film on a liquid metal surface*. Science **298**, 1404 (2002).

[Kum00] C. Kumpf, O. Bunk, J. Zeysing, Y. Su, M. Nielsen, R. Johnson, R. Feidenhans'l, and K. Bechgaard. *Low-temperature structure of indium quantum chains on silicon*. Phys. Rev. Lett. **85** (23), 4916 (2000).

[Len99a] B. Lengeler, C. Schroer, M. Richwin, J. Tümmler, M. Drakopoulos, A. Snigirev, and I. Snigireva. *A microscope for hard x-rays based on parabolic compound refractive lenses*. Appl. Phys. Lett. **74** (26), 3924 (1999).

[Len99b] B. Lengeler, C. Schroer, J. Tümmler, B. Benner, M. Richwin, A. Snigirev, I. Snigireva, and M. Drakopoulos. *Imaging by parabolic refractive lenses in the hard x-ray range*. J. Synchrotron Rad. **6** (6), 115 (1999).

[Li94] L. Li, C. Koziol, K. Wurm, Y. Hong, E. Bauer, and I. Tong. *Surface morphology of Pb overlayers grown on Si(100)*-(2×1). Phys. Rev. B **50** (15), 10834 (1994).

[Li02] D. Li, B. Yang, and S. Rice. *Structure of the liquid-vapor interface of a dilute ternary alloy: Pb and Sn and Ga*. Phys. Rev. B **65**, 224202 (2002).

[Lin94] X. Lin and J. Nogami. *Au on Si(001) surface: room-temperature growth*. J. Vac. Sci. Technol. B **12** (3), 2090 (1994).

[LL88] G. Le Lay, J. Peretti, M. Hanbücken, and W. Yang. *Surface spectroscopy studies of Pb monolayers on Si(111)*. Surf. Sci. **204**, 57 (1988).

[Lüs80] E. Lüscher and H. Coufal, eds. *Liquid and Amorphous Metals*. Series E: Applied Sciences - No.36. Sijthoff & Noordhoff, Alphen aan den Rijn, The Netherlands (1980).

[Mad01] A. Madsen, O. Konovalov, R. Aymeric, and G. Grübel. *Surface ordering in a concentrated suspension of colloidal particles investigated by x-ray scattering methods*. Phys. Rev. E **64** (06), 061406 (2001).

[Mag95] O. Magnussen and B. Ocko. *X-ray reflectivity measurements of surface layering in liquid mercury*. Phys. Rev. Lett. **74** (22), 4444 (1995).

[Mar79] W. Marra, P. Eisenberger, and A. Cho. *X-ray total-external-reflection-Bragg diffraction: A structural study of the GaAs-Al interface*. J. Appl. Phys. **50** (11), 6927 (1979).

[Mar82] W. Marra, P. Fuoss, and P. Eisenberger. *X-ray diffraction studies: melting of Pb monolayers on Cu(100) surfaces*. Phys. Rev. Lett. **49** (16), 1169 (1982).

[Mar02] N. March and M. Tosi. *Introduction to liquid state physic*. World scientific publishing, Singapore, London (2002).

[Mas90] T. Massalski. *Binary alloy phase diagrams*, volume 3. William W. Scott, Jr., Ohio, 2nd edition (1990).

[Mön93] W. Mönch. *Semiconductor surfaces and interfaces*. Springer Series in Surface Sciences 26, Berlin (1993).

[Nel89] D. Nelson and F. Spaepen. *Polytetrahedral order in condensed matter*. Solid State Physics **42**, 1 (1989).

[Nog88] J. Nogami, S. Park, and C. Quate. *Behavior of Ga on Si(100) as studied by scanning tunneling microscopy*. Appl. Phys. Lett. **53** (21), 2086 (1988).

[Noh94] H. Noh, C. Park, D. Jeon, K. Cho, T. Hashizume, and T. Sakurai. *Adsorption of Bi on Si(001) surface: an atomic view*. J. Vac. Sci. Technol. B **12** (3), 2097 (1994).

[Nor91] J. Northrup, M. Schabel, C. Karlsson, and R. Uhrberg. *Structure of low-coverage phases of Al, Ga, and In on Si(100)*. Phys. Rev. B **44**, 13799 (1991).

[Név80] L. Névot and P. Croce. *Caractérisation des surfaces par réflexion rasante de rayons x. application à l'étude du polissage de quelques verres silicates*. Revue Phys. Appl. **15**, 761 (1980).

[Pal67] P. Palmberg and W. Peira. *Low energy electron diffraction studies on Ge and Na-covered Ge*. Surf. Sci. **6** (1), 57 (1967).

[Pan81] K. Pandey. *New π-bonded chain model for Si$(111)-(2\times1)$ surface*. Phys. Rev. Lett. **47** (26), 1913 (1981).

[Par54] L. Parratt. *Surface studies of solids by total reflection of x-rays.*. Phys. Rev. **95** (2), 359 (1954).

[Par02] S.-H. Park and G. Sposito. *Structure of water adsorbed on a mica surface*. Phys. Rev. Lett. **89** (8), 085501 (2002).

[Pat89] J. Patel, J. Zegenhagen, P. Freeland, and M. Hybertsen. *Arsenic and gallium atom location on silicon (111)*. J. Vac. Sci. Technol. B **7** (4), 894 (1989).

[Pau38] L. Pauling. *The nature of the interatomic forces in metals*. Phys. Rev. **54**, 899 (1938).

[Pel73] B. Pellegrini. *New quantum and electronic theory of metal-semiconductor contacts*. Phys. Rev. B **7** (12), 5299 (1973).

[Pel76] B. Pellegrini. *Properties of silicon-metal contacts versus metal work-function, silicon impurity cncentration and bias voltage*. J. Phys. D: Appl. Phys. **9**, 55 (1976).

[Pie94] G. Pietsch, G. Higashi, and Y. Chabal. *Chemomechanical polishing of silicon: Surface termination and mechanism of removal*. Appl. Phys. Lett. **64** (23), 3115 (1994).

[Rai92] W. Raith et al. *Bergmann Schäfer, Festkörper, Band 6*. de Gruyter, Berlin, New York (1992).

[Rau05] M. Rauscher, H. Reichert, S. Engemann, and H. Dosch. *Local density profiles in thin films and multilayers from diffuse x-ray and neutron scattering*. Phys. Rev. B **72** (20), 205401 (2005).

[Reg95] M. Regan, E. Kawamoto, S. Lee, P. Pershan, N. Maskil, M. Deutsch, O. Magnussen, B. Ocko, and L. Berman. *Surface layering in liquid gallium: an X-ray reflectivity study*. Phys. Rev. Lett. **75** (13), 2498 (1995).

[Reg97] M. Regan, P. Pershan, O. Magnussen, B. Ocko, M. Deutsch, and L. Berman. *X-ray reflectivity studies of liquid metal and alloy surfaces.*. Phys. Rev. B **55** (23), 15874 (1997).

[Rei86] G. Reiter and S. Moss. *X-ray scattering from a two-dimensional liquid modulated by its periodic host*. Phys. Rev. B **33** (10), 7209 (1986).

[Rei99] H. Reichert. *courtesy of* (1999).

[Rei00] H. Reichert, O. Klein, H. Dosch, M. Denk, V. Honkimäki, T. Lippmann, and G. Reiter. *Observation of five-fold local symmetry in liquid lead*. Nature **408**, 839 (2000).

[Rho78] E. Rhoderick. *Metal-semiconductor contacts*. Clarendon Press, Oxford (1978).

[Rob88] I. Robinson. *The role of strain in Si(111)*7×7 *and related reconstructed surfaces*. J. Vac. Sci. Technol. A **6** (3), 1966 (1988).

[Sch59] S. Schlier and H. Farnsworth. *Structure and adsorption characteristics of clean surfaces of germanium and silicon*. J. Chem. Phys. **30** (4), 917 (1959).

[Sch87] J. Schneir, O. Marti, G. Remmers, D. Gläser, R. Sonnenfeld, B. Drake, P. Hansma, and V. Elings. *Scanning tunneling microscopy and atomic force microscopy of the liquid-solid interface*. J. Vac. Sci. Technol. A **6** (2), 283 (1987).

[Sch96] W. Schmickler. *Electronic effects in the electric double layer*. Chem. Rev. **96**, 3177 (1996).

[Sch98] T. Schmidt. *Untersuchungen zur Surfactant-modifizierten Epitaxie von Germanium auf Silizium(111)*. Ph.D. thesis, Universität Hamburg, DESY (1998).

[Sch01a] A. Schreiber, I. Ketelsen, and G. Findenegg. *Melting and freezing of water in ordered mesoporous silica materials*. Phys. Chem. Chem. Phys. **3**, 1185 (2001).

[Sch01b] C. Schroer, B. Lengeler, B. Benner, M. Kuhlmann, T. Günzler, J. Tümmler, C. Rau, T. Weitkamp, A. Snigirev, and I. Snigireva. *Parabolic compound refractive lenses for hard x-rays*. Adv. in X-ray optics **4145**, 274 (2001).

[Sch02] T. Schenk, D. Holland-Moritz, V. Simonet, R. Bellisent, and D. Herlach. *Icosahedral short-range order in deeply undercooled metallic melts*. Phys. Rev. Lett. **89** (7), 075507 (2002).

[Sch03] A. Schöps. *Diffuse Röntgenstreuung an binären Legierungen*. Ph.D. thesis, Max-Planck-Institut für Metallforschung, Stuttgart (2003).

[Sco00] T. Scopigno, U. Balucani, G. Ruocco, and F. Sette. *Density fluctuations in molten lithium: inelastic x-ray scattering study*. J. Phys.: Condens. Matter **12**, 8009 (2000).

[See02] O. Seeck, H. Kim, D. Lee, D. Shu, I. Kaendler, J. Basu, and S. Sinha. *Observation of thickness quantization in liquid films confined to molecular dimension*. Europhys. Lett. **60** (3), 376 (2002).

[Sen00] S. Senapati and A. Chandra. *Surface charge induced modifications of the structure and dynamics of mixed dipolar liquids at solid-liquid interfaces: a molecular dynamics simulation study*. J. Chem. Phys. **113** (19), 8817 (2000).

[Sha60] P. Sharrah, J. Petz, and R. Kruh. *Determination of atomic distributions in liquid lead-bismuth alloys by neutron and x-ray diffraction*. J. Chem. Phys. **32** (1), 241 (1960).

[Sha76] R. Shannon. *Revised effective ionic radii and systematic studies of interatomic distances in halides and chalcogenides*. Acta Cryst. A **32**, 751 (1976).

[She04] G. Shen, V. Prakapenka, M. Rivers, and S. Sutton. *Structure of liquid iron at pressures up to 58GPa*. Phys. Rev. Lett. **92**, 185701 (2004).

[Sik87] J. Sikkenk, J. Indekeu, J. van Leeuwen, and E. Vossnack. *Molecular-dynamics simulation of wetting and drying at solid-fluid interfaces*. Phys. Rev. Lett. **59** (1), 98 (1987).

[Siv91] D. Sivia, W. Hamilton, and G. Smith. *Analysis of neutron reflectivity data: maximum entropy Bayesian spectral analysis and speckle holography*. Physica B **173** (1-2), 121 (1991).

[Siw03] B. Siwick, J. Dwyer, R. Jordan, and R. Miller. *An atomic-level view of melting using femtosecond electron diffraction*. Science **302**, 1382 (2003).

[Smo41] R. Smoluchowski. *Anisotropy of the electronic work function of metals*. Phys. Rev. **60** (11), 661 (1941).

[Sno77] I. Snook and D. Henderson. *Monte Carlo studies of a hard-sphere fluid near a hard wall*. J. Chem. Phys. **68** (5), 2134 (1977).

[Spa75] F. Spaepen. *A structural model for the solid-liquid interface in monatomic systems*. Acta Met. **23**, 729 (1975).

[Spa76] F. Spaepen and R. Meyer. *The surface tension in a structural model for the solid-liquid interface*. Scr. Mett. **10**, 257 (1976).

[Ste83] P. Steinhardt, D. Nelson, and M. Ronchetti. *Bond-orientational order in liquids and glasses*. Phys. Rev. B **28** (2), 784 (1983).

[Str03] R. Streitel. *Oxidation von CoGa Oberflächen untersucht mit oberflächensensitiver Röntgenbeugung*. Ph.D. thesis, Max-Planck-Institut für Metallforschung, Stuttgart (2003).

[Suo02] P. Suortti and T. Tschentscher. *High-energy x-ray scattering at third-generation synchrotron radiation sources*. In *Third-generation hard x-ray synchrotron radiation sources*, edited by D. Mills, chapter 7, 237–266. John Wiley & Sons, Inc. (2002).

[Tal86] J. Tallon. *Layerwise structure in the fcc(111) solid-liquid interface*. Phys. Rev. Lett. **57** (11), 1328 (1986).

[Tol99] M. Tolan. *X-ray scattering from soft-matter thin films*, volume 148 of *Springer Tracts in Modern Physics*. Springer-Verlag, Berlin, Heidelberg (1999).

[Ton94] M. Toney, J. Howard, J. Richer, G. Borges, J. Gordon, O. Melroy, D. Wiesler, D. Yee, and L. Sorensen. *Voltage-dependent ordering of water molecules at an electrode-electrolyte interface*. Nature **368**, 444 (1994).

[Ton95] M. Toney, J. Howard, J. Richer, G. Borges, J. Gordon, O. Melroy, D. Wiesler, D. Yee, and L. Sorensen. *Distribution of water molecules at Ag(111)/electrolyte interface as studied with surface x-ray scattering*. Surf. Sci. **335**, 326 (1995).

[Ton99] Q.-Y. Tong and U. Gösele. *Semiconductor Wafer Bonding*. Science and Technology. John Wiley & Sons, Inc., New York, 1 edition (1999).

[Tor00] S. Torquato, T. Truskett, and P. Debenedetti. *Is random close packing of spheres well defined?*. Phys. Rev. Lett. **84** (10), 2064 (2000).

[Tos99] H. Tostmann, E. DiMasi, B. Ocko, M. Deutsch, and P. Pershan. *X-ray studies of liquid metal surfaces*. J. Non-Cryst. Sol. **250-252**, 182 (1999).

[Tos00] H. Tostmann, E. DiMasi, O. Shyrpko, P. Pershan, B. Ocko, and M. Deutsch. *Microscopic structure of the wetting film at the surface of liquid Ga-Bi alloys*. Phys. Rev. Lett. **84** (19), 4385 (2000).

[Tsu96] K. Tsuji, Y. Katayama, Y. Morimoto, and O. Shimomura. *Structure of liquid rubidium under high pressure*. J. of Non-Cryst. Sol. **205-207**, 295 (1996).

[UBn02] E. Urrutia-Bañuelos, A. Posada-Amarillas, and I. Garzón. *Temperature effect on the local order of liquid Ni, Ag, and Pb: a molecular dynamics study*. Phys. Rev. B **66** (14), 144205 (2002).

[Uji01] T. Ujihara, G. Sazaki, K. Fujiwara, N. Usami, and K. Nakajima. *Physical model for the evaluation of solid-liquid interfacial tension in silicon*. J. Appl. Phys. **90** (2), 750 (2001).

[Upt04] M. Upton, C. Wei, M. Chou, T. Millter, and T.-C. Chiang. *Thermal stability and electronic stucture of atomically uniform Pb films on Si(111)*. Phys. Rev. Lett. **93** (2), 026802 (2004).

[vdV85] J. van der Veen. *Ion beam crystallography of surfaces and interfaces*. Surf. Sci. Rep. **5** (5-6), 199 (1985).

[vH79] H. von Helmholtz. Wied. Ann. **7**, 337 (1879).

[vL75] J. van Loef. *Hard core size at the melting point and Lindemann law*. J. of Chem. Phys. **61** (4), 1605 (1975).

[War69] B. Warren. *X-ray Diffraction*. Dover Publications Inc., New York, 1990 edition (1969).

[Was72] Y. Waseda and K. Suzuki. *Structure factor and atomic distribution in liquid metals by x-ray diffraction*. Phys. Stat. Sol. b **49**, 339 (1972).

[Was80] Y. Waseda. http://www.iamp.tohoku.ac.jp (1980).

[Was81] Y. Waseda. *The structure of liquids, amorphous solids and solid fast ion conductors*. Prog. Mat. Sci. **26**, 1 (1981).

[Wei92] H. Weitering, D. Heslinga, and T. Hibma. *Structure and growth of epitaxial Pb on Si(111)*. Phys. Rev. B. **45** (11), 5991 (1992).

[Wer63] W. Wertheim. *Exact solution of the Percus-Yevick integral equation for hard spheres*. Phys. Rev. Lett. **10** (8), 321 (1963).

[Win94] D. Winau, H. Itoh, A. Schmid, and T. Ichinokawa. *Ag on Si(001)*(2×1) *formation of a* 2×3 *superstructure*. J. Vac. Sci. Technol. B **12** (3), 2082 (1994).

[Win05] M. Winter. *www.webelements.com* (2005).

[Wri46] D. Wrinch. *Fourier Transforms and Structure Factors*. ASXRED monograph, Number 2. The american society for x-ray and electron diffraction (1946).

[Yeo95] H. Yeom, T. Abukawa, M. Nakamura, S. Suzuki, S. Sato, K. Sakamoto, T. Sakamoto, and S. Kono. *Initial stage growth of In and Al on a single-domain Si(001)*2×1 *surface*. Surf. Sci. **341**, 328 (1995).

[Yeo02] H. Yeom, K. Horikoshi, H. Zhang, K. Ono, and R. Uhrberg. *Nature of the broken-symmetry phase of the one-dimensional metallic In/Si(111) surface*. Phys. Rev. B. **65**, 241307 (2002).

[Yu01] C.-J. Yu, A. Richter, J. Kmetko, S. Dugan, S. Datta, and P. Dutta. *Structure of interfacial liquids: x-ray scattering studies*. Phys. Rev. E **63**, 021205 (2001).

[Zha92] R. Zhao, J. Jia, and W. Yang. *Surface superstructures of the Pb/Si(100) system*. Surf. Sci. Lett. **274**, 519 (1992).

[Zha93] R. Zhao, J. Jia, and W. Yang. *Intermixing at Pb/Si(111) and Pb/Si(001) interfaces studied with electron- energy-loss spectroscopy*. Phys. Rev. B. **48** (8), 5333 (1993).

[Zha98] Z. Zhang, Q. Niu, and C.-K. Shih. *"Electronic growth" of metallic overlayers on semiconductor substrates*. Phys. Rev. Lett. **80** (24), 5381 (1998).

[Zha05] T. Zhang, T. Gu, and X. Zhang. *Simulations of structures of liquid copper under pressure*. Mod. Sim. Mater. Sci. Eng. **13**, 753 (2005).

[Zwa00] M. Zwanenburg, J. Bongaerts, J. Peters, D. Riese, and J. van der Veen. *X-ray waveguiding studies of ordering phenomena in confined fluids*. Phys. Rev. Lett. **85** (24), 5154 (2000).

Acknowledgments

Zum Schluß dieser Arbeit möchten ich mich noch bei all denen bedanken, die das Gelingen dieser Arbeit überhaupt erst ermöglicht haben.

Herr Prof. Dr. H. Dosch danke ich für die Aufnahme in seine Arbeitsgruppe. Insbesondere möchte ich mich bei ihm für die Unterstützung in der Zeit nach meinem Unfall bedanken. Herr Prof. Dr. C. Bechinger danke ich für die freundliche Übernahme des Zweitgutachtens und dem Interesse an dieser Arbeit. Harald Reichert danke ich für die Betreuung dieser Arbeit und die Organisation der vielen Strahlzeit. Veijo Honkimäki und Thomas Buslaps danke ich für Unterstützung während der Strahlzeiten in Grenoble, sowie Andreas Freund für die Politur der Silizium Proben.

Am Max-Planck-Institut hatte ich so viele nette Kollegen, die immer hilfsbereit waren, so dass es wahrscheinlich nicht möglich ist, hier eine vollständige Liste anzugeben. Die Kollegen der Werkstätten und verschiedenen Service-Einrichtungen sind immer eine große Hilfe bei der Durchführung von diffizilen Experimenten wie in dieser Arbeit. Insbesondere Annette Weißhardt und Frank Adams ließen mich nie im Labor im Stich.

Viele Mitdoktoranden und Diplomanden waren oft mehr als nur Diskussionspartner, sie waren immer dabei etwas Leben in den Institutsalltag zu bringen: Matthias Linde, Bert Nickel, Christian Ern, Bärbel Krause, Dina Carbone, Ulrich Gebhardt, Reinhard Streitel, Alina Vlad, Mélissa Delheusy, Max Nülle, Alexander Udyansky, Oleg Shchyglo, Thomas Eckert, Sebastian Schöder, Cristian Mocuta, Hans Trenkler.

Noch manches mal denke ich an Oliver Klein, der mir in so kurzer Zeit manchen Kniff im Labor zeigte und der mehr als nur ein "Vorgänger" war, dann aber so schmerzlich aus dem Leben gerissen wurde.

Besonders hervorzuheben sind die "5G1 Jungens", ohne die so vieles undenkbar gewesen wäre: Andreas Schöps (Der Schöppes), Simon Engemann und Ingo Ramsteiner.

Ich danke meiner Familie für die konstante Unterstützung und schließlich – was wäre das alles ohne Andrea gewesen?